UNIVERSITY OF CALIFORNIA, MERCED

Ancient Predators in a Changing World: How Eocene Climate Shifts Shaped Shark Ecology in Antarctica

A dissertation submitted in partial satisfaction of the requirements
for the degree Doctor of Philosophy

in

Environmental Systems

by

Gabriele Larocca Conte

Committee in charge:

Dr. Jessica L. Blois, Chair
Dr. Sora L. Kim
Dr. Matthew Hutchinson
Dr. Jürgen Kriwet

2024

The Dissertation of Gabriele Larocca Conte is approved, and it is acceptable in quality and form for publication on microfilm and electronically:

_____
Sora L. Kim, Advisor

_____
Jessica L. Blois, Chair

_____
Matthew Hutchinson

_____
Jürgen Kriwet

University of California, Merced

2024

Table of Contents

List of Tables

List of Figures

Acknowledgments

This has been an incredible journey, shaped by the contributions of many. First and foremost, I want to express my heartfelt gratitude to my wife, Carlotta Leoncini, for her unwavering support and encouragement throughout these years. Her strength and belief in me have been invaluable, and I could not have achieved this milestone without her by my side.

Next, I want to extend my deepest gratitude to my Ph.D. advisor, Sora Kim, for her endless support, both as a mentor and as a person. Her guidance over the past years has reignited my hope in fostering a community that values collaboration and fosters a healthy work environment grounded in diversity, equity, and inclusion. She has shown me that such environments do exist—and that advocating for respect and understanding, especially during challenging times, is always worth the effort. I want to also thank my committee members, Jessica Blois, Matthew Hutchinson, and Jürgen Kriwet, for their mentorship and support throughout my Ph.D. journey.

I am deeply thankful to all past and present members of the SIELO lab at UC Merced, Robin Trayler, Jon Kuntz, Gina Palefsky, Ashley Liao, Hyejoo Ro, Leila Wahab, Valor Smallwood, Anna Jurisick, Lauren Lopes, Mario Hernandez, DaeVionn Chew, Molly Karnes, Rachel Chan, Divia Feinstein, Anthony Vasquez, Antonio Gonzalez, James Waterford, Alyssa Valdez, Pedro Valencia Landa, Maya Morris, Lelah Munier, Anthony Vazquez, Allison Greer, and Alejandro Montiel. You have all been like family to me and thank you so much for your professional and personal support.

Many thanks to all collaborators and educators who have made me a better scientist and educator, including Thomas Mörs, Aric Mine, Linda Ivany, Matthew Huber, Alexandra Jahn, Michael Bizimis, Howard Scher, Adam Aleksinski, Gabriel Franco, Jeremy McCormack, Mohamad Bazzi, Patricia Holroyd, Seth Finnegan, Marta Biarnes, Jasmine Graham, Teamrat Ghezzhei, Liza Gomez Daglio, Sylvain Masclin, Claire Lukens, and Stephen Hart.

Last but not least, I want to thank Lucia Cresci, Giacomo Larocca Conte, Emilio Larocca Conte, and all my family members and friends for their unwavering support, even from afar.

This project was supported by the National Science Foundation through the grants *Collaborative Research: Integrating Eocene Shark Paleoecology and Climate Modeling to Reveal Southern Ocean Circulation and Antarctic Glaciation* (award #1842049) and *CAREER: Shark Survivor! Interdisciplinary Approaches to Modern and Paleoecology in Research and Education* (award #2239981), both awarded to Sora Kim.

Chapter 1 is a full reprint of the material as it appears in *Chemical Geology*: https://doi.org/10.1016/j.chemgeo.2024.122000. © 2024 Elsevier. The dissertation author, Gabriele Larocca Conte, contributed to writing, reviewing, and editing both the original and final drafts, as well as visualization, validation, supervision, resources, project

administration, methodology, investigation, formal analysis, data curation, and conceptualization. Lauren E. Lopes contributed to writing, reviewing, and editing both the original and final drafts, as well as software, methodology, investigation, formal analysis, data curation, and conceptualization. Aric H. Mine contributed to writing, reviewing, and editing, as well as the original draft, visualization, validation, supervision, resources, methodology, investigation, formal analysis, and conceptualization. Robin B. Trayler contributed to visualization, validation, software, resources, methodology, investigation, formal analysis, and data curation. Sora L. Kim contributed to writing, reviewing, and editing both the original draft and final drafts, as well as visualization, validation, supervision, software, resources, project administration, methodology, investigation, funding acquisition, formal analysis, data curation, and conceptualization.

Chapter 2 is a full reprint of the material as it appears in *Paleoceanography and Paleoclimatology*: https://doi.org/10. 1029/2024PA004965. © 2024 Wiley Open Access CC BY. The dissertation author, Gabriele Larocca Conte, contributed to writing, reviewing, and editing the original and final draft, data curation, formal analysis, methodology, investigation, and conceptualization. Adam Aleksinski contributed to writing, reviewing, and editing the original and final drafts, formal analysis, data curation, and conceptualization. Ashley Liao contributed to writing, reviewing, and editing, data curation, formal analysis, and investigation. Jürgen Kriwet contributed to writing, reviewing, and editing, data curation, formal analysis, and conceptualization. Thomas Mörs contributed to writing, reviewing, and editing, data curation, formal analysis, and conceptualization. Robin B. Trayler contributed to writing, reviewing, and editing, data curation, formal analysis, and visualization. Linda C. Ivany contributed to writing, reviewing, and editing, data curation, formal analysis, and conceptualization. Matthew Huber contributed to writing, reviewing, and editing, data curation, formal analysis, and conceptualization. Sora L. Kim contributed to writing, reviewing, and editing, supervision, project administration, funding acquisition, and conceptualization.

Curriculum Vitae

EDUCATION

- Aug. 2019 to Dec. 2024

Doctor of Philosophy in Environmental Systems
University of California Merced (UCM), Merced, CA, USA

- Sep. 2015 to Mar. 2018

Master of Science in Geology and Land Management
Alma Mater Studiorum – University of Bologna, Bologna, Italy

- Sep. 2011 to Mar. 2015

Bachelor of Science in Natural Sciences
Alma Mater Studiorum – University of Bologna, Bologna, Italy

PUBLICATIONS

- **Larocca Conte G.**, Aleksinski A., Liao A., Kriwet J., Mörs T., Trayler R. B., Ivany L. C., Huber M., Kim S. L. Eocene Shark Teeth From Peninsular Antarctica: Windows to Habitat Use and Paleoceanography. Paleoceanography and Paleoclimatology, 39(11): e2024PA004965. https://doi.org/10. 1029/2024PA004965

- **Larocca Conte G.,** Lopes L., Mine A. H., Trayler R.B., Kim. S.L., 2024. SPORA, a new silver phosphate precipitation protocol for oxygen isotope analysis of small, organic-rich bioapatite samples. Chemical Geology 651, 122000. https://authors.elsevier.com/sd/article/S0009-2541(24)00080-9.

- **Larocca Conte G.**, Trevisani T., Guaschi P., Fanti F., 2020. New specimen of the rare requiem shark *Eogaleus bolcensis* from the Bolca Lagerstätte, Italy. Acta Palaeontologica Polonica, 65(3): 547-560. https://www.app.pan.pl/article/item/app007252020.html

- **Larocca Conte G.**, Bazzi M., Trevisani T., Guaschi P., Barbieri R., Fanti F., 2019. Redescription of a large lamniform shark from the Upper Cretaceous (Santonian) of Italy. Cretaceous Research, 99: 156-158. https://doi.org/10.1016/j.cretres.2019.02.011

- Fanti F., **Larocca Conte G.**, Angelicola L., Cau A., 2016. Why so many dipnoans? A multidisciplinary approach on the lower cretaceous lungfish record from Tunisia. Palaeogeography, Palaeoclimatology, Palaeoecology, 449: 255-256. https://doi.org/10.1016/j.palaeo.2016.02.024

- Fanti F., Minelli D., **Larocca Conte G.**, Miyashita T, 2016. An exceptionally preserved Eocene shark and the rise of modern predator-prey interactions in the coral reef food web. Zoological Letters, 2:9 p. https://zoologicalletters.biomedcentral.com/articles/10.1186/s40851-016-0045-4

TALKS

- **Larocca Conte G.**, Liao A., Kriwet J., Mörs T., Trayler R. B., Aleksinski A., Ivany L. C., Huber, M., Kim S. L. Investigating Habitat Use of Sharks and Their Relatives in Seymour Island, Antarctica, across the Eocene Epoch. GSA Connects 2024 meeting in Anaheim, United States, on September 23, 2024. https://gsa.confex.com/gsa/2024AM/meetingapp.cgi/Paper/400732

POSTERS

- Chew D., Bazzi M., **Larocca Conte G.** A morphometric approach to dietary identification within prehistoric sharks. UC Merced Undergraduate Research Opportunities Center (UROC) Annual Undergraduate Research Symposium. Merced, United States, August 2, 2024.

- **Larocca Conte G.**, Liao A., Kriwet J., Mörs T., Kim S. L. From Eocene Greenhouse to Icehouse: Probing environmental and palaeoecological processes on sharks and their relatives from Seymour Island, Antarctica. American Geophysical Union (AGU) Fall meeting. San Francisco, United States, December 11-15, 2023. https://ui.adsabs.harvard.edu/abs/2023AGUFMPP43E1712L/abstract

- **Larocca Conte G.**, Lopes L., Mine A. H., Trayler R. B., Kim S. L. Purified phosphate and low sample size: SPORA, a new silver phosphate precipitation procedure for $\delta^{18}O_p$ analysis. American Geophysical Union (AGU) Fall meeting. San Francisco, United States, December 11-15, 2023. https://ui.adsabs.harvard.edu/abs/2023AGUFM.V21B0121L/abstract

- **Larocca Conte G.**, Lopes L., Mine A. H., Trayler R. B., Kim S. L. A new silver phosphate rapid precipitation protocol for oxygen stable isotope analysis minimizes organic and inorganic contamination. 1st Northern California Geobiology Symposium, Stanford, United States, April 15, 2023.

- **Larocca Conte G.**, Kriwet J., Mörs T., Kim S. L. Shark assemblage in La Meseta Formation: the interplay between paleoecology and paleoenvironment. 12th International Conference on Climatic and Biotic Events of the Paleogene (CBEP12), Bremen, Germany, August 22-25, 2022.

- **Larocca Conte G.** An exceptionally preserved Eocene shark and the origins of modern reef communities. Progressive Paleontology, Oxford, United Kingdom, May 19-22, 2016.

- **Larocca Conte G.**, Minelli D., Zorzin R., Fanti F. Gli squali fossili di Bolca conservati a Verona e Bologna. XXIV Conference of Associazione Nazionale Musei Scientifici (ANMS), Livorno, Italy, November 11-14, 2014.

ANALYTICAL AND TECHNICAL EXPERIENCE

Instrumentation:

- ThermoFisher Delta V+ IRMS
- ThermoFisher TC/EA
- Costech 4010 Elemental Analyzer
- ThermoScientific Evolution 300 UV-Vis spectrophotometer
- Agilent Cary 60 UV-Vis spectrophotometer
- Bruker VERTEX 70v FT-IR spectrophotometer
- ThermoFisher GasBench II

Wet Chemistry Techniques:

- Silver phosphate precipitation protocols for stable oxygen isotope analysis
- Molybdate blue spectrophotometric technique for phosphate concentration measurements
- Lipid and urea extractions from muscle tissues for stable carbon and nitrogen isotope measurements

Computational:

- *R* Studio programming language: proficient users of tidyverse package, moderate user of for loops, and Bayesian statistics
- Geochemical data correction for stable isotope analysis in IRMS continuous flow systems
- Adobe Illustrator and Photoshop
- tpsUtil and tpsDig2 for 2D landmark morphometric digitalization for fossil specimens

AWARDS

2024:

- Summer 2024 ES Summer Fellowship: Did sand tiger sharks share habitat and resources across the Eocene?

- 1st Annual LES Student Paper Award 2024: the manuscript "SPORA, a new silver phosphate precipitation protocol for oxygen isotope analysis of small, organic-rich bioapatite samples" was awarded "Best Paper" submitted by graduate students as first author by the LES department.

2023:

- MacKenzie Scott Graduate Student Supplemental Travel Award 2023: travel grant to attend AGU 2023 Fall meeting.

2020:

- Summer 2020 ES Summer Fellowship: Overcome analytical limits: a new slow silver phosphate (Ag_3PO_4) precipitation protocol for small-sized shark teeth.

SCIENTIFIC OUTREACH

2024:

- Shark Survivor! Workshop led by CalTeach UC Merced, Bobcat Summer STEM Academy: co-instructor.
- Young Naturalist Academy Program at Merced's Kids Discovery Stations.

2022 – 2023:

- Diversifying Ocean Science program led by Minority in Shark Scientists (MISS): laboratory Techniques Concentration co-mentor.

2021:

- Unlearning Racism in Geoscience (URGE). Member of the Stable Isotope Ecology Group Pod.
- Shark Survivor! Workshop led by CalTeach UC Merced, Bobcat Summer STEM Academy, Virtual Edition: co-instructor.

2020:

- Shark Survivor! Workshop led by CalTeach UC Merced, Bobcat Summer STEM Academy, Virtual Edition: co-instructor.

2019:

- Oct. 2019: Scientists Uncover Shark Fossil Secrets in Italy, Forbes interview.

PROFESSIONAL DEVELOPMENT

May to Jul. 2020, 2021, and 2024:

- Designing scientific outreach activities for middle school students. Workshops led by Marta Biarnes, founder and CEO of STEMSpark.

TEACHING ASSISTANTSHIP

2024 – 2024

- BIO 174 01/ESS 174 01, Stable Isotopes in Ecosystems. IOR: Dr. Sora L. Kim (present)
- ESS 015 01, Weather, Climate, and the Environment. IOR: Dr. Sylvain Masclin (Spring Semester).

2021 – 2022:

- ESS 020 01, Fundamentals in Geology. IOR: Dr. Claire Lukens (Fall Semester 2021 and 2022).

2020:

- ESS 002 01, Sustainability Science. IORs: Dr. Liza Gomez Daglio (Spring Semester) and Dr. Sylvain Masclin (Fall Semester).

MENTORED STUDENTS

2023 - 2024

- DaeVionn Chew: undergraduate student from UC Merced enrolled in the UROC-SURI summer program. The student has been trained in morphometric techniques on shark tooth specimens (data acquisition and analysis).

- James Waterford: undergraduate student from UC Merced mentored on extrapolation and analysis of offline climatic model output data.

- Ashley Liao: undergraduate student from UC Merced trained in phosphate bioapatite analysis of bone and tooth specimens (sampling strategies, silver phosphate precipitation procedures, Isotope Ratio Mass Spectrometry analysis, and data correction).

2022:

- Lauren Lopes: undergraduate student from UC Merced trained in phosphate bioapatite analysis of bone and tooth specimens (sampling strategies and silver phosphate precipitation procedures)

Abstract of the Dissertation

Ancient Predators in a Changing World: How Eocene Climate Shifts Shaped Shark Ecology in Antarctica

by

Gabriele Larocca Conte

Doctor of Philosophy, Environmental Systems
University of California, Merced 2024
Dr. Sora L. Kim, Graduate Advisor
Dr. Jessica L. Blois, Chair

Sharks and their relatives have been successful predators for over 400 million years, playing critical ecological roles in marine environments. Their recent, dramatic population decline—largely due to climate change—poses a serious threat to ecosystem stability. Their fossil record provides a valuable system to document how sharks have coped, survived, or declined in response to major climatic changes over geological time. Insights from these records are vital to inform current conservation practices. This dissertation investigates how major climatic events influenced the temperature, salinity, and dietary preferences of sharks that lived during the Eocene Epoch (54–33.9 Ma) in Antarctica, a region that underwent significant environmental shifts as the global climate cooled at the Epoch's end. The study develops a new protocol to isolate silver phosphate for geochemical analysis, enabling temperature and salinity estimations from bones and teeth, including various shark tooth sizes. Temperature and salinity preferences were inferred for both pelagic and benthic shark taxa (n = 16) across the Eocene. The study also examines geochemical and morphological metrics of Eocene sand tiger sharks and compares them with the critically endangered modern species *Carcharias taurus*. By addressing a longstanding analytical variability enigma affecting temperature and salinity estimates derived from shark teeth, we found that pelagic and benthic Eocene sharks generally preferred similar conditions, with only cooler-adapted species continuing in the fossil record likely surviving climate change. Additionally, our results suggest that fossil sand tiger sharks serve as valuable analogs for the extant *C. taurus* in terms of habitat and dietary preferences. Altogether, this study underscores the significant impact of climate on sharks and highlights how their fossil record can illuminate aspects of modern shark ecology.

1. Introduction of the Dissertation

1.1 Introduction

Sharks and rays (Chondrichthyes: Elasmobranchii) are among the ocean's largest and most wide-ranging predators, playing crucial roles as meso- or apex predators depending on size, ontogeny, seasons, and the presence of other marine predators (Compagno, 2002; Heithaus et al., 2008; Heupel et al., 2019; Hussey et al., 2011; Latour & Gartland, 2020; Pantoja-Echevarría et al., 2022; Roff et al., 2016; Vilmar & Di Santo, 2022). By regulating prey populations, elasmobranchs help maintain balance within food webs, supporting ecosystem diversity and structure (Ferretti et al., 2010; Roff et al., 2016). However, removing sharks from these ecosystems can disrupt this balance, leading to cascading effects and potentially irreversible ecological changes.

Sharks have complex life histories, with movement patterns controlled by environmental factors and prey availability (Compagno, 2002; Kneebone et al., 2012; Schlaff et al., 2014; Sulikowski et al., 2010), making them especially vulnerable to human impacts. In recent decades, shark populations have sharply declined due to overfishing (Baum et al., 2003; Myers & Worm, 2003), with global warming likely compounding these effects (Birkmanis et al., 2020; Lubitz et al., 2024; Vilmar & Di Santo, 2022). Despite these threats, understanding the impact of warming on sharks is challenging. Shark ecology is an emerging field, with logistical challenges posed by their high mobility and ability to inhabit multiple ecosystems under diverse conditions (Heupel et al., 2019). Furthermore, population monitoring only began after centuries of human impact, complicating the assessment of their decline's full ecological effects.

The fossil record of sharks provides valuable insights into their habitats and resources in a changing world. Chondrichthyans, one of the oldest vertebrate groups, date back around 400 million years, having survived four major mass extinctions and becoming dominant in marine ecosystems 65 million years ago (Benton, 2014; Cappetta, 2012). Investigating how past climate shifts affected these species can inform how modern sharks might cope with current environmental changes, providing a foundation for conservation practices. Building on this link between past and present shark ecology, this dissertation addresses the following questions: 1) How can we study the interplay between ecology and environment in ancient settings? 2) How did habitat use and diet shift in sharks with climate change?

Shark and batoid fossils mainly consist of isolated teeth found in ocean sediments (Cappetta, 2012), preserving key ecological information through geochemistry (Kim et al., 2014, 2020; Vennemann et al., 2001; Zacke et al., 2009). For decades, stable isotope analysis has been invaluable for investigating aspects of animal ecology (Bryant et al., 1996; Burton & Koch, 1999; Fox-Dobbs et al., 2006; Pederzani & Britton, 2019) and reconstructing past environments (Ivany et al., 2004, 2008; C. Lécuyer et al., 1993; Longinelli, 1965; Zachos et al., 2001), as isotope ratios vary predictably in biological and ecological systems. Phosphate

oxygen stable isotope analysis ($\delta^{18}O_p$), for example, reveals temperature and salinity preferences, offering insights into the environmental conditions of ancient shark habitats (Kim et al., 2014, 2020; Picard et al., 1998; Vennemann et al., 2001; Zacke et al., 2009). This method requires isolating and precipitating phosphate as silver phosphate (Ag_3PO_4), followed by $\delta^{18}O_p$ measurements using Isotope Ratio Mass Spectrometry (IRMS) (Firsching, 1961; Griffin et al., 2015; Christophe Lécuyer, 2004; Mine et al., 2017; Pederzani et al., 2020; Shabaga et al., 2018; Stephan, 2000; Tütken et al., 2006; Wiedemann-Bidlack et al., 2008). Traditional silver phosphate precipitation methods, however, could require large sample sizes (Firsching, 1961; Pederzani et al., 2020; Shabaga et al., 2018; Tütken et al., 2006) and face contamination challenges (Mine et al., 2017; Stephan, 2000), particularly with samples that have high collagen content (> 4%wt.) and complex burial histories (Pederzani et al., 2020). These issues can introduce analytical errors and limit our ability to interpret past environments accurately. In Chapter 1, I develop a new silver phosphate precipitation method—the SPORA protocol (**S**ilver **P**hosphate **O**xygen **R**esin **A**nalysis)—designed to isolate and precipitate phosphate as pristine Ag_3PO_4 salt from bioapatite materials, such as teeth and bones, using a minimal amount of material (~1.5 mg) regardless the amount of collagen contamination present in specimens. To test SPORA's performance, I use varying reference materials and fossil and extant bioapatite specimens to compare its results with those obtained from a traditional method (i.e., Rapid UC; Mine et al., 2017) using the same reference and bioapatite samples. This protocol involves dissolving powdered samples in an acidic solution, followed by an anion exchange resin step that isolates and elutes phosphate ions irrespective of the amount of organic contamination prior to Ag_3PO_4 precipitation. The SPORA protocol development overcomes analytical limitations, enabling $\delta^{18}O_p$ measurements on a wider range of bones and tooth specimens, including the small shark and ray teeth commonly found in the fossil record.

After addressing analytical uncertainties related to silver phosphate applications, this dissertation explores shifts in habitat use and paleoenvironmental insights from Eocene shark and ray tooth geochemistry. The Eocene Epoch (56–33.9 million years ago) has received significant attention as a potential analog for future environmental conditions (Burke et al., 2018). During this period, elasmobranchs reached peak diversity, spanning regions from the Arctic to the Antarctic and experiencing major climatic shifts of the Cenozoic Era (Bazzi et al., 2021; Cappetta, 2012; Condamine et al., 2019; Cooper et al., 2023; Kim et al., 2022). These shifts, driven by declining pCO_2 levels and tectonic events like the opening of oceanic gateways near Antarctica (Tasman Gateway and Drake Passage), marked the transition from a "Greenhouse" to an "Icehouse" world (Zachos et al., 2001, 2008). The opening of tectonic gateways to deep oceanic circulation facilitated cold currents around Antarctica, likely contributing to glaciation near the Eocene-Oligocene transition (Egan et al., 2013; Kennett, 1977; Kennett & Exon, 2004; Scher et al., 2011; Scher & Martin, 2006; Stickley et al., 2004). However, uncertainties remain about the full impact of the Drake Passage deepening given limited data on water conditions during this period (Eagles et al., 2006; Hodel et al., 2021; Lagabrielle et al., 2009; Latimer & Filippelli, 2002; Lawver & Gahagan, 2003), confounding our understanding of the tectonic impact on global climate.

Elasmobranchs have different habitat preferences in agreement with their lifestyles (Compagno, 2002; Kneebone et al., 2014; Sulikowski et al., 2010). These environmental signals, like temperature and salinity, are preserved in the oxygen isotope composition as individuals mineralize new teeth and move elsewhere (Kim et al., 2014, 2020; Vennemann et al., 2001; Zacke et al., 2009). The shark and ray fossil record in the high-latitude, near-shore Eocene deposits of Seymour Island in Antarctica—close to the Drake Passage—could therefore reveal valuable insights into habitat use and oceanographic conditions amid the environmental changes that occurred across the Eocene. In Chapter 2, I present a geochemical analysis of $\delta^{18}O_p$ measurements from 243 shark and ray tooth specimens, representing 16 taxa, including previously published values for *Striatolamia macrota* (n = 42; Kim et al., 2020). This study has three main objectives. First, I determine whether $\delta^{18}O_p$ values in elasmobranch teeth reflect local and colder environmental conditions in Seymour Island over time. If so, this could be indicated by a shift toward higher $\delta^{18}O_p$ values similar to what is observed from the coeval bivalve $\delta^{18}O_c$ values (Ivany et al., 2008). Second, I evaluate whether $\delta^{18}O_p$ values in elasmobranchs reflect regional or seasonal signals related to habitat use and their movements. To do so, I compare $\delta^{18}O$ data from elasmobranch teeth with those from isotope-enabled climate model simulations (Zhu et al., 2020) and co-occurring, infaunal bivalves (Ivany et al., 2008; Judd et al., 2019). I expect that sharks and ray teeth would record seasonal trends if their $\delta^{18}O$ values overlap with those observed in co-occurring bivalves and simulated values for Seymour Island. Alternatively, a broader variation in $\delta^{18}O_p$ values in elasmobranchs indicates movements across a suite of habitats around the Seymour Island shore, while a narrower variation would indicate movements within specific environmental conditions across the region as seasonal and secular temperatures change unfold. Lastly, I investigate whether these teeth record oceanographic changes associated with the end of the Eocene, providing evidence of the Drake Passage deepening's impact on global cooling. If so, benthic taxa would have higher $\delta^{18}O_p$ values following the deepening of the Drake Passage and the colder conditions at depth relative to surface waters inhabited by pelagic taxa.

Finally, this dissertation explores the ecological roles of both fossil and extant shark species by assessing the concept of ecological redundancy, which refers to the extent to which different species fulfill similar roles within ecosystems. By examining environmental factors, dietary preferences, and population structures, this study constructs a multidimensional framework to define the ecological niches of various fossil and extant shark taxa. This framework, traditionally applied to modern and ancient ecosystems, helps identify species that may serve as functional replacements for one another, which has important conservation implications for enhancing ecosystem resilience if one or more species declines (Rosenfeld, 2002; Walker, 1992, 1995). Although commonly applied in studies of living organisms, this approach is challenging to implement in the fossil record due to limited data. Nonetheless, bridging the ecology of fossil and modern sharks could offer insights into the ecological roles of endangered species and guide better-informed management strategies.

In Chapter 3, I delve into the ecology of Eocene fossil sand tiger sharks from the Middle-to-Late Eocene deposits of Seymour Island: *Striatolamia macrota* and *Carcharias* sp. cf. *C. hopei*. These species, known primarily for their isolated teeth (Cappetta, 2012; Kim

et al., 2022; Kriwet et al., 2016; Long, 1992; Padilla et al., 2014), share similar morphologies with their extant relative, *Carcharias taurus* (Cappetta, 2012; Cunningham, 2000; Shimada, 2004), a critically endangered cosmopolitan species (Rigby et al., 2021). The modern sand tiger shark has a specialized feeding ecology, feeding mostly on fish (Gelsleichter et al., 1999; Smale, 2005) and exhibiting high site fidelity within a limited temperature and a broad salinity range (Kneebone et al., 2012, 2014; Otway & Ellis, 2011; Teter et al., 2015). These morphological traits suggest possible ecological similarities with the Eocene counterparts, although differences in tooth size across the fossil species hint at potential ecological distinctions that are yet to be fully quantified. Here, the scope of this chapter is twofold. First, I assess the degree of ecological redundancy among fossil sand tiger sharks in terms of habitat use, feeding ecology, and population structure across time. To do this, I employ morphometric analysis—such as tooth shape and crown height—to infer the extent of dietary preference overlap (Bazzi et al., 2021; Cooper et al., 2023) and total body size of individual specimens (Shimada, 2004), as well as geochemical tracers ($\delta^{18}O_p$ and $\delta^{66}Zn$) to assess environmental preferences (Kim et al., 2014, 2020; Vennemann et al., 2001; Zacke et al., 2009) and trophic levels (Bourgon et al., 2020; Jaouen et al., 2016; McCormack et al., 2022, 2023), respectively. Finally, I leverage current knowledge of the extant sand tiger shark's ecology to interpret morphometric and geochemical tracers of fossil taxa, assessing ecological redundancy between modern and fossil counterparts. I compare the total body size and geochemical proxies of the extant *C. taurus* population from Delaware Bay (Karnes et al., 2024; McCormack et al., 2023) to quantify the extent of niche overlap between fossil and modern sand tiger sharks, highlighting how the conservation of ecological traits across the evolution of closely related species could serve as a tool to constrain the ecological role of modern taxa.

1.2 References

Baum, J. K., Myers, R. A., Kehler, D. G., Worm, B., Harley, S. J., & Doherty, P. A. (2003). Collapse and conservation of shark populations in the Northwest Atlantic. *Science*, *299*(5605), 389–392. https://doi.org/10.1126/science.1079777

Bazzi, M., Campione, N. E., Kear, B. P., Pimiento, C., & Ahlberg, P. E. (2021). Feeding ecology has shaped the evolution of modern sharks. *Current Biology*, *31*(23), 5138-5148.e4. https://doi.org/10.1016/j.cub.2021.09.028

Benton, M. J. (2014). *Vertebrate Palaeontology* (4th editio). Wiley-Blackwell.

Birkmanis, C. A., Freer, J. J., Simmons, L. W., Partridge, J. C., & Sequeira, A. M. M. (2020). Future Distribution of Suitable Habitat for Pelagic Sharks in Australia Under Climate Change Models. *Frontiers in Marine Science*, *7*(July), 1–11. https://doi.org/10.3389/fmars.2020.00570

Bourgon, N., Jaouen, K., Bacon, A. M., Jochum, K. P., Dufour, E., Duringer, P., et al. (2020). Zinc isotopes in Late Pleistocene fossil teeth from a Southeast Asian cave setting preserve paleodietary information. *Proceedings of the National Academy of Sciences of the United States of America*, *117*(9), 4675–4681.

https://doi.org/10.1073/PNAS.1911744117/SUPPL_FILE/PNAS.1911744117.SAPP.PDF

Bryant, J. D., Koch, P. L., Froelich, P. N., Showers, W. J., & Genna, B. J. (1996, December 1). Oxygen isotope partitioning between phosphate and carbonate in mammalian apatite. *Geochimica et Cosmochimica Acta*. Pergamon. https://doi.org/10.1016/S0016-7037(96)00308-0

Burke, K. D., Williams, J. W., Chandler, M. A., Haywood, A. M., Lunt, D. J., & Otto-Bliesner, B. L. (2018). Pliocene and Eocene provide best analogs for near-future climates. *Proceedings of the National Academy of Sciences of the United States of America*, *115*(52), 13288–13293. https://doi.org/10.1073/pnas.1809600115

Burton, R. K., & Koch, P. L. (1999). Isotopic tracking of foraging and long-distance migration in northeastern Pacific pinnipeds. *Oecologia*, *119*(4), 578–585. https://doi.org/10.1007/S004420050822/METRICS

Cappetta, H. (2012). *Handbook of paleoichthyology volume 3E. Chondrichthyes. Mesozoic and Cenozoic elasmobranchii: Teeth*. (H.-P. Schultze, Ed.) (Vol. 3E). Munich: Verlag Dr. Friedrich Pfeil.

Compagno, L. J. (2002). Sharks of the world: An Annotated and illustrated catalogue of shark species known to date. *Food and Agriculture Organization of the United Nations*, *2*(1), 249. Retrieved from http://www.fao.org/3/x9293e/x9293e00.htm

Condamine, F. L., Romieu, J., & Guinot, G. (2019). Climate cooling and clade competition likely drove the decline of lamniform sharks. *Proceedings of the National Academy of Sciences of the United States of America*, *116*(41), 20584–20590. https://doi.org/10.1073/pnas.1902693116

Cooper, J. A., Griffin, J. N., Kindlimann, R., & Pimiento, C. (2023). Are shark teeth proxies for functional traits? A framework to infer ecology from the fossil record. *Journal of Fish Biology*, *103*(4), 798–814. https://doi.org/10.1111/jfb.15326

Cunningham, S. B. (2000). A comparison of isolated teeth of early Eocene Striatolamia macrota (Chondrichthyes , Lamniformes), with those of a Recent sand shark , Carcharias taurus. *Tertiary Research*, *20*(1–4), 17–31.

Eagles, G., Livermore, R., & Morris, P. (2006). Small basins in the Scotia Sea: The Eocene Drake Passage gateway. *Earth and Planetary Science Letters*, *242*(3–4), 343–353. https://doi.org/10.1016/J.EPSL.2005.11.060

Egan, K. E., Rickaby, R. E. M., Hendry, K. R., & Halliday, A. N. (2013). Opening the gateways for diatoms primes Earth for Antarctic glaciation. *Earth and Planetary Science Letters*, *375*, 34–43. https://doi.org/10.1016/j.epsl.2013.04.030

Ferretti, F., Worm, B., Britten, G. L., Heithaus, M. R., & Lotze, H. K. (2010, August 1). Patterns and ecosystem consequences of shark declines in the ocean. *Ecology Letters*. John Wiley & Sons, Ltd. https://doi.org/10.1111/j.1461-0248.2010.01489.x

Firsching, F. H. (1961). Precipitation of Silver Phosphate from Homogeneous Solution. *Analytical Chemistry*, *33*(7), 873–874. https://doi.org/10.1021/ac60175a018

Fox-Dobbs, K., Stidham, T. A., Bowen, G. J., Emslie, S. D., & Koch, P. L. (2006). Dietary controls on extinction versus survival among avian megafauna in the late Pleistocene. *Geology*, *34*(8), 685–688. https://doi.org/10.1130/G22571.1

Gelsleichter, J., Musick, J. A., & Nichols, S. (1999). Food habits of the smooth dogfish, Mustelus canis, dusky shark, Carcharhinus obscurus, Atlantic sharpnose shark, Rhizoprionodon terraenovae, and the sand tiger, Carcharias taurus, from the northwest Atlantic Ocean. *Environmental Biology of Fishes*, *54*(2), 205–217. https://doi.org/10.1023/A:1007527111292/METRICS

Griffin, J. M., Montañez, I. P., Matthews, J. A., Bates, S., & Lyons, T. W. (2015). A refined protocol for δ18OPO4 analysis of conodont bioapatite. *Chemical Geology*, *417*, 11–20. https://doi.org/10.1016/j.chemgeo.2015.08.025

Heithaus, M. R., Frid, A., Wirsing, A. J., & Worm, B. (2008). Predicting ecological consequences of marine top predator declines. *Trends in Ecology and Evolution*, *23*(4), 202–210. https://doi.org/10.1016/j.tree.2008.01.003

Heupel, M. R., Munroe, S. E. M., Lédée, E. J. I., Chin, A., & Simpfendorfer, C. A. (2019). Interspecific interactions, movement patterns and habitat use in a diverse coastal shark assemblage. *Marine Biology*, *166*(6), 1–17. https://doi.org/10.1007/S00227-019-3511-7/TABLES/5

Hodel, F., Grespan, R., de Rafélis, M., Dera, G., Lezin, C., Nardin, E., et al. (2021). Drake Passage gateway opening and Antarctic Circumpolar Current onset 31 Ma ago: The message of foraminifera and reconsideration of the Neodymium isotope record. *Chemical Geology*, *570*(November 2020). https://doi.org/10.1016/j.chemgeo.2021.120171

Hussey, N. E., Dudley, S. F. J., McCarthy, I. D., Cliff, G., & Fisk, A. T. (2011). Stable isotope profiles of large marine predators: Viable indicators of trophic position, diet, and movement in sharks? *Canadian Journal of Fisheries and Aquatic Sciences*, *68*(12), 2029–2045. https://doi.org/10.1139/F2011-115

Ivany, L. C., Wilkinson, B. H., Lohmann, K. C., Johnson, E. R., McElroy, B. J., & Cohen, G. J. (2004). Intra-Annual Isotopic Variation in Venericardia Bivalves: Implications for Early Eocene Temperature, Seasonality, and Salinity on the U.S. Gulf Coast. *Journal of Sedimentary Research*, *74*(1), 7–19. https://doi.org/10.1306/052803740007

Ivany, L. C., Lohmann, K. C., Hasiuk, F., Blake, D. B., Glass, A., Aronson, R. B., & Moody, R. M. (2008). Eocene climate record of a high southern latitude continental shelf: Seymour Island, Antarctica. *Bulletin of the Geological Society of America*, *120*(5–6), 659–678. https://doi.org/10.1130/B26269.1

Jaouen, K., Beasley, M., Schoeninger, M., Hublin, J. J., & Richards, M. P. (2016). Zinc isotope ratios of bones and teeth as new dietary indicators: results from a modern food

web (Koobi Fora, Kenya). *Scientific Reports 2016 6:1*, *6*(1), 1–8. https://doi.org/10.1038/srep26281

Judd, E. J., Ivany, L. C., DeConto, R. M., Halberstadt, A. R. W., Miklus, N. M., Junium, C. K., & Uveges, B. T. (2019). Seasonally Resolved Proxy Data From the Antarctic Peninsula Support a Heterogeneous Middle Eocene Southern Ocean. *Paleoceanography and Paleoclimatology*, *34*(5), 787–799. https://doi.org/10.1029/2019PA003581

Karnes, M. E., Chan, R. L., Kuntz, J. P., Griffiths, M. L., Shimada, K., Becker, M. A., et al. (2024). Enigmatic carbonate isotope values in shark teeth: Evidence for environmental and dietary controls. *Palaeogeography, Palaeoclimatology, Palaeoecology*, *635*, 111943. https://doi.org/10.1016/j.palaeo.2023.111943

Kennett, J. P. (1977). Cenozoic evolution of Antarctic glaciation, the circum-Antarctic Ocean, and their impact on global paleoceanography. *Journal of Geophysical Research*, *82*(27), 3843–3860. https://doi.org/10.1029/jc082i027p03843

Kennett, J. P., & Exon, N. F. (2004). Paleoceanographic evolution of the tasmanian seaway and its climatic implications. In *Geophysical Monograph Series* (Vol. 151, pp. 345–367). American Geophysical Union (AGU). https://doi.org/10.1029/151GM19

Kim, S. L., Eberle, J. J., Bell, D. M., Fox, D. A., & Padilla, A. (2014). Evidence from shark teeth for a brackish Arctic Ocean in the Eocene greenhouse. *Geology*, *42*(8), 695–698. https://doi.org/10.1130/G35675.1

Kim, S. L., Zeichner, S. S., Colman, A. S., Scher, H. D., Kriwet, J., Mörs, T., & Huber, M. (2020). Probing the Ecology and Climate of the Eocene Southern Ocean With Sand Tiger Sharks Striatolamia macrota. *Paleoceanography and Paleoclimatology*, *35*(12), 1–21. https://doi.org/10.1029/2020PA003997

Kim, S. L., Yeakel, J. D., Balk, M. A., Eberle, J. J., Zeichner, S., Fieman, D., & Kriwet, J. (2022). Decoding the dynamics of dental distributions: insights from shark demography and dispersal. *Proceedings of the Royal Society B: Biological Sciences*, *289*(1977). https://doi.org/10.1098/rspb.2022.0808

Kneebone, J., Chisholm, J., & Skomal, G. B. (2012). Seasonal residency, habitat use, and site fidelity of juvenile sand tiger sharks Carcharias taurus in a Massachusetts estuary. *Marine Ecology Progress Series*, *471*, 165–181. https://doi.org/10.3354/meps09989

Kneebone, J., Chisholm, J., & Skomal, G. (2014). Movement patterns of juvenile sand tigers (Carcharias taurus) along the east coast of the USA. *Marine Biology*, *161*(5), 1149–1163. https://doi.org/10.1007/s00227-014-2407-9

Kriwet, J., Engelbrecht, A., Mörs, T., Reguero, M., & Pfaff, C. (2016). Ultimate Eocene (Priabonian) chondrichthyans (Holocephali, Elasmobranchii) of Antarctica. *Journal of Vertebrate Paleontology*, *36*(4). https://doi.org/10.1080/02724634.2016.1160911

Lagabrielle, Y., Goddéris, Y., Donnadieu, Y., Malavieille, J., & Suarez, M. (2009). The tectonic history of Drake Passage and its possible impacts on global climate. *Earth and*

Planetary Science Letters, *279*(3–4), 197–211. https://doi.org/10.1016/j.epsl.2008.12.037

Latimer, J. C., & Filippelli, G. M. (2002). Eocene to Miocene terrigenous inputs and export production: geochemical evidence from ODP Leg 177, Site 1090. *Palaeogeography, Palaeoclimatology, Palaeoecology*, *182*(3–4), 151–164. https://doi.org/10.1016/S0031-0182(01)00493-X

Latour, R. J., & Gartland, J. (2020). Dynamics of the shark community in the Mid-Atlantic Bight. *Marine Biology*, *167*(7), 1–14. https://doi.org/10.1007/S00227-020-03720-Y/FIGURES/5

Lawver, L. A., & Gahagan, L. M. (2003). Evolution of Cenozoic seaways in the circum-Antarctic region. *Palaeogeography, Palaeoclimatology, Palaeoecology*, *198*(1–2), 11–37. https://doi.org/10.1016/S0031-0182(03)00392-4

Lécuyer, C., Grandjean, P., O'Neil, J. R., Cappetta, H., & Martineau, F. (1993). Thermal excursions in the ocean at the Cretaceous-Tertiary boundary (northern Morocco): δ18O record of phosphatic fish debris. *Palaeogeography, Palaeoclimatology, Palaeoecology*, *105*(3–4), 235–243. https://doi.org/10.1016/0031-0182(93)90085-W

Lécuyer, Christophe. (2004). Oxygen Isotope Analysis of Phosphate. *Handbook of Stable Isotope Analytical Techniques*, (September 2004), 482–496. https://doi.org/10.1016/B978-044451114-0/50024-7

Long, D. J. (1992). Sharks from the La Meseta Formation (Eocene), Seymour Island, Antarctic Peninsula. *Journal of Vertebrate Paleontology*, *12*(1), 11–32. https://doi.org/10.1080/02724634.1992.10011428

Longinelli, A. (1965). Oxygen isotopic composition of orthophosphate from shells of living marine organisms. *Nature*, *207*(4998), 716–719. https://doi.org/10.1038/207716a0

Lubitz, N., Daly, R., Smoothey, A. F., Vianello, P., Roberts, M. J., Schoeman, D. S., et al. (2024). Climate change-driven cooling can kill marine megafauna at their distributional limits. *Nature Climate Change*, *14*(5), 526–535. https://doi.org/10.1038/s41558-024-01966-8

McCormack, J., Griffiths, M. L., Kim, S. L., Shimada, K., Karnes, M., Maisch, H., et al. (2022). Trophic position of Otodus megalodon and great white sharks through time revealed by zinc isotopes. *Nature Communications*, *13*(1), 1–10. https://doi.org/10.1038/s41467-022-30528-9

McCormack, J., Karnes, M., Haulsee, D., Fox, D., & Kim, S. L. (2023). Shark teeth zinc isotope values document intrapopulation foraging differences related to ontogeny and sex. *Communications Biology*, *6*(1), 1–10. https://doi.org/10.1038/s42003-023-05085-6

Mine, A. H., Waldeck, A., Olack, G., Hoerner, M. E., Alex, S., & Colman, A. S. (2017). Microprecipitation and δ18O analysis of phosphate for paleoclimate and biogeochemistry research. *Chemical Geology*, *460*(March), 1–14. https://doi.org/10.1016/j.chemgeo.2017.03.032

Myers, R. A., & Worm, B. (2003). Rapid worldwide depletion of predatory fish communities. *Nature*, *423*(6937), 280–283. https://doi.org/10.1038/nature01610

Otway, N. M., & Ellis, M. T. (2011). Pop-up archival satellite tagging of Carcharias taurus: movements and depth/temperature-related use of south-eastern Australian waters. *Marine and Freshwater Research*, *62*(6), 607–620. https://doi.org/10.1071/MF10139

Padilla, A., Eberle, J. J., Gottfried, M. D., Sweet, A. R., & Hutchison, J. H. (2014). A sand tiger shark-dominated fauna from the Eocene Arctic greenhouse. *Journal of Vertebrate Paleontology*, *34*(6), 1307–1316. https://doi.org/10.1080/02724634.2014.880446

Pantoja-Echevarría, L. M., Tamburin, E., Elorriaga-Verplancken, F. R., Marmolejo-Rodríguez, A. J., Galván-Magaña, F., Tripp-Valdez, A., et al. (2022). How to stay together? Habitat use by three sympatric sharks in the western coast of Baja California Sur, Mexico. *Environmental Science and Pollution Research*, *29*(41), 61685–61697. https://doi.org/10.1007/S11356-022-19530-2/FIGURES/5

Pederzani, S., & Britton, K. (2019, January 1). Oxygen isotopes in bioarchaeology: Principles and applications, challenges and opportunities. *Earth-Science Reviews*. Elsevier. https://doi.org/10.1016/j.earscirev.2018.11.005

Pederzani, S., Snoeck, C., Wacker, U., & Britton, K. (2020). Anion exchange resin and slow precipitation preclude the need for pretreatments in silver phosphate preparation for oxygen isotope analysis of bioapatites. *Chemical Geology*, *534*, 119455. https://doi.org/10.1016/j.chemgeo.2019.119455

Picard, S., Garcia, J. P., Lécuyer, C., Sheppard, S. M. F., Cappetta, H., & Emig, C. C. (1998). δ 18 O values of coexisting brachiopods and fish: Temperature differences and estimates of paleo-water depths. *Geology*, *26*(11), 975–978. https://doi.org/10.1130/0091-7613(1998)026<0975:OVOCBA>2.3.CO;2

Rigby, C. L., Carlson, J., Derrick, D., Dicken, M., & Pacoureau, N. Simpfendorfer, C. (2021). Carcharias taurus. *The IUCN Red List of Threatened Species 2021: E.T3854A2876505*. https://doi.org/https://dx.doi.org/10.2305/IUCN.UK.2021-2.RLTS.T3854A2876505.en

Roff, G., Doropoulos, C., Rogers, A., Bozec, Y. M., Krueck, N. C., Aurellado, E., et al. (2016, May 1). The Ecological Role of Sharks on Coral Reefs. *Trends in Ecology and Evolution*. Elsevier Current Trends. https://doi.org/10.1016/j.tree.2016.02.014

Rosenfeld, J. S. (2002). Functional redundancy in ecology and conservation. *Oikos*, *98*(1), 156–162. https://doi.org/10.1034/j.1600-0706.2002.980116.x

Scher, H. D., & Martin, E. E. (2006). Timing and climatic consequences of the opening of drake passage. *Science*, *312*(5772), 428–430. https://doi.org/10.1126/science.1120044

Scher, H. D., Bohaty, S. M., Zachos, J. C., & Delaney, M. L. (2011). Two-stepping into the icehouse: East Antarctic weathering during progressive ice-sheet expansion at the Eocene-Oligocene transition. *Geology*, *39*(4), 383–386. https://doi.org/10.1130/G31726.1

Schlaff, A. M., Heupel, M. R., & Simpfendorfer, C. A. (2014, July 24). Influence of environmental factors on shark and ray movement, behaviour and habitat use: a review. *Reviews in Fish Biology and Fisheries*. Springer. https://doi.org/10.1007/s11160-014-9364-8

Shabaga, B. M., Gough, H., Fayek, M., & Hoppa, R. D. (2018). A simplified silver phosphate extraction method for oxygen isotope analysis of bioapatite. *Rapid Communications in Mass Spectrometry*, *32*(15), 1237–1242. https://doi.org/10.1002/rcm.8149

Shimada, K. (2004). The relationship between the tooth size and total body length in the sandtiger shark, Carcharias taurus (Lamniformes : Odontaspididae). *Journal of Fossil Research*, *37*(2), 76–81. https://doi.org/10.2305/IUCN.UK.2009-2.RLTS.T3854A10132481.en

Smale, M. J. (2005). The diet of the ragged-tooth shark Carcharias taurus Rafinesque 1810 in the Eastern Cape, South Africa. *African Journal of Marine Science*, *27*(1), 331–335. https://doi.org/10.2989/18142320509504091

Stephan, E. (2000). Oxygen isotope analysis of animal bone phosphate: Method refinement, influence of consolidants, and reconstruction of palaeotemperatures for Holocene sites. *Journal of Archaeological Science*, *27*(6), 523–535. https://doi.org/10.1006/jasc.1999.0480

Stickley, C. E., Brinkhuis, H., Schellenberg, S. A., Sluijs, A., Röhl, U., Fuller, M., et al. (2004). Timing and nature of the deepening of the Tasmanian Gateway. *Paleoceanography*, *19*(4), 1–18. https://doi.org/10.1029/2004PA001022

Sulikowski, J. A., Galuardi, B., Bubley, W., Furey, N. B., Driggers, W. B., Ingram, G. W., & Tsang, P. C. W. (2010). Use of satellite tags to reveal the movements of spiny dogfish Squalus acanthias in the western North Atlantic Ocean. *Marine Ecology Progress Series*, *418*, 249–254. https://doi.org/10.3354/meps08821

Teter, S. M., Wetherbee, B. M., Fox, D. A., Lam, C. H., Kiefer, D. A., & Shivji, M. (2015). Migratory patterns and habitat use of the sand tiger shark (Carcharias taurus) in the western North Atlantic. *Marine and Freshwater Research*, *66*(2), 158–169. https://doi.org/10.1071/MF14129

Tütken, T., Vennemann, T. W., Janz, H., & Heizmann, E. P. J. (2006). Palaeoenvironment and palaeoclimate of the Middle Miocene lake in the Steinheim basin, SW Germany: A reconstruction from C, O, and Sr isotopes of fossil remains. *Palaeogeography, Palaeoclimatology, Palaeoecology*, *241*(3–4), 457–491. https://doi.org/10.1016/j.palaeo.2006.04.007

Vennemann, T. W., Hegner, E., Cliff, G., & Benz, G. W. (2001). Isotopic composition of recent shark teeth as a proxy for environmental conditions. *Geochimica et Cosmochimica Acta*, *65*(10), 1583–1599. https://doi.org/https://doi.org/10.1016/S0016-7037(00)00629-3

Vilmar, M., & Di Santo, V. (2022, March 8). Swimming performance of sharks and rays under climate change. *Reviews in Fish Biology and Fisheries*. Springer. https://doi.org/10.1007/s11160-022-09706-x

Walker, B. H. (1992). Biodiversity and Ecological Redundancy. *Conservation Biology*, *6*(1), 18–23. https://doi.org/10.1046/j.1523-1739.1992.610018.x

Walker, B. H. (1995). Conserving Biological Diversity through Ecosystem Resilience. *Conservation Biology*, *9*(4), 747–752. https://doi.org/10.1046/j.1523-1739.1995.09040747.x

Wiedemann-Bidlack, F. B., Colman, A. S., & Fogel, M. L. (2008). Phosphate oxygen isotope analysis on microsamples of bioapatite: removal of organic contamination and minimization of sample size. *Rapid Communications in Mass Spectrometry*, *22*, 1457–1466. https://doi.org/10.1002/rcm.3553

Zachos, J. C., Pagani, H., Sloan, L., Thomas, E., & Billups, K. (2001). Trends, rhythms, and aberrations in global climate 65 Ma to present. *Science*, *292*(5517), 686–693. https://doi.org/10.1126/science.1059412

Zachos, J. C., Dickens, G. R., & Zeebe, R. E. (2008). An early Cenozoic perspective on greenhouse warming and carbon-cycle dynamics. *Nature*, *451*(7176), 279–283. https://doi.org/10.1038/nature06588

Zacke, A., Voigt, S., Joachimski, M. M., Gale, A. S., Ward, D. J., & Tütken, T. (2009). Surface-water freshening and high-latitude river discharge in the Eocene North Sea. *Journal of the Geological Society*, *166*(5), 969–980. https://doi.org/10.1144/0016-76492008-068

Zhu, J., Poulsen, C. J., Otto-Bliesner, B. L., Liu, Z., Brady, E. C., & Noone, D. C. (2020). Simulation of early Eocene water isotopes using an Earth system model and its implication for past climate reconstruction. *Earth and Planetary Science Letters*, *537*, 116164. https://doi.org/10.1016/j.epsl.2020.116164

2. Chapter 1: SPORA, a new silver phosphate precipitation protocol for oxygen isotope analysis of small, organic-rich bioapatite samples

2.1 Abstract

Isotopic analysis of phosphate oxygen from bones and teeth ($^{18}O_p/^{16}O_p$, $\delta^{18}O_p$) is a common tool used to investigate modern and ancient ecosystems and their climate. However, existing methods have expanded to use pretreatments for organic removal, or require large sample sizes, or require extended precipitation timing. All together, these factors could affect accuracy and precision of $\delta^{18}O_p$ measurement by promoting the formation of oxygen-bearing or nitrogen-rich contaminants. However, the nature and occurrence of contamination are not fully explored. Here we sought to develop a method of silver phosphate precipitation that tests the effect of different sample treatments and reduced sample sizes while preserving sample isotopic composition.

Our protocol (SPORA) precipitates Ag_3PO_4 crystals from ~1.5 mg of starting material while purifying phosphate from contaminants, like nitrogen or carbonate. Isolation and purification of phosphate are achieved with an anion exchange resin, followed by precipitation of silver phosphate using an updated silver ammine solution that targets small amounts of phosphate in solution. We used a variety of phosphate oxygen reference materials and biogenic apatite materials, such as modern and fossil specimens with varying collagen content, to test the SPORA protocol and its effects on the resultant phosphate oxygen isotopic composition. Results were then compared to those from another published silver phosphate precipitation method (i.e., Rapid University of Chicago Dilute, Rapid UC). Overall, $\delta^{18}O_p$ values of standards and biogenic apatites were similar between protocols ($R^2 = 0.99$, $p << 0.05$). In addition to isotope composition comparisons, UV-Vis spectroscopy and Fourier Transform Infrared (FTIR) analyses discerned phosphate recovery and material composition of crystals precipitated via different protocols, respectively. We found that the resin *i*) may retain ~10 % of phosphate with no isotopic effects and *ii*) the SPORA protocol produces Ag_3PO_4 with more accurate $\delta^{18}O_p$ measurements by preventing the formation of contaminant oxygen phases, silver oxide (Ag_2O) and silver carbonate (Ag_2CO_3), that confound the phosphate oxygen isotope composition.

The SPORA Ag_3PO_4 precipitation procedure overcomes analytical limitations such as sample size and collagen contamination, conditions that other procedures for $\delta^{18}O_p$ analysis cannot address simultaneously. The SPORA protocol can be used on a large array of bioapatite materials for paleoecological, paleoclimatic, and archaeological applications, while reducing the required sample size and ensuring pure Ag_3PO_4 for isotopic analysis.

2.2 Introduction

Skeletal materials and their phosphate oxygen isotope composition ($^{18}O/^{16}O$, $\delta^{18}O$) provide invaluable environmental records to investigate climatic variability (e.g.,

temperature, salinity, aridity) and ecology of humans and animals across modern and geological time scales (e.g., movements, breastfeeding, and weaning practices) (Kim et al., 2020, 2014; Kirsanow et al., 2008; Kocsis et al., 2014; Kohn and Cerling, 2003; McMahon et al., 2013; Newsome et al., 2010; Pearson et al., 2009; Pederzani and Britton, 2019; Tsutaya and Yoneda, 2015; Vennemann and Hegner, 1998; Zacke et al., 2009). These applications rely on the body temperature-dependent fractionation of oxygen isotopes between ingested water and mineral phases, primarily composed of biogenic apatite ($Ca_{10}(PO_4, xCO_3)_{6-x}(OH, F, yCO_3)_{2-y}$) (Dorozhkin, 2009; Enax et al., 2012; Lübke et al., 2015). Phosphate oxygen ($\delta^{18}O_p$) is often preferred over carbonate (CO_3^{2-}) $\delta^{18}O$ values given its stability against diagenetic alteration (Koch et al., 1997; Kohn et al., 1999; Kolodny et al., 1983; Shemesh et al., 1983; Stephan, 2000; Zazzo et al., 2004).

The analysis of stable oxygen isotope compositions ($^{18}O_p/^{16}O_p$, $\delta^{18}O_p$) from vertebrate skeletal remains requires the isolation of the phosphate component (i.e., PO_4^{3-} ion) after dissolving bioapatite in an acid solution and precipitating it into a salt that serves as an analytical substrate. Silver phosphate (Ag_3PO_4) is considered a suitable analyte given its non-hygroscopic nature, preventing adsorption of ambient water and incorporation of oxygen derived from moisture. Silver phosphate crystals are commonly measured via high temperature reduction (i.e., HTR) of Ag_3PO_4 to carbon monoxide (CO) methods coupled to an Isotope Ratio Mass Spectrometer (IRMS) (Fourel et al., 2011; Lécuyer et al., 2007; Vennemann et al., 2002). Current Ag_3PO_4 precipitation protocols for IRMS analysis differ in terms of the starting amount of apatite material, treatments to remove organics (e.g., pre-treatments via NaOCl vs anion exchange purification before Ag_3PO_4 precipitation), phosphate dissolution (e.g., HF, HNO_3, or both) and rate of crystal precipitation (e.g., rapid (~10 minutes) or slow (~13 hours)) (Crowson et al., 1991; Dettman et al., 2001; Firsching, 1961; Griffin et al., 2015; Lécuyer et al., 1998, 1993; Mine et al., 2017; O'Neil et al., 1994; Pederzani et al., 2020; Quinton et al., 2016; Royer et al., 2013; Shabaga et al., 2018; Stephan, 2000; Sun et al., 2016; Tütken et al., 2006; Wiedemann-Bidlack et al., 2008). These techniques result in silver phosphate for $\delta^{18}O_p$ values, but may not be ideal for variably organic-rich biogenic apatite, small sample sizes, and starting material of varying burial history. Finally, many previous silver phosphate methodologies do not directly test or quantify the possibility of contamination in silver phosphate crystals.

Sample size, contaminant inclusions, and the form of apatite (i.e., bone, dentin, enamel, enameloid) may affect the oxygen isotope composition of the precipitated Ag_3PO_4. Protocols often recommend 4 to 10 mg of drilled starting materials (e.g., Pederzani et al., 2020; Tükten et al., 2006; Shabaga et al., 2018), which is a problem when dealing with smaller specimens, such as teeth. Small tooth specimens (i.e., <2cm tall) often necessitate crushing, yielding a mixture of enamel (or enameloid in sharks) and dentin. Like bone samples, dentin, contains a high collagen content (up to ~20 %wt. against <4 %wt. in enamel or enameloid) (Koch et al., 1997; Lee-Thorp, 2002; Lee-Thorp and van der Merwe, 1991; LeGeros, 1981), which, if not removed, releases nitrogen-rich compounds that could contaminate Ag_3PO_4 crystals and leads to inaccurate $\delta^{18}O_p$ values during IRMS analysis (Kornexl et al., 1999). Common collagen removal treatments require soaking powdered samples in sodium hypochlorite solution (NaOCl, "bleach") before bioapatite dissolution to minimize the coprecipitation of such nitrogen compounds during the precipitation of Ag_3PO_4

crystals (Lécuyer, 2004; Mine et al., 2017; O'Neil et al., 1994; Pederzani et al., 2020; Stephan, 2000; Vennemann et al., 2002; Wiedemann-Bidlack et al., 2008). However, NaOCl pre-treatment for Ag_3PO_4 protocols is discouraged due to unpredictable isotopic shifts (Grimes and Pellegrini, 2013; Pederzani et al., 2020). If nitrogen-rich organic compounds are not the cause of contamination, collagen breakdown after bleach pre-treatment could possibly promote carbonate contamination (Crowley and Wheatley, 2014; Pellegrini and Snoeck, 2016; Snoeck and Pellegrini, 2015), but its specific effect on Ag_3PO_4 isotopic fidelity has not been explored. Finally, extended reaction times to precipitate silver phosphate crystals (e.g., Griffin et al., 2015; Pederzani et al., 2020; Royer et al., 2013; Wiedemann-Bidlack et al., 2008) may lead to the incorporation of oxygen-bearing minerals (e.g., Ag_2CO_3 and/or silver oxide (Ag_2O)) and associated isotopic shifts. More rapid reaction times when precipitating Ag_3PO_4 crystals are desired to prevent contamination. Ideally, a silver phosphate precipitation method would require minimal bioapatite sample, isolate apatite phosphate despite the presence of contaminants, and limit the incorporation of these contaminants in silver phosphate crystals.

In addition, structural differences and burial processes determine the carbonate content in biological apatite materials. Bone and dentin have higher structural carbonate content (i.e. carbonate within the bioapatite crystal lattice structure) and porosity than enamel or enameloid (Lee-Thorp and van der Merwe, 1991; LeGeros, 1981). Exogenous compounds, such as natural asphalt or secondary carbonate minerals like calcite, often fill pore spaces of dentin and bone following the burial of skeletal remains (Fox-Dobbs et al., 2014, 2006; France et al., 2015; Fuller et al., 2014; Pederzani and Britton, 2019; Schwarcz and Schoeninger, 1991; Zazzo et al., 2004). Protocols for Ag_3PO_4 precipitation would ideally prevent carbonate contamination, which could be structural from inorganics or organic sources, including carbon dioxide outgassing during the apatite dissolution in acid mediums. The formation of silver carbonate (Ag_2CO_3) was recently identified as a possible major contaminant phase in the silver phosphate salt (Mine et al., 2017), and therefore the occurrence and contribution of all such carbonate contaminants in Ag_3PO_4 crystals needs to be assessed.

Here, we aimed to design a new precipitation protocol: the SPORA protocol (i.e., **S**ilver **P**hosphate **O**xygen **R**esin **A**nalysis). This approach requires less starting material (~1.5 mg or less) and precipitates silver phosphate crystals following phosphate isolation via an anion exchange resin. Anion exchange resins were previously used to isolate phosphate from bioapatite and water (Colman, 2002; Colman et al., 2005; Crowson et al., 1991; Goldhammer et al., 2011, 2010; Lécuyer et al., 1998; Pederzani et al., 2020; Royer et al., 2013), but the SPORA protocol is unique given its minimal starting material (~1.5 mg or less), exclusion of organic contaminants, and consistent phosphate oxygen isotope composition. We tested the SPORA protocol with respect to carbonate and nitrogen-rich samples, hypothesizing that the resin adsorbs phosphate while excluding contaminants and improving phosphate $\delta^{18}O$ values. We assessed silver phosphate recovery, composition, and purity within our method using Fourier-Transform Infrared (FTIR) and UV-Vis spectrophotometry analyses as complementary tools to quantify mineral composition and quality of silver phosphate crystals as well as phosphate yield, respectively.

2.3 Materials and Methods

We compared our new silver phosphate protocol with the Rapid University of Chicago Dilute (i.e., Rapid UC) technique after Mine et al. (2017) because both procedures include two similar, fundamental steps: *i*) calcium fluoride (CaF_2) precipitation to isolate phosphate from the structural ions of apatite (e.g., Ca^{2+} and F^-) and *ii*) an instantaneous silver phosphate (Ag_3PO_4) precipitation using a silver ammine solution. The main difference between protocols is the organic matter removal step. SPORA uses an anion exchange resin (Bio-Rad AG^{TM} 1-X8) (Bio-Rad Laboratories, 2000) to isolate phosphate ions from organic residuals between the CaF_2 precipitation and Ag_3PO_4 precipitation (Figure 2.1).

We assess the SPORA protocol performance in terms of $\delta^{18}O$ accuracy, phosphate recovery, and contaminant exclusion. We tested the SPORA protocol on samples of varying nature, such as organic content and depositional settings. Data were processed using R Studio (RStudio Team, 2021). The complete dataset and R code scripts to elaborate on corrections and analysis are found in supplementary materials for transparency. A detailed description and a schematic diagram of the procedure are also part of the supplementary materials.

2.3.1 Sample Descriptions

We used biogenic apatite specimens and commercially available inorganic reference materials to test the similarity in $\delta^{18}O_p$ values between protocols. Inorganic working reference materials included: NIST SRM 120c (Florida phosphate rock, National Institute of Standards and Technology), synthetic hydroxyapatite (Sigma Aldrich, CAS: 12167-74-7), and naturally occurring fluorapatite (Fisher Scientific, CAS: 1306-05-4). Enamel and enameloid powder (i.e., enamel and enameloid powder, <4 %wt collagen) were drilled from *i*) a modern goat tooth specimen, *ii*) teeth of the functional file series of a modern, blue shark jaw, and *iii*) two fossil sand tiger shark teeth (SM1 and SM2 specimens, Table 2.1). We used a mixture of enamel and dentin from the same tooth specimens and bone samples (Table 2.1) to test the anion exchange resin on materials of different burial settings and with an expected high organic content (>4 %wt collagen). A goat tooth was drilled on the occlusal surface of the second cusp to obtain the enameloid/dentin mixture and modern shark teeth were crushed. Bone specimens used for this study belong to a modern deer individual and two indeterminate, fossil mammal taxa, including a specimen from tar seep deposits (MM1; Table 2.1). Natural asphalt inclusions lead to inaccurate $\delta^{13}C$ and $\delta^{15}N$ values (Fox-Dobbs et al., 2014, 2006; Fuller et al., 2014), and therefore we believed that $\delta^{18}O_p$ measurements are no exception. We used the MM1 specimen to test whether the resin efficiently removes tar from samples. We dissolved the natural asphalt from the powdered bone by sonicating the powder in a toluene-methanol solution following Fuller et al. (2014) (MM1, bone (tar removed), Table 2.1; see Appendix 2.9.1 for a detailed description of the procedure) and compared results with those of the untreated powder.

Given the initial application of this method, we also specifically tested SPORA with modern and fossil shark teeth. We used a mixture of enameloid and dentin in shark teeth from the same specimen to test the anion exchange resin. We treated individual teeth of the modern shark as separate samples, except for "TOM_1" that includes a homogeneous

mixture of enameloid powder from two clipped teeth (Table 2.1). Additionally, we prepared an enameloid/dentin mixture by ball-milling a mixture of shark teeth clipped from the same jaw (TOM_6; Table 2.1) to test the resin's application on materials with an expected high organic content (>4 %wt collagen). Similarly, for each fossil shark tooth sample, we crushed a single chunk of the crown to obtain a mixture of dentin and enameloid of the same specimens.

We tested the features of inorganic or organic contaminant inclusions in silver phosphate crystals and their effect on $\delta^{18}O$ accuracy. We used a silver phosphate standard (Alfa Aesar; CAS: 7784-09-0) and mixed it with collagen from bovine achilles tendon (Sigma Aldrich; CAS: 9007-34-5) or silver oxide (Ag_2O) crystals to observe FTIR spectra features of pristine and contaminated silver phosphate crystals (Appendix 2.9.5). Silver oxide crystals were prepared in-house by mixing 300 µL 3M $AgNO_3$ and 700 µL 2M NaOH. Crystals were rinsed three times with deionized water and dried overnight. The same crystals were also used for $\delta^{18}O$ analysis to monitor significant isotopic shifts in Ag_3PO_4 crystals due to inclusion of this oxygen-bearing mineral. Finally, we prepared five in-house silver carbonate (Ag_2CO_3) samples to test the degree of isotopic shift due to the incorporation of inorganic contaminants in different amounts, like the apatite structural carbonate. Crystals were precipitated by mixing 0.75 ml 1 M $AgNO_3$ and 0.75 ml 0.5 M $NaHCO_3$. Crystals were rinsed three times with deionized water and dried overnight. All samples were homogenized into a single powder batch.

2.3.2 Rapid UC Precipitation

Phosphate standard materials and biogenic apatite samples were chemically processed with the Rapid UC method after Mine et al. (2017). We weighed ~1.5 mg of each apatite replicates to the nearest 10^{-3} mg (Table 2.1). Specimens with high organic content (i.e., tooth crown surface/dentin mixture and bone specimens; Table 2.1) were treated in 300 µL 2.5% NaClO for ~17h to oxidize organics (Tube A; Figure 2.1). Samples were rinsed five times with deionized water (DIW) and dried overnight. All samples were pre-dissolved in 50 µL 2 M nitric acid (HNO_3) overnight (Tube A). To precipitate calcium fluoride (CaF_2), 30 µL 2.9 M hydrofluoric acid (HF) was added, then the solution was buffered with 50 µL 2 M sodium hydroxide (NaOH) (Tube A; Figure 2.1). Samples were gently shaken for 120 min and then centrifuged to pellet CaF_2. The supernatant with dissolved phosphate ions was transferred into a clean microcentrifuge tube (Tube B; Figure 2.1). The CaF_2 was rinsed with 100 µL 0.1 M sodium fluoride (NaF) to recover phosphate adsorbed on the pellet surface. The CaF_2 crystals were re-centrifuged and the supernatant was transferred into Tube B with the first aliquot of supernatant. Dissolved phosphate was precipitated as Ag_3PO_4 with 180 µL of silver ammine solution, a mixture of 0.37 M silver nitrate ($AgNO_3$) and 1.09 M ammonium hydroxide (NH_4OH) (Figure 2.1). We adjusted the pH close to neutrality (pH range between 5.5 and 7.5) by adding small aliquots (~10 µL) of 2 M HNO_3 or 2 M NaOH solution to optimize Ag_3PO_4 precipitation, which lasted ~15 min. The precipitated Ag_3PO_4 crystals were rinsed five times with DIW and dried overnight. All steps were run in 1.75 mL microcentrifuge vials.

2.3.3 SPORA Protocol: Decision-Making Process In Establishing the New Technique

The new protocol has three components: *i*) CaF_2 precipitation, *ii*) anion exchange purification, and *iii*) Ag_3PO_4 precipitation (Figure 2.1). These chemical steps were designed and tested in several preliminary experiments exploring efficiency of phosphate isolation, elution from the resin, and precipitation as silver phosphate. These steps were designed to *i*) dissolve bioapatite without using reagent(s) that may interfere during the phosphate adsorption (i.e., nitrate), *ii*) purify phosphate from organic and carbonate contamination, and *iii*) precipitate phosphate rapidly to minimize coprecipitation of oxygen-bearing minerals (e.g., Ag_2O). Dissolved phosphate concentrations were measured via UV-Vis spectrophotometry in each step, respectively (Mine et al., 2017; Murphy and Riley, 1962) (See Section 2.5 for a detailed description of the application).

2.3.3.1 Apatite Dissolution and CaF_2 Precipitation

Many protocols require soaking the apatite powder in a 2 M HF solution for 24h (Crowson et al., 1991; Lécuyer et al., 1998, 1993; Pederzani et al., 2020; Shabaga et al., 2018; Stephan, 2000; Tütken et al., 2006; Vennemann et al., 2002), whereas others pre-dissolve samples in a 2 M HNO_3 before adding the HF reagent (Dettman et al., 2001; Mine et al., 2017; O'Neil et al., 1994; Wiedemann-Bidlack et al., 2008). We avoided the latter step as NO_3^- ions can interfere with resin affinity for phosphate during the purification step (Bio-Rad Laboratories, 2000; Crowson et al., 1991; Pederzani et al., 2020). A preliminary test on synthetic hydroxyapatite and NIST SRM 120c standards shows that a 300 µL aliquot of 2M HF solution yields similar amounts of phosphate as the Rapid UC protocol (see Appendix 2.9.2 for a detailed description). Therefore, the SPORA protocol starts with ~1.5 mg apatite powder in a 1.75 mL microcentrifuge tube (Tube A; Figure 2.1) with the addition of 300 µL 2M HF. Samples are soaked for 24h on a shaker table to complete the dissolution reaction. Once CaF_2 pellets form (Figure 2.1), the phosphate-rich supernatant is pipetted into a clean tube (Tube B; Figure 2.1). CaF_2 pellets in Tube A are further rinsed one time with 100 µL with DIW, and the solution is transferred into Tube B.

2.3.3.2 Anion Exchange Purification

An anion exchange purification step was included before the Ag_3PO_4 precipitation in order to isolate phosphate from other compounds (e.g., organics or carbonate) that could contaminate silver phosphate crystals. Several protocols used the AMBERLITE™ IRN78 resin in hydroxide form to purify phosphate from organics in slow silver phosphate precipitation protocols (Crowson et al., 1991; Lécuyer et al., 1993; Pederzani et al., 2020; Royer et al., 2013). However, this product does not fit our goals because the resin beads *i*) are large (630 ± 50 µm), *ii*) contain chlorine ions in their structure (Dupont, 2019a), which may be released during the desorption step and precipitate as silver chloride (AgCl) alongside Ag_3PO_4 (Grimes and Pellegrini, 2013; Lécuyer, 2004), and *iii*) require circumneutral working solutions to adsorb phosphate, necessitating time-consuming pH adjustments following apatite dissolution. Other protocols for phosphate extraction from soil and water samples use the Dowex (AmberChrom™) 1-X8 anion exchange resin

(Andersohn, 1996; Dupont, 2019b; Lapworth et al., 2014; Sibbesen, 1978). However, phosphate adsorption is optimal when the resin is converted into a ~75% bicarbonate/~25% chloride form (Sibbesen, 1978) and chlorine/based solutions (either hydrochloric acid or potassium chloride) are often required to elute phosphate (e.g., Sibbesen 1978, Lapworth et al., 2014). Again, this resin does not fit our requirements due to potential downstream AgCl contamination during later Ag_3PO_4 precipitation.

We scaled the purification step to a 400 µL working volume (see the combined HF solution and deionized water volumes in Section 2.3.1) by using the chloride-free Bio-Rad AG™ 1-X8 anion exchange resin in hydroxide form (Figure 2.1). These resin beads prefer small, inorganic, monovalent ions (e.g., phosphate as $H_2PO_4^-$) and are successfully employed in phosphate extraction and elution protocols for water samples (Colman, 2002; Colman et al., 2005; Goldhammer et al., 2011, 2010). Because the resin beads are small (106 -180 µm) and sticky, we used Millipore Sigma Ultrafree™ – CL centrifugal tubes with a polytetrafluoroethylene (PTFE) microporous membrane (pore size of 0.2 µm) (Merck KGaA, 2018) to facilitate adsorption and desorption steps. These vials have a 2 mL filter unit that can be removed from the 5 mL collector tube (Tube B and C, Figure 2.1).

We conducted several preliminary experiments to assess the proper working pH, type, and concentration of counter ions to efficiently isolate phosphate from impurities. These results demonstrated that phosphate adsorption to resin is independent of pH and 0.44 M sodium nitrate ($NaNO_3$) is the optimal solution for eluting phosphate (Figure 2.1; see Appendix 2.9.3 for a detailed description). The anion exchange purification process in SPORA reflects these optimized conditions. The phosphate-rich supernatant is pipetted into the filter unit pre-loaded with resin (Tube B, Figure 2.1). The resin uptakes phosphate in exchange for hydroxide ions (Bio-Rad Laboratories, 2000). Then, the solution is centrifuged down at 4,500 RPM for 30 minutes to the collector tube to isolate dissolved impurities. At this stage, the filter unit is plugged into a clean collector tube (Tube C) to elute phosphate with seven rinses of 200 µL 0.44 M $NaNO_3$ (Figure 2.1).

2.3.3.3 Ag_3PO_4 Precipitation

Silver phosphate crystals precipitate when the phosphate-rich solution is combined with a silver ammine solution (Figure 2.1) that has high concentration of Ag^+ compared to phosphate (0.37 M $AgNO_3$; Ag^+:PO_4^{3-} ratio ≥ 10:1) (Mine et al., 2017; O'Neil et al., 1994). The elution of phosphate is achieved using a $NaNO_3$ eluent. The elution process involves transferring the phosphate from the resin into a large working volume of the eluent (1,400 µL; Appendix 2.9.3). It is important to note that this solution also contains water, which may lead to coprecipitation of oxygen-bearing compounds like silver oxide (Ag_2O) given a large amount of hydroxide ions in solution. To avoid Ag_2O contamination while precipitating Ag_3PO_4, the silver ammine solution for SPORA uses 180 µL of a solution containing 0.22 M $AgNO_3$ and 1.09 M NH_4OH (Tube D, Figure 2.1). This solution has a lowered $AgNO_3$ concentration compared to that used in the Rapid UC protocol (Mine et al. 2017) (Appendix 2.9.4).

2.3.4 Stable Oxygen Isotope Analysis

The $\delta^{18}O_p$ values of silver phosphate crystals were measured with a Thermal Conversion Elemental Analyzer (TC/EA)-ConFlo IV-Delta V Plus continuous flow isotope ratio mass spectrometer system (Thermo Scientific, Bremen, Germany) at the Stable Isotope Ecosystem Laboratory of (SIELO) University of California, Merced (California, USA). Samples were run in triplicates of ~0.2 mg each and were packed into silver capsules. Silver phosphate is reduced to CO gas by heating the TC/EA graphite column at 1,450 °C. Drift and linearity correction were applied. Then, samples were calibrated to the Vienna Standard Mean Ocean Water scale (V-SMOW) with a 2-point calibration using Ag_3PO_4 reference materials. The USGS 80 ($\delta^{18}O_p$ = 13.1 ± 0.2 ‰ (n = 234), United States Geological Survey [USGS]; > 99% purity) and USGS 81 ($\delta^{18}O_p$ = 35.4 ± 0.3 ‰ (n = 231), USGS; > 99% purity) are the certified silver phosphate reference materials used to calibrate samples and to assess analytical accuracy and precision. Analytical precision of biogenic and working reference apatite materials are reported as mean ± 1σ.

2.3.5 UV-Vis Spectrophotometry - Soluble Reactive Phosphate Measurements

To determine phosphate recovery performance and compare it to isotopic composition, we measured dissolved phosphate concentrations with a molybdate blue spectrophotometric technique. The approach determines the amount of dissolved, inorganic soluble reactive phosphate (SRP) irrespective of phosphate species (i.e., ΣPO_4^{3-}) via formation of a molybdate blue complex (Murphy and Riley, 1962). Phosphate concentrations were determined following acid dissolution (i.e., “starting concentration”, *SC*), phosphate adsorption to resin (i.e., “resin step 1”, *RS1*), phosphate elution (i.e., “resin step 2”, *RS2*), and after Ag_3PO_4 crystal precipitation (i.e., “precipitation", *P*) for the SPORA protocol (Figure 2.1). Similarly, samples processed with the Rapid UC method were measured for phosphate concentration following apatite dissolution and crystal precipitation (i.e., aliquots *SC* and *P*, Figure 2.1).

Aliquots were diluted up to a 5,000-fold factor to constrain the phosphate concentration of samples within the absorbance-concentration linear response range given by the potassium dihydrogen phosphate (KH_2PO_4)-based standard curve (0 to 20 μM phosphate). Diluted samples were mixed with the colorimetric reagent made of a mixture of 2.5 M sulfuric acid (CAS: 7664-93-9), 24 mM ammonium molybdate tetrahydrate (CAS: 12054-85-2), 0.31 M ascorbic acid (CAS: 50-81-7), and 2 mM antimony potassium tartrate (CAS: 331753-56-1) in a 5:2:2:1 volume ratio, respectively (Mine et al., 2017). Because residual silver may interfere with the colorimetric reagents, aliquots collected after the precipitation (i.e., aliquots *P* in Figure 2.1) were treated with a 1 M sodium chloride (NaCl) solution to remove Ag^+ as AgCl (Mine et al., 2017). Additionally, we matched standard curve matrices to samples, ensuring solution compositions were the same.

Absorbance values were measured with a Thermo Scientific Evolution 300 (Thermo Fisher Scientific) spectrophotometer equipped with a xenon lamp set at 883 nm housed in the Ghezzhei Lab of Soil Physics at the University of California, Merced (California, USA). We checked potential departures of absorbance accuracy by comparing KH_2PO_4-based standard curves generated at each run. Finally, we monitored the fraction of phosphate moles

at each chemical step and calculated the phosphate recovery (ΣPO_4^{3-} recovery (%)) relative to the initial amount of dissolved phosphate. The total phosphate recovery for the SPORA protocol was calculated as follows:

$$\sum PO_4^{3-}\ recovery_{SPORA}\ (\%) = (\sum PO_{4\ RS2}^{3-} - \sum PO_{4\ P}^{3-}) / \sum PO_{4\ SC}^{3-}) * 100$$

where $\Sigma PO_4^{3-}{}_{RS2}$ is the phosphate amount following phosphate elution (Tube C), $\Sigma PO_4^{3-}{}_{P}$ is the residual amount after the precipitation, and $\Sigma PO_4^{3-}{}_{SC}$ is the starting amount of dissolved phosphate. Because the Rapid UC has two major steps (Figure 2.1), phosphate recovery was calculated as follows:

$$\sum PO_4^{3-}\ recovery_{Rapid\ UC}\ (\%) = (\sum PO_{4\ SC}^{3-} - \sum PO_{4\ P}^{3-}) / \sum PO_{4\ SC}^{3-}) * 100$$

2.3.6 FTIR Analysis

We used Fourier-Transform Infrared Spectroscopy (FTIR) to evaluate the material composition of crystals precipitated with both protocols and their corresponding apatite materials. If contaminated, FTIR spectra of Ag_3PO_4 crystals would show infrared-active vibrational bands of nitrogen-based compounds, silver-oxygen, silver-carbonate, or a mixture of both along with absorption bands of phosphate groups. Such bands are produced via the inclusion of amide groups from collagen, silver oxide, and silver carbonate particles in silver phosphate crystals (Al Sekhaneh et al., 2021; Grunenwald et al., 2014; Haq et al., 2018; Köck et al., 2013; Kumar and Rani, 2013; Lebon et al., 2016; Oje et al., 2019; Rahman et al., 2018; Rashmi et al., 2020; Shimabukuro et al., 2022; Siddiqui et al., 2013; Slager et al., 1972; Suthanthiraraj and Sarumathi, 2012; Suwanprateeb et al., 2012; Trayler et al., 2023; Trivedi et al., 2015). For reference spectra, we analyzed the material composition of silver phosphate (>99 % purity, Alfa Aesar) mixed with ~20 %wt of collagen standard or Ag_2O to verify vibrational modes of these functional groups (Appendix 2.9.5).

Before FTIR analysis, replicates of silver phosphate crystals precipitated from a specific apatite material and protocol were combined to improve sample size. Thus, all silver phosphate spectra show the average molecular composition when precipitated with a specific protocol. Spectra were collected with a Bruker Vertex 70 Far-Infrared in ATR mode held by the Nuclear Magnetic Resonance Facility at the University of California, Merced (California, USA). Spectra were collected within 400 – 4000 cm^{-1} and were smoothed by overlapping 32 scans of the same sample at a resolution of 4 cm^{-1}. We corrected spectra to level down the baseline of absorbance bands. The correction fits several spline curves to subtract the background at points with expected absorbance intensity equal to 0 following R code scripts published elsewhere (RStudio Team, 2021; Trayler et al., 2023).

2.3.7 Exploration of Silver Oxide and Carbonate

We measured $\delta^{18}O$ values of in-house precipitated silver oxide (Ag_2O) and carbonate (Ag_2CO_3) to monitor the deviation of Ag_3PO_4 oxygen isotope composition due to coprecipitation of these two oxygen-bearing compounds. Replicates of Ag_2O (n = 8) and Ag_2CO_3 (n = 22) were packed into silver capsules and $\delta^{18}O$ values were measured as described in Section 2.4.

We tested the isotopic effect of inorganic carbonate contamination (e.g., structural carbonate) as silver carbonate inclusion by simulating Ag_2CO_3 – Ag_3PO_4 mixtures in varying silver carbonate quantities (i.e., ~1 to ~10 %wt Ag_2CO_3). The Ag_3PO_4 substrate of the simulated mixtures derives from the working fluorapatite reference that was treated with both protocols (n = 22; Table 2.1 and Table 2.2). We ran 10,000 simulations to estimate the degree of isotopic shift in contaminated Ag_3PO_4 crystals using the following equation:

$$\delta^{18}O_{mix} = (\delta^{18}O_p * Ag_3PO_{4\,wt\%}) + (\delta^{18}O_{Ag_2CO_3} * Ag_2CO_{3\,wt\%})$$

Where $\delta^{18}O_p$ and $Ag_3PO_{4\ wt\%}$ are the isotopic composition and fraction of Ag_3PO_4 in the mixture, $\delta^{18}O_{Ag2CO3}$ and $Ag_2CO_{3\ wt\%}$ are the isotopic composition and fraction of Ag_2CO_3 in the mixture, and $\delta^{18}O_{mix}$ is the isotopic composition of the Ag_2CO_3 – Ag_3PO_4 mixture.

Finally, we compared contaminated $\delta^{18}O$ values from the simulations to measurements of manually contaminated silver phosphate. The $\delta^{18}O_{mix}$ values are from Ag_3PO_4 crystals (n = 13) that were manually contaminated with Ag_2CO_3 aliquots to ensure agreement between simulations and empirical values. We used Ag_3PO_4 crystals precipitated from the working fluorapatite reference material via Rapid UC protocol as substrate for the mixture. Each sample was homogenized with varying Ag_2CO_3 fractions between ~1 to ~10 %wt. All samples were run in triplicates of ~0.2 mg and packed into silver capsules for oxygen isotope analysis in the TCEA as described above.

2.4 Results and Discussion

2.4.1 SPORA and Rapid UC Protocols Yield Similar $\delta^{18}O_p$ Values

We developed a new silver phosphate precipitation procedure, the SPORA protocol, that closely preserves the phosphate oxygen isotope composition of biogenic and reference apatite materials. The $\delta^{18}O_p$ measurements of apatite materials treated with SPORA and the Rapid UC protocols have high, linear correlation with a 1:1 linear regression ($R^2 = 0.99$; $p << 0.05$; Figure 2.2). Notably, reference materials and low-organic content specimens such as tooth enameloid and enamel from modern samples exhibit the highest agreement between protocols. These specimens show $\delta^{18}O_p$ values within the accepted analytical error (~0.3 ‰) when comparing protocol performances (Figure 2.2; Table 2.2), indicating similarity between treatment outcomes.

Divergences between treatments arise in samples with higher organic content or diagenetic alteration. Fossil specimens, the modern deer bone, and tooth mixtures are indeed

those that behave differently. Apatite materials of modern specimens with expected high organic contents, such as tooth crown surface and dentin mixtures or bone specimens (OV and MM2) show a larger isotopic offset between protocols ($\Delta^{18}O$, $\delta^{18}O_{p\ SPORA} - \delta^{18}O_{p\ Rapid\ UC}$) ranging from -0.4 ± 0.1 ‰ to -0.9 ± 0.2 ‰ (Figure 2.2; Table 2.2). The fossil bone MM1 has similar $\delta^{18}O_p$ values between protocols if tar is removed, but an isotopic shift of ~-0.5 ‰ is observed when comparing the untreated and the tar-removed powder precipitated with SPORA protocol. Finally, the enemaloid of the shark specimen SM1 has a $\Delta^{18}O$ offset of ~-0.5 ‰ (Table 2.2). The isotopic composition of fossil shark tooth mixtures is quite different from that of pure enameloid within the same tooth specimen regardless of the protocol used. This difference ranges from ~1.6 ‰ in SM2 to ~3 ‰ in SM1 specimen (Table 2.2) and is likely due to diagenetic alteration or variably isotopic composition between tissues.

Overall, both protocols yield similar isotopic values when using apatite materials with expected low or no organic content, while protocols perform differently on samples with expected high amounts of collagen or fossil materials with diagenesis. Five possible explanations for protocol differences are: *i*) SPORA contains contamination derived from the used reagents; *ii*) SPORA successfully isolates phosphate from organics; *iii*) incomplete Ag_3PO_4 precipitation affects isotopic fractionation; *iv*) isotopic heterogeneity in samples generates apparent isotopic effects; *v*) protocols behave differently if samples are diagenetically altered.

2.4.2 SPORA Mitigates Ag_2O Contamination In Ag_3PO_4 Crystals

Infrared spectra detected the nature of contamination in precipitated Ag_3PO_4 crystals (Figure 2.3) that caused the observed isotopic variation between protocols (Table 2.3 and Appendix 2.9.5). All crystals show sharp ν_4PO_4 and ν_3PO_4 absorption bands at 542 and 930 cm^{-1}, and small peaks also occur at 603 and 1095 cm^{-1}, respectively. A small oxygen-silver-oxygen band occurs in crystals precipitated with the Rapid UC method at ~1072 cm^{-1} (Figure 2.3), which we interpreted as Ag_2O inclusion (Figure 2.3). No silver oxide infrared band is shown in crystals precipitated with SPORA protocol (Figure 2.3).

These observations suggest that the Rapid UC protocol incorporates Ag_2O during precipitation of Ag_3PO_4 crystals. This is likely due to the higher concentration of silver used to promote Ag_3PO_4 precipitation (see Appendix 2.9.4) (Mine et al., 2017). Water and/or air are the likely oxygen sources in Ag_2O (Biedermann et al., 1960; Charlot, 1969):

$$Ag^{+}_{(aq)} + OH^{-}_{(aq)} \rightarrow AgOH_{(s)} \rightarrow \tfrac{1}{2}\, Ag_2O_{(s)} + \tfrac{1}{2}\, H_2O_{(aq)}$$

The mean oxygen isotope value from our in-house precipitated Ag_2O (0.4 ± 1.7 ‰; Appendix 2.9.9) likely reflects the isotopic composition of the silver oxide contamination in Ag_3PO_4 crystals precipitated via Rapid UC procedure. These values suggest that incorporation of Ag_2O introduces ^{16}O-enrichments that may cause a shift toward low $\delta^{18}O_p$ values. However, Ag_2O contamination alone cannot explain variability in $\delta^{18}O_p$ values between protocols. Such shift should be systematic in all crystals precipitated via Rapid UC method regardless of the nature of the starting material, which is not the case (Figure 2.2 and

Table 2.2). Again, the greatest variability occurs with apatite materials high in organic content and in fossil specimens.

2.4.3 SPORA Contains the Inclusion of Organic-Altered Carbonate As Silver Carbonate (Ag_2CO_3)

No crystals show amide vibration bands (Figure 2.3), indicating that anion exchange resin and bleach removed nitrogen-rich organic fraction or they are below detection limits in agreement with other studies (Grimes and Pellegrini, 2013; Pederzani et al., 2020; Wiedemann-Bidlack et al., 2008). Instead, silver carbonate is likely a contaminant phase for most silver phosphate methods. Infrared absorption occurs at ~1405 and 1545 cm^{-1}, which are modes of carbonate functional groups (Figure 2.3; see also Appendix 2.9.5). Carbonate peaks are small for both protocols, but the SPORA method produces crystals with a slightly larger ν_3CO_3 band at 1545 cm^{-1} (Appendix 2.9.8), which is likely due to structural carbonate, an inevitable confounding factor in Ag_3PO_4 precipitation methods.

The inclusion of carbonate may be strictly related to its source types and conversion into different species (i.e., CO_2, HCO_3^-, CO_3^{2-}) as pH varies (Abderrahim et al., 2016). There are a variety of sources for carbonate that could potentially contaminate Ag_3PO_4 crystals. First, oxidized metals such as Ag_2O or reagents like the silver ammine solution may absorb atmospheric or dissolved CO_2 from the headspace of vials (L'vov, 1999; Mine et al., 2017; Slager et al., 1972; Trivedi et al., 2015) (see also Appendix 2.9.5). Second, structural carbonate precipitates as a substitute for phosphate and hydroxide (or fluorine in shark enameloid) crystallographic sites during apatite mineralization (Enax et al., 2014, 2012; LeGeros, 1981; Leventouri, 2006) (see also Appendix 2.9.6). Lastly, carbonate could be an unwanted effect as a result of organic degradation (Crowley and Wheatley, 2014; Grimes and Pellegrini, 2013).

If samples contain low or no organic content, structural carbonate and/or atmospheric CO_2 are likely the main source of contamination for both protocols. When apatite materials are dissolved in weak acid solutions like the HF reagent (pH ~ 1; Figure 2.1), structural carbonate is released as free gas (Abderrahim et al., 2016)' that could equilibrate with the solvent forming dissolved carbon dioxide (CO_2) at standard temperature and pressure conditions (Cox and Head, 1962). For example, assuming that 1 mg of bioapatite yields 6 %wt carbonate (Crowley and Wheatley, 2014), a Henry's law constant for CO_2 (K_{CO2}) of 0.0357 mol * L^{-1} atm^{-1} for a 2.5 M HF solution (Cox and Head, 1962), and 300 µL of solvent in a 1.5 mL capped vial (i.e., close system), about 21% of the carbon dioxide gas yielded from the structural carbonate dissociation could stay dissolved in the reagent (full calculation is found in Appendix 2.9.10). In strong acid media like the HNO_3 initially used in the Rapid UC protocol, the structural carbonate pool should evolve as CO_2 gas and have no interaction with the solution. Bicarbonate (HCO_3^-) would also form because silver ammine solutions are always prepared to change the pH close to neutrality (Abderrahim et al., 2016; Mine et al., 2017; O'Neil et al., 1994) (see also Appendix 2.9.4). As a result, the remaining silver ions coprecipitate silver carbonate (Ag_2CO_3) given the following chemical equilibria (Abderrahim et al., 2016; Atwater, 2002; Barnes et al., 1971):

$$CO_{2\,(aq)} + H_2O_{\,(aq)} \rightleftharpoons H_2CO_{3\,(aq)} \rightleftharpoons HCO_3^-{}_{(aq)} + H^+_{(aq)} \rightleftharpoons CO_3^-{}_{(aq)} + 2H^+_{(aq)}$$

$$Ag_2O_{\,(s)} + CO_{2\,(aq\ \text{or}\ g)} \rightarrow Ag_2CO_{3\,(s)}$$

$$2AgNO_3^+{}_{\,(s)} + H_2CO_{3\,(aq)} \rightarrow 2AgNO_3^+{}_{\,(s)} + HCO_3^-{}_{(aq)} + H^+_{\,(aq)} \rightarrow Ag_2CO_{3\,(s)} + 2HNO_{3\,(aq)}$$

Inclusions of mainly structural carbonate and/or atmospheric CO_2 into Ag_3PO_4 crystals could explain why protocols show low $\Delta^{18}O$ offset for these types of materials. However, there is added complexity when using bones or teeth with high collagen content. When exposing bone and tooth mixtures to NaOCl solution (pH = 9.5; Figure 2.1**,** Rapid UC protocol), amide groups undergo decomposition but bleach does not remove completely the organic fabric (Grimes and Pellegrini, 2013; Gu et al., 2017; Marending et al., 2007; Snoeck and Pellegrini, 2015). Amino acids that survive to bleach, such as glycine and alanine, adsorb CO_2 under circumneutral pH conditions (Guo et al., 2013). If this occurs during Ag_3PO_4 precipitation, ^{18}O-depleted CO_2 molecules could be adsorbed from the vial headspace, leaving the heavier isotopologues behind. The ^{18}O-enriched CO_2 in the headspace will be adsorbed by the silver ammine solution (Mine et al., 2017) and promote ^{18}O-enriched Ag_2CO_3 coprecipitation. This mechanism could offer insights into the consistent presence of Ag_2CO_3 contamination across samples (Figure 2.3, Appendix 2.9.8), where the crucial factor is how organics influence modifications to atmospheric CO_2 in the vial headspace. Indeed, samples showing high organic content subjected to bleach pretreatment exhibit isotopic shifts higher than 0.3‰ compared to samples treated via SPORA or their corresponding enameloid materials processed with Rapid UC (Figure 2.2, Table 2.2, Appendix 2.9.6).

In contrast, the SPORA protocol does not use a NaOCl pretreatment and isolates phosphate from collagen with an anion exchange resin, preventing undesired isotopic shifts during the Ag_3PO_4 precipitation. SPORA dissolves samples in HF, a weak acid where collagen proteins break down into simple amino acids polarized with positively charged organic compounds ($R\text{-}NH_3^+$) (Bowes et al., 1955; Liu and Huang, 2016; Nishiyama et al., 2003). These organic compounds should have no interactions with an anion exchange resin. As a result, we speculated that the SPORA protocol produces Ag_3PO_4 with more accurate measurements by preventing the inclusion of organic-altered carbonate. The exclusion of this proposed carbonate contaminant is key to precipitating Ag_3PO_4 crystals with $\delta^{18}O_p$ values closer to the actual phosphate isotopic composition of biogenic apatite materials. This hypothesis is also supported by $\delta^{18}O_p$ values of enameloid and tooth mixtures in modern shark teeth, where the SPORA protocol yields very similar values between mixed substrate material types (i.e., enameloid and dentin) compared to the Rapid UC method (Figure 2.2 and Table 2.2). Therefore, inorganic structural carbonate and/or unaltered atmospheric CO_2 should be the main contaminant in Ag_3PO_4 crystals precipitated with the SPORA protocol.

Although the SPORA protocol produces Ag_3PO_4 crystals with slightly more carbonate contamination than the Rapid UC method (Figure 2.3 and Appendix 2.9.8), such contamination does not cause a significant shift in $\delta^{18}O_p$ values. Our experimental test on simulated and manually created Ag_2CO_3-Ag_3PO_4 mixtures (Figure 2.4) demonstrates the potential ~13 ‰ offset ($\delta^{18}O_{p\ \text{Fluorapatite}} = 8.9 \pm 0.4$ ‰; $\delta^{18}O_{\text{Ag2CO3}} = 21.6 \pm 0.7$ ‰) observed in some taxa (e.g., sharks, small rodents, and lagomorphs) (Karnes et al., 2024; Tütken et al.,

2006; T. W. Vennemann et al., 2001). The choice of the fluorapatite working reference material used in this experiment is justified by the fact that *i*) it is the material with the least amount of carbonate in its structure (Appendix 2.9.6) and *ii*) $\delta^{18}O_p$ values and FTIR carbonate peaks are equivocal between protocols (Figure 2.2, Figure 2.3, Table 2.2, Appendix 2.9.8). Both simulated and empirical values largely agree that inclusions of 1.5 %wt Ag_2CO_3 or higher cause a shift toward higher $\delta^{18}O$ values, making measurements inaccurate (Figure 2.4). Given that protocols yield similar $\delta^{18}O_p$ values (Figure 2.2 and Table 2.2), we speculate that the Ag_2CO_3 fraction in Ag_3PO_4 crystals produced with the SPORA technique is below this threshold.

2.4.4 SPORA Protocol Recovers Less Phosphate Than Rapid UC With No Isotope Effects

Contrary to the Rapid UC method, the SPORA protocol requires more wet chemistry steps to treat phosphate (Figure 2.1). Anion exchange purification and precipitation steps to isolate, extract, and precipitate phosphate could increase losses of dissolved phosphate relative to the starting amount. Incomplete resin exchange coupled with incomplete crystal precipitation may lead to isotopic fractionation by altering the original phosphate oxygen isotopologue ratios. Fractionation effects may also occur particularly when the total amount of phosphate recovered is less than 95% (Mine et al., 2017).

UV-Vis spectrophotometry measurements show that increasing the number of wet chemistry steps results in less phosphate recovered. Phosphate recovery distributions of Rapid UC and SPORA protocols are skewed, but the Rapid UC shows a smaller interquartile range (3.9 % for Rapid UC and 12.8 % for SPORA) compared to the SPORA protocol (Table 2.3). The latter has a median value of 91.2 % against 97.8 % of the Rapid UC (Table 2.3), and this difference is statistically significant (Kruskal-Wallis test, $p = 1.264 \times 10^{-8}$). Overall, these data show that the SPORA protocol recovers on average ~90 % of dissolved phosphate and recovery is highly variable (Table 2.3). Among chemical steps, our observations show that resin desorption causes the highest loss and variability in phosphate recovery, where ~10 % of phosphate is lost after this chemical step (Appendix 2.9.3 and Appendix 2.9.7).

Despite the SPORA protocol recovering less phosphate than the Rapid UC protocol, our results suggest that phosphate recovery alone does not explain the variability in $\delta^{18}O_p$ values. If recovery were the cause of isotopic fractionation, a persistent and variable offset in $\delta^{18}O_p$ values between protocols would be evident, but the greatest variability occurs with apatite materials containing high organic content, such as bone samples and tooth crown surface/dentin mixtures of modern specimens (Figure 2.2 and Table 2.2). As such, our results do not support the hypothesis that phosphate recovery with the SPORA protocol has an isotopic effect.

2.4.5 Specific Concerns With Shark Teeth

We developed SPORA to use on shark teeth given the challenges to analyzing small, fossil specimens. Tooth enameloid and dentin in sharks incorporate oxygen isotopes during

the early stages of tooth apatite formation. Sharks do not remodel their teeth once they are fully mineralized, but they continuously replace them in a conveyor belt-like fashion across their life (Dorozhkin, 2009; LeGeros, 1981; Pucéat et al., 2010; Vennemann et al., 2001). Assuming a homogeneous isotopic composition in their apatite structure in both enameloid and dentin within a single tooth and tooth rows, we tested SPORA's performance on shark teeth to address the following hypotheses: *i*) no difference between protocols in $\delta^{18}O_p$ values when using only enameloid; *ii*) tooth enameloid/dentin mixtures yield different $\delta^{18}O_p$ values among protocols; *iii*) no $\delta^{18}O_p$ offset between enameloid and enameloid/dentin mixture when using SPORA.

We initially tested the SPORA protocol on modern shark teeth that indicated offset between protocols due to organic contamination (Table 2.2). However, this is not the case for fossil shark tooth specimens. The shape of FTIR spectra for tooth enameloid and tooth mixtures of both fossil specimens are indistinguishable (Appendix 2.9.6), suggesting that organics degraded during the time of fossilization (Ramírez-Bommer et al., 2018). Instead, we ascribed such discrepancies between protocols and between tooth tissues (Table 2.2) to heterogeneities similar to those observed in mammal teeth. In sharks, apatite mineralization in tooth dentin occurs after the enameloid is fully mature (Enax et al., 2014; LeGeros, 1981; Sasagawa, 1999). Tooth replacement rates are species-specific and can be as slow as 190 days per row tooth series (Botella et al., 2009). In contrast to teeth from the modern blue shark, the fossil sand tiger shark individuals could have slow tooth mineralization rates while experiencing varying environmental conditions, causing isotopic zonation within the enameloid and between enameloid and dentin. Several previous studies have also shown that shark teeth may differ by as much as a few per mille from one area to another and between tooth tissues (Vennemann et al., 2001; Žigaite and Whitehouse, 2014). Therefore, the isotopic differences among the samples from a single fossil specimen could be biologically mediated rather than an artifact of silver phosphate precipitation protocol.

2.4.6 SPORA Protocol's Limitations: Natural Asphalt and Diagenetic Carbonate Removal

The analysis of fossil mammal bones offers a valuable case study to explore limitations of the SPORA protocol with respect to two exogenous contaminants: natural asphalt and diagenetic carbonate (Table 2.2; Appendix 2.9.6). Although FTIR analysis on MM1 failed to detect the asphalt component in the untreated specimen (Appendix 2.9.6), we speculated that the high isotopic offset between tar-removed and untreated sample (Table 2.2) is due to tar-derived carbonate formed during the HF dissolution step that the anion exchange resin cannot isolate properly and, eventually, interacts with the silver ammine solution during the Ag_3PO_4 precipitation reaction. Natural asphalt is a complex polymer that includes organics with methyl ($-CH_3$), hydroxyl (-OH), and ether bonds such as aromatic compounds and fulvic acid. These molecules undergo weak oxidation and release CO_2 when exposed to acidic solutions like the HF reagent (Ni et al., 2022; Xue et al., 2019; Yürüm et al., 1985; Zhang et al., 2016, 2020, 2021). The free CO_2 gas could dissolve in the supernatant and interact subsequently with the resin during the phosphate adsorption step. As a result, we recommend using an asphalt removal procedure on tar-contaminated specimens

before preparing samples for phosphate oxygen isotope analysis, regardless of whether samples are purified with anion exchange resin or not.

The infrared spectrum of specimen MM2 bone powder displays alteration features due to calcium carbonate inclusion ($CaCO_3$; Appendix 2.9.6). Inclusions of secondary carbonate sources may shift measurements toward ^{18}O-depleted isotopic values (Garvie-Lok et al., 2004; Koch et al., 1997; Zazzo et al., 2004), a pattern we saw in Ag_3PO_4 crystals precipitated via SPORA procedures when comparing protocols (Table 2.2). Infrared spectra show more pronounced carbonate peaks for the SPORA protocol (Figure 2.3, Appendix 2.9.8) and an additional carbonate band at 870 cm^{-1} (ν_2CO_3), a feature that is unique to Ag_3PO_4 crystals for this bone specimen in both protocols (Figure 2.3). Such carbonate source should not impact the purity and isotopic composition of crystals precipitated via Rapid UC because samples are dissolved in a HNO_3 solution (pH ~ 0) and diagenetic carbonate readily forms free CO_2. Carbon dioxide-trapping bubbles should break apart as the supernatant is agitated and transferred in another vial during the following steps (Figure 2.1) but some could also reach stability with the solution in low pH conditions (Tabor et al., 2011). These bubbles could eventually coalesce and dissolve the trapped CO_2 in the supernatant at circumneutral pH (Tabor et al., 2011), a condition achieved when the silver ammine solution is added to precipitate Ag_3PO_4 crystals. This mechanism could explain the occurrence of small ν_2CO_3 bands in Ag_3PO_4 crystals precipitated via Rapid UC method, but, again, diagenetic carbonate has a limited impact on Ag_3PO_4 the isotopic composition given that samples were dissolved in a strongly acidic medium and most of the bubbles formed during the dissolution step should break apart. For diagenetically altered samples like MM2 treated via SPORA method, we recommend removing secondary carbonate minerals like $CaCO_3$ before the procedure given its reaction in HF solution (see also Section 2.4.4 and Appendix 2.9.10) or CO_2 bubbles may stabilize in the supernatant (Tabor et al., 2011); in both cases, the CO_2 gas could interact with the resin during the phosphate adsorption step. A possible pretreatment is soaking the stock powder in a 1 M acetic acid buffered with calcium acetate solution. The reagent dissolves secondary carbonates with minor effects on apatite integrity and oxygen isotopes as described elsewhere (Crowley and Wheatley, 2014; Garvie-Lok et al., 2004; Koch et al., 1997).

2.5 Conclusions

We have designed a new Ag_3PO_4 precipitation protocol (SPORA) for phosphate oxygen isotope analysis that accounts for small sample sizes (i.e., 1.5 mg or less) and collagen contamination. The SPORA protocol performs very closely to current methodologies in terms of oxygen isotope measurements of the Ag_3PO_4 crystals precipitated from different apatite specimens. The use of the anion exchange resin in the SPORA protocol decreases the phosphate recovery to around 90% without causing isotopic shifts in the Ag_3PO_4 crystals. The SPORA protocol minimizes Ag_2CO_3 contamination and prevents the inclusion of Ag_2O and collagen-altered carbonate in Ag_3PO_4 crystals even in organic-rich, crushed, shark tooth samples. While bleach pretreatment to remove collagen is unnecessary when using the SPORA protocol, pretreatments to remove exogenous contaminants like tar or diagenetic carbonate are recommended.

Further, this study is the first to identify secondary oxygen-bearing phases included in Ag_3PO_4 crystals and place them in context to assess the analytical accuracy and precision of $\delta^{18}O_p$ measurements. Deviations from expected $\delta^{18}O_p$ values may occur when contaminants like Ag_2O and Ag_2CO_3 coprecipitate with Ag_3PO_4, the latter being a confounding factor for most silver phosphate protocols to date. Specimens with high collagen content or those being diagenetically altered are the ones that show isotopic shifts higher than ~0.3‰ between different treatments. More experiments on the contribution of each carbonate source to the bulk carbonate contamination as Ag_2CO_3 inclusion are needed in order to test the performance between protocols with respect to isotopic fidelity and Ag_3PO_4 crystal purity.

Current silver phosphate precipitation protocols are faster for samples with low or no expected collagen content or when large samples are available. However, pretreating organic-rich samples with bleach causes undesirable ^{18}O-enrichment as shown in other studies. Samples with a low starting amount of material and high collagen content require an anion exchange purification step to effectively remove organic contaminants (i.e., collagen). The SPORA method isolates phosphate from collagen contamination and enhances the reliability of $\delta^{18}O_p$ measurements, making the application suitable for bioapatite materials of varying organic content, including crushed tooth specimens, for paleoenvironmental, palaeoecological, and archeological applications.

2.6 References

Abderrahim, B., Mohamed, H., & Abla, F. (2016). Study on thermal desalination effect on the solids' precipitation variation. *Desalination and Water Treatment*, *57*(13), 5926–5931. https://doi.org/10.1080/19443994.2015.1038733

Andersohn, C. (1996). Phosphate cycles in energy crop systems with emphasis on the availability of different phosphate fractions in the soil. *Plant and Soil*, *184*(1), 11–21. https://doi.org/10.1007/BF00029270

Atwater, J. E. (2002). Complex dielectric permittivities of the Ag2O-Ag2CO3 system at microwave frequencies and temperatures between 22 °C and 189 °C. *Applied Physics A: Materials Science and Processing*, *75*(5), 555–558. https://doi.org/10.1007/s003390201308

Barnes, P. A., O'Connor, M. F., & Stone, F. S. (1971). Reactivity of silver oxide in the absorption of carbon dioxide. *Journal of the Chemical Society A: Inorganic, Physical, and Theoretical Chemistry*, 3395–3398. https://doi.org/10.1039/J19710003395

Biedermann, G., Sillén, L. G., Lindberg, B., & Dodson, R. M. (1960). Studies on the Hydrolysis of Metal Ions. Part 30. A Critical Survey of the Solubility Equilibria of Ag2O. *Acta Chemica Scandinavica*, *14*, 717–725. https://doi.org/10.3891/acta.chem.scand.14-0717

Bio-Rad Laboratories. (2000). AG 1, AG MP-1, and AG 2 Strong Anion Exchange Resin Instruction Manual Table of Contents. Retrieved from https://www.bio-

rad.com/webroot/web/pdf/lsr/literature/LIT212.pdf

Botella, H., Valenzuela-Ríos, J. I., & Martínez-Perez, C. (2009). Tooth replacement rates in early chondrichthyans: A qualitative approach. *Lethaia*, *42*(3), 365–376. https://doi.org/10.1111/j.1502-3931.2009.00152.x

Bowes, J. H., Elliott, R. G., & Moss, J. A. (1955). The composition of collagen and acid-soluble collagen of bovine skin. *The Biochemical Journal*, *61*(1), 143–150. https://doi.org/10.1042/bj0610143

Charlot, G. (1969). *Les réactions chimiques en solution; l'analyse qualitative minérale*. (Toray-Masson, Ed.) (6th ed.). Paris: Masson et Cie.

Colman, A. S. (2002). *The Oxygen Isotope Composition of Dissolved Inorganic Phosphate and the Marine Phosphorus Cycle*. Yale University.

Colman, A. S., Blake, R. E., Karl, D. M., Fogel, M. L., & Turekian, K. K. (2005). Marine phosphate oxygen isotopes and organic matter remineralization in the oceans. *Proceedings of the National Academy of Sciences of the United States of America*, *102*(37), 13023–13028. https://doi.org/10.1073/PNAS.0506455102/SUPPL_FILE/06455SUPPTEXT.PDF

Cox, J. D., & Head, A. J. (1962). Solubility of carbon dioxide in hydrofluoric acid solutions: "Standard state" correction for the combustion calorimetry of organo-fluorine compounds. *Transactions of the Faraday Society*, *58*(0), 1839–1845. https://doi.org/10.1039/TF9625801839

Crowley, B. E., & Wheatley, P. V. (2014). To bleach or not to bleach? Comparing treatment methods for isolating biogenic carbonate. *Chemical Geology*, *381*, 234–242. https://doi.org/10.1016/j.chemgeo.2014.05.006

Crowson, R. A., Showers, W. J., Wright, E. K., & Hoering, T. C. (1991). Preparation of Phosphate Samples for Oxygen Isotope Analysis. *Analytical Chemistry*, *63*(20), 2397–2400. https://doi.org/10.1021/ac00020a038

Dettman, D. L., Kohn, M. J., Quade, J., Ryerson, F. J., Ojha, T. P., & Hamidullah, S. (2001). Seasonal stable isotope evidence for a strong Asian monsoon throughout the past 10.7 m.y. *Geology*, *29*(1), 31–34. https://doi.org/10.1130/0091-7613(2001)?029<0031:SSIEFA>?2.0.CO

Dorozhkin, S. V. (2009). Calcium orthophosphates in nature, biology and medicine. *Materials*. Multidisciplinary Digital Publishing Institute (MDPI). https://doi.org/10.3390/ma2020399

Dupont. (2019a). AmberChrom™ Fine Mesh Ion Exchange Resins Technical Manual For Fine Chemical and Pharmaceutical Column.

Dupont. (2019b). Product Data Sheet AMBERLITE ™ IRN78 OH Ion Exchange Resin.

Enax, J., Prymak, O., Raabe, D., & Epple, M. (2012). Structure, composition, and mechanical properties of shark teeth. *Journal of Structural Biology*, *178*(3), 290–299.

https://doi.org/10.1016/j.jsb.2012.03.012

Enax, J., Janus, A. M., Raabe, D., Epple, M., & Fabritius, H. O. (2014). Ultrastructural organization and micromechanical properties of shark tooth enameloid. In *Acta Biomaterialia* (Vol. 10, pp. 3959–3968). Elsevier Ltd. https://doi.org/10.1016/j.actbio.2014.04.028

Firsching, F. H. (1961). Precipitation of Silver Phosphate from Homogeneous Solution. *Analytical Chemistry*, *33*(7), 873–874. https://doi.org/10.1021/ac60175a018

Fourel, F., Martineau, F., Lécuyer, C., Kupka, H. J., Lange, L., Ojeimi, C., & Seed, M. (2011). 18O/16O ratio measurements of inorganic and organic materials by elemental analysis-pyrolysis-isotope ratio mass spectrometry continuous-flow techniques. In *Rapid Communications in Mass Spectrometry* (Vol. 25, pp. 2691–2696). John Wiley and Sons Ltd. https://doi.org/10.1002/rcm.5056

Fox-Dobbs, K., Stidham, T. A., Bowen, G. J., Emslie, S. D., & Koch, P. L. (2006). Dietary controls on extinction versus survival among avian megafauna in the late Pleistocene. *Geology*, *34*(8), 685–688. https://doi.org/10.1130/G22571.1

Fox-Dobbs, K., Dundas, R. G., Trayler, R. B., & Holroyd, P. A. (2014). Paleoecological implications of new megafaunal 14C ages from the McKittrick tar seeps, California. *Journal of Vertebrate Paleontology*, *34*(1), 220–223. https://doi.org/10.1080/02724634.2013.791694

France, C. A. M., Giaccai, J. A., & Doney, C. R. (2015). The effects of Paraloid B-72 and Butvar B-98 treatment and organic solvent removal on δ13C, δ15N, and δ18O values of collagen and hydroxyapatite in a modern bone. *American Journal of Physical Anthropology*, *157*(2), 330–338. https://doi.org/10.1002/ajpa.22697

Fuller, B. T., Fahrni, S. M., Harris, J. M., Farrell, A. B., Coltrain, J. B., Gerhart, L. M., et al. (2014). Ultrafiltration for asphalt removal from bone collagen for radiocarbon dating and isotopic analysis of Pleistocene fauna at the tar pits of Rancho La Brea, Los Angeles, California. *Quaternary Geochronology*, *22*, 85–98. https://doi.org/10.1016/j.quageo.2014.03.002

Garvie-Lok, S. J., Varney, T. L., & Katzenberg, M. A. (2004). Preparation of bone carbonate for stable isotope analysis: The effects of treatment time and acid concentration. *Journal of Archaeological Science*, *31*(6), 763–776. https://doi.org/10.1016/j.jas.2003.10.014

Goldhammer, T., Brüchert, V., Ferdelman, T. G., & Zabel, M. (2010). Microbial sequestration of phosphorus in anoxic upwelling sediments. *Nature Geoscience 2010 3:8*, *3*(8), 557–561. https://doi.org/10.1038/ngeo913

Goldhammer, T., Max, T., Brunner, B., Einsiedl, F., & Zabel, M. (2011). Marine sediment pore-water profiles of phosphate δ18O using a refined micro-extraction. *Limnology and Oceanography: Methods*, *9*(APRIL), 110–120. https://doi.org/10.4319/lom.2011.9.110

Griffin, J. M., Montañez, I. P., Matthews, J. A., Bates, S., & Lyons, T. W. (2015). A refined protocol for δ18OPO4 analysis of conodont bioapatite. *Chemical Geology*, *417*, 11–20. https://doi.org/10.1016/j.chemgeo.2015.08.025

Grimes, V., & Pellegrini, M. (2013). A comparison of pretreatment methods for the analysis of phosphate oxygen isotope ratios in bioapatite. *Rapid Communications in Mass Spectrometry*, *27*(3), 375–390. https://doi.org/10.1002/rcm.6463

Grunenwald, A., Keyser, C., Sautereau, A. M., Crubézy, E., Ludes, B., & Drouet, C. (2014). Novel contribution on the diagenetic physicochemical features of bone and teeth minerals, as substrates for ancient DNA typing. *Analytical and Bioanalytical Chemistry*, *406*(19), 4691–4704. https://doi.org/10.1007/s00216-014-7863-z

Gu, L. sha, Huang, X. qing, Griffin, B., Bergeron, B. R., Pashley, D. H., Niu, L. na, & Tay, F. R. (2017). Primum non nocere – The effects of sodium hypochlorite on dentin as used in endodontics. *Acta Biomaterialia*, *61*, 144–156. https://doi.org/10.1016/j.actbio.2017.08.008

Guo, D., Wang, J., Silva, G., & Gao, S. (2013). Reactivity and mechanism study of CO2 with amino acids as carbon capture solvents. *Energy and Fuels*, *27*(7), 3898–3904. https://doi.org/10.1021/EF400413R/SUPPL_FILE/EF400413R_SI_001.PDF

Haq, S., Rehman, W., Waseem, M., Meynen, V., Awan, S. U., Saeed, S., & Iqbal, N. (2018). Fabrication of pure and moxifloxacin functionalized silver oxide nanoparticles for photocatalytic and antimicrobial activity. *Journal of Photochemistry and Photobiology B: Biology*, *186*(July), 116–124. https://doi.org/10.1016/j.jphotobiol.2018.07.011

Karnes, M. E., Chan, R. L., Kuntz, J. P., Griffiths, M. L., Shimada, K., Becker, M. A., et al. (2024). Enigmatic carbonate isotope values in shark teeth: Evidence for environmental and dietary controls. *Palaeogeography, Palaeoclimatology, Palaeoecology*, *635*, 111943. https://doi.org/10.1016/j.palaeo.2023.111943

Kim, S. L., Eberle, J. J., Bell, D. M., Fox, D. A., & Padilla, A. (2014). Evidence from shark teeth for a brackish Arctic Ocean in the Eocene greenhouse. *Geology*, *42*(8), 695–698. https://doi.org/10.1130/G35675.1

Kim, S. L., Zeichner, S. S., Colman, A. S., Scher, H. D., Kriwet, J., Mörs, T., & Huber, M. (2020). Probing the Ecology and Climate of the Eocene Southern Ocean With Sand Tiger Sharks Striatolamia macrota. *Paleoceanography and Paleoclimatology*, *35*(12), 1–21. https://doi.org/10.1029/2020PA003997

Kirsanow, K., Makarewicz, C., & Tuross, N. (2008). Stable oxygen (δ18O) and hydrogen (δD) isotopes in ovicaprid dentinal collagen record seasonal variation. *Journal of Archaeological Science*, *35*(12), 3159–3167. https://doi.org/10.1016/J.JAS.2008.06.025

Koch, P. L., Tuross, N., & Fogel, M. L. (1997). The effects of sample treatment and diagenesis on the isotopic integrity of carbonate in biogenic hydroxylapatite. *Journal of Archaeological Science*, *24*(5), 417–429. https://doi.org/10.1006/jasc.1996.0126

Köck, E. M., Kogler, M., Bielz, T., Klötzer, B., & Penner, S. (2013). In situ FT-IR spectroscopic study of CO2 and CO adsorption on Y2O3, ZrO2, and yttria-stabilized ZrO 2. *Journal of Physical Chemistry C*, *117*(34), 17666–17673. https://doi.org/10.1021/JP405625X/SUPPL_FILE/JP405625X_SI_001.PDF

Kocsis, L., Gheerbrant, E., Mouflih, M., Cappetta, H., Yans, J., & Amaghzaz, M. (2014). Comprehensive stable isotope investigation of marine biogenic apatite from the late Cretaceous-early Eocene phosphate series of Morocco. *Palaeogeography, Palaeoclimatology, Palaeoecology*, *394*, 74–88. https://doi.org/10.1016/j.palaeo.2013.11.002

Kohn, M. J., & Cerling, T. E. (2003). Stable Isotope Compositions of Biological Apatite. *Reviews in Mineralogy and Geochemistry*, *48*(1), 455–488. Retrieved from https://doi.org/10.2138/rmg.2002.48.12

Kohn, M. J., Schoeninger, M. J., & Barker, W. W. (1999). Altered states: Effects of diagenesis on fossil tooth chemistry. *Geochimica et Cosmochimica Acta*, *63*(18), 2737–2747. https://doi.org/10.1016/S0016-7037(99)00208-2

Kolodny, Y., Luz, B., & Navon, O. (1983). Oxygen isotope variations in phosphate of biogenic apatites, I. Fish bone apatite-rechecking the rules of the game. *Earth and Planetary Science Letters*, *64*(3), 398–404. https://doi.org/10.1016/0012-821X(83)90100-0

Kornexl, B. E., Gehre, M., Höfling, R., & Werner, R. A. (1999). On-line δ18O measurement of organic and inorganic substances. *Rapid Communications in Mass Spectrometry*, *13*(16), 1685–1693. https://doi.org/10.1002/(sici)1097-0231(19990830)13:16<1685::aid-rcm699>3.0.co;2-9

Kumar, H., & Rani, R. (2013). Structural Characterization of Silver Nanoparticles Synthesized by Micro emulsion Route. *International Journal of Engineering and Innovative Technology*, *3*(3), 344–348.

L'vov, B. V. (1999). Kinetics and mechanism of thermal decomposition of silver oxide. *Thermochimica Acta*, *333*(1), 13–19. https://doi.org/10.1016/S0040-6031(99)00085-4

Lapworth, D. J., Surridge, B., Williams, P. J., Heaton, T. H. E., & Gooddy, D. C. (2014). Method for analysing phosphate 18O/16O ratios for waters with high C:P ratios. *British Geological Survey*, 16.

Lebon, M., Reiche, I., Gallet, X., Bellot-Gurlet, L., & Zazzo, A. (2016). Rapid quantification of bone collagen content by ATR-FTIR spectroscopy. *Radiocarbon*, *58*(1), 131–145. https://doi.org/10.1017/RDC.2015.11

Lécuyer, C., Grandjean, P., O'Neil, J. R., Cappetta, H., & Martineau, F. (1993). Thermal excursions in the ocean at the Cretaceous-Tertiary boundary (northern Morocco): δ18O record of phosphatic fish debris. *Palaeogeography, Palaeoclimatology, Palaeoecology*, *105*(3–4), 235–243. https://doi.org/10.1016/0031-0182(93)90085-W

Lécuyer, Christophe. (2004). Oxygen Isotope Analysis of Phosphate. *Handbook of Stable*

Isotope Analytical Techniques, (September 2004), 482–496. https://doi.org/10.1016/B978-044451114-0/50024-7

Lécuyer, Christophe, Grandjean, P., Barrat, J. A., Nolvak, J., Emig, C., Paris, F., & Robardet, M. (1998). δ18O and REE contents of phosphatic brachiopods: A comparison between modern and lower Paleozoic populations. *Geochimica et Cosmochimica Acta*, *62*(14), 2429–2436. https://doi.org/10.1016/S0016-7037(98)00170-7

Lécuyer, Christophe, Fourel, F., Martineau, F., Amiot, R., Bernard, A., Daux, V., et al. (2007). High-precision determination of 18O/16O ratios of silver phosphate by EA-pyrolysis-IRMS continuous flow technique. *Journal of Mass Spectrometry*, *42*(1), 36–41. https://doi.org/10.1002/jms.1130

Lee-Thorp, J. (2002). Two decades of progress towards understanding fossilization processes and isotopic signals in calcified tissue minerals. *Archaeometry*, *44*(3), 435–446. https://doi.org/10.1111/1475-4754.t01-1-00076

Lee-Thorp, J. A., & van der Merwe, N. J. (1991). Aspects of the chemistry of modern and fossil biological apatites. *Journal of Archaeological Science*, *18*(3), 343–354. https://doi.org/10.1016/0305-4403(91)90070-6

LeGeros, R. Z. (1981). Apatites in biological systems. *Progress In Crystal Growth And Characterization*, *4*(1–2), 1–45. https://doi.org/10.1016/0146-3535(81)90046-0

Leventouri, T. (2006). Synthetic and biological hydroxyapatites: Crystal structure questions. *Biomaterials*, *27*(18), 3339–3342. https://doi.org/10.1016/j.biomaterials.2006.02.021

Liu, H., & Huang, K. (2016). Structural Characteristics of Extracted Collagen from Tilapia (Oreochromis mossambicus) Bone: Effects of Ethylenediaminetetraacetic Acid Solution and Hydrochloric Acid Treatment. *International Journal of Food Properties*, *19*(1), 63–75. https://doi.org/10.1080/10942912.2014.951939

Lübke, A., Enax, J., Loza, K., Prymak, O., Gaengler, P., Fabritius, H. O., et al. (2015). Dental lessons from past to present: Ultrastructure and composition of teeth from plesiosaurs, dinosaurs, extinct and recent sharks. *RSC Advances*, *5*(76), 61612–61622. https://doi.org/10.1039/c5ra11560d

Marending, M., Luder, H. U., Brunner, T. J., Knecht, S., Stark, W. J., & Zehnder, M. (2007). Effect of sodium hypochlorite on human root dentine - Mechanical, chemical and structural evaluation. *International Endodontic Journal*, *40*(10), 786–793. https://doi.org/10.1111/j.1365-2591.2007.01287.x

McMahon, K. W., Hamady, L. L., & Thorrold, S. R. (2013, March 1). A review of ecogeochemistry approaches to estimating movements of marine animals. *Limnology and Oceanography*. John Wiley & Sons, Ltd. https://doi.org/10.4319/lo.2013.58.2.0697

Merck KGaA. (2018). Ultrafree ® -MC and -CL Centrifugal Filter Devices with microporous membranes.

Mine, A. H., Waldeck, A., Olack, G., Hoerner, M. E., Alex, S., & Colman, A. S. (2017). Microprecipitation and δ18O analysis of phosphate for paleoclimate and biogeochemistry research. *Chemical Geology*, *460*(March), 1–14. https://doi.org/10.1016/j.chemgeo.2017.03.032

Murphy, J., & Riley, J. P. (1962). A Modified Single Solution Method for Natural Determination of Phosphate in Natural Waters. *Analytica Chimica Acta*, *27*, 13–19.

Newsome, S. D., Clementz, M. T., & Koch, P. L. (2010). Using stable isotope biogeochemistry to study marine mammal ecology. *Marine Mammal Science*, *26*(3), 509–572. https://doi.org/10.1111/j.1748-7692.2009.00354.x

Ni, G., Dou, H., Li, Z., Zhu, C., Sun, G., Hu, X., et al. (2022). Study on the combustion characteristics of bituminous coal modified by typical inorganic acids. *Energy*, *261*, 125214. https://doi.org/10.1016/j.energy.2022.125214

Nishiyama, N., Suzuki, K., Nagatsuka, A., Yokota, I., & Nemoto, K. (2003). Dissociation states of collagen functional groups and their effects on the priming efficacy of HEMA bonded to collagen. *Journal of Dental Research*, *82*(4), 257–261. https://doi.org/10.1177/154405910308200403

O'Neil, J. R., Roe, L. J., Reinhard, E., & Blake, R. E. (1994). A rapid and precise method of oxygen isotope analysis of biogenic phosphate. *Israel Journal of Earth Sciences*, *43*(3–4), 203–212.

Oje, A. I., Ogwu, A. A., Mirzaeian, M., Tsendzughul, N., & Oje, A. M. (2019). Pseudo-capacitance of silver oxide thin film electrodes in ionic liquid for electrochemical energy applications. *Journal of Science: Advanced Materials and Devices*, *4*(2), 213–222. https://doi.org/10.1016/j.jsamd.2019.04.003

Pearson, P. N., Foster, G. L., & Wade, B. S. (2009). Atmospheric carbon dioxide through the Eocene-Oligocene climate transition. *Nature*, *461*(7267), 1110–1113. https://doi.org/10.1038/nature08447

Pederzani, S., & Britton, K. (2019, January 1). Oxygen isotopes in bioarchaeology: Principles and applications, challenges and opportunities. *Earth-Science Reviews*. Elsevier. https://doi.org/10.1016/j.earscirev.2018.11.005

Pederzani, S., Snoeck, C., Wacker, U., & Britton, K. (2020). Anion exchange resin and slow precipitation preclude the need for pretreatments in silver phosphate preparation for oxygen isotope analysis of bioapatites. *Chemical Geology*, *534*, 119455. https://doi.org/10.1016/j.chemgeo.2019.119455

Pellegrini, M., & Snoeck, C. (2016). Comparing bioapatite carbonate pre-treatments for isotopic measurements: Part 2 - Impact on carbon and oxygen isotope compositions. *Chemical Geology*, *420*, 88–96. https://doi.org/10.1016/j.chemgeo.2015.10.038

Pucéat, E., Joachimski, M. M., Bouilloux, A., Monna, F., Bonin, A., Motreuil, S., et al. (2010). Revised phosphate-water fractionation equation reassessing paleotemperatures derived from biogenic apatite. *Earth and Planetary Science Letters*, *298*(1–2), 135–

142. https://doi.org/10.1016/j.epsl.2010.07.034

Quinton, P. C., Leslie, S. A., Herrmann, A. D., & MacLeod, K. G. (2016). Effects of extraction protocols on the oxygen isotope composition of conodont elements. *Chemical Geology*, *431*, 36–43. https://doi.org/10.1016/j.chemgeo.2016.03.023

Rahman, M. M., Alam, M. M., Hussain, M. M., Asiri, A. M., & Zayed, M. E. M. (2018). Hydrothermally prepared Ag2O/CuO nanomaterial for an efficient chemical sensor development for environmental remediation. *Environmental Nanotechnology, Monitoring and Management*, *10*(December 2017), 1–9. https://doi.org/10.1016/j.enmm.2018.04.001

Ramírez-Bommer, C., Gulabivala, K., Ng, Y. L., & Young, A. (2018). Estimated depth of apatite and collagen degradation in human dentine by sequential exposure to sodium hypochlorite and EDTA: a quantitative FTIR study. *International Endodontic Journal*, *51*(4), 469–478. https://doi.org/10.1111/iej.12864

Rashmi, B. N., Harlapur, S. F., Avinash, B., Ravikumar, C. R., Nagaswarupa, H. P., Anil Kumar, M. R., et al. (2020). Facile green synthesis of silver oxide nanoparticles and their electrochemical, photocatalytic and biological studies. *Inorganic Chemistry Communications*, *111*(August 2019), 107580. https://doi.org/10.1016/j.inoche.2019.107580

Royer, A., Lécuyer, C., Montuire, S., Escarguel, G., Fourel, F., Mann, A., & Maureille, B. (2013). Late Pleistocene (MIS 3-4) climate inferred from micromammal communities and δ18O of rodents from Les Pradelles, France. *Quaternary Research (United States)*, *80*(1), 113–124. https://doi.org/10.1016/j.yqres.2013.03.007

RStudio Team. (2024). RStudio: Integrated Development for R. Boston, MA: RStudio, PBC. Retrieved from http://www.rstudio.com/.

Sasagawa, I. (1999). Fine structure of dental epithelial cells and the enameloid during the enameloid formation stages in an elasmobranch, Heterodontus japonicus. *Anatomy and Embryology*, *200*(5), 477–486. https://doi.org/10.1007/s004290050296

Schwarcz, H. P., & Schoeninger, M. J. (1991). Stable isotope analyses in human nutritional ecology. *American Journal of Physical Anthropology*, *34*(13 S), 283–321. https://doi.org/10.1002/ajpa.1330340613

Al Sekhaneh, W., Akkam, Y. H., Kamel, G., Drabee, A., & Popp, J. (2021). Investigation of ancient teeth using Raman spectroscopy and synchrotron radiation Fourier-transform infrared (SR-μFTIR): mapping and novel method of dating. *Digest Journal of Nanomaterials and Biostructures*, *16*(2), 713–724.

Shabaga, B. M., Gough, H., Fayek, M., & Hoppa, R. D. (2018). A simplified silver phosphate extraction method for oxygen isotope analysis of bioapatite. *Rapid Communications in Mass Spectrometry*, *32*(15), 1237–1242. https://doi.org/10.1002/rcm.8149

Shemesh, A., Kolodny, Y., & Luz, B. (1983). Oxygen isotope variations in phosphate of

biogenic apatites, II. Phosphorite rocks. *Earth and Planetary Science Letters*, *64*(3), 405–416. https://doi.org/10.1016/0012-821X(83)90101-2

Shimabukuro, M., Hayashi, K., Kishida, R., Tsuchiya, A., & Ishikawa, K. (2022). No-Observed-Effect Level of Silver Phosphate in Carbonate Apatite Artificial Bone on Initial Bone Regeneration. *ACS Infectious Diseases*, *8*(1), 159–169. https://doi.org/10.1021/acsinfecdis.1c00480

Sibbesen, E. (1978). An investigation of the anion-exchange resin method for soil phosphate extraction. *Plant and Soil*, *50*(1), 305–321. https://doi.org/10.1007/BF02107180

Siddiqui, M. R. H., Adil, S. F., Assal, M. E., Ali, R., & Al-Warthan, A. (2013). Synthesis and characterization of silver oxide and silver chloride nanoparticles with high thermal stability. *Asian Journal of Chemistry*, *25*(6), 3405–3409. https://doi.org/10.14233/ajchem.2013.13874

Slager, T. L., Lindgren, B. J., Mallmann, A. J., & Greenler, R. G. (1972). Infrared spectra of the oxides and carbonates of silver. *The Journal of Physical Chemistry*, *76*(6), 940–943. https://doi.org/10.1021/j100650a029

Snoeck, C., & Pellegrini, M. (2015). Comparing bioapatite carbonate pre-treatments for isotopic measurements: Part 1-Impact on structure and chemical composition. *Chemical Geology*, *417*, 394–403. https://doi.org/10.1016/j.chemgeo.2015.10.004

Stephan, E. (2000). Oxygen isotope analysis of animal bone phosphate: Method refinement, influence of consolidants, and reconstruction of palaeotemperatures for Holocene sites. *Journal of Archaeological Science*, *27*(6), 523–535. https://doi.org/10.1006/jasc.1999.0480

Sun, Y., Wiedenbeck, M., Joachimski, M. M., Beier, C., Kemner, F., & Weinzierl, C. (2016). Chemical and oxygen isotope composition of gem-quality apatites: Implications for oxygen isotope reference materials for secondary ion mass spectrometry (SIMS). *Chemical Geology*, *440*, 164–178. https://doi.org/10.1016/j.chemgeo.2016.07.013

Suthanthiraraj, S. A., & Sarumathi, R. (2012). XRD and FTIR studies on a new solid electrolyte system containing Ag 3PO4 and SbI3. *AIP Conference Proceedings*, *1447*(1), 1005–1006. https://doi.org/10.1063/1.4710345

Suwanprateeb, J., Thammarakcharoen, F., Wasoontararat, K., Chokevivat, W., & Phanphiriya, P. (2012). Preparation and characterization of nanosized silver phosphate loaded hydroxyapatite by single step co-conversion process. *Materials Science and Engineering C*, *32*(7), 2122–2128. https://doi.org/10.1016/j.msec.2012.05.051

Tabor, R. F., Chan, D. Y. C., Grieser, F., & Dagastine, R. R. (2011). Anomalous Stability of Carbon Dioxide in pH-Controlled Bubble Coalescence. *Angewandte Chemie*, *123*(15), 3516–3518. https://doi.org/10.1002/ange.201006552

Trayler, R. B., Landa, P. V., & Kim, S. L. (2023). Evaluating the efficacy of collagen isolation using stable isotope analysis and infrared spectroscopy. *Journal of*

Archaeological Science, *151*, 105727. https://doi.org/10.1016/j.jas.2023.105727

Trivedi, K. M., Tallapragada, R. M., Branton, A., Trivedi, D., Nayak, G., Jana, S., & Latiyal, O. (2015). The Potential Impact of Biofield Energy Treatment on the Physical and Thermal Properties of Silver Oxide Powder. *International Journal of Biomedical Science and Engineering*, *3*(5), 62. https://doi.org/10.11648/j.ijbse.20150305.11

Tsutaya, T., & Yoneda, M. (2015). Reconstruction of breastfeeding and weaning practices using stable isotope and trace element analyses: A review. *American Journal of Physical Anthropology*, *156*(S59), 2–21. https://doi.org/10.1002/AJPA.22657

Tütken, T., Vennemann, T. W., Janz, H., & Heizmann, E. P. J. (2006). Palaeoenvironment and palaeoclimate of the Middle Miocene lake in the Steinheim basin, SW Germany: A reconstruction from C, O, and Sr isotopes of fossil remains. *Palaeogeography, Palaeoclimatology, Palaeoecology*, *241*(3–4), 457–491. https://doi.org/10.1016/j.palaeo.2006.04.007

Vennemann, T. W., & Hegner, E. (1998). Oxygen, strontium, and neodymium isotope composition of fossil shark teeth as a proxy for the palaeoceanography and palaeoclimatology of the Miocene northern Alpine Paratethys. *Palaeogeography, Palaeoclimatology, Palaeoecology*, *142*(3–4), 107–121. https://doi.org/10.1016/S0031-0182(98)00062-5

Vennemann, T. W., Hegner, E., Cliff, G., & Benz, G. W. (2001a). Isotopic composition of recent shark teeth as a proxy for environmental conditions. *Geochimica et Cosmochimica Acta*, *65*(10), 1583–1599. https://doi.org/10.1016/S0016-7037(00)00629-3

Vennemann, T. W., Hegner, E., Cliff, G., & Benz, G. W. (2001b). Isotopic composition of recent shark teeth as a proxy for environmental conditions. *Geochimica et Cosmochimica Acta*, *65*(10), 1583–1599. https://doi.org/https://doi.org/10.1016/S0016-7037(00)00629-3

Vennemann, T. W., Fricke, H. C., O'Neil, J. R., & Colman, A. (2002). Oxygen isotope analysis of phosphates : A comparison of techniques for for analysis of Ag3PO4. *Chemical Geology*, *185*(October), 321–336. https://doi.org/10.1016/S0009-2541(01)00413-2

Wiedemann-Bidlack, F. B., Colman, A. S., & Fogel, M. L. (2008). Phosphate oxygen isotope analysis on microsamples of bioapatite: removal of organic contamination and minimization of sample size. *Rapid Communications in Mass Spectrometry*, *22*, 1457–1466. https://doi.org/10.1002/rcm.3553

Xue, Y., Hu, Z., Wang, C., & Xiao, Y. (2019). Evaluation of dissolved organic carbon released from aged asphalt binder in aqueous solution. *Construction and Building Materials*, *218*, 465–476. https://doi.org/10.1016/j.conbuildmat.2019.05.060

Yürüm, Y., Dror, Y., & Levy, M. (1985). Effect of acid dissolution on the mineral matrix and organic matter of Zefa EFE oil shale. *Fuel Processing Technology*, *11*(1), 71–86.

https://doi.org/10.1016/0378-3820(85)90017-7

Zacke, A., Voigt, S., Joachimski, M. M., Gale, A. S., Ward, D. J., & Tütken, T. (2009). Surface-water freshening and high-latitude river discharge in the Eocene North Sea. *Journal of the Geological Society*, *166*(5), 969–980. https://doi.org/10.1144/0016-76492008-068

Zazzo, A., Lécuyer, C., & Mariotti, A. (2004). Experimentally-controlled carbon and oxygen isotope exchange between bioapatites and water under inorganic and microbially-mediated conditions. *Geochimica et Cosmochimica Acta*, *68*(1), 1–12. https://doi.org/10.1016/S0016-7037(03)00278-3

Zhang, L., Li, Z., Yang, Y., Zhou, Y., Kong, B., Li, J., & Si, L. (2016). Effect of acid treatment on the characteristics and structures of high-sulfur bituminous coal. *Fuel*, *184*, 418–429. https://doi.org/10.1016/j.fuel.2016.07.002

Zhang, M., Hao, P., Dong, S., Li, Y., & Yuan, G. (2020). Asphalt binder micro-characterization and testing approaches: A review. *Measurement: Journal of the International Measurement Confederation*, *151*, 107255. https://doi.org/10.1016/j.measurement.2019.107255

Zhang, X., Hoff, I., & Saba, R. G. (2021). Response and Deterioration Mechanism of Bitumen under Acid Rain Erosion. *Materials*, *14*(4911). Retrieved from https://doi.org/10.3390/ma14174911%0AAbstract:

Žigaite, Ž., & Whitehouse, M. (2014). Stable oxygen isotopes of dental biomineral: Differentiation at the intra- and inter-tissue level of modern shark teeth. *GFF*, *136*(1), 337–340. https://doi.org/10.1080/11035897.2013.878747

2.7 Tables

Table 2.1. The SPORA protocol was tested on apatite materials of varying nature and organic content using small sample size (~ 1.5 mg). The table shows samples used, ID code assigned to samples, number of replicates, starting amount, and material types analyzed with SPORA and Rapid UC protocols, which was used to compare protocols' performance. The mass of the starting amount is calculated from the weight of each replicate per protocol and reported as mean ± 1σ.

Sample	**ID**	**# Specimens**	**Material**	**# Replicates**		**Mass (mg; mean ± sd)**	
				Rapid UC	**SPORA**	**Rapid UC**	**SPORA**
Fluorapatite	FA	1	Naturally occurring crystal	10	12	1.02 ± 0.04	1.07 ± 0.07
Fossil mammal indet (1)	MM1	1	Bone (tar not removed)	-	5	-	1.86 ± 0.11
			Bone (tar removed)	5	5	1.71 ± 0.15	1.81 ± 0.06
Fossil mammal indet (2)	MM2	1	Bone	5	5	1.76 ± 0.16	1.79 ± 0.15
Fossil shark	SM1	1	Enameloid	5	5	1.06 ± 0.02	1.13 ± 0.06
			Enameloid + dentin	5	5	1.71 ± 0.15	1.80 ± 0.14
Fossil shark	SM2	1	Enameloid	5	5	1.05 ± 0.04	1.17 ± 0.07
			Enameloid + dentin	5	5	1.76 ± 0.16	1.73 ± 0.14
Hydroxyapatite	HAP	1	Synthetic crystal	10	11	1.04 ± 0.05	1.10 ± 0.09
Modern deer	OV	1	Bone	5	5	1.97 ± 0.05	1.84 ± 0.09
Modern goat	CH	1	Enamel	10	5	1.14 ± 0.09	1.13 ± 0.04
			Enamel + dentin	5	5	1.77 ± 0.16	1.89 ± 0.14
Modern shark	TOM_1	2	Enameloid	1	1	1.08	1.25
			Enameloid + dentin	1	1	1.03	1.75
	TOM_2	1	Enameloid	1	1	1.12	1.25
			Enameloid + dentin	1	1	1.1	1.98
	TOM_3	1	Enameloid	1	1	1.07	1.24
			Enameloid + dentin	1	1	1.09	1.8
	TOM_4	1	Enameloid	1	1	1.03	1.3
			Enameloid + dentin	1	1	1.01	1.84

	TOM_5	1	Enameloid	1	1	1.03	1.24
			Enameloid + dentin	1	1	1.02	1.89
	TOM_6	15	Enameloid + dentin	1	1	1.08	2.02
NIST SRM 120c	NIST120c	1	Phosphate rock	10	11	1.04 ± 0.06	1.16 ± 0.10

Table 2.2. The $\delta^{18}O_p$ values for the Rapid UC and SPORA protocols are compared across a range of biogenic apatites, reference materials, and phosphatic standards. Several specimens were sampled multiple times for different material types (i.e., enamel(oid) vs. dentin). The variation between protocols ($\Delta^{18}O$) is represented as the difference between mean values ($\delta^{18}O_{p\ SPORA}$ - $\delta^{18}O_{p\ Rapid\ UC}$). The uncertainty around the mean difference between protocols is represented by the standard error. The column "Type" reports whether samples are working standard materials (S) or biogenic apatite materials with expected low- (LOC) or high-organic content (HOC).

Sample	**Material**	**ID**	**Type**	**$\delta^{18}O_{p\ Rapid\ UC}$ (‰)**	**$\delta^{18}O_{p\ SPORA}$ (‰)**	**$\Delta^{18}O$ (‰)**
Fossil mammal indet.2	Bone	MM2	HOC	14.5 ± 0.1	13.7 ± 0.1	-0.7 ± 0.1
Modern deer	Bone	OV	HOC	16.2 ± 0.3	15.6 ± 0.2	-0.5 ± 0.2
Fossil mammal indet.1	Bone (tar not removed)	MM1	HOC	NA	17.3 ± 0.2	NA
	Bone (tar removed)	MM1		17.7 ± 0.3	17.8 ± 0.1	0.0 ± 0.1
Fluorapatite	Naturally occurring crystal	FA	S	9.0 ± 0.4	8.8 ± 0.3	-0.2 ± 0.2
Modern goat	Enamel	CH	LOC	14.1 ± 0.2	14.2 ± 0.2	0.1 ± 0.1
	Enamel + dentin	CH	HOC	12.8 ± 0.1	12.4 ± 0.2	-0.4 ± 0.1
Fossil shark	Enameloid	SM1	LOC	17.4 ± 0.2	16.9 ± 0.4	-0.5 ± 0.2
	Enameloid + dentin	SM1	HOC	13.8 ± 0.3	13.6 ± 0.4	-0.2 ± 0.2
Fossil shark	Enameloid	SM2	LOC	8.0 ± 0.3	7.8 ± 0.5	-0.2 ± 0.3
	Enameloid + dentin	SM2	HOC	9.7 ± 0.1	9.4 ± 0.2	-0.2 ± 0.1
Modern shark	Enameloid	TOM	LOC	22.7 ± 0.2	22.4 ± 0.3	-0.3 ± 0.2
	Enameloid + dentin	TOM	HOC	23.3 ± 0.3	22.4 ± 0.3	-0.9 ± 0.2
NIST SRM 120c	Phosphate rock	NIST120c	S	21.9 ± 0.1	21.7 ± 0.3	-0.2 ± 0.1
Hydroxyapatite	Synthetic crystal	HAP	S	22.2 ± 0.2	21.8 ± 0.3	-0.4 ± 0.1

Table 2.3. Soluble reactive phosphate was measured for SPORA and compared to Rapid UC to determine phosphate recovery (ΣPO_4^{3-} Recovery (%)) at key points of possible loss in the protocol. The summary statistics include median, interquartile range (IQR), mean, and standard deviation values are reported.

Protocol	**ΣPO_4^{3-} Recovery (%)**			
	# Replicates	**median**	**IQR**	**mean ± sd**
Rapid UC	91	97.8	3.9	96.3 ± 5.4
SPORA	95	91.2	12.8	89.2 ± 9.6

2.8 Figures

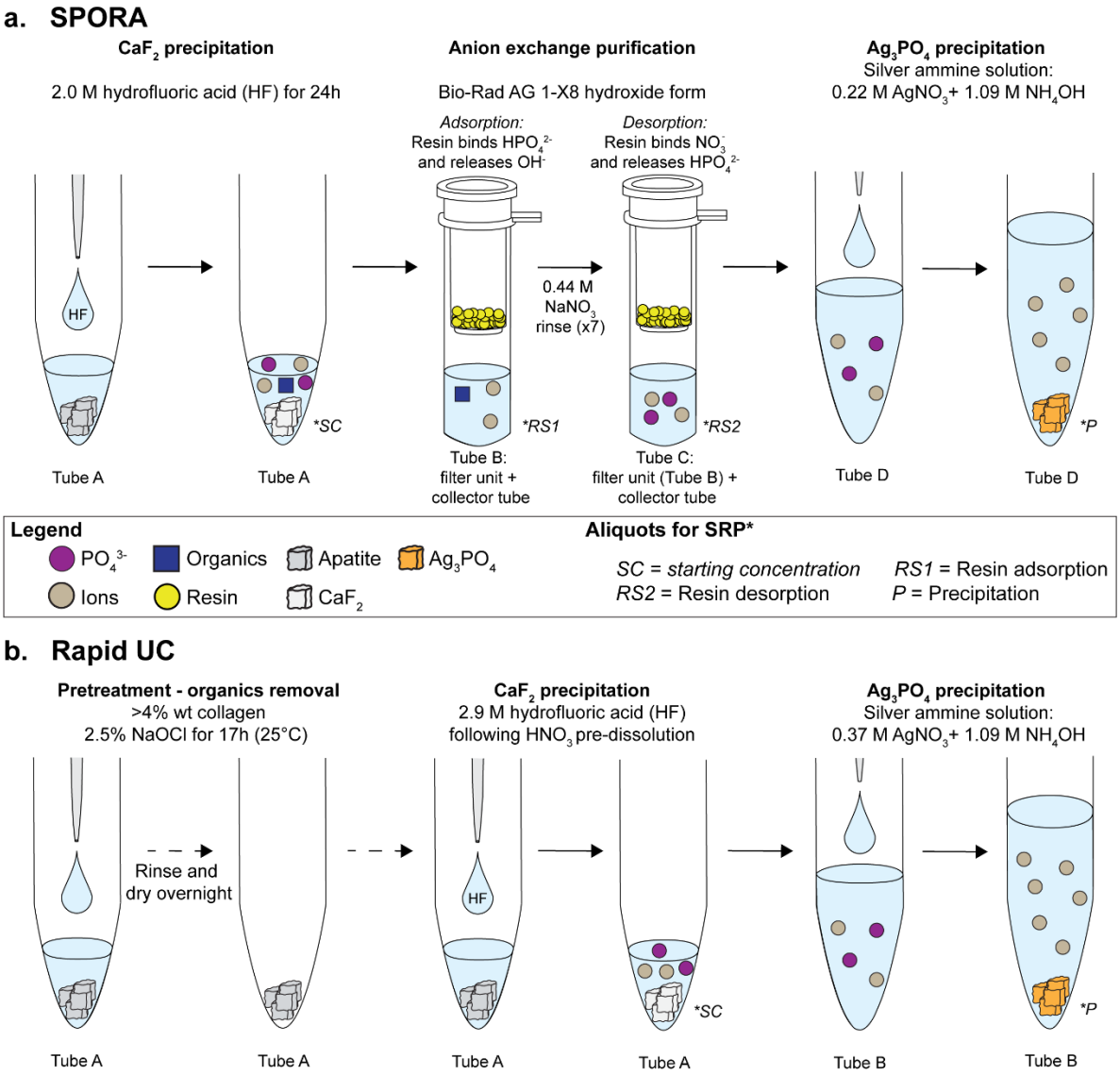

Figure 2.1. A graphical overview of SPORA and Rapid UC protocols indicating similar steps in CaF_2 removal and Ag_3PO_4 precipitation as well as deviations, such as pretreatment and anion exchange purification. Dashed arrows indicate that the pretreatment step for Rapid UC method is not mandatory, but it is applied only when samples are of high organic content. Italicized abbreviations indicate where aliquots for SRP analysis were taken.

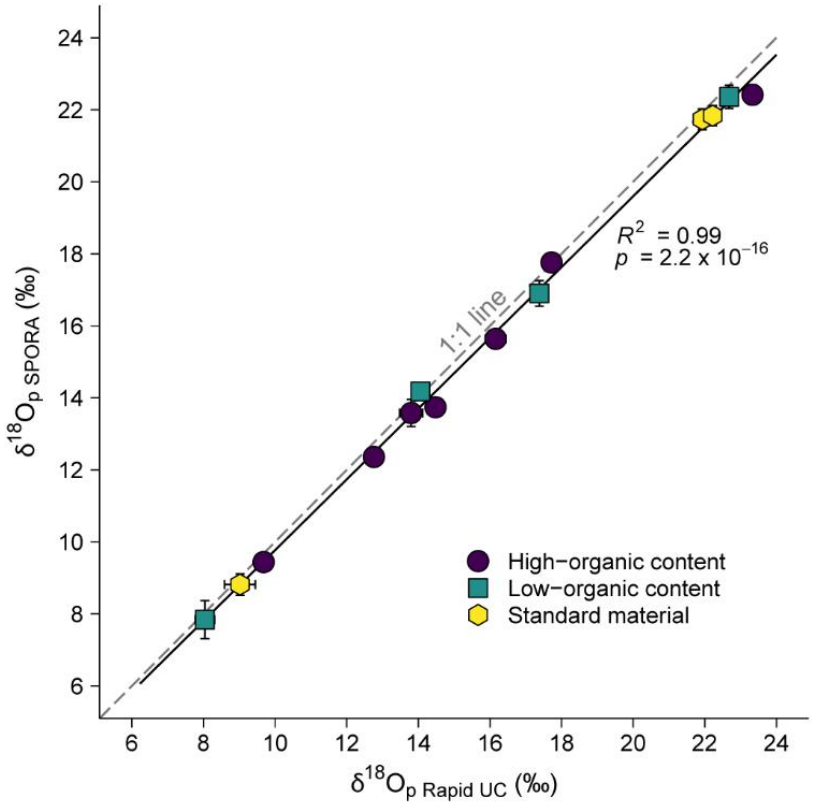

Figure 2.2. The mean $\delta^{18}O_p$ values of standard and biogenic apatite materials converted into Ag_3PO_4 crystals with SPORA and Rapid UC methods are equivocal. Both protocols yield similar oxygen isotope compositions and plot along a 1:1 line (shown in grey; (R^2 = 0.99; *p* = 2.2 x 10^{-16}). Error bars represent the uncertainty of measurements as 1σ. Point shapes and color show whether crystals are precipitated from working standard materials or from biogenic apatite materials with expected low- or high-organic content. See Results and Discussion section for samples that vary.

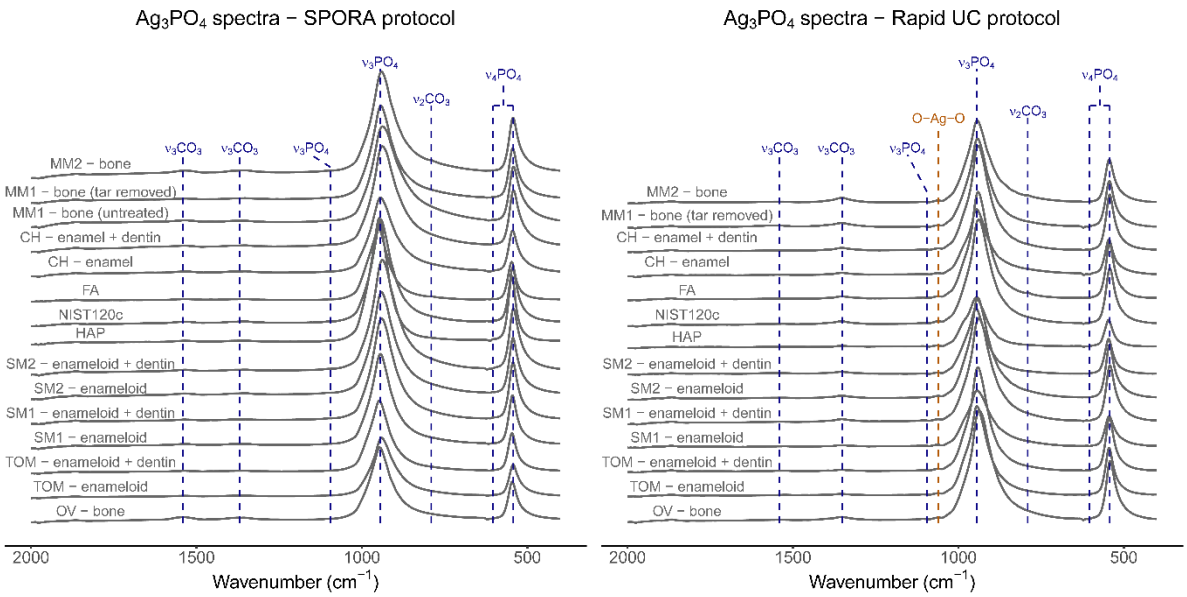

Figure 2.3. The SPORA protocol prevents the inclusion of Ag_2O and mitigates carbonate contaminants as demonstrated by FTIR spectra. The left panel shows infrared spectra of Ag_3PO_4 crystals produced with the SPORA protocol, whereas the right panel displays spectra of the same apatite specimens treated with the Rapid UC method. Crystals precipitated with both protocols show similar phosphate and carbonate infrared features. Silver phosphate crystals precipitated via Rapid UC method show silver oxide bands.

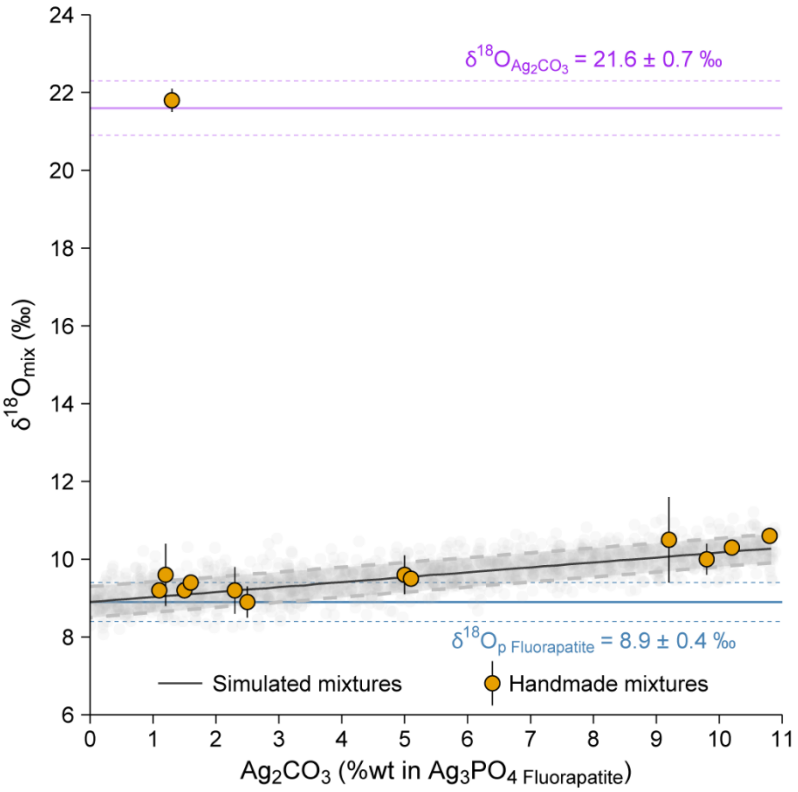

Figure 2.4. Inaccurate $\delta^{18}O$ values occur if the inorganic carbonate contaminant fraction as Ag_2CO_3 is ~1.5 wt% or higher. The gray lines show $\delta^{18}O$ values ($\delta^{18}O_{mix}$) by drawing 10,000 simulations of contaminated Ag_3PO_4 crystals considering varying Ag_2CO_3 fractions with an isotopic composition of 21.6 ± 0.7 ‰ (purple lines). The silver phosphate substrate for the simulated values uses $\delta^{18}O_p$ measurements of working fluorapatite by combining results from both SPORA and Rapid UC protocols (8.9 ± 0.4 ‰, n = 22; blue lines). Orange dots show $\delta^{18}O_{mix}$ values of Ag_3PO_4 crystals precipitated from the fluorapatite working standard via Rapid UC protocol that were manually contaminated with varying Ag_2CO_3 aliquots. All dashed lines and shaded areas indicate intervals within ± 1σ.

2.9 Appendix

2.9.1 Natural Asphalt Removal Pretreatment From MM1 Bone Sample.

We pretreated the bone specimen to dissolve natural asphalt residuals in pore spaces (Fuller et al., 2014). About 50 mg of bone powder was poured into a 12 mL Labco™ vial and placed in an ultrasonic bath device (Branson™ 3800 Ultrasonic Cleaner). A plastic hose was zip tied to form a coil and it was placed on the sink of the ultrasonic device. The hose was attached to a cold tap water line to keep the temperature cold during sonications. The powder was sonicated eight times in a 2:1 toluene–methanol solution until the solvent was clear. Following, the powder was washed in a methanol solution and, lastly, with deionized water. Each wash elapsed 1h. The sample was freeze-dried overnight and showed a profound discoloration (from dark to light brown) and loss of mass (around 26 mg after tar removal).

2.9.2 Testing Apatite Dissolution and CaF_2 Precipitation With 300 µL 2 M HF Solution

To design the first major step of the SPORA protocol, around 1 mg of hydroxyapatite (n = 5) and NIST SRM 120c (n = 5) were weighed into 1.75 mL microcentrifuge tubes (Tube A). Samples were dissolved in 300 µL 2 M HF (pH = 0.5) solutions and agitated on a 2D shaker table for 24h at 500 RPM. CaF_2 residues were pelleted by centrifuging samples at high speed. The phosphate-rich supernatant was transferred into a clean tube (Tube B). CaF_2 pellets were rinsed with 100 µL deionized water and centrifuged at high speed for a few minutes. The solution was pipetted again and poured into tube B. At this stage, a 10 µL aliquot was taken and diluted with deionized water in a clean microcentrifuge tube by applying a 1000-fold dilution factor (aliquot SC, Tube SC). These samples were additionally diluted using a 5-fold factor in 1.5 mL cuvettes for SRP analysis (section 2.4). The amount of phosphate in Tube B was calculated as follows:

$$PO_4^{3-}\ (\mu mol) = [\sum PO_4^{3-}]_{SRP}\ (\mu M)\ *\ DF\ *\ Volume\ (\mu L)\ *\ (1\ L\ /10^6\ \mu L) \qquad [1]$$

where $[\Sigma PO_4^{3-}]_{SRP}$ is the measured concentration of phosphate diluted 5000 times (DF, which stands for "dilution factor").

To evaluate whether this amount of hydrofluoric acid dissolves apatite, we compared these results with data from the Rapid UC (Mine et al., 2017) (Table A2.1). Calcium fluoride was precipitate from hydroxyapatite and NIST SRM 120c replicates following the procedure described in Section 2.2. Following the supernatant transfer into a clean tube (Tube B, volume = 180 µL), a 5 µL aliquot was taken and diluted 100 folds in deionized water into a clean microcentrifuge tube (Tube SC). This solution was re-diluted with a 25- or 50-fold factor in cuvettes for SRP analysis and phosphate amount was calculated using equation [1].

Table A2.1 shows that protocols yield similar results. Therefore, the tested solution properly digests apatite.

Table A2.1. Comparing CaF_2 precipitation step results of SPORA and Rapid UC (Mine et al., 2017) protocols. Replicates of synthetic hydroxyapatite and NIST SRM 120c were weighed to around 1 mg. The same materials yield similar phosphate amounts ($PO_4^{3-}{}_{SC}$) when treated with different protocols.

Sample	**# samples**		**Mass (mg; mean ± 1σ)**		**$PO_4^{3-}{}_{SC}$ (µmol; mean ± 1σ)**	
	Rapid UC	**SPORA**	**Rapid UC**	**SPORA**	**Rapid UC**	**SPORA**
Hydroxyapatite	10	5	1.037 ± 0.048	0.989 ± 0.057	6.27 ± 0.80	6.77 ± 0.32
NIST SRM 120c	10	5	1.043 ± 0.056	1.037 ± 0.077	5.34 ± 0.63	4.95 ± 0.34

2.9.3 Anion Exchange Purification: Preliminary Data of Phosphate Adsorption and Desorption Kinetics

Several experiments were designed to test the performance of the Bio-Rad AG^{TM} 1-X8 in treating phosphate. Dissolved phosphate is found as three major ionic species that are $H_2PO_4^-$, HPO_4^{2-}, and PO_4^{3-}, and the concentration of these ionic forms is pH dependent. Because the resin beads absorb or eject monovalent anions (Bio-Rad Laboratories, 2000) and $H_2PO_4^-$ is the dominant ionic species at low pH values (Gizaw et al., 2021; Jiang et al., 2018), we tested whether phosphate recovery is maximized in acid solutions.

Around 1 mg potassium phosphate grains (Fisher Scientific, CAS: 7778-77-0) were loaded into Millipore Sigma Ultrafree^{TM} – CL centrifugal tubes and dissolved in 1000 µL 0.1 M NaF of different pH. We prepared a total of nineteen samples and 0.1 M NaF stock solutions that covered a pH range from 3 to 12. The pH of the untreated 0.1 M NaF solution was 5.5 and we spiked the other stock reagents by adding aliquots of 2 M HNO_3 or 2 M NaOH to reach the desired pH. Following, ~0.4 mL of resin charged with OH^- ions was poured into the tube. Samples were agitated for 24h at 600 rpm and centrifuged. The filtered solution was transferred to a 1.5 mL cuvette and diluted to a 1.5-fold factor for SRP analysis. Figure A2.1 and Table A2.2 show the measured concentration of phosphate ($[\Sigma PO_4^{3-}]_{RS1\text{-}SRP}$) against the pH of the working solution after the resin absorption phase. Data are compared to lower and upper detection limit values (0.202 – 10 µM) (red horizontal lines in Figure A2.1) of the absorbance-SRP concentration standard curve ($R^2 = 0.99$, $p < 0.05$) used to estimate concentrations of the unknowns. From 3 to 8 pH values, the phosphate concentration is below the lower limit, whereas phosphate may be detected at a working pH of 8.5 or higher (Figure A2.1**,** Table A2.2). Samples with detected concentration were corrected using equation [1] to estimate the undiluted concentration and phosphate moles of the filtered solution (Table A2.2). These amounts were compared to the starting phosphate moles by converting the mass stoichiometrically (Table A2.2). The residual amount of phosphate ($Moles_{RS1}$ in Table A2.2) after the adsorption step is three to four orders of magnitude lower than the starting amount, suggesting that at least 99% of dissolved phosphate is adsorbed (ΣPO_4^{3-} (%) in Table A2.2). Contrary to our initial hypothesis, these observations suggest that phosphate adsorption is independent of pH.

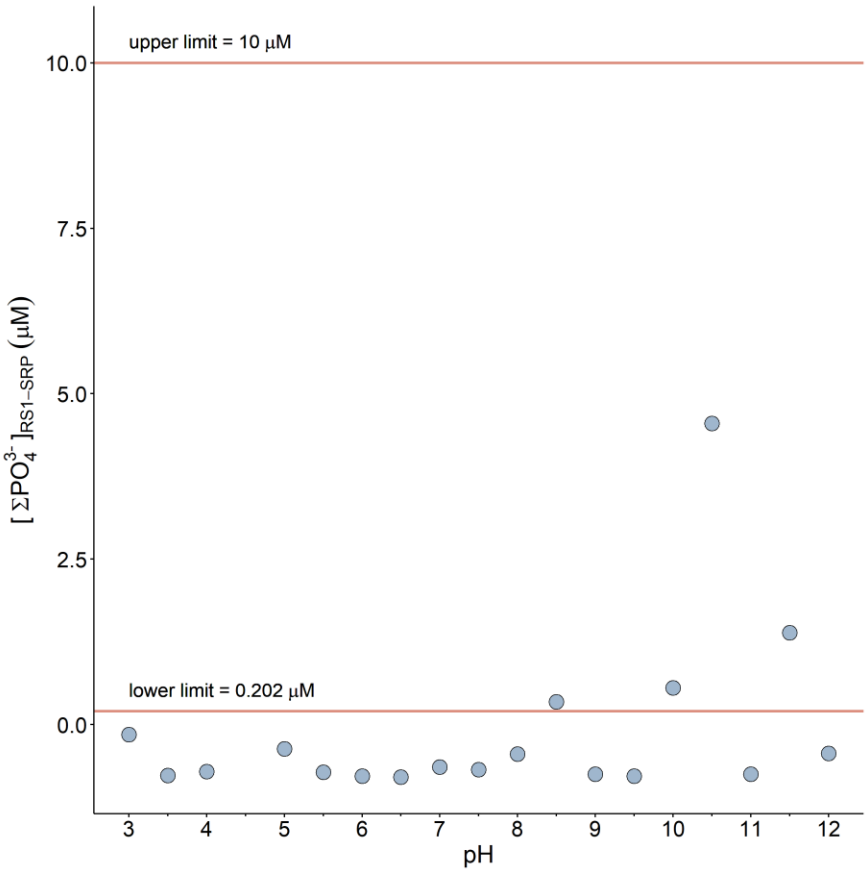

Figure A2.1. Phosphate is fully adsorbed by Bio-Rad AG^{TM} 1-X8 resin beads within a pH of 3 to 8. The measured SRP phosphate concentration at the first resin step (RS1 - adsorption) is plotted against the pH of the 0.1M NaF working solution (1000 μL). The red horizontal lines are the lower and upper detection limits calibrated by the absorbance – SRP concentration standard curve ($R^2 = 0.99$, $p < 0.05$).

Table A2.2: sample ID, starting mass, pH of 0.1 NaF solution, moles of phosphate before ($Moles_{sc}$ (µmol)) and after ($Moles_{RS1}$(µmol)), and phosphate recovery (ΣPO_4^{3-} (%)) of KH_2PO_4 samples used to test the working pH at which the Bio-Rad AG™ 1-X8 resin beads maximize phosphate adsorption. The starting moles are computed stoichiometrically ($Moles_{sc}$ (µmol)).

ID	Mass (mg)	pH	$Moles_{SC}$ (µmol)	$[\Sigma PO_4^{3-}]_{RS1-SRP}$	$Moles_{RS1}$ (µmol)	ΣPO_4^{3-} (%)
MPP_3PH_B	0.965	3	7.091	-0.152	NA	100.00
MPP_3.5PH_B	0.974	3.5	7.157	-0.77	NA	100.00
MPP_4PH_B	0.986	4	7.246	-0.709	NA	100.00
MPP_5PH_B	1.058	5	7.775	-0.365	NA	100.00
MPP_5.5PH_B	1.05	5.5	7.716	-0.72	NA	100.00
MPP_6PH_B	1.08	6	7.936	-0.78	NA	100.00
MPP_6.5PH_B	1.052	6.5	7.731	-0.791	NA	100.00
MPP_7PH_B	1.036	7	7.613	-0.639	NA	100.00
MPP_7.5PH_-B	1.048	7.5	7.701	-0.679	NA	100.00
MPP_8PH_B	1.016	8	7.466	-0.446	NA	100.00
MPP_8.5PH_B	0.963	8.5	7.077	0.345	0.0005	99.99
MPP_9PH_B	0.965	9	7.091	-0.75	NA	100.00
MPP_9.5PH_B	1.069	9.5	7.855	-0.78	NA	100.00
MPP_10PH_B	1.042	10	7.657	0.557	0.0008	99.99
MPP_10.5PH_B	1.01	10.5	7.422	4.551	0.0068	99.91
MPP_11PH_B	1.09	11	8.010	-0.75	NA	100.00
MPP_11.5PH_B	1.028	11.5	7.554	1.389	0.0021	99.97
MPP_12PH_B	0.96	12	7.054	-0.436	NA	100.00

For the desorption step, we run several experiments by testing different counterions and concentrations in order to maximize phosphate recovery and time management of the procedure. We selected two counter-anion exchanger candidates for phosphate desorption: bicarbonate (HCO_3^-, resin relative selectivity = 6) and nitrate (NO_3^-, resin relative selectivity = 65) (Bio-Rad Laboratories, 2000).

As a first test, we prepared two stock solutions of 1 M $NaHCO_3$ (pH = 9.5) and 1 M $NaNO_3$ (pH = 5.5) and compared their phosphate recovery performance. About 1 mg of apatite standard materials (synthetic hydroxyapatite, NIST SRM 120c, and naturally occurring fluorapatite in $NaNO_3$ experiments only) were dissolved in 300 µL 2 M hydrofluoric acid overnight (Tube A). The phosphate-rich solution was transferred into a Millipore Sigma Ultrafree™ – CL centrifugal vial (Tube B). CaF_2 pellets were rinsed with 100 µL deionized water and the solution was poured into Tube B. ~400 µL of Bio-Rad AG™ 1-X8 resin charged with hydroxide ions were loaded into the centrifugal vials (Tube B) and agitated overnight. The phosphate-depleted solution was filtered from the resin by centrifuging tubes. The filter unit loaded with resin beads was transferred into a clean collector unit. Samples were rinsed five times with 200 µL 1 M $NaHCO_3$ or 1 M $NaNO_3$

solutions for 30 min on a shaking table. The solution was centrifuged after each rinse into different collector tubes (Tube C1, C2, C3, C4, and C5). 10 µL aliquots were taken before loading the resin (vial SC), after resin adsorption (vial RS1), and after each $NaHCO_3$ or $NaNO_3$ washes (vial RS2 rinse #1 to 5) for SRP analysis (Mine et al., 2017; Murphy and Riley, 1962) to measure the starting amount of phosphate, double-check whether phosphate adsorption reached completion, and amount of phosphate desorbed after each rinse, respectively. Aliquots for SRP were diluted up to a 5,000-fold factor and phosphate amount was calculated using equation [1]. The phosphate recovery (ΣPO_4^{3-} $recovery_{RS2}$ (%)) after each rinse was measured as follows:

$$\sum PO_4^{3-}\ recovery_{RS2}\ (\%) = (\sum PO_{4-RS2\ rinse\ i)}^{3-}\ /\ \sum PO_{4-SC)}^{3-}) * 100 \quad [2]$$

where *i* is the number of rinses from 1 to 5, $\Sigma PO_4^{3-}{}_{RS2-rinse\ i}$ is the amount of phosphate after each rinse *i,* and $\Sigma PO_4^{3-}{}_{SC}$ is the starting amount of phosphate.

Among the two selected counterions, nitrate elutes phosphate more efficiently than bicarbonate (Figure A2.2, Table A2.3). Washing the resin with a 1 M $NaHCO_3$ solution recovers around 20% of phosphate at the first rinse, and phosphate recovery plateaus at around 70% after the fourth rinse. Contrary to bicarbonate, the resin exchanges around 30% of phosphate with dissolved nitrate (1M_NaNO3 panel in Figure A2.2) in the first rinse and the recovery stops at ~80% after the fourth rinse. Following, we tested different concentrations of $NaNO_3$ solutions in order to improve desorption efficiency. Apatite standards materials were treated using the same procedure, but phosphate was desorbed with 3 M, 0.55 M, 0.44 M, and 0.22 M $NaNO_3$ solutions.

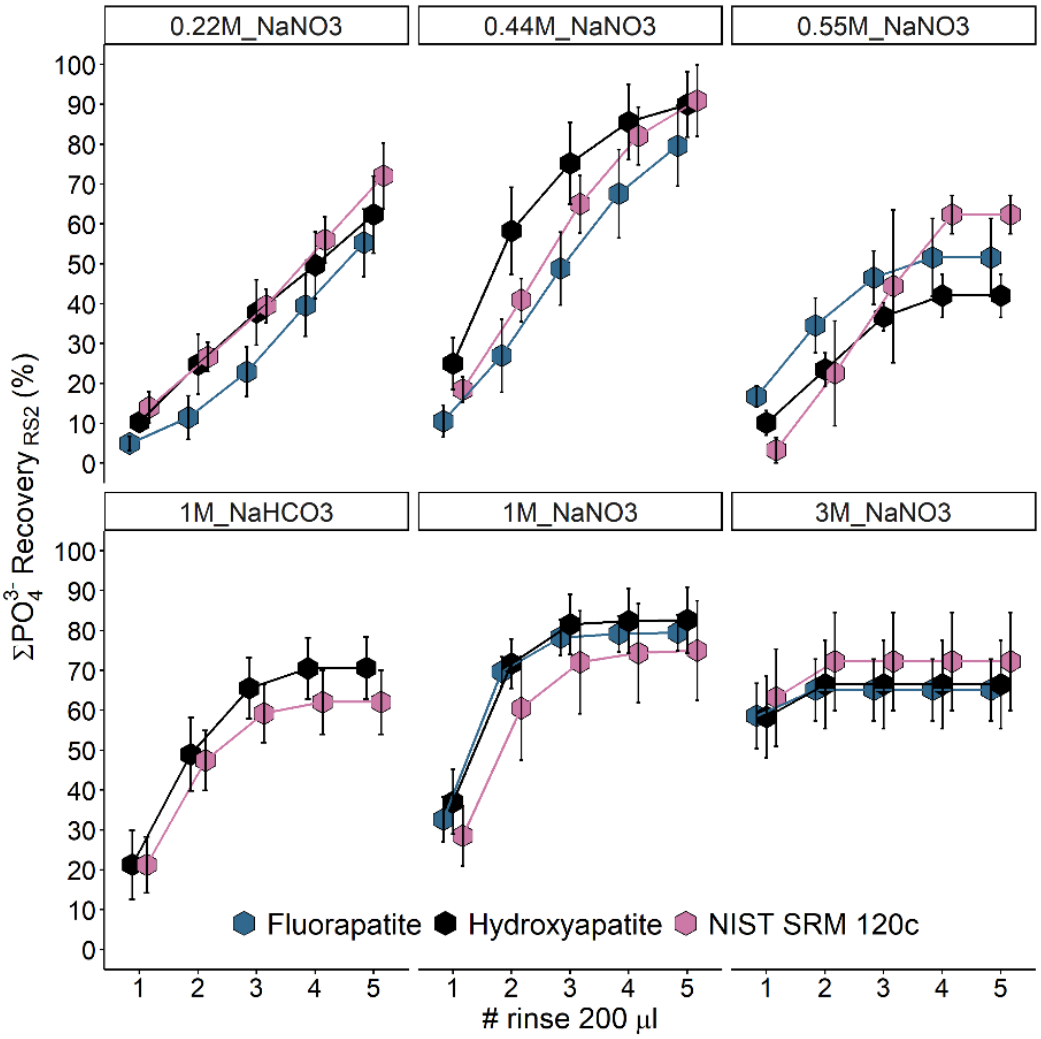

Figure A2.2. a 0.44 M $NaNO_3$ solution improves the phosphate desorption kinetics. Panels display different phosphate desorption experiments by using $NaHCO_3$ and $NaNO_3$ solutions. Data are plotted cumulative phosphate recovery (ΣPO_4^{3-} $recovery_{RS2}$ (%)) across rinses of 200 µL of solution. The recovery at each resin rinse is calculated following equation [2].

Concentrated $NaNO_3$ solutions like 3 M do not improve recovery (Figure A2.2, Table A2.3). Up to 50% of the starting phosphate pool is eluted, but the cumulative phosphate recovery plateaus at ~60% after the second rinse. A similar observation is shown when using a 0.55 M stock solution, where the cumulative recovery slowly hits a value of ~50% and plateaus at the fourth rinse (Figure A2.2, Table A2.3). Among the tested stock solutions, 0.22 M and 0.44 M are the concentrations that perform better (Figure A2.2, Table A2.3). The recovery increases in a linear fashion reaching a value of 60% when using a 0.22 M solution, whereas ~85% of phosphate is recovered when resin beads are washed with a 0.44 M $NaNO_3$ solution after five times. Altogether, these data follow the general rule that desorption performance is higher when anion exchange resins are soaked in low-

concentrated solutions of targeted counterions with higher relative selectivity (Wheaton and Bauman, 1951; Yoon et al., 2009). However, these results show that phosphate may be recovered by increasing the number of rinses (0.22_M NaNO3 and 0.44_M NaNO3 panels in Figure A2.2).

Among the two lowest concentrated solutions used, a 0.44 M $NaNO_3$ solution performs better in terms of phosphate recovery and time management. We rerun an additional experiment using the same apatite standard materials where the resin beads are washed and centrifuged seven times with a 0.44 M $NaNO_3$ solution. Data in Figure A2.3 show that around 90% of the starting amount of phosphate is recovered at the seventh rinse for all apatite standards used. Finally, we selected this procedure as the best desorption kinetic performance.

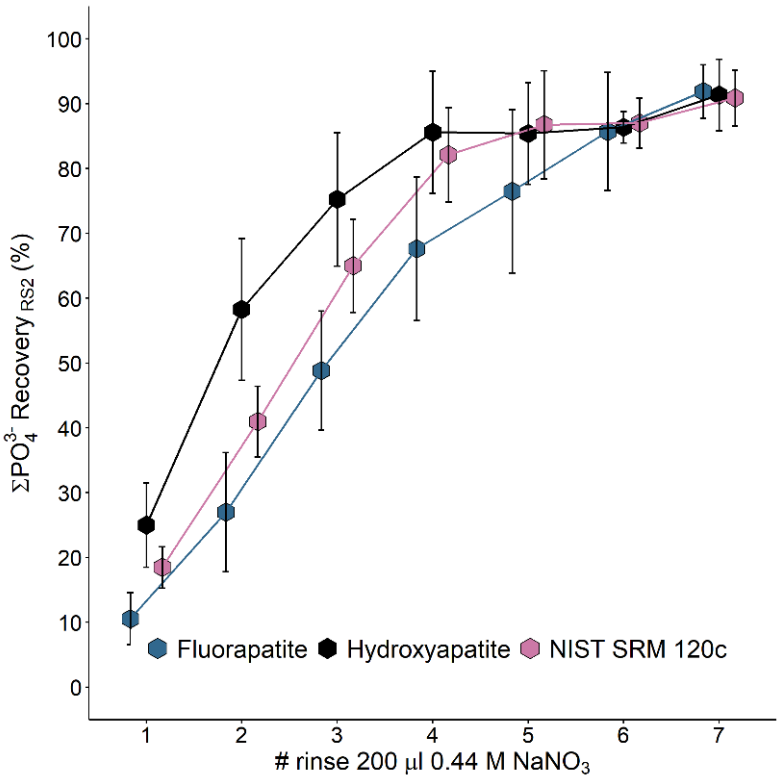

Figure A2.3. Seven rinses of 200 µL 0.44 M $NaNO_3$ desorb almost all the starting amount of phosphate. While recovery after rinses is variable across materials, the amount of desorbed phosphate is ~90% for either naturally occurring fluorapatite, synthetic hydroxyapatite, and NIST SRM 120c.

2.9.4 Comparison Between Silver Ammine Solutions Among SPORA and Rapid UC Protocols

Table A2.4 compares the stoichiometric Ag^+:PO_4^{3-} ratio used for SPORA and Rapid UC protocols. We calculated the stoichiometric ratio by considering the amount of phosphate desorbed after seven rinses with 200 µL 0.44 M $NaNO_3$ from the naturally occurring fluorapatite, synthetic hydroxyapatite, and NIST SRM 120c standard apatite materials (data from Appendix 2.9.3**;** $PO_4^{3-}{}_{RS2}$ (µmol) in Table A2.4).

The Rapid UC protocol requires 180 µL 0.37 M $AgNO_3$ + 1.09 M NH_4OH silver ammine solution to precipitate phosphate dissolved in 180 µL of working solution before the precipitation step (Mine et al., 2017). The silver ammine reagent adds 66.6 µmol Ag^+ into the system (Table A2.4). If the same amount of desorbed phosphate from the resin ($PO_4^{3-}{}_{RS2}$ in Table A2.4) were dissolved in a 180 µL solution, the stoichiometric Ag^+:PO_4^{3-} would be over the recommended 10:1 ratio (O'Neil et al., 1994) ($Ag^+{}_{Rapid\ UC}$: $PO_4^{3-}{}_{RS2}$ in Table A2.4). While having higher ratios is usually the ideal case, we hypothesized that a high silver excess would have side effects for the SPORA protocol. Because phosphate is dissolved in a 1,400 µL working solution following the desorption step (Appendix 2.9.3), large working volumes may promote coprecipitation of oxygen-bearing crystals like silver oxide due to an excess of hydroxide ions given the following reactions (Biedermann et al., 1960; Charlot, 1969; Molleman and Hiemstra, 2017): Ag^+ (aq) + OH^- (aq) → AgOH → ½ Ag_2O (s) + ½ H_2O.

We decided to lower the concentration of the $AgNO_3$ reagent to minimize the inclusion of contaminants like silver oxide. We used 180 µL 0.22 M $AgNO_3$ + 1.09 M NH_4OH silver ammine solution to precipitate silver phosphate crystals. This solution would ideally add 39.6 µmol Ag^+, reducing the stoichiometric Ag^+:PO_4^{3-} below 10:1 (Table A2.4). The proposed silver ammine solution would precipitate phosphate without compromising phosphate recovery and crystal quality.

Table A2.4. Phosphate moles ($PO_4^{3-}{}_{RS2}$) of naturally occurring fluorapatite, synthetic hydroxyapatite, and NIST SRM 120c measured after the seven 0.2 µL 0.44 M $NaNO_3$ rinses as described in Appendix 2.9.3. The amount of phosphate was used to compare the stoichiometric silver to phosphate ratio ($Ag^+{}_{SPORA}$: $PO_4^{3-}{}_{RS2}$ and $Ag^+{}_{Rapid\ UC}$: $PO_4^{3-}{}_{RS2}$) based on the added moles of Ag^+ ($Ag^+{}_{SPORA}$ and $Ag^+{}_{Rapid\ UC}$) using the following silver ammine solution: 180 µL 0.22 M $AgNO_3$ + 1.09 M proposed for the SPORA protocol and 180 µL 0.37 M $AgNO_3$ + 1.09 M used in the Rapid UC protocol (Mine et al., 2017).

Sample	**$PO_4^{3-}{}_{RS2}$ (µmol)**	**$Ag^+{}_{SPORA}$ (µmol)**	**$Ag^+{}_{Rapid\ UC}$ (µmol)**	**$Ag^+{}_{SPORA}$: $PO_4^{3-}{}_{RS2}$**	**$Ag^+{}_{Rapid\ UC}$: $PO_4^{3-}{}_{RS2}$**
Fluorapatite	5.40 ± 0.51	39.6	66.6	7.33	12.33
Hydroxyapatite	5.77 ± 0.34	39.6	66.6	6.86	11.54
NIST SRM 120c	4.46 ± 0.21	39.6	66.6	8.88	14.94

2.9.5 FTIR Spectra On Pristine and Contaminated Silver Phosphate Standard Materials

Pure silver phosphate crystals have the typical bending and stretching absorption bands of phosphate groups at 542 (ν_4PO_4) and 930 cm^{-1} (ν_3PO_4). The same vibration modes can be found at 603 and 930 cm^{-1}, but the absorbance intensity is very low. Additionally, pure silver phosphate may show Ag-O bending mode at 621 cm^{-1}, but it is poorly resolved since it overlaps with the major ν_3PO_4 band (Figure A2.4) (Shimabukuro et al., 2022; Suthanthiraraj and Sarumathi, 2012; Suwanprateeb et al., 2012). If silver phosphate has organic impurities such as collagen, phosphate absorbance modes broaden, and the Amide III, II, and I functional groups (1235, 1530, and 1636 cm^{-1}, respectively) alter the shape of spectra (Figure A2.4) (Al Sekhaneh et al., 2021; Grunenwald et al., 2014; Lebon et al., 2016; Trayler et al., 2023). The collagen-Ag_3PO_4 mixture shown in Figure A2.4 also displays absorbance bands of lipids (Liden et al., 1995) since the organic material used for the mixture is a bovine Achilles tendon. While we resolved these peaks for clarity, FTIR spectra on apatite materials do not show any of the lipid absorbance modes (Appendix 2.9.6). Thus, we ruled out lipids as a source of contamination.

Infrared vibration bands of pure silver oxide show absorbance within the same wavenumber region of silver phosphate bands (Figure A2.4). However, a characteristic vibrational peak of this contaminant is distinguishable in the silver phosphate-silver oxide mixture at 1072 cm^{-1} (Figure A2.4).

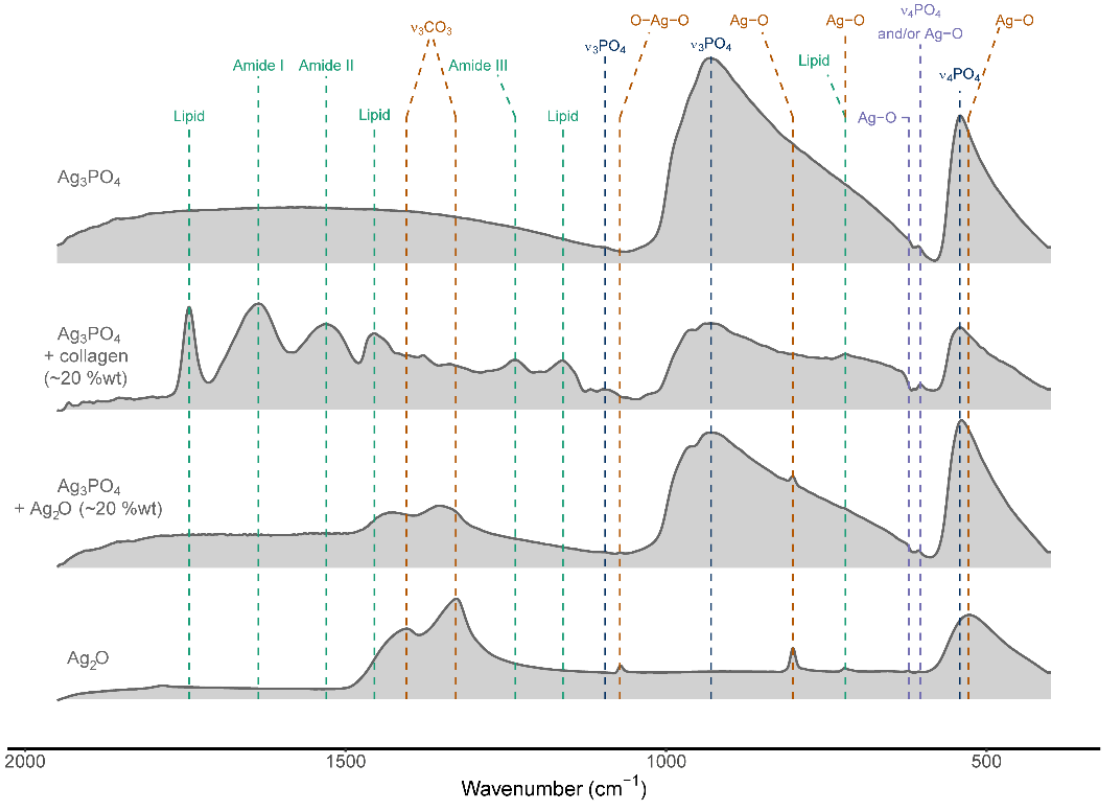

Color	Material
- - - -	Ag_3PO_4
- - - -	Ag_2O
- - - -	Ag_3PO_4 or Ag_2O
- - - -	Collagen

Wavenumber	Group
528	AgO – Ag–O bending
542	ν_4PO_4 – P–O–P bending
603	ν_4PO_4 and/or Ag–O bending
621	AgO – Ag–O bending
720	Organic lipid – C=O stretch
720	AgO – Ag–O–Ag stretch
802	AgO – Ag–O–Ag stretch
930	ν_3PO_4 – P–O–P stretch
1072	AgO – O–Ag–O vibration
1095	ν_3PO_4 – P–O–P stretch
1161	Organic Lipid – C–O–C stretch
1235	Amide III – CO–NH bending
1328	ν_3CO_3 – C–O stretch
1405	ν_3CO_3 – C–O stretch
1455	Organic Lipid – CH_2 bending
1530	Amide II – methylene (C-H) bending
1636	Amide I – carbonyl (C=O) stretch
1744	Organic lipid – carbonyl (C=O) stretch

Figure A2.4. FTIR analysis as a tool to discern pristine Ag_3PO_4 from collogen- and Ag_2O-contaminated crystals (~20 %wt for each contaminant) based on spectra shape. If Ag_3PO_4 crystals are contaminated, spectra display a more complex shape proportional to the type of contamination. Infrared bands are colored based on the functional groups assigned to specific inorganic and organic materials.

2.9.6 FTIR Spectra On Apatite Materials

Infrared spectra on biogenic and standard apatite materials reflect their molecular composition (Figure A2.5 and Table A2.5). All apatite materials show the expected phosphate vibrational bands at 470, 560, 630, 960, and 1025 cm^{-1} (ν_2PO_4 stretch, ν_4PO_4 banding, ν_4PO_4 banding, ν_1PO_4 stretch, and ν_3PO_4 stretch, respectively). Vibration modes of amide and carbonate vary in absorbance intensity in agreement with the nature of the materials. Amide groups of organic compounds (i.e., collagen) usually absorb infrared light at 1235 cm^{-1}, 1551, and 1636 cm^{-1}, while carbonate shows multiple vibrational bands based on whether it substitutes hydroxyl and fluorine groups (Type-A) or phosphate ions (Type-B) or both in the crystallographic ions (Figure A2.5 and Table A2.5) (Al Sekhaneh et al., 2021; Amir et al., 2004; Enax et al., 2014, 2012; Grimes and Pellegrini, 2013; Grunenwald et al., 2014; Lebon et al., 2016; Lécuyer et al., 2010; LeGeros, 1981; Leventouri, 2006; Ren et al., 2014; Trayler et al., 2023).

All standard samples (i.e., naturally occurring fluorapatite, synthetic hydroxyapatite, and NIST SRM 120c) are carbonated apatite materials (Figure A2.5 and Table A2.5). Fluorapatite seems to have the least amount, showing very weak ν_2CO_3 and ν_3CO_3 bands. The synthetic hydroxyapatite shows a more pronounced ν_2CO_3 at 870 cm^{-1} and a libration mode of hydroxyl groups at 870 cm^{-1}, with the latter being a characteristic feature of synthetic crystals only (Ren et al., 2014). Lastly, the NIST SRM 120c has the highest carbonate content among standards, showing distinct and relatively strong ν_2CO_3 and ν_3CO_3 vibration modes.

As expected, modern specimens show varying organic content given the nature of materials. Bone and tooth mixtures samples from deer, goat, and shark individuals have stronger amide vibrational bands of collagen than tooth enamel or enameloid (Figure A2.5 and Table A2.5). In contrast to modern samples, all fossil materials analyzed here show a low organic content (Figure A2.5 and Table A2.5) because the organic matter in the apatite structure degrades over time (Al Sekhaneh et al., 2021), especially in very old samples like the considered shark tooth specimens.

Infrared spectra of pretreated and untreated asphalt-impregnated fossil mammal bone (Fossil mammal indet.1 in Figure A2.5) are virtually indistinguishable. Similar to fossil shark teeth, both spectra show carbonate ν_2CO_3 and ν_3CO_3 bands and a weak amide I vibrational mode of the residual collagen content. We were not able to detect infrared-active bands of natural asphalt in the untreated sample because samples should be pressed into a thin film on a zinc selenide prism and heated before the analysis (Hou et al., 2018). However, the spectra confirm that asphalt removal treatment described in Appendix 2.9.1 did not alter the chemical and structural composition of bone apatite.

Finally, the specimen collected from, presumably, the Modesto Formation (Fossil mammal indet.1 in Figure A2.5) has distinct carbonate bands compared to apatite materials considered here. ν_2CO_3 and ν_3CO_3 peaks are very strong, and another carbonate vibration mode occurs at 712 cm^{-1} (ν_4CO_3; Figure A2.5 and Table A2.5). These features occur when, following the burial of specimens, acid fluids dissolve apatite materials and partially recrystallize it as calcite (i.e., diagenesis) (Koch et al., 1997; Ren et al., 2014; Zazzo et al.,

2004). Thus, carbonate bands in this specimen reflect a mixed bulk of both structural carbonate and external calcite.

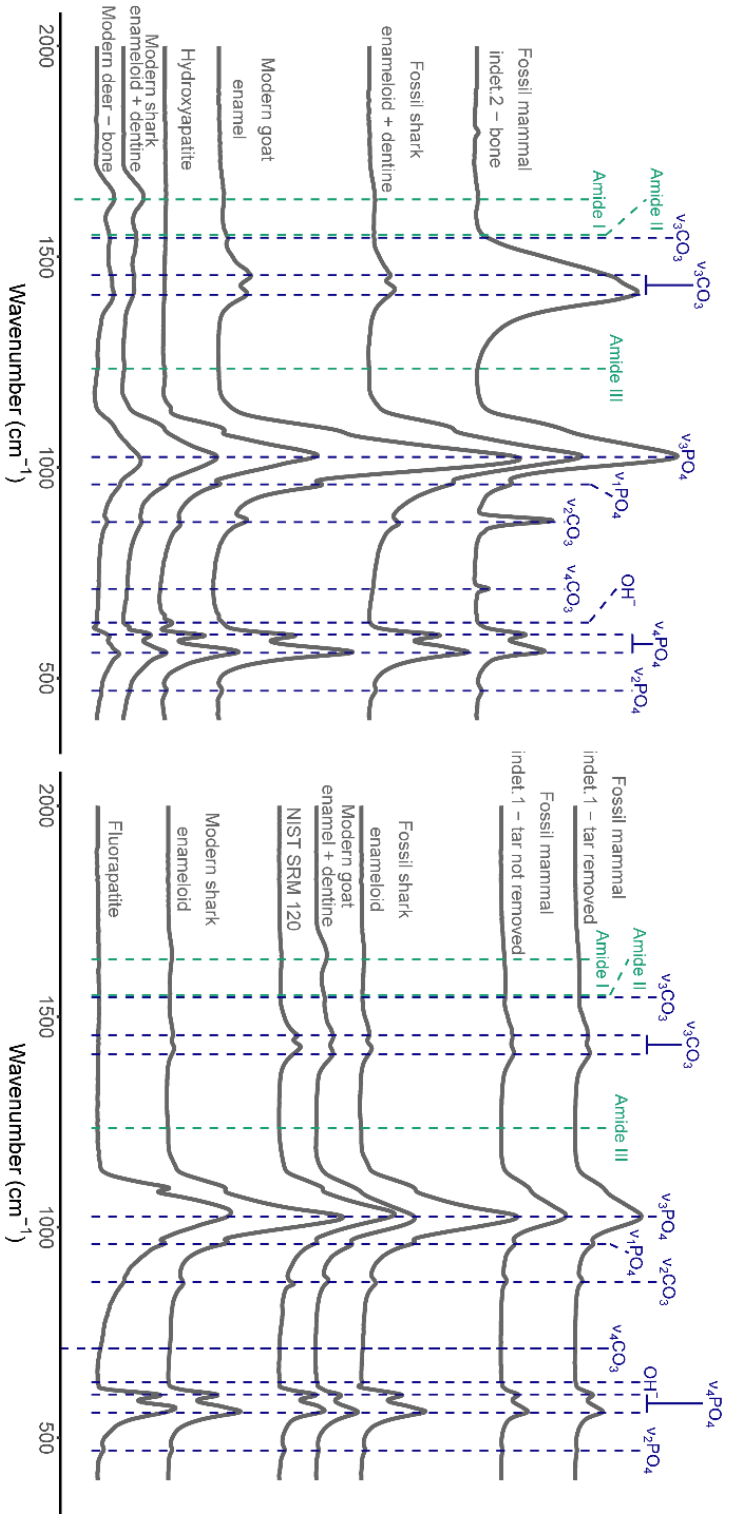

Figure A2.5. FTIR spectra of standard and biogenic apatite materials.

Table A2.5. Identified infrared absorbance bands of apatite functional groups.

Wavenumber (cm^{-1})	**Functional group**
470	ν_2PO_4 - P-O-P stretch
560	ν_4PO_4 - P-O-P bending
603	ν_4PO_4 - P-O-P bending
632	OH - OH-P libration
712	ν_4CO_3 - C-O bending (diagenetic CO_3)
870	ν_2CO_3 - C-O bending (Type-A or Type-B or diagenetic CO_3)
960	ν_1PO_4 - P-O-P stretch
1025	ν_3PO_4 - P-O-P stretch
1235	Amide III - CO-NH bending
1410	ν_3CO_3 - C-O bending (Type-B or diagenetic CO_3)
1456	ν_3CO_3 - C-O bending (Type-B or diagenetic CO_3)
1545	ν_3CO_3 - C-O stretch (Type-A)
1551	Amide II – methylene (C-H) bending
1636	Amide I – carbonyl (C=O) stretch

2.9.7 Phosphate Recovery By Steps For SPORA Protocol

We calculated the phosphate recovered from standard and biogenic apatite materials treated with SPORA protocol after each chemical step. We used the following equations (Table A2.6):

$$\sum PO_4^{3-}\ recovery_{RS1}\ (\%) = (\sum PO_4^{3-}{}_{SC}\ -\ \sum PO_4^{3-}{}_{RS1}) / \sum PO_4^{3-}{}_{SC}) * 100 \quad [3]$$

$$\sum PO_4^{3-}\ recovery_{RS2}\ (\%) = (\sum PO_4^{3-}{}_{RS2}\ /\ \sum PO_4^{3-}{}_{SC}) * 100 \quad [4]$$

$$\sum PO_4^{3-}\ recovery_{P}\ (\%) = (\sum PO_4^{3-}{}_{RS2}\ -\ \sum PO_4^{3-}{}_{P}) / \sum PO_4^{3-}{}_{SC}) * 100 \quad [5]$$

where $\Sigma PO_4^{3-}{}_{SC}$ is the amount of starting phosphate, $\Sigma PO_4^{3-}{}_{RS1}$ is the amount of phosphate left in solution after resin desorption, $\Sigma PO_4^{3-}{}_{RS2}$ is the amount of phosphate after resin desorption, and $\Sigma PO_4^{3-}{}_{P}$ is the amount of phosphate left in solution after Ag_3PO_4 precipitation. Equation [5] provides the total amount of phosphate recovered as Ag_3PO_4 crystals.

Table A2.6. Phosphate recovery (mean ± 1σ) after resin adsorption (RS1), resin desorption (RS2), and precipitation (P). Data are shown as mean recovery and standard deviation calculated from 95 samples.

ΣPO_4^{3-} Recovery (%) - SPORA		
RS1	**RS2**	**P**
99.17 ± 0.86	91.73 ± 7.72	89.22 ± 9.58

2.9.8 Infrared Carbonate Bands In Ag_3PO_4 Crystals

Silver phosphate crystals produced with both SPORA and Rapid UC protocols are contaminated with oxygen-bearing minerals. Specifically, FTIR spectra show that all crystals have carbonate precipitated as Ag_2CO_3. We attempted to semi-quantify carbonate contamination by calculating the $CO_{3\ (1405\ cm^{-1})}$ / $PO_{4\ (930\ cm^{-1})}$ and $CO_{3\ (1545\ cm^{-1})}$ / $PO_{4\ (930\ cm^{-1})}$ indexes, which compare the amount of carbonate relative to phosphate peaks based on the absorbance intensities of ν_3CO_3 and ν_3PO_4 functional groups in crystals.

Figure A2.6 show the carbonate-to-phosphate ratios grouped by protocols based on the indexes calculated for each apatite material type reported in Table A2.7. Data by protocols cluster in two separate groups. While $CO_{3\ (1405\ cm^{-1})}$ / $PO_{4\ (930\ cm^{-1})}$ do not significantly change between protocols (Kruskal-Wallis test, $p = 0.97$), $CO_{3\ (1545\ cm^{-1})}$ / $PO_{4\ (930\ cm^{-1})}$ ratios in crystals produced with the SPORA method cluster to higher values (Kruskal-Wallis test, $p = 6 \times 10^{-4}$). These observations suggest that the SPORA protocol may contribute to a slightly higher amount of carbonate inclusions. Probably, the resin uptakes a discrete amount of dissolved bicarbonate ions along with phosphate that is eventually desorbed and precipitated afterward. However, the calculated ratio values are very small, suggesting that the amount of contamination is contained with both protocols.

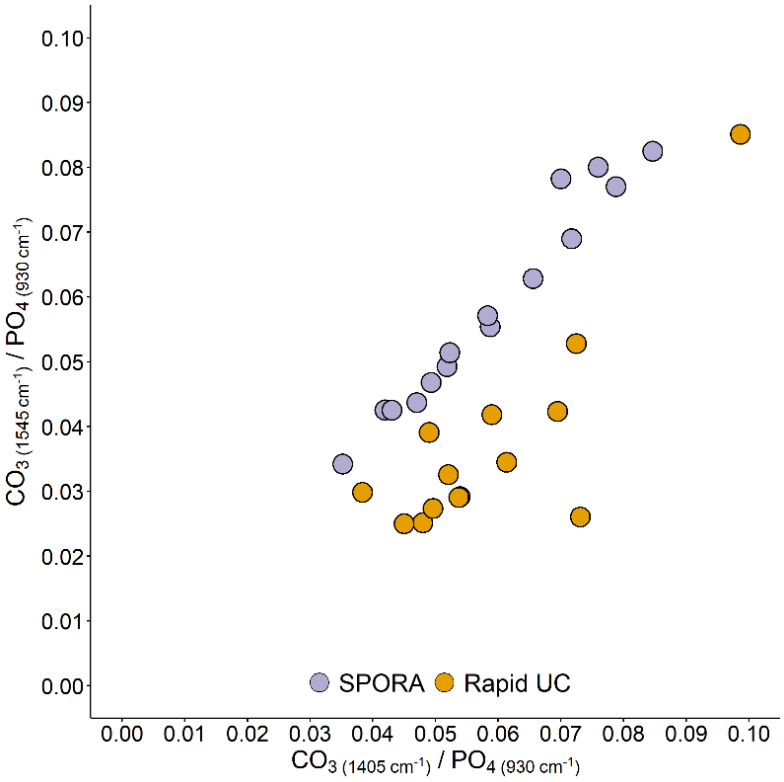

Figure A2.6. Despite the SPORA protocol promoting higher carbonate inclusion, carbonate contamination is contained in crystals produced with both methods. The graph plots $CO_{3\ (1405}$

$_{cm^{-1}}$) / PO_4 $_{(930\ cm^{-1})}$ and CO_3 $_{(1545\ cm^{-1})}$ / PO_4 $_{(930\ cm^{-1})}$ index values grouped by protocol obtained by infrared carbonate and phosphate bands detected on Ag_3PO_4 crystals.

Table A2.7. CO_3 $_{(1405\ cm^{-1})}$ / PO_4 $_{(930\ cm^{-1})}$ and CO_3 $_{(1545\ cm^{-1})}$ / PO_4 $_{(930\ cm^{-1})}$ index values of Ag_3PO_4 crystals derived from standard and biogenic apatite samples.

Sample	**Material**	**ID**	**CO_3 $_{(1405\ cm^{-1})}$ / PO_4 $_{(930\ cm^{-1})}$**		**CO_3 $_{(1545\ cm^{-1})}$ / PO_4 $_{(930\ cm^{-1})}$**	
			SPORA	**Rapid UC**	**SPORA**	**Rapid UC**
Fossil mammal indet.2	Bone	MM2	0.085	0.073	0.082	0.026
Modern deer	Bone	OV	0.070	0.054	0.078	0.029
Fossil mammal indet.1	Bone (tar not removed)	MM1	0.076	-	0.080	-
	Bone (tar removed)	MM1	0.059	0.061	0.055	0.034
Fluorapatite	Naturally occurring crystal	FA	0.042	0.052	0.043	0.033
Modern goat	Enamel	CH	0.079	0.069	0.077	0.042
	Enamel + dentin	CH	0.072	0.048	0.069	0.025
Fossil shark	Enameloid	SM1	0.058	0.072	0.057	0.053
	Enameloid + dentin	SM1	0.052	0.054	0.049	0.029
	Enameloid	SM2	0.066	0.045	0.063	0.025
	Enameloid + dentin	SM2	0.052	0.059	0.051	0.042
Modern shark	Enameloid	TOM	0.047	0.049	0.044	0.039
	Enameloid + dentin	TOM	0.043	0.038	0.043	0.030
NIST SRM 120c	Phosphate rock	NIST120c	0.049	0.050	0.047	0.027
Hydroxyapatite	Synthetic crystal	HAP	0.035	0.099	0.034	0.085

2.9.9 $\delta^{18}O$ Values of In-House Silver Oxide (Ag_2O) Crystals

Table A2.8. $\delta^{18}O$ values of in-house silver oxide (Ag_2O) crystal replicates.

Sample	**Replicate #**	**$\delta^{18}O$**
Ag_2O	1	-1.9
Ag_2O	2	-1.0
Ag_2O	3	-1.4
Ag_2O	4	1.1
Ag_2O	5	0.3
Ag_2O	6	0.8
Ag_2O	7	1.9
Ag_2O	8	3.1

2.9.10 Carbonate Solubility Estimates In Hydrofluoric Acid (HF) Solution

The following calculations assume that only the carbonate in the apatite lattice structure (i.e., structural carbonate) as the only carbonate source and the capped 1.5 mL vial as a close system (i.e., the free CO_2 produced in the headspace does not escape and equilibrates with the solvent). Assuming that an amount of structural carbonate of 6 wt% (Crowley and Wheatley, 2014), 1 mg of bioapatite yields $9.83*10^{-7}$ mol of CO_2 gas:

$$CO_3^{2-}g = 1\ mg_{bioapatite} * 0.06\ \frac{mg_{CO_3^{2-}}}{mg_{bioapatite}} * \frac{1\ g_{CO_3^{2-}}}{1000\ mg_{CO_3^{2-}}} = 6\ * 10^{-5}\ g_{CO_3^{2-}}$$

$$CO_{2\,(g)}\ g = 6\ * 10^{-5} g_{CO_3^{2-}} * \frac{44.01 \frac{g_{CO_2}}{mol_{CO_2}}}{61.02 \frac{g_{CO_3^{2-}}}{mol_{CO_3^{2-}}}} = 4.33 * 10^{-5}\ g\ CO_2$$

$$CO_{2\,(g)}\ mol = 4.33 * 10^{-5}\ g_{CO_2} *\ 44.01 \frac{g_{CO_2}}{mol_{CO_2}} = 9.83 * 10^{-7}\ mol_{CO_2}$$

If this amount of CO_2 is produced as a gas in a closed 1.5 mL vial with 300 µL of solvent, the partial pressure of the gas at ambient temperature (298.15 K) in the headspace (1.2 mL) is:

$$pCO_{2\,(g)}\ atm = \frac{9.83 * 10^{-7}\ mol_{CO_2} * 298.15\ K * 0.0821\ \frac{L\ atm}{mol_{CO_2} * K}}{1.2 * 10^{-3}\ L} = = 0.02\ atm_{CO_2}$$

Where 0.0821 L atm mol^{-1} K^{-1} is the Boltzmann constant. Considering that a 2.5 M HF solution at ambient temperature and pressure (25 °C and 1 atm) has a Henry's law constant for CO_2 ($K(CO_2)$) of 0.0357 mol L^{-1} atm^{-1} (Cox and Head, 1962), the amount of dissolved carbon dioxide in 300 µL of the acid medium is:

$$CO_{2\,(s)}\ mol = 0.02\ atm_{CO_{2\,(g)}} * 3 * 10^{-4}\ L * 0.0357 \frac{mol_{CO_{2\,(g)}}}{L * atm} = 2.15 * 10^{-7}\ mol_{CO_{2\,(s)}}$$

The amount of dissolved CO_2 in the HF reagent is therefore the ~21% of the total amount of carbonate released in the headspace as CO_2 gas:

$$\%\ dissolved\ CO_{2\,(s)} = \left(\frac{2.15 * 10^{-7}\ mol_{CO_{2\,(s)}}}{9.83 * 10^{-7}\ mol_{CO_2}}\right) * 100 = 21.8\ \%$$

2.9.11 References From the Appendix

Al Sekhaneh, W., Akkam, Y.H., Kamel, G., Drabee, A., Popp, J., 2021. Investigation of ancient teeth using Raman spectroscopy and synchrotron radiation Fourier-transform infrared (SR-μFTIR): mapping and novel method of dating. Dig. J. Nanomater. Biostructures 16, 713–724.

Amir, S., Hafidi, M., Merlina, G., Hamdi, H., Revel, J.-C., 2004. Elemental analysis, FTIR and 13C-NMR of humic acids from sewage sludge composting. Agronomie 24, 13–18. https://doi.org/10.1051/agro

Bio-Rad Laboratories, 2000. AG 1, AG MP-1, and AG 2 Strong Anion Exchange Resin Instruction Manual Table of Contents.

Cox, J.D., Head, A.J., 1962. Solubility of carbon dioxide in hydrofluoric acid solutions: "Standard state" correction for the combustion calorimetry of organo-fluorine compounds. Trans. Faraday Soc. 58, 1839–1845. https://doi.org/10.1039/TF9625801839

Crowley, B.E., Wheatley, P. V., 2014. To bleach or not to bleach? Comparing treatment methods for isolating biogenic carbonate. Chem. Geol. 381, 234–242. https://doi.org/10.1016/j.chemgeo.2014.05.006

Enax, J., Janus, A.M., Raabe, D., Epple, M., Fabritius, H.O., 2014. Ultrastructural organization and micromechanical properties of shark tooth enameloid, in: Acta Biomaterialia. Elsevier Ltd, pp. 3959–3968. https://doi.org/10.1016/j.actbio.2014.04.028

Enax, J., Prymak, O., Raabe, D., Epple, M., 2012. Structure, composition, and mechanical properties of shark teeth. J. Struct. Biol. 178, 290–299. https://doi.org/10.1016/j.jsb.2012.03.012

Fuller, B.T., Fahrni, S.M., Harris, J.M., Farrell, A.B., Coltrain, J.B., Gerhart, L.M., Ward, J.K., Taylor, R.E., Southon, J.R., 2014. Ultrafiltration for asphalt removal from bone collagen for radiocarbon dating and isotopic analysis of Pleistocene fauna at the tar pits of Rancho La Brea, Los Angeles, California. Quat. Geochronol. 22, 85–98. https://doi.org/10.1016/j.quageo.2014.03.002

Gizaw, A., Zewge, F., Kumar, A., Mekonnen, A., Tesfaye, M., 2021. A comprehensive review on nitrate and phosphate removal and recovery from aqueous solutions by adsorption. Aqua Water Infrastructure, Ecosyst. Soc. https://doi.org/10.2166/aqua.2021.146

Grimes, V., Pellegrini, M., 2013. A comparison of pretreatment methods for the analysis of phosphate oxygen isotope ratios in bioapatite. Rapid Commun. Mass Spectrom. 27, 375–390. https://doi.org/10.1002/rcm.6463

Grunenwald, A., Keyser, C., Sautereau, A.M., Crubézy, E., Ludes, B., Drouet, C., 2014. Revisiting carbonate quantification in apatite (bio)minerals: A validated FTIR methodology. J. Archaeol. Sci. 49, 134–141. https://doi.org/10.1016/j.jas.2014.05.004

Hou, X., Lv, S., Chen, Z., Xiao, F., 2018. Applications of Fourier transform infrared spectroscopy technologies on asphalt materials. Meas. J. Int. Meas. Confed. 121, 304–316. https://doi.org/10.1016/j.measurement.2018.03.001

Jiang, D., Chu, B., Amano, Y., Machida, M., 2018. Removal and recovery of phosphate from water by Mg-laden biochar: Batch and column studies. Colloids Surfaces A Physicochem. Eng. Asp. 558, 429–437. https://doi.org/10.1016/J.COLSURFA.2018.09.016

Koch, P.L., Tuross, N., Fogel, M.L., 1997. The effects of sample treatment and diagenesis on the isotopic integrity of carbonate in biogenic hydroxylapatite. J. Archaeol. Sci. 24, 417–429. https://doi.org/10.1006/jasc.1996.0126

Lebon, M., Reiche, I., Gallet, X., Bellot-Gurlet, L., Zazzo, A., 2016. Rapid quantification of bone collagen content by ATR-FTIR spectroscopy. Radiocarbon 58, 131–145. https://doi.org/10.1017/RDC.2015.11

Lécuyer, C., Balter, V., Martineau, F., Fourel, F., Bernard, A., Amiot, R., Gardien, V., Otero, O., Legendre, S., Panczer, G., Simon, L., Martini, R., 2010. Oxygen isotope fractionation between apatite-bound carbonate and water determined from controlled experiments with synthetic apatites precipitated at 10-37 °C. Geochim. Cosmochim. Acta 74, 2072–2081. https://doi.org/10.1016/j.gca.2009.12.024

LeGeros, R.Z., 1981. Apatites in biological systems. Prog. Cryst. Growth Charact. 4, 1–45. https://doi.org/10.1016/0146-3535(81)90046-0

Leventouri, T., 2006. Synthetic and biological hydroxyapatites: Crystal structure questions. Biomaterials 27, 3339–3342. https://doi.org/10.1016/j.biomaterials.2006.02.021

Mine, A.H., Waldeck, A., Olack, G., Hoerner, M.E., Alex, S., Colman, A.S., 2017. Microprecipitation and δ18O analysis of phosphate for paleoclimate and biogeochemistry research. Chem. Geol. 460, 1–14. https://doi.org/10.1016/j.chemgeo.2017.03.032

Murphy, J., Riley, J.P., 1962. A Modified Single Solution Method for Natural Determination of Phosphate in Natural Waters. Anal. Chim. Acta 27, 13–19.

O'Neil, J.R., Roe, L.J., Reinhard, E., Blake, R.E., 1994. A rapid and precise method of oxygen isotope analysis of biogenic phosphate. Isr. J. Earth Sci. 43, 203–212.

Ren, F., Ding, Y., Leng, Y., 2014. Infrared spectroscopic characterization of carbonated apatite: A combined experimental and computational study. J. Biomed. Mater. Res. - Part A 102, 496–505. https://doi.org/10.1002/jbm.a.34720

Shimabukuro, M., Hayashi, K., Kishida, R., Tsuchiya, A., Ishikawa, K., 2022. No-Observed-Effect Level of Silver Phosphate in Carbonate Apatite Artificial Bone on Initial Bone Regeneration. ACS Infect. Dis. 8, 159–169. https://doi.org/10.1021/acsinfecdis.1c00480

Suthanthiraraj, S.A., Sarumathi, R., 2012. XRD and FTIR studies on a new solid electrolyte

system containing Ag 3PO4 and SbI3. AIP Conf. Proc. 1447, 1005–1006. https://doi.org/10.1063/1.4710345

Suwanprateeb, J., Thammarakcharoen, F., Wasoontararat, K., Chokevivat, W., Phanphiriya, P., 2012. Preparation and characterization of nanosized silver phosphate loaded hydroxyapatite by single step co-conversion process. Mater. Sci. Eng. C 32, 2122–2128. https://doi.org/10.1016/j.msec.2012.05.051

Trayler, R.B., Landa, P.V., Kim, S.L., 2023. Evaluating the efficacy of collagen isolation using stable isotope analysis and infrared spectroscopy. J. Archaeol. Sci. 151, 105727. https://doi.org/10.1016/j.jas.2023.105727

Wheaton, R.M., Bauman, W.C., 1951. Properties of Strongly Basic Anion Exchange Resins. Ind. Eng. Chem. 43, 1088–1093. https://doi.org/10.1021/ie50497a027

Yoon, I.H., Meng, X., Wang, C., Kim, K.W., Bang, S., Choe, E., Lippincott, L., 2009. Perchlorate adsorption and desorption on activated carbon and anion exchange resin. J. Hazard. Mater. 164, 87–94. https://doi.org/10.1016/J.JHAZMAT.2008.07.123

Zazzo, A., Lécuyer, C., Mariotti, A., 2004. Experimentally-controlled carbon and oxygen isotope exchange between bioapatites and water under inorganic and microbially-mediated conditions. Geochim. Cosmochim. Acta 68, 1–12. https://doi.org/10.1016/S0016-7037(03)00278-3

3. Chapter 2: Eocene Shark Teeth from Peninsular Antarctica: Windows to Habitat Use and Paleoceanography

3.1 Abstract

Eocene climate cooling, driven by the falling pCO_2 and tectonic changes in the Southern Ocean, impacted marine ecosystems. Sharks in high-latitude oceans, sensitive to these changes, offer insights into both environmental shifts and biological responses, yet few paleoecological studies exist. The Middle-to-Late Eocene units on Seymour Island, Antarctica, provide a rich, diverse fossil record, including sharks. We analyzed the oxygen isotope composition of phosphate from shark tooth bioapatite ($\delta^{18}O_p$) and compared our results to co-occurring bivalves and predictions from an isotope-enabled global climate model to investigate habitat use and environmental conditions. Bulk $\delta^{18}O_p$ values (mean 22.0 ± 1.3‰) show no significant changes through the Eocene. Furthermore, the variation in bulk $\delta^{18}O_p$ values often exceeds that in simulated seasonal and regional values. Pelagic and benthic sharks exhibit similar $\delta^{18}O_p$ values across units but are offset relative to bivalve and modeled values. Some taxa suggest movements into warmer or more brackish waters (e.g., *Striatolamia*, *Carcharias*) or deeper, colder waters (e.g., *Pristiophorus*). Taxa like *Raja* and *Squalus* display no shift, tracking local conditions in Seymour Island. The lack of difference in $\delta^{18}O_p$ values between pelagic and benthic sharks in the Late Eocene could suggest a poorly stratified water column, inconsistent with a fully opened Drake Passage. Our findings demonstrate that shark tooth bioapatite tracks the preferred habitat conditions for individual taxa rather than recording environmental conditions where they are found. A lack of secular variation in $\delta^{18}O_p$ values says more about species ecology than the absence of regional or global environmental changes.

3.2 Introduction

Sharks and rays (Chondrichthyes: Elasmobranchii) have thrived in marine environments during periods of climate change throughout geological time. Their success is documented in their fossil record mostly as isolated teeth, which accumulate in ocean sediments and indirectly record their evolutionary history and the environmental conditions in which they lived (Cappetta, 2012; Condamine et al., 2019; Vennemann et al., 2001). Elasmobranchs have survived four major mass extinction events (Benton, 2014; Cappetta, 2012), with the wax and wane of clades shaped by some combination of clade competition (Condamine et al., 2019), niche adaptation (Bazzi et al., 2021), or global temperature changes (Condamine et al., 2019) based on correlation with benthic foraminifera isotope records (Zachos et al., 2008). While these studies focus on patterns of diversity and tooth morphology, exploring the environmental conditions that elasmobranchs experienced during these periods of global climate change could shed light on their ecological plasticity over geological time.

The Eocene Epoch (56 – 33.9 Ma) was characterized by major climatic shifts within the Cenozoic Era (Zachos et al., 2001, 2008) and elasmobranchs were spatially abundant spanning the Arctic to Antarctic (Cappetta, 2012; Kim et al., 2022). Geochemical proxies and climate simulations suggest that these temperature shifts were caused by some combination of a decrease in pCO_2 levels (DeConto & Pollard, 2003; Hönisch et al., 2023) and the opening of oceanic gateways (Kennett, 1977; Kennett & Exon, 2004) approaching the Eocene-Oligocene transition (EOT), setting the stage for a shift from a Greenhouse to an Icehouse world (Zachos et al., 1996, 2001). The widening of the Tasman Gateway and the Drake Passage could have enabled the formation of cold currents around Antarctica (i.e., Antarctic Circumpolar Currents, ACC) and eventually facilitated the rapid establishment of ice caps during the EOT (Egan et al., 2013; Kennett, 1977; Kennett & Exon, 2004; Scher et al., 2011; Scher & Martin, 2004, 2006; Stickley et al., 2004). While the Tasman Gateway opened to deep circulation between 35.5 and 33.3 Ma (Stickley et al., 2004), the timing of the Drake Passage deepening raises uncertainties about its impact on climate and strength of an ACC-like current. Geological and geochemical evidence suggests that the sector began opening at shallow depths ~41 Ma, continuing to widen throughout the Eocene (Eagles et al., 2006; Kim et al., 2020; Lagabrielle et al., 2009; Scher & Martin, 2006). However, many authors argue the opening to deep eastward circulation in the Drake Passage likely occurred ~32 Ma (Eagles et al., 2006; Hodel et al., 2021; Lagabrielle et al., 2009; Latimer & Filippelli, 2002; Lawver & Gahagan, 2003) — the degree to which the opening of the Drake Passage contributed to global cooling during the Eocene might be better evaluated by info on the thermal structure of the water column. Several simulations with varying complexity, resolution, and boundary conditions agree that deepening the Drake Passage reduces poleward heat transport making sea surface waters colder and saltier. However, the magnitude of this shift in density structures (both temperature and salinity changes) due to tectonic deepening varies, with some studies suggesting minimal influence (Goldner et al., 2014; Zhang et al., 2010) and others indicating a moderate impact (Nong et al., 2000; Sijp & England, 2004). Additionally, the deepening of gateways could impact regional and global climate without promoting the formation of an ACC current that thermally isolates the continent like modern-day scenarios (Sauermilch et al., 2021). To better predict the impact on climate related to the opening of the Drake Passage throughout the Eocene, more empirical observations accounting for patterns of surface and deeper waters within this sector are necessary, given that current records are sparse.

Because Eocene global climate change impacted flora and fauna, including elasmobranchs in high-latitude areas (Cione et al., 2007; Condamine et al., 2019; Egan et al., 2013; Gelfo et al., 2019; Ivany et al., 2000; Kim et al., 2020; Krug et al., 2010; Millar, 1993; Mörs et al., 2020), their fossil record is likely to offer insight into the timing of and mechanisms for cooling. Analyzing the geochemistry of elasmobranch teeth can provide valuable insights into their habitat use to assess their resilience to climate change. In addition, because some elasmobranchs are highly mobile and could conceivably have traveled well offshore into deeper water (Compagno, 2002), the difference between pelagic and benthic elasmobranchs can also provide insight into the structure of the water column and hence into the configuration of the Drake Passage during the Eocene.

The Eocene fossil record in Antarctica offers context to elucidate habitat use and environmental conditions experienced by elasmobranchs during the time leading up to glaciation. In this study, we seek to explore the interplay between elasmobranch ecology and environmental shifts from fossil shark teeth collected from the Middle to Late Eocene, in shallow marine deposits of the La Meseta Formation and estuarine-coastal deposits of the Submeseta Formation (Amenábar et al., 2020; Marenssi et al., 1998; Montes et al., 2013; Porębski, 2000; Sadler, 1988). These nearshore Eocene deposits are located in Seymour Island (James Ross Basin, Weddell Sea, West Antarctica), an area ~600 km south of the Drake Passage (Figure 1a) that experienced warmer sea surface temperatures (10-17 °C) than today (~0 °C) during the Eocene (Douglas et al., 2014; Huck et al., 2017; Ivany et al., 2008; Judd et al., 2019; Kim et al., 2020; Langton et al., 2016; Zachos et al., 2008). The stratigraphical units of these deposits capture a variably diverse chondrichthyan fossil record, comprised of isolated teeth that are the focus of extensive taxonomic identification during the last forty years (Engelbrecht et al., 2016a, 2016b, 2017a, 2017b; Kriwet, 2005; Kriwet et al., 2016; Long, 1992b; Marramá et al., 2018; Porębski, 2000; Welton & Zinsmeister, 1980). The taxonomy of fossil sharks and rays from Seymour Island suggests variations in their habitat preferences, but tooth geochemistry could provide further insights into habitat use, as well as ocean chemistry and temperature (Kim et al., 2020; Vennemann et al., 2001; Zacke et al., 2009).

The oxygen isotope composition of elasmobranch teeth ($\delta^{18}O$) preserves the environmental conditions in agreement with the lifestyles of individuals. The $\delta^{18}O$ values of elasmobranch tooth enameloid and dentin bioapatite depend on water composition ($\delta^{18}O_w$), which is controlled by global ice volume modified by local to regional salinity, and body temperature, which is assumed to approximate water temperature in ectothermic sharks and rays. Teeth incorporate oxygen starting from the initial stages of tooth mineralization, and oxygen isotope fractionation between body water and bioapatite is temperature-dependent in both phosphate and carbonate substrates (Kemp, 1985; Kohn & Cerling, 2003; Lécuyer et al., 2013; Longinelli & Nuti, 1973b, 1973a; Shemesh et al., 1983; Vennemann et al., 2002). In elasmobranch teeth, the phosphate component of the bioapatite is preferred for measuring $\delta^{18}O$ values ($\delta^{18}O_p$) due to its resistance to diagenetic alteration unlike other oxygen substrates, such as structural carbonate (Enax et al., 2012; Zazzo et al., 2004). While teeth develop, the bioapatite records snapshot seawater temperature and salinity conditions along the direction of mineralization (i.e., from the apex to the basal portion of the crown in enameloid, outer to inner portion in the dentin) (Jambura et al., 2018; Vennemann et al., 2001; Žigaite & Whitehouse, 2014). Teeth move forward in the jaw in a conveyor belt motion and become fully mineralized once they reach the functional position (Jambura et al., 2018). The time elapsed between tooth formation and shedding is species-specific and could be relatively long. For example, tooth replacement rates per row in *Negaprion brevirostris*, *Triakis semifasciata*, and *Carcharodon carcharias* are 8, 55, and 227 days, respectively (Botella et al., 2009; Bruner, 1998; Kim et al., 2012). As teeth mineralize, shark individuals experience variable environmental conditions across time and space. Chondrichthyans demonstrate diverse life history strategies, with some species living in the water column (pelagic) and others on the ocean floor near the coast out to the continental slope (benthic). Some taxa inhabit more restricted areas with less movement, while others undergo extensive seasonal migration across latitudinal or depth gradients (Compagno, 2002; Kneebone et al.,

2014; Sulikowski et al., 2010). Therefore, $\delta^{18}O_p$ values of elasmobranchs likely record preferred environmental conditions across broader or narrower areas dependent upon the combination of their lifestyles and tooth replacement rates.

Here, we characterize habitat use and environmental conditions captured in elasmobranch tooth $\delta^{18}O_p$ values and compare the oxygen isotope composition of elasmobranchs with those of co-occurring bivalves as well as predictions from isotope-enabled climate model simulations. First, we assess whether the composition of elasmobranch teeth from the Eocene deposits of Seymour Island reflects a local climatic signal. If so, we expect an increase in mean and median $\delta^{18}O_p$ values from older to younger deposits similar to $\delta^{18}O_c$ values from co-occurring bivalves (*Cucullaea* and *Retrotapes*) (Ivany et al., 2008). These bivalve taxa, as infaunal individuals inhabiting the benthos of the Seymour Island marine shelf, provide a point of comparison with elasmobranchs, which are vagile and hence capable of moving among environments. Second, we evaluate whether elasmobranch teeth capture seasonal or spatial variability in their $\delta^{18}O$ values, a hypothesis that was previously proposed for *Striatolamia macrota* (Kim et al., 2020). We use water temperature and $\delta^{18}O_w$ values from model outputs to predict $\delta^{18}O_p$ values (denoted as $\delta^{18}O_p^*$) using the isotope-enabled Community Earth System Model version 1.2 for the Early Eocene (iCESM; Zhu et al., 2020). If elasmobranch taxa remain in the region and in the same habitats year-long, the range of variation in their teeth will match seasonal $\delta^{18}O_p^*$ values for Seymour Island (i.e., local environmental signal). Alternatively, a wider range in $\delta^{18}O_p$ values than those predicted by the climatic model would indicate that elasmobranchs range widely across the suite of habitats around the Peninsula, while a narrower range in tooth bioapatite suggests instead that they track their preferred temperatures across the region as seasonal and secular temperature change unfolds. Lastly, we explore whether elasmobranchs experienced shifts in habitat use in response to changes in thermal stratification in the ocean due to tectonic changes in the Drake Passage throughout the Middle to the Late Eocene. If the deepening of the Drake Passage is involved in Eocene cooling, regional conditions would likely reflect the broader shift toward enhanced thermal stratification associated with the developing ACC (Hodel et al., 2021). We hypothesize that at least some teeth from benthic elasmobranchs would record colder water indicated by higher $\delta^{18}O_p$ values compared to pelagic relatives toward the end of the Eocene. If so, benthic elasmobranchs would also have higher $\delta^{18}O_p$ values than predicted $\delta^{18}O_p^*$ and the $\delta^{18}O$ of co-occurring bivalves and model simulations for Seymour Island (Ivany et al., 2008; Zhu et al., 2020). This shift could result from the deepening of the Drake Passage and colder conditions at depth relative to surface water (Hodel et al., 2021), which would be offshore areas inhabited by benthic sharks.

3.3 Geological Setting

The La Meseta (LMF) and Submeseta formations (SMF) crop out on Seymour Island, which is located east of the Antarctica Peninsula within the James Ross Basin at 64°17′S, 56°45′W (Figure 1) (Dutton et al., 2002; Elliot, 1988). The sedimentary succession forms the Seymour Island Group together with the Middle-Upper Paleocene Cross Valley Formation and overlays the Upper Cretaceous-Lower Paleocene Marambio Group

(Gaździcki et al., 1992; Ivany et al., 2008; Marenssi et al., 1998; Porębski, 2000). The LMF and SMF include shell beds, siltstones, and sandstones that are deposited in shallow coastal and estuarine environments. The depositional motif repeats in seven lithofacies known as Tertiary Eocene La Meseta units (TELMs, Figure 1c), which are bounded by angular unconformities and are categorized by biostratigraphy (Marenssi et al., 1998; Porębski, 2000; Sadler, 1988). The succession is further divided into six allomembers based on the relationship between lithology and facies: Valle de Las Focas (TELM 1), Acantilados I (TELM 2), Acantilados II/Campamento (TELM 3), Cucullaea I and II (TELMs 4 and 5). The Submeseta Allomember was formerly used to describe the top of the sedimentary succession included in TELM 6 and 7, but some now consider it to be a new formation (i.e., Submeseta Formation) (Marenssi et al., 1998; Montes et al., 2013). While the stratigraphic position of the Eocene TELMs is well established, the absolute age model of the units has been frequently revised and is still uncertain. Previous $^{87}Sr/^{86}Sr$ measurements on carbonate of co-occurring bivalves tentatively assigned the deposition of TELM 2 to 3 to 55-51 Ma (i.e., Ypresian age, Early Eocene) (Ivany et al., 2006, 2008). However, uncertainties in the global marine strontium-isotope seawater curve for the Early to Middle Eocene (McArthur et al., 2001), combined with the incorporation of external, local strontium sources in co-occurring bivalves (e.g., freshwater mixing), confound the geochronological positioning of TELM units at the bottom of the sedimentary succession when using this approach (Douglas et al., 2014). Despite this uncertainty, robust biostratigraphic and isotope analyses suggest deposition between the Middle and Late Eocene for the lithofacies: 1) the biostratigraphy of TELMs units (Amenábar et al., 2020; Douglas et al., 2014) match the dinoflagellate cyst zonation SPDZ 10 to 13 applied for the Southern Ocean across the Middle and Late Eocene, calibrated with magnetostratigraphy (Chron C20n to C13n) (Bijl et al., 2013); 2) $^{87}Sr/^{86}Sr$ chemostratigraphy analyses on co-occurring bivalves from SMF match the global marine strontium-isotope seawater curve (Douglas et al., 2014; Ivany et al., 2006, 2008); 3) neodymium isotope measurements ($^{143}Nd/^{144}Nd$, ε_{Nd}) from *Striatolamia macrota* teeth collected from LMF deposits reflect shifts toward more radiogenic values observed in sediments from deep-sea sites IODP 689 and 1090 during the Middle Eocene (Scher & Martin, 2006). Given this evidence, the uncertainty in the absolute age models does not significantly impact the paleoecological and environmental interpretations presented in this study.

The shark tooth specimens preserved in the Eocene deposits of Seymour Island are common in TELM 2 to 6, with TELM 4 and 5 having the highest abundance and richness of taxa while isolated teeth are rare in TELM 1 and 7 (Engelbrecht et al., 2016a, 2016b, 2017a, 2017b, 2019; Kriwet, 2005; Kriwet et al., 2016; Long, 1992b; Marramá et al., 2018). The age model for these lithofacies is summarized in Kim et al. (2020), which combines the updated biostratigraphy based on dinoflagellate cyst content (Amenábar et al., 2020) and $^{87}Sr/^{86}Sr$ chemostratigraphy analyses after Douglas et al. (2014) and Ivany et al. (2006, 2008). The lower unit of the LMF (TELM 1) is marked by the alternate occurrence of the endemic, "Transantarctic" *Enneadocysta dictyostila* and *Deflandrea antarctica*, which is calibrated to ~46 - ~45 Ma (Amenábar et al., 2020; Douglas et al., 2014). The endemic fauna found in TELM 2 and 3 (*E. dictyostila*, *Arachnodinium antarcticum*, and *Hystricosphaerodoim truswelliae*) suggests deposition between ~45 Ma and ~38 Ma (Amenábar et al., 2020; Douglas et al., 2014). In TELM 4, the palynological content is

similar to that of the lower TELM 3 unit but the unique occurrence of *Deflandrea granulata* and the presence of *Glaphyrocysta semitecta* and *Deflandrea cygniformis* at the bottom of overlying TELM 5 indicates deposition between ~41 and 39.10 Ma (Amenábar et al., 2020; Douglas et al., 2014). The upper section of the LMF (TELM 5) was deposited between ~41-~37 Ma as suggested by the occurrence of *E. dictyostila, Alterbidinium distinctum, Brigantedinium spp., Lejeunecysta spp., and Selenopemphix nephroides* (Amenábar et al., 2020; Douglas et al., 2014). The palynological content in TELM units from LMF suggests coeval deposition with the Eocene deposits from the Río Turbo, Río Baguales, and Loreto formations that outcrop in Chile (Sierra Dorotea, Río Baguales, and Río de Las Minas; Magallanes Basin); all formations preserve an elasmobranch fossil fauna similar in genus richness to that found in LFM (Amenábar et al., 2020; Estebenet et al., 2017; Kriwet et al., 2016; Otero et al., 2012, 2013; Otero & Soto-Acuña, 2015b). The Submeseta Formation includes TELM 6 and 7, where $^{87}Sr/^{86}Sr$ chemostratigraphy estimated an age of ~41 Ma or younger for the lower and immediately before the Eocene-Oligocene Transition (EOT) for the upper unit, respectively (Douglas et al., 2014; Ivany et al., 2006). To summarize, the shark assemblage found in LMF and SMF was likely formed between the Middle Lutetian (~46 Ma, Middle Eocene) and the Late Priabonian (~34 Ma, Late Eocene).

3.4 Materials and Methods

3.4.1 Material

The elasmobranch fossil material was collected as isolated teeth specimens from Eocene TELMs 2 to 7 during the 2011-2013 summer campaigns led by the collaboration of the Instituto Antàrctico Argentino (DNA-IAA) and the Swedish Polar Research Secretary (SPFS) on Seymour Island. We analyzed 201 tooth specimens from the Paleozoological Collection of the Swedish Museum of Natural History (NRM-PZ; Stockholm, Sweden). All taxa were assigned to pelagic and benthic habitats, respectively, based on modern analogs (n species = 10) determined by tooth morphology and taxonomy. Fossil taxa classified into the genera *Carcharias*, *Pristiophorus*, and *Squalus* are more closely related to their modern representatives compared to other fossil-modern analogies (Table 3.1) (Cunningham, 2000; Engelbrecht et al., 2016a, 2017a, 2017b, 2019; Kriwet et al., 2016; Long, 1992a; Marramá et al., 2018; Parmley et al., 2003). We summarize in Table 3.1 the taxa featured in this study with specimens per TELM along with the expected habitat, temperature, and depth ranges based on modern analogs. Temperature variations in modern analogs reflect a combination of spatial gradients (such as latitudinal and depth transects) and seasonal environmental variations in a single locality. This occurs because sharks and rays move to preferred environmental conditions (e.g., Compagno 1984, Sulikowsky et al., 2010, Kneebone et al., 2016). Environmental preferences were inferred based on AquaMaps, FishBase, and published literature on modern analogs (Compagno, 2002; Froese & Pauly, 2024; Kaschner et al., 2015; Kneebone et al., 2014; Sulikowski et al., 2010; Weigmann, 2016). In addition to the material analyzed here (Table 3.1), we included *Striatolamia macrota* tooth specimens collected from TELMs 2 to 5 (n = 42) analyzed in Kim et al. (2020) and Zeichner et al. (2015), a taxon displaying morphological similarities to the modern sand tiger shark

Carcharias taurus (Cunningham, 2000). We note that expected habitat preferences are based on taxonomy comparisons and may not necessarily reflect the actual temperatures or depths preferred by fossil taxa in Seymour Island across the Eocene.

3.4.2 Analytical Techniques

3.4.2.1 Stable Oxygen Isotope Analysis

We used two different protocols to precipitate silver phosphate (Ag_3PO_4) from elasmobranch tooth bioapatite based on specimen size. Larger specimens (i.e., crown height > 2 cm) where enameloid could be drilled were prepared following Mine et al. (2017) whereas smaller specimens requiring crushing were prepared following Larocca Conte et al. (2024); an account of the decision-making process and description of the silver phosphate precipitation protocols are detailed in the Appendix 3.13.1. Briefly, biological bioapatite was dissolved in hydrofluoric acid, phosphate ions isolated in solution, and silver phosphate precipitated with a silver amine solution. Silver phosphate crystals were rinsed five times with deionized water and dried overnight at 50°C. Triplicate analyses of ~0.2 mg Ag_3PO_4 per specimen were packed into silver capsules and run in a Thermal Conversion Elemental Analyzer (TC/EA)-ConFlo IV-Delta V Plus continuous flow isotope ratio mass spectrometer system (Thermo Scientific, Bremen, Germany) at the Stable Isotope Ecosystem Laboratory of (SIELO) University of California, Merced (California, USA). Silver phosphate reduction to CO gas was achieved by heating the TC/EA graphite column at 1,450 °C. Raw measurements were corrected for drift and linearity effects using the silver phosphate reference materials USGS 80 and USGS 81 (USGS; >99% purity). A 2-point calibration was applied to calibrate corrected $\delta^{18}O_p$ measurements to the Vienna Standard Mean Ocean Water scale (V-SMOW) using the same Ag_3PO_4 reference materials (USGS 80 $\delta^{18}O_p$ = 13.1‰, USGS 81 $\delta^{18}O_p$ = 35.4‰). Analytical precision within runs (n = 19) ranged from 0.1 to 0.4‰ for USGS 80 and from 0.2 to 0.4‰ for USGS 81, while the analytical uncertainty across runs is 0.3‰ for both reference materials (USGS 80 n = 237, USGS 81 n = 228). Shark and ray tooth $\delta^{18}O_p$ values are reported as mean ± 1σ.

3.4.2.2 Fourier-Transform Infrared Spectroscopy (FTIR)

In addition to isotopic composition, we tested the extent of diagenetic alteration in a selected group of shark tooth specimens (n = 14) via Fourier-Transform Infrared analysis (FTIR). Although the selected specimens do not cover all taxa studied, we chose specimens with varying degrees of preservation (e.g., whole teeth versus specimens with only crown height) and materials (enameloid only versus enameloid-dentin mixtures). This approach was intended to assess the degree of post-burial alteration and provide context for biological-environmental signals recorded in $\delta^{18}O_p$ values of elasmobranchs. We obtained spectra in the 400 – 4000 cm-1 range using a Bruker Vertex 70 Far-Infrared in ATR mode, located at the Nuclear Magnetic Resonance Facility at the University of California, Merced (California, USA). Each sample's spectra underwent smoothing by averaging 32 scans with a 4 cm^{-1} resolution each. We applied posterior baseline correction to align infrared peaks on points

where absorbance intensity is expected to be 0. We fitted and subtracted spline curves to these points to obtain a flat baseline (Trayler et al., 2023).

3.5 Data analysis

We built a framework with model simulations and empirical measurements that comprises independent sets of oxygen isotope values aiming to explain ecological and environmental signals measured from shark tooth $\delta^{18}O_p$ values. We analyzed the probability density distribution of bulk elasmobranchs' $\delta^{18}O_p$ measurements across TELMs to evaluate shifts in their central tendency across time. Statistical significance between TELMs was evaluated with a Kruskal-Wallis test and post-hoc Dunn test analysis for pairwise comparisons between different stratigraphic units.

We explored possible seasonal and spatial signals embedded in elasmobranchs' $\delta^{18}O_p$ values by comparing measurements with predictions from a global climate model. We used the Early Eocene isotope-enabled iCESM 1.2 simulations outputs of temperature and $\delta^{18}O_w$ composition (Brady et al., 2019; Zhu et al., 2019, 2020) to predict $\delta^{18}O_p^*$ values. The model is calibrated with paleogeographic boundary conditions for the Early Eocene (Herold et al., 2014), which includes the Drake Passage and the Tasman Gateway open to shallow, epicontinental circulation in the Southern Ocean (i.e., bathymetry set to <100 m and 30 m b.s.l., respectively). This early Eocene paleogeography is used for all simulations, so while it reflects the general conditions of the time, it may not perfectly align with the specific paleogeographic features of the Middle to Late Eocene study interval. However, the model includes simulations with different climate states, allowing us to test environmental settings across the Eocene Epoch. We used offline outputs of temperature and $\delta^{18}O_w$ values using simulations equilibrated at 3× and 6× pre-industrial CO_2 levels (i.e., 284.7 ppmv) within a water column of 25 m. We averaged the last 100-year simulations per climatic state. To define which climatic state would best represent seasonal environmental trends in Seymour Island, we compared monthly averaged model outputs with serial $\delta^{18}O_c$ values from the co-occurring bivalves *Cucullaea* and *Retrotapes* (Buick & Ivany, 2004; Ivany et al., 2008; Judd et al., 2019). Serial $\delta^{18}O_c$ measurements within single bivalve specimens (n = 8) provide high-resolution seasonal trends in Seymour Island; these previously published bivalve data were only available for TELM 5. Model $\delta^{18}O_c$ estimates ($\delta^{18}O_c^*$) were computed using the Grossman and Ku (1986) paleothermometer equation for aragonitic shells, solving equation [1] for $\delta^{18}O_c$:

$$T\,(°C) = 20.6 - 4.34 * (\delta^{18}O_{c\,V-PDB} - \delta^{18}O_{w\,V-SMOW}) \quad [1]$$

where T is the temperature, $\delta^{18}O_c$ (in V-PDB), and $\delta^{18}O_w$ are carbonate (i.e., aragonite) and water oxygen isotope compositions.

Following, we explored the habitat use of elasmobranch taxa and estimated their temperature preferences to inform whether $\delta^{18}O_p$ values from each taxon would reflect local or regional environmental signals. We compared density distributions for $\delta^{18}O_p$ values from pelagic and benthic taxa with predicted seasonal and regional $\delta^{18}O_p^*$ values from the iCESM

simulation and co-occurring bivalves' bulk $\delta^{18}O_c$ values (Ivany et al., 2008; Zhu et al., 2020). We used the recalibrated paleothermometer equation of Kolodny et al. (1983) in Lécuyer et al. (2013) to compute forward $\delta^{18}O_p$* predictions and solved for $\delta^{18}O_p$:

$$T\ (°C) = 117.4(\pm 9.5) - 4.50(\pm 0.43) * (\delta^{18}O_{p\ V-SMOW} - \delta^{18}O_{w\ V-SMOW}) \quad [2]$$

Where T is the estimated temperature in Celsius degrees given the fractionation between phosphate ($\delta^{18}O_p$) and modeled water oxygen isotope composition ($\delta^{18}O_w$; Zhu et al., 2020). We preferred to use this equation over others found in literature (Kolodny et al., 1983; Longinelli & Nuti, 1973b; Pucéat et al., 2010) because: 1) it performs comparably to other paleothermometer equations (Figure A3.5), except for the Pucéat et al. (2010) equation, which generates estimates higher by a few per mil compared to other oxygen isotope fractionation equations (Figure A3.5). These differences likely arose from experimental errors, as the Pucéat et al. equation was derived from controlled experiments on fish in aquaria, where the isotopic composition of the water was not constant, leading to error in the determination of the oxygen-isotope fractionation equation (Lécuyer et al., 2013; Pucéat et al., 2010); 2) it provides temperature values from fish tooth specimens consistent with estimates of co-existing bivalves or brachiopod carbonate shells (Lécuyer et al., 2013). Estimated $\delta^{18}O_p$* values from co-occurring bivalves were obtained after applying the following transfer functions [3] and [4] (Ivany et al., 2008; Kim et al., 2015; Longinelli & Nuti, 1973b; Zhu et al., 2020):

$$\delta^{18}O_{c\ V-SMOW} = 30.92 + 1.03092 * \delta^{18}O_{c\ V-PDB} \quad [3]$$

$$\delta^{18}O_{p\ V-SMOW} = \frac{\delta^{18}O_{c\ V-SMOW} - 8.67\ (\pm 1.24)}{1.02\ (\pm 0.06)} \quad [4]$$

These equations involve first the conversion of $\delta^{18}O_c$ values from V-PDB to V-SMOW scale (equation 3; Kim et al., 2015) and subsequent transformation into $\delta^{18}O_p$* values using equation [4] ($R^2 = 0.93$) after the oxygen isotope measurements for both carbonate and phosphate components in invertebrates (n = 27; Figure A3.7; Longinelli and Nuti, 1973b). These estimates from bivalves' bulk $\delta^{18}O_c$ measurements were compared with $\delta^{18}O_p$ values of sharks and rays as a supplementary marker for local conditions in Seymour Island along with predictions from the iCESM model, which are in good agreement with seasonal simulated values for Seymour Island (see Section 3.7.2**,** Table A3.2, and Table A3.4).

We determined temperature represented by pelagic and benthic taxa using a Bayesian approach similar to that of Griffith et al. (2023; full description is found in the Appendix 3.12.3). This framework attempts to estimate probable environmental temperature using model outputs as prior information (i.e., simulated temperature and $\delta^{18}O_w$, discussed above), assuming that sharks and rays do not necessarily inhabit unique environments (Table 3.1). We integrated equation [2] in the Bayesian model to estimate temperature from elasmobranchs' $\delta^{18}O_p$ values.

Finally, we compared the central tendency observed from $\delta^{18}O_p$ values in pelagic and benthic elasmobranchs to explore shifts in habitat use between groups. This shift could result from deepening of the Drake Passage and stronger thermal stratifications between surface and deeper waters, which are habitats that pelagic and benthic elasmobranchs would inhabit, respectively. We used the Kruskal-Wallis test to quantify statistical differences between groups per TELM unit.

All datasets were analyzed in R Studio (R Development Core Team, 2024). Model outputs are extracted using XArray, MatplotLib, and Cartopy libraries in Python before their analysis (Hoyer & Joseph, 2017; Hunter, 2007; Met Office, 2015).

3.6 Results

3.6.1 Elasmobranch Bioapatite $\delta^{18}O_p$ Values

Phosphate oxygen isotope values measured from elasmobranch teeth have a mean value of 22.0 ± 1.3‰ (n = 243). Bulk $\delta^{18}O_p$ distributions exhibit skewed shapes and a similar broad variability across TELMs (Figure 3.2, Table 3.2). Mean $\delta^{18}O_p$ varies from 22.0 ± 1.5‰ in TELM 2 (n = 28; Middle Eocene) to 21.4 ± 1.8‰ in TELM 7 (n = 10; Late Eocene) (Table 3.2). Generally, the median $\delta^{18}O_p$ value is a few per mil higher than the mean values across TELMs, but the distributions are similar across units (Table 3.2). A Kruskal-Wallis test indicates no statistically significant differences in the distributions between TELMs ($H = 6.81$, $df = 5$, $p = 0.07$). Post-hoc Dunn Test suggests that $\delta^{18}O_p$ values across TELMs remain relatively stable ($p < 0.05$), with TELM 5 and 6 being the only units showing statistical dissimilarity ($p > 0.05$; Table 3.3). Although the mean $\delta^{18}O_p$ value notably increases from 21.9 ± 1.2‰ to 22.5 ± 0.6‰ across these units, TELM 5 and 6 do not exhibit statistical differences with any other TELM (Table 3.3), and this statistical result may be due to sample size. In summary, bulk $\delta^{18}O_p$ values of shark and ray teeth cannot establish significant changes throughout TELMs.

3.6.2 iCESM Model Validation for Seasonal Trends in Seymour Island: 3× vs 6× Pre-Industrial CO_2 Level Simulations

Seasonal variation in Early Eocene environmental conditions at Seymour Island is represented by monthly averaged $\delta^{18}O_c^*$ values estimated from the iCESM simulations within a 25 m sea-surface column (Zhu et al., 2020) (Table A3.2). Model $\delta^{18}O_c^*$ ranges vary based on pCO_2 conditions: for 3× pre-industrial levels, $\delta^{18}O_c^*$are -1.5 to 0.8‰ and for 6× pre-industrial levels, $\delta^{18}O_c^*$ are -3.5 to -0.7‰ (Figure 3.3), corresponding to the austral summer and winter temperature peaks in March and September-October (Table A3.3). When simulated values are compared to serial $\delta^{18}O_c$ values of the bivalves *Cucullaea* and *Retrotapes* (Judd et al., 2019), $\delta^{18}O_c^*$ values for the 6× CO_2 case are too low (Figure 3.3). Although $\delta^{18}O_c$ measurements in *Cucullaea* and *Retrotapes* specimens sometimes exceed simulated values by up to 1.1‰ (*Retrotapes* specimen 01-77-E1; Figure 3.3), these instances of proxy-model mismatch are few. Overall, simulated $\delta^{18}O_c^*$ values for the 3× CO_2 case have

a better correspondence with seasonal environmental conditions for Seymour Island during the Eocene, aligning well with empirical data measured from mollusks. Furthermore, simulated environmental conditions under such CO_2 boundary levels well agree with current pCO_2 estimates from benthic foraminifera and biomarkers for the Middle-Late Eocene (i.e., ~800 p.p.m.; Anagnostou et al., 2016; Pearson et al., 2009; Zachos et al., 2008).

3.6.3 Comparisons with Seasonal Trends from iCESM Model at Seymour Island

In contrast to bivalves, the bulk $\delta^{18}O_p$ values from elasmobranchs exhibit greater variability than expected considering predicted seasonal $\delta^{18}O_p^*$ values from the Zhu et al. (2020) iCESM simulations (Figure 3.4, Table 3.2, Table A3.5). Model $\delta^{18}O_p^*$ values predict the seasonal variation at Seymour to range from 20.0 to 22.3‰ for the 3× pre-industrial CO_2 case and 19.0 to 21.2‰ for the 6× case during the Eocene (Figure 3.4, Table A3.5). Between the two scenarios, the 3× pre-industrial CO_2 level simulation captures variability closer to that observed in elasmobranchs, but the variation in empirical $\delta^{18}O_p$ values exceeds the seasonal range derived from the model predictions (Figure 3.4). The largest discrepancy between mean $\delta^{18}O_p$ values across TELMs and model predictions is during TELM 2 and 6 (Figure 3.4, Table 3.1) where a large number of observations are greater than 22.1‰ (Figure 3.4, Table 3.2, Table A3.5). In addition, several outliers are observed across TELMs, often with values between 16.6 to18.7‰, showing a *z* score lower than -2 (Figure 3.4; Table A3.6). FTIR spectra suggest that these outliers are not a result of diagenetic alteration (Appendix 3.13.2).

3.6.4 Spatial $\delta^{18}O_p^*$ Estimates from Model Simulations

We use sea surface temperature and $\delta^{18}O_w$ values from iCESM output (Zhu et al. 2020) to estimate $\delta^{18}O_p^*$ values in the region between the South America and Antarctic continents (Figure 3.5). Spatial $\delta^{18}O_p^*$ distribution for the 6× pre-industrial CO_2 levels exhibit $\delta^{18}O_p^*$ mean ± 2σ values of 18.0 and 20.4‰, which are too low compared to values in elasmobranch teeth and are observed only as outliers (Figure 3.5). In contrast, model $\delta^{18}O_p^*$ distribution for the 3× pre-industrial CO_2 levels captures the variation from empirical measurements of elasmobranch bioapatite $\delta^{18}O_p$ values with mean ± 2σ values of 19.2‰ and 22.1‰ across the latitudinal gradient in both Pacific and Atlantic sectors (Figure 3.5). However, $\delta^{18}O_p$ values from elasmobranch bioapatite exhibit larger variations, with values being up to ~2.0‰ higher than those predicted from model simulation for the 3× CO_2 case (Figure 3.4, Table 3.2). This suggests that the simulated spatial $\delta^{18}O_p^*$ distribution within shallow waters cannot fully explain the variation observed in elasmobranch bioapatite.

3.6.5 Environmental Conditions Experienced by Pelagic and Benthic Sharks across TELMs

Our dataset comprises elasmobranch tooth specimens from pelagic (n = 149; $\delta^{18}O_p$ = 22.0 ± 1.4‰) and benthic (n = 94, $\delta^{18}O_p$ = 22.1 ± 1.1‰) taxa with $\delta^{18}O_p$ values similar between groups (Figure 3.6, Table 3.4). Mean $\delta^{18}O_p$ values from pelagic specimens dropped from 22.0 ± 1.5‰ in TELM 2 to a minimum of 21.6 ± 1.6‰ in TELM 5, then increased to a

maximum of 22.2 ± 0.9‰ in TELM 6 (Figure 3.3a, Table 3.4). Benthic taxa follow a similar trend with slightly higher $\delta^{18}O_p$ values compared to their pelagic relatives (Figure 3.6, Table 3.4), although this distinction is not statistically significant based on a Kruskal-Wallis test (Table 3.4).

3.7 Discussion

3.7.1 No Trend in Elasmobranch Bioapatite $\delta^{18}O_p$ Variation Across the Eocene

The observed mean and median in bulk $\delta^{18}O_p$ values of elasmobranch teeth from the Middle and Late Eocene deposits of LMF and SMF do not show significant shifts over time (Figure 3.2, Table 3.2, and Table 3.3), which at face value suggests no directional environmental change through the Eocene in this setting. These results are unexpected given evidence for global paleoceanographic and paleoclimatic trends as well as marked changes in the compositions of marine bivalves in the section (Ivany et al., 2008). One possible explanation for this trend across TELM units could be a time-averaging effect within individual teeth, reflecting environmental signals over the period during which the teeth form. The temporal resolution available at LMF and SMF are over millions of years per TELM while the $\delta^{18}O_p$ values of elasmobranchs indicate snapshots of environmental conditions during mineralization. If, for example, teeth are consistently produced in one season over another, the lack of a trend over time could mean that $\delta^{18}O_p$ values of elasmobranch bioapatite do not record the full range of environmental conditions experienced in LMF and SMF waters. However, this mismatch in temporal resolution is not an issue for co-occurring bivalves. Bulk $\delta^{18}O_c$ values from *Cucullaea* and *Retrotapes* exhibit a shift toward higher values across TELMs (*Cucullaea* mean $\delta^{18}O_c$ values shift from 0.02 ± 0.34‰ in TELM 2 to 1.04 ± 0.43‰ in TELM 7; *Retrotapes* mean $\delta^{18}O_c$ values shift from 0.72 ± 0.18‰ in TELM 2 to 0.90 ± 0.32‰ in TELM 7) (Ivany et al., 2008) (Figure A3.6 and Table A3.3). These two bivalve species record environmental conditions in their carbonate oxygen isotopes with alternate growing seasons consistent with the seasonal variability captured by the forward iCESM simulation at 3× pre-industrial CO_2 levels, with *Cucullaea* usually biased toward the colder, winter temperatures (i.e. ^{18}O-enriched values) than *Retrotapes* (Ivany et al., 2008; Judd et al., 2019) (Figure 3.3, Figure A3.6 and Table A3.3). Despite this slight seasonal bias, $\delta^{18}O_c$ values are higher toward the top of the sedimentary succession, especially in TELM 7 where $\delta^{18}O_c$ values of both taxa exceed the seasonal $\delta^{18}O_c^*$ range for Seymour Island as predicted by the iCESM simulation (Figure A3.6 and Table A3.3). The discrepancy between modeled and bivalves $\delta^{18}O_c$ values in TELM 7 could arise from the iCESM simulation's boundary conditions being scaled for the Early Eocene (Zhu et al., 2020), resulting in less correspondence between later TELM predictions and empirical results. Overall, bulk $\delta^{18}O_c$ values of bivalves increase toward the Late Eocene, consistent with global marine records of deep-sea foraminifera $\delta^{18}O$ values that reflect a combination of cooling temperatures and higher $\delta^{18}O_w$ values, the latter of which is influenced globally by changes in continental ice volume and other regional factors (Zachos et al., 2001). While isotopic composition in elasmobranch bioapatite tracks averaged

environmental signals as teeth mineralize (Vennemann et al., 2001), time-averaging effects cannot explain the lack of trends across TELM units in $\delta^{18}O_p$ values of elasmobranchs.

Similarly, time-averaging effects that occurred during the deposition of TELMs cannot explain the environmental stasis observed in elasmobranch' $\delta^{18}O_p$ values across time. Some sediment reworking effects were hypothesized in TELM 4 given that a significant number of co-occurring bivalve shells have a carbon and oxygen isotopic composition similar to those recovered from TELM 3 (Ivany et al., 2008; Figure A3.6). However, multiple pieces of evidence exclude strong sediment reworking effects: 1) palynological analysis of TELMs reveals distinct assemblages (Aménabar et al., 2020): 2) empirical and simulated seasonally resolved precipitation trends in Seymour Island indicate little difference in precipitation regimes between winter and summer seasons (Judd et al., 2019).

Nor is diagenesis likely to offer an explanation: TELM deposits were not buried below 1 Km and did not experience temperatures higher than 80°C (Marenssi et al., 2002); and diagenetic recrystallization of co-occurring bivalves *Cucullaea* and *Retrotapes* has been extensively studied in the past. Shells usually display primary shell microtextures, an aragonite mineralogy, and comparable trace element concentrations to modern bivalves (Dutton et al., 2002; Buick and Ivany, 2004; Ivany et al., 2008; Douglas et al., 2014; Judd et al., 2019). Moreover, FTIR analysis suggests that diagenetic alteration in elasmobranch bioapatite materials is minimal (Sections 3.2.1 and 3.2.2; Appendix 3.13.2).

Other possible explanations for the lack of observed environmental trends across TELMs could derive from analytical uncertainty. The variability in elasmobranch bioapatite $\delta^{18}O_p$ values is larger compared to forward simulations, with 1σ ranging from 0.6 to 1.8‰ within TELMs when considering bulk measurements (Figure 3.2, Table 3.2). However, analytical uncertainty as 1σ is low (≤ 0.4‰) when monitoring reference materials. Therefore, variability in $\delta^{18}O_p$ values of elasmobranch bioapatite reflects a real signal of habitat heterogeneity captured during sharks' and rays' lifetimes due to some combination of environments experienced in the Seymour Island setting and other places to which the animals may have traveled.

3.7.2 Discerning Migration and Sedentary Habits From $\delta^{18}O_p$ Values of Pelagic and Benthic Elasmobranch Species.

The lack of observed environmental trends across TELMs from elasmobranch bioapatite $\delta^{18}O_p$ values could derive from seasonal and ontogenetic movement patterns. Environmental conditions such as temperature and salinity combined with prey availability are primary drivers that influence movements of elasmobranchs. Some elasmobranchs undergo extensive latitudinal and vertical movements to track their preferred temperatures, salinity, and biological conditions across horizontal or vertical isoclines, while others display more sedentary habits (Compagno, 2002; Kneebone et al., 2012; Schlaff et al., 2014). The distribution of $\delta^{18}O_p$ values from elasmobranch teeth partially aligns with seasonal, local trends at Seymour Island but also suggests a spatial extension based on $\delta^{18}O_p^*$ values from the forward 3× CO_2 iCESM simulation (Figures 3.4 and 3.5). Given the combination of variable lifestyles and the time elapsed between tooth mineralization and shedding in different shark and ray species, the $\delta^{18}O_p$ variability of elasmobranch bioapatite collected

from LMF and SMF likely record seasonal signals at Seymour Island and the surrounding region.

We developed a framework to hypothesize habitat use among the most abundant pelagic and benthic taxa in our dataset across TELMs (i.e., taxa with $n \geq 4$, see also Table 3.1). We compared $\delta^{18}O_p$ distribution from elasmobranch bioapatite with co-occurring bivalves after applying transfer functions [3] and [4] (Table A3.4; Ivany et al., 2008; Kim et al., 2015; Longinelli & Nuti, 1973b) and predicted $\delta^{18}O_p^*$ values based on iCESM simulations for 3× pre-industrial CO_2 level scenario using equation [2] (Lécuyer et al., 2013). We extracted seasonal $\delta^{18}O_p^*$ range for Seymour Island and southern Chile (Appendix 3.13.6), an area within migration range of elasmobranchs that includes coeval fossil assemblages from the Río Turbo and Loreto Formations (Magallanes Basin) with a similar diversity of elasmobranch taxa to Seymour Island (Otero & Soto-Acuña, 2015a). Species that exhibit distributions in agreement with the predicted values for Seymour Island and co-occurring bivalves indicate local, seasonal conditions resulting from a relatively sedentary habit without long-range migration (Figure 3.7a). Elasmobranch taxa that exhibit a broader variation in $\delta^{18}O_p$ values or shifts in their median value compared to $\delta^{18}O_p^*$ values of bivalves and those predicted from the model simulation in Seymour Island are likely capturing environmental conditions over a broader region, including warmer, low latitudes or deeper, colder depths, or brackish environments with low $\delta^{18}O_w$ values (Figure 3.7a). We estimated preferred temperatures of elasmobranch taxa using a Bayesian approach that considers model temperature and $\delta^{18}O_w$ outputs for the 3× CO_2 between Antarctica and South America case as priors (Griffiths et al., 2023, Zhu et al., 2020; full description in Appendix 3.13.2). Temperature values (T(°C)) are reported as mean ± 95% confidence interval (CI; Figure 3.8, Table A3.8).

Pelagic and benthic species on the whole have similar mean $\delta^{18}O_p$ values, but their $\delta^{18}O_p$ distributions indicate differences in preferred environments across TELMs (Figure 3.7b). Compared to predicted $\delta^{18}O_p^*$ values, the distribution of $\delta^{18}O_p$ values of pelagic taxa indicates movement toward warmer, lower-latitude settings like southern Chile or to brackish environments (Figure 3.7b; Table A3.4, Table A3.5, and Table A3.6). For example, the sand tiger sharks *Brachycarcharias lerichei*, *Carcharias* sp. cf. *C. hopei*, and *Striatolamia* (including *S. macrota* and *Striatolamia* sp. cf. *S. macrota*) exhibit a broad variation in $\delta^{18}O_p$ values, overlapping with transposed $\delta^{18}O_p$ values of bivalves and $\delta^{18}O_p^*$ predictions from model outputs for Seymour Island in some TELMs (i.e., TELM 2 and TELM 3 for *B. lerichei* and *Carcharias* sp., TELM 2 to 4 for *S. macrota*, and TELM 7 for *Striatolamia* sp. cf. *S. macrota*; Figure 3.7b, Table A3.4, Table A3.5, and Table A3.7). Among the sand tiger sharks, *Striatolamia* has lower mean and median values compared to other pelagic taxa, suggesting a preference for shallower and/or warmer waters compared to *B. lerichei* and *Carcharias* sp. (Figure 3.7b; Table A3.4, Table A3.5, and Table A3.7). Temperature estimates (i.e., T(°C) ± CI) agree with this interpretation, showing that *S. macrota* preferred temperatures of 14.2 ± 7.4°C in contrast with *B. lerichei* and *Carcharias* sp., which preferred temperatures of 11.7 ± 7.4°C and 10.2 ± 6.4°C (Figure 3.8, Table A3.8). Finally, *B. lerichei* and *Carcharias* sp. from TELM 4 and 5 have several more ^{18}O-depleted outliers, lower than any predicted $\delta^{18}O_p^*$ values (Figure 3.4, Figure 3.7b, Figure 3.8, Table A3.6). These outliers could indicate movements toward the inner part of the estuary in

Seymour Island (Marenssi et al., 2002; Porębski, 2000), a brackish environment with meteoric input influence, resulting in lower $\delta^{18}O_w$ and $\delta^{18}O_p$ values at the time of tooth formation.

Extant sand tiger sharks migrate seasonally to maintain suitable temperature and salinity conditions (Kneebone et al., 2014), indicating that their ability to track isoclines in space and time could be a conservative trait in their lineages. For example, $\delta^{18}O_p$ values of the fossil sand tiger sharks suggest that they tracked preferred temperatures across latitudes similar to their modern analog *C. taurus* (Kim et al., 2014, 2020), indicating that this trait is conservative in their lineages. In addition, movements to estuarine environments could be another conservative trait among sand tiger sharks. Prolonged residency in such habitat, especially in juvenile individuals, is documented for both modern *C. taurus* (e.g., in Plymouth, Kingston, Duxbury Bay, USA) and fossil *S. macrota* and *Carcharias* cf. *cuspidatus* specimens from the Arctic (e.g., Eureka Sound, Canada) and the Alps (e.g., Swiss Molasse Basin, Switzerland) (Kim et al., 2014, 2020; Kneebone et al., 2012; Kocsis et al., 2007).

Among the pelagic taxa, *Otodus auriculatus* has a $\delta^{18}O_p$ distribution that does not overlap with bivalves or simulated $\delta^{18}O_p^*$ (Figure 3.7b, Table A3.7). This taxon exhibits a 2‰ shift in median $\delta^{18}O_p$ values from that of bivalves' equivalent $\delta^{18}O_p$ (*O. auriculatus* median $\delta^{18}O_p = 20.5$‰, TELM 4 Bivalve median $\delta^{18}O_p^* = 22.2$‰), with values falling in between predicted seasonal $\delta^{18}O_p^*$ range for Seymour Island and Chile (Figure 3.7b, Table A3.4, Table A3.5, and Table A3.7). Interestingly, *O. auriculatus* is the taxon with the narrowest variation in $\delta^{18}O_p$ values, which are also the lowest compared to other elasmobranch species (Figure 3.7b, Table A3.7). This results in warmer temperature preferences of 18.7 ± 7.3°C compared to other fossil shark taxa, which aligns with the preferred range of the modern *C. carcharias* (Figure 3.8, Table 3.1, and Table A3.8; Bradford et al., 2020, Froese & Pauly, 2024). We assumed an ectotherm physiology for all elasmobranchs in this study with the assumption that $\delta^{18}O_p$ values tracked temperature and $\delta^{18}O_w$ isoclines. However, the relatively low and consistent $\delta^{18}O_p$ values could indicate the ability of *O. auriculatus* to maintain a constant body temperature warmer than the surrounding water. Endothermy is common in lamniform sharks, including extant species (e.g., *C. carcharias*) and recent isotope results from the *Otodus* lineage (Griffiths et al., 2023; Watanabe et al., 2019), which could indicate an evolutionary history of endothermy within this lineage. With endothermy, $\delta^{18}O_p$ values would reflect consistent elevated temperatures with variation primarily due to $\delta^{18}O_w$ gradients with salinity, depth, or latitude. Combined $\delta^{18}O_p$ and clumped isotope measurements (i.e., Δ_{47}) on the same tooth specimens could support this hypothesis.

Benthic taxa in our dataset display species-specific variability in habitat use (Figure 3.7b, Table A3.7). The $\delta^{18}O_p$ distributions of *Raja amphitrita*, *Squalus weltoni*, and *Squalus woodburnei* are in agreement with $\delta^{18}O_p^*$ of co-occurring bivalves and $\delta^{18}O_p^*$ range of Seymour Island from the iCESM model (Figure 3.7b; Table A3.4, Table A3.5, and Table A3.7). Temperature estimates for these taxa are 11.7 ± 6.6 °C, 13.3 ± 6.8°C, and 10.9 ± 7.1°C for *R. amphitrita*, *S. weltoni*, and *S. woodburnei*, respectively (Figure 3.8, Table A3.8), which suggest that these species inhabited coastal shelf habitats emblematic of the La

Meseta Formation, and their bioapatite tracks local, seasonal environmental conditions. A comparatively sedentary habit for these species is in contrast to the active lifestyles of their modern analogs *Bathyraja griseocauda* and *S. acanthias*, which frequently move between coastal areas and the seafloor of the continental slope (Arkhipkin et al., 2012; Casselberry & Carlson, 2015; Engelbrecht et al., 2017a, 2019; Sulikowski et al., 2010). In contrast, the saw shark *Pristiophorus laevis* has median $\delta^{18}O_p$ values consistently higher than co-occurring bivalves and predicted $\delta^{18}O_p^*$ values (Figure 3.7b; Table A3.4, Table A3.5, and Table A3.7), suggesting a preference for colder and deeper environments (T(°C) ± CI = 9.1 ± 6.9°C; Figure 3.8, Table A3.8). This behavior is common in the modern *P. cirratus*, a taxon occurring on the continental shelf at depths between 40 and 630 m b.s.l. (Froese & Pauly, 2024; Raoult et al., 2020). Finally, $\delta^{18}O_p$ values of *Squatina* sp. and *Kallodentis rhytistemma* in TELM 5 exhibit a bimodal distribution, with modes overlapping with predicted $\delta^{18}O_p^*$ values of co-occurring bivalves and with those estimated for southern Chile and Seymour Island from the iCESM model (Figure 3.7b). The sample size for *Squatina* sp. in TELM 6 is too small for reliable inferences but the $\delta^{18}O_p$ values of *Squatina* sp. and *K. rhytistemma* from TELM 5 indicate that these taxa were active species inhabiting shallow, warm waters with estimated temperature preferences of 14.3 ± 7.8°C and 16.8 ± 8.2°C, respectively (Figure 3.8, Table A3.8). These findings contrast with habitat preferences of their modern analogs *S. squatina* for *Squatina* sp. and *Triakis semifasciata* for *K. rhytistemma*, which themselves differ from one another: *Triakis semifasciata* is an active bottom-dweller in estuarine environments with seasonal movement patterns, while *S. squatina* is a sedentary taxon inhabiting coastal settings (Carlisle & Starr, 2009; Meyers et al., 2017; Nosal et al., 2014). Instead, *K. rhytistemma* and *Squatina* sp. likely had habitat preferences similar to their co-occurring pelagic taxa, favoring shallow, warmer waters and exhibiting seasonal migration to lower latitudes (Figures 3.7b and 3.8; Table A3.7, and Table A3.8).

In summary, the inferred habitat use strategies suggest that $\delta^{18}O_p$ values of different elasmobranch taxa can reflect local environmental signals at Seymour Island or regional signals along spatial gradients. Of note, transposed $\delta^{18}O_p$ values of bivalves and empirical $\delta^{18}O_p$ measurements from *Striatolamia* sp. cf. *S. macrota* teeth poorly overlap with seasonal simulated values for Seymour Island. Again, the mismatch is likely driven by boundary conditions unsuitable for capturing seawater temperature and $\delta^{18}O_w$ values for the Late Eocene. Although we cannot precisely determine the paths of migratory elasmobranchs, isotope-enabled climate simulations provide predictions to track environmental conditions.

3.7.3 Do $\delta^{18}O_p$ Values of Elasmobranchs Support Regional or Global Environmental Changes?

We explored evidence for stronger thermal stratification between warm shallow and cold deep waters by comparing $\delta^{18}O_p$ values of pelagic and benthic elasmobranchs within and between TELMs (Figure 3.6, Table 3.4). This approach is analogous to the Mg/Ca ratios observed in planktic and benthic foraminifera from Eocene-Oligocene deposits at Maud Rise (Southern Atlantic Ocean, ODP 689b), where benthic foraminifera encountered colder conditions as the Drake Passage deepened (Hodel et al., 2021). We expected that benthic elasmobranchs would have higher mean $\delta^{18}O_p$ values than their pelagic relatives in the younger TELMs, suggesting movements off the shelf to deeper, colder environments if the

Drake Passage had deepened (Arkhipkin et al., 2012; Casselberry & Carlson, 2015; Engelbrecht et al., 2017a; Hodel et al., 2021; Lagabrielle et al., 2009; Marenssi et al., 2002; Montes et al., 2013; Sulikowski et al., 2010). Contrary to our expectations, we found no statistically significant difference between the two groups (Table 3.4); pelagic and benthic taxa from Seymour Island indicate the presence of a similar suite of environmental conditions across all TELMs (Figure 3.5, Figure 3.7b, Table 3.4, Table A3.7). This result suggests either that sharks never migrated off the shelf to experience any cooling of deep waters, or that there was only weak thermal stratification and thus no deepening in the Drake Passage area during sedimentation of LMF and SMF.

One possibility is that $\delta^{18}O_p$ values of pelagic and benthic elasmobranchs reflect differences not only in temperature but also in salinity. While $\delta^{18}O_p$ values for the two groups are indistinguishable, it is conceivable that each group experienced a different combination of temperature and salinity such that a decrease in salinity effectively canceled out the $\delta^{18}O_p$ signal of any temperature decrease over time. Mineralogical and geochemical evidence in the Atlantic sector of the Southern Ocean shows a discrete amount of continental input in the seawater as ice caps expanded and melted, which were redistributed by the westward Antarctic Coastal Current along the Weddell Sea and Antarctic Peninsula (Carter et al., 2017; Scher et al., 2011, 2014). The coast along the Weddell Sea would be influenced by these cold freshening events, which would affect the $\delta^{18}O_p$ values in elasmobranchs. However, it is unlikely elasmobranchs would track regional changes in salinity so closely. First, this regional freshening is constrained to nearshore, coastal waters and primarily affects the isotopic composition of elasmobranchs inhabiting shallow waters in Seymour Island — mostly pelagic and some benthic taxa. If major regional salinity shifts had occurred, we would expect lower mean and median $\delta^{18}O_p$ values in taxa living close to the surface and nearshore in younger TELMs compared to simulated values and co-occurring bivalves, or between the same elasmobranch taxa relative to older TELMs, which is not the case. Local recorders like *R. amphitrita*, *S. weltoni*, and *S. woodburnei* track salinity gradients in good agreement with mollusks and simulated $\delta^{18}O_p^*$ values, and pelagic taxa like the sand tiger sharks have just a handful of low $\delta^{18}O_p$ values (Figure 3.4, Figure 3.7b, Appendix 3.13.7). The latter result indicates that sand tiger sharks could live in or move to brackish waters during the early stages of ontogenetic developments (Kim et al., 2022) rather than reflecting regional salinity changes. Today, adult sand tiger sharks move seasonally (Kneebone et al., 2014); in the Eocene, these taxa could potentially move to areas where such regional shifts in salinity would not occur (e.g., southern Chile; Figure 3.7b). Lastly, seasonal freshening due to ice melting minimally lowers seawater salinity by approximately 0.2 PSU in waters above the pycnocline in today's Weddell Sea (Graham et al., 2012), leading to shifts in $\delta^{18}O_w$ values that are ~0.05‰ lower than expected (calculated using the Southern Ocean $\delta^{18}O_w$ - salinity relationship from LeGrande & Schmidt, 2006, $\delta^{18}O_w = 0.24*\text{salinity (PSU)} - 8.45$). Therefore, it is unlikely that $\delta^{18}O_p$ values of elasmobranchs track these minor salinity changes in seawater.

Another plausible reason for the lack of change between pelagic and benthic taxa mean and median $\delta^{18}O_p$ across TELMs is that elasmobranchs track their preferred temperature and salinity gradients, which shape species-specific niche spaces. This hypothesis better explains why $\delta^{18}O_p$ values of elasmobranchs provide a broad, regional (or

more localized if they move in brackish waters) environmental perspective instead of the environmental and oceanographic changes documented in global records. This tracking behavior may also explain the decline in diversity toward the Late Eocene (Figures 3.7b and 3.7c), where global changes exerted selective pressure on elasmobranchs, favoring species adapted to colder conditions. Global cooling and oceanographic changes throughout the Eocene could result in increased productivity and intensification of wind-driven upwelling of cold waters in the Weddell Sea (Amenábar et al., 2020; Borrelli et al., 2021; Ladant et al., 2018; Scher & Martin, 2006). These environmental and oceanographic shifts could cause physiological challenges for many elasmobranch taxa, as well as for their prey (Lubitz et al., 2024; Vilmar & Di Santo, 2022). Indeed, such changes likely impacted sharks on Seymour Island, leading to a decline in chondrichthyan diversity from TELM 5 onward (Figure 3.7c). Among the species we analyzed, only *Carcharias* sp., *P. laevis*, and *Squatina* sp., along with a few other taxa not analyzed here, persisted after TELM 5 (Engelbrecht et al., 2017a, 2017b; Kriwet, 2005; Kriwet et al., 2016). Among these three species, we were perplexed that *P. laevis* is the only benthic taxon evidently preferring colder, potentially deeper waters, and such habitats are available to *Carcharias* sp. across all TELMs (Figure 3.7b, Figure 3.8, and Table A3.7). These isotopic and occurrence data suggest that some elasmobranch species exhibit ecological plasticity and can withstand environmental changes. For example, *S. macrota* occurs in LMF deposits only, from TELM 1 to 5 (Lutetian to Bartonian age, Middle to Late Eocene) and exhibits similar mean $\delta^{18}O_p$ but a decreasing range of variation through time (1σ decreases from 1 to 0.6‰) (Figure 3.7b, Table A3.7; Kriwet et al., 2016; Long, 1992; Kim et al., 2020). The falling variation in $\delta^{18}O_p$ values combined with occurrence data indicate that *S. macrota* reduced its geographic range as high-latitude waters turned colder until cooling and associated changes drove the extirpation of this taxon (Kim et al., 2020). Global cooling and associated environmental change could also explain the worldwide decline of *S. macrota* in other settings at varying latitudes, such as the North Sea or the Eocene deposits of Southern Chile at the beginning of the Late Eocene (i.e., Bartonian) (Cappetta, 2012; Kim et al., 2020; Otero et al., 2013; Otero & Soto-Acuña, 2015a; Zachos et al., 2001; Zacke et al., 2009). In contrast, *Carcharias* sp. and *P. laevis* could accommodate Eocene climate cooling given their tolerance to colder conditions. Therefore, the $\delta^{18}O_p$ values in the bioapatite of these taxa may not directly track the environmental changes we anticipated as they preferred similar environmental conditions.

3.8 Conclusions

Geochemistry of elasmobranch teeth records the environmental conditions where individuals lived and offers context on how sharks and rays coped during periods of climate change. Variability in $\delta^{18}O_p$ measurements of elasmobranch tooth specimens from the LMF and SMF shed light on habitat use and regional environmental conditions near Seymour Island during the Eocene. The overall stability in bulk $\delta^{18}O_p$ values across TELMs suggests that sharks and rays generally seek habitats with preferred conditions rather than behaving as passive tracers in a constant location like bivalves or foraminifera.

Unlike co-occurring bivalves, the variability in elasmobranch $\delta^{18}O_p$ values aligns only partially with seasonal predictions from the iCESM model simulation for the Eocene.

Similarly, spatial gradients of predicted model outputs in shallow waters do not fully explain the variation in shark $\delta^{18}O_p$ values. The higher $\delta^{18}O_p$ values often observed in some elasmobranchs' bioapatite compared to predicted model values likely reflect movements to deeper, colder waters not captured by the simulation. Conversely, lower $\delta^{18}O_p$ values than those simulated suggest movements to warmer or brackish, estuarine environments not captured in the simulation.

We explored the potential for the Drake Passage during the Late Eocene by comparing $\delta^{18}O_p$ values between pelagic sharks, typically found in warmer, shallower waters, and benthic taxa capable of traveling to colder, deeper depths far from Seymour Island shore. Benthic elasmobranchs did not, by and large, encounter colder conditions relative to pelagic sharks. We did not observe a significant difference in $\delta^{18}O_p$ values between the groups, suggesting that all lived in the same well-mixed water mass or that individual taxon-specific preferences within each group canceled each other out. Global cooling in the Eocene, though, likely exerted a selective pressure on sharks with those tolerant of colder waters coping better than those with preference for warm water.

Using a framework that combines $\delta^{18}O_p$ values of elasmobranchs with other empirical oxygen isotope measurements and model outputs, we found that some pelagic species evidently traveled to warmer or more brackish settings while others preferred forays into deeper or colder waters. Likewise, benthic species display differing thermal preferences, such that taxon-specific $\delta^{18}O_p$ values say more about the habitat tolerances of mobile taxa than about the environmental conditions at the site in which their teeth are found. These data not only provide insights into the environmental plasticity of elasmobranchs in a changing world, but also offer a valuable framework for refining model simulations of past oceanic conditions, particularly for deeper waters, which remain poorly understood.

3.9 Open Research

All data and codes for this study are available on Dryad (Larocca Conte et al., 2024).

3.10 References

Amenábar, C. R., Montes, M., Nozal, F., & Santillana, S. (2020). Dinoflagellate cysts of the la Meseta Formation (middle to late Eocene), Antarctic Peninsula: Implications for biostratigraphy, palaeoceanography and palaeoenvironment. *Geological Magazine*, *157*(3), 351–366. https://doi.org/10.1017/S0016756819000591

Anagnostou, E., John, E. H., Edgar, K. M., Foster, G. L., Ridgwell, A., Inglis, G. N., et al. (2016). Changing atmospheric CO2 concentration was the primary driver of early Cenozoic climate. *Nature*, *533*(7603), 380–384. https://doi.org/10.1038/nature17423

Arkhipkin, A., Brickle, P., Laptikhovsky, V., Pompert, J., & Winter, A. (2012). Skate assemblage on the eastern Patagonian Shelf and Slope: structure, diversity and abundance. *Journal of Fish Biology*, *80*(5), 1704–1726. https://doi.org/10.1111/J.1095-8649.2012.03260.X

Bazzi, M., Campione, N. E., Kear, B. P., Pimiento, C., & Ahlberg, P. E. (2021). Feeding ecology has shaped the evolution of modern sharks. *Current Biology*, *31*(23), 5138-5148.e4. https://doi.org/10.1016/j.cub.2021.09.028

Benton, M. J. (2014). *Vertebrate Palaeontology* (4th editio). Wiley-Blackwell.

Bijl, P. K., Sluijs, A., & Brinkhuis, H. (2013). A magneto- and chemostratigraphically calibrated dinoflagellate cyst zonation of the early Palaeogene South Pacific Ocean. *Earth-Science Reviews*, *124*, 1–31. https://doi.org/10.1016/J.EARSCIREV.2013.04.010

Borrelli, C., Katz, M. E., & Toggweiler, J. R. (2021). Middle to Late Eocene Changes of the Ocean Carbonate Cycle. *Paleoceanography and Paleoclimatology*, *36*(12), e2020PA004168. https://doi.org/10.1029/2020PA004168

Botella, H., Valenzuela-Ríos, J. I., & Martínez-Perez, C. (2009). Tooth replacement rates in early chondrichthyans: A qualitative approach. *Lethaia*, *42*(3), 365–376. https://doi.org/10.1111/j.1502-3931.2009.00152.x

Brady, E., Stevenson, S., Bailey, D., Liu, Z., Noone, D., Nusbaumer, J., et al. (2019). The Connected Isotopic Water Cycle in the Community Earth System Model Version 1. *Journal of Advances in Modeling Earth Systems*, *11*(8), 2547–2566. https://doi.org/10.1029/2019MS001663

Bruner, J. C. (1998). Tooth replacement rate of Carcharodon carcharias (Linnaeus, 1758). In *AES 14th annual meeting, Program and Abstracts* (p. 98).

Buick, D. P., & Ivany, L. C. (2004). 100 years in the dark: Extreme longevity of Eocene bivalves from Antarctica. *Geology*, *32*(10), 921–924. https://doi.org/10.1130/G20796.1

Cappetta, H. (2012). *Handbook of paleoichthyology volume 3E. Chondrichthyes. Mesozoic and Cenozoic elasmobranchii: Teeth*. (H.-P. Schultze, Ed.) (Vol. 3E). Munich: Verlag Dr. Friedrich Pfeil.

Carlisle, A. B., & Starr, R. M. (2009). Habitat use, residency, and seasonal distribution of female leopard sharks Triakis semifasciata in Elkhorn Slough, California. *Marine Ecology Progress Series*, *380*, 213–228. https://doi.org/10.3354/MEPS07907

Carter, A., Riley, T. R., Hillenbrand, C. D., & Rittner, M. (2017). Widespread Antarctic glaciation during the Late Eocene. *Earth and Planetary Science Letters*, *458*, 49–57. https://doi.org/10.1016/j.epsl.2016.10.045

Casselberry, G. A., & Carlson, J. K. (2015). Endagered species act status review of the graytale skate (Bathyraja griseocauda). *Report to the National Marine Fisheries Service, Office of Protected Resources. SFD Contribution PCB-15-04*, 1–18.

Cione, A. L., Reguero, M. A., & Acosta Hospitaleche, C. (2007). Did the continent and sea have different temperatures in the Northern Antarctic Peninsula during the Middle Eocene? *Revista de La Asociacion Geologica Argentina*, *62*(4), 586–596.

Compagno, L. J. V. (1984). FAO Species Catalogue. Vol. 4. Sharks of the world. An annotated and illustrated catalogue of shark species known to date. Part 2 -

Carcharhiniformes. FAO Fisheries Synopses, 125(4/2), 251–655. Retrieved from http://www.fao.org/docrep/009/ad123e/ ad123e00.HTM

Compagno, L. J. (2002). Sharks of the world: An Annotated and illustrated catalogue of shark species known to date. Volume 2. Bullhead, mackerel and carpet sharks (Heterodontiformes, Lamniformes and Orectolobiformes). FAO Species Catalogue for Fishery Purposes, 2(1), 269. Retrieved from http://www.fao.org/3/x9293e/x9293e00.htm

Condamine, F. L., Romieu, J., & Guinot, G. (2019). Climate cooling and clade competition likely drove the decline of lamniform sharks. *Proceedings of the National Academy of Sciences of the United States of America*, *116*(41), 20584–20590. https://doi.org/10.1073/pnas.1902693116

Cunningham, S. B. (2000). A comparison of isolated teeth of early Eocene Striatolamia macrota (Chondrichthyes , Lamniformes), with those of a Recent sand shark , Carcharias taurus. *Tertiary Research*, *20*(1–4), 17–31.

DeConto, R. M., & Pollard, D. (2003). Rapid Cenozoic glaciation of Antarctica induced by declining atmospheric CO2. *Nature*, *421*, 245–249. https://doi.org/10.1038/nature01290

Douglas, P. M. J., Affek, H. P., Ivany, L. C., Houben, A. J. P., Sijp, W. P., Sluijs, A., et al. (2014). Pronounced zonal heterogeneity in Eocene southern high-latitude sea surface temperatures. *Proceedings of the National Academy of Sciences of the United States of America*, *111*(18), 6582–6587. https://doi.org/10.1073/pnas.1321441111

Dutton, A. L., Lohmann, K. C., & Zinsmeister, W. J. (2002). Stable isotope and minor element proxies for Eocene climate of Seymour Island, Antarctica. *Paleoceanography*, *17*(2), 6-1-6–13. https://doi.org/10.1029/2000pa000593

Eagles, G., Livermore, R., & Morris, P. (2006). Small basins in the Scotia Sea: The Eocene Drake Passage gateway. *Earth and Planetary Science Letters*, *242*(3–4), 343–353. https://doi.org/10.1016/J.EPSL.2005.11.060

Egan, K. E., Rickaby, R. E. M., Hendry, K. R., & Halliday, A. N. (2013). Opening the gateways for diatoms primes Earth for Antarctic glaciation. *Earth and Planetary Science Letters*, *375*, 34–43. https://doi.org/10.1016/j.epsl.2013.04.030

Elliot, D. H. (1988). Tectonic setting and evolution of the James Ross Basin, northern Antarctic Peninsula. *Memoir - Geological Society of America*, *169*(January 1988), 541–555. https://doi.org/10.1130/mem169-p541

Enax, J., Prymak, O., Raabe, D., & Epple, M. (2012). Structure, composition, and mechanical properties of shark teeth. *Journal of Structural Biology*, *178*(3), 290–299. https://doi.org/10.1016/j.jsb.2012.03.012

Engelbrecht, A., Mörs, T., Reguero, M. A., & Kriwet, J. (2016a). A new sawshark, Pristiophorus laevis, from the Eocene of Antarctica with comments on Pristiophorus lanceolatus. *Historical Biology*, *29*(6), 841–853.

https://doi.org/10.1080/08912963.2016.1252761

Engelbrecht, A., Mörs, T., Reguero, M. A., & Kriwet, J. (2016b). Revision of Eocene Antarctic carpet sharks (Elasmobranchii, Orectolobiformes) from Seymour Island, Antarctic Peninsula. *Journal of Systematic Palaeontology*, *15*(12), 969–990. https://doi.org/10.1080/14772019.2016.1266048

Engelbrecht, A., Mörs, T., Reguero, M. A., & Kriwet, J. (2017a). Eocene squalomorph sharks (Chondrichthyes, Elasmobranchii) from Antarctica. *Journal of South American Earth Sciences*, *78*, 175–189. https://doi.org/10.1016/j.jsames.2017.07.006

Engelbrecht, A., Mörs, T., Reguero, M. A., & Kriwet, J. (2017b). New carcharhiniform sharks (Chondrichthyes, Elasmobranchii) from the early to middle Eocene of Seymour Island, Antarctic Peninsula. *Journal of Vertebrate Paleontology*, *37*(6). https://doi.org/10.1080/02724634.2017.1371724

Engelbrecht, A., Mörs, T., Reguero, M. A., & Kriwet, J. (2019). Skates and rays (Elasmobranchii, Batomorphii) from the Eocene La Meseta and Submeseta formations, Seymour Island, Antarctica. *Historical Biology*, *31*(8), 1028–1044. https://doi.org/10.1080/08912963.2017.1417403

Estebenet, M. S. G., Guerstein, G. R., Rodríguez Raising, M. E., Ponce, J. J., & Alperín, M. I. (2017). Dinoflagellate cyst zonation for the middle to upper Eocene in the Austral Basin, southwestern Atlantic Ocean: Implications for regional and global correlation. *Geological Magazine*, *154*(5), 1022–1036. https://doi.org/10.1017/S0016756816000601

Froese, R., & Pauly, D. (2024). FishBase. Retrieved from www.fishbase.org

Gaździcki, A., Gruszczyński, M., Hoffman, A., Małkowski, K., Marenessi, S. A., Halas, S., & Tatur, A. (1992). Stable carbon and oxygen isotope record in the Paleogene La Meseta Formation, Seymour Island, Antarctica. *Antarctic Science*, *4*(4), 461–468. https://doi.org/10.1017/S0954102092000671

Gelfo, J. N., Goin, F. J., Bauza, N., & Reguero, M. A. (2019). The fossil record of Antarctic land mammals : commented review and hypotheses for future research. *Advances in Polar Science*, *30*(3), 274–292. https://doi.org/10.13679/j.advps.2019.0021

Goldner, A., Herold, N., & Huber, M. (2014). Antarctic glaciation caused ocean circulation changes at the Eocene-Oligocene transition. *Nature*, *511*(7511), 574–577. https://doi.org/10.1038/nature13597

Griffiths, M. L., Eagle, R. A., Kim, S. L., Flores, R. J., Becker, M. A., IV, H. M. M., et al. (2023). Endothermic physiology of extinct megatooth sharks. *Proceedings of the National Academy of Sciences*, *120*(27), e2218153120. https://doi.org/10.1073/PNAS.2218153120

Grossman, E. L., & Ku, T. L. (1986). Oxygen and carbon isotope fractionation in biogenic aragonite: Temperature effects. *Chemical Geology: Isotope Geoscience Section*, *59*(C), 59–74. https://doi.org/10.1016/0168-9622(86)90057-6

Herold, N., Buzan, J., Seton, M., Goldner, A., Green, J. A. M., Müller, R. D., et al. (2014). A suite of early Eocene (~ 55 Ma) climate model boundary conditions. *Geoscientific Model Development*, *7*(5), 2077–2090. https://doi.org/10.5194/gmd-7-2077-2014

Hodel, F., Grespan, R., de Rafélis, M., Dera, G., Lezin, C., Nardin, E., et al. (2021). Drake Passage gateway opening and Antarctic Circumpolar Current onset 31 Ma ago: The message of foraminifera and reconsideration of the Neodymium isotope record. *Chemical Geology*, *570*(November 2020). https://doi.org/10.1016/j.chemgeo.2021.120171

Hönisch, B., Royer, D. L., Breecker, D. O., Polissar, P. J., Bowen, G. J., Henehan, M. J., et al. (2023). Toward a Cenozoic history of atmospheric CO2. *Science*, *382*(6675). https://doi.org/10.1126/SCIENCE.ADI5177/SUPPL_FILE/SCIENCE.ADI5177_SM.PDF

Hoyer, S., & Joseph, H. (2017). xarray: N-D labeled Arrays and Datasets in Python. *Journal of Open Research Software*, *5*(1), 17. https://doi.org/10.5334/jors.148

Huck, C. E., van de Flierdt, T., Bohaty, S. M., & Hammond, S. J. (2017). Antarctic climate, Southern Ocean circulation patterns, and deep water formation during the Eocene. *Paleoceanography*, *32*(7), 674–691. https://doi.org/10.1002/2017PA003135

Hunter, J. D. (2007). Matplotlib: A 2D graphics environment. *Computing in Science & Engineering*, *9*(3), 90–95. https://doi.org/10.1109/MCSE.2007.55

Ivany, L. C., Patterson, W. P., & Lohmann, K. C. (2000). Cooler winters as a possible cause of mass extinctions at the Eocene/Oligocene boundary. *Nature*, *407*(6806), 887–890. https://doi.org/10.1038/35038044

Ivany, L. C., Van Simaeys, S., Domack, E. W., & Samson, S. D. (2006). Evidence for an earliest Oligocene ice sheet on the Antarctic Peninsula. *Geology*, *34*(5), 377–380. https://doi.org/10.1130/G22383.1

Ivany, L. C., Lohmann, K. C., Hasiuk, F., Blake, D. B., Glass, A., Aronson, R. B., & Moody, R. M. (2008). Eocene climate record of a high southern latitude continental shelf: Seymour Island, Antarctica. *Bulletin of the Geological Society of America*, *120*(5–6), 659–678. https://doi.org/10.1130/B26269.1

Jambura, P. L., Pfaff, C., Underwood, C. J., Ward, D. J., & Kriwet, J. (2018). Tooth mineralization and histology patterns in extinct and extant snaggletooth sharks, hemipristis (carcharhiniformes, hemigaleidae)—evolutionary significance or ecological adaptation? *PLoS ONE*, *13*(8), e0200951. https://doi.org/10.1371/journal.pone.0200951

Judd, E. J., Ivany, L. C., DeConto, R. M., Halberstadt, A. R. W., Miklus, N. M., Junium, C. K., & Uveges, B. T. (2019). Seasonally Resolved Proxy Data From the Antarctic Peninsula Support a Heterogeneous Middle Eocene Southern Ocean. *Paleoceanography and Paleoclimatology*, *34*(5), 787–799. https://doi.org/10.1029/2019PA003581

Kaschner, K., Kesner-Reyes, K., Garilao, C., Rius-Barile, J., Rees, T., & Froese, R. (2015). AquaMaps: Predicted range maps for aquatic species. *World Wide Web Electronic Publication*, *08/2015*, www.aquamaps.org. Retrieved from https://www.gbif.org/tool/81356/aquamaps-predicted-range-maps-for-aquatic-species

Kemp, N. E. (1985). Ameloblastic secretion and calcification of the enamel layer in shark teeth. *Journal of Morphology*, *184*(2), 215–230. https://doi.org/10.1002/jmor.1051840211

Kennett, J. P. (1977). Cenozoic evolution of Antarctic glaciation, the circum-Antarctic Ocean, and their impact on global paleoceanography. *Journal of Geophysical Research*, *82*(27), 3843–3860. https://doi.org/10.1029/jc082i027p03843

Kennett, J. P., & Exon, N. F. (2004). Paleoceanographic evolution of the tasmanian seaway and its climatic implications. In *Geophysical Monograph Series* (Vol. 151, pp. 345–367). American Geophysical Union (AGU). https://doi.org/10.1029/151GM19

Kim, S. L., Casper, D. R., Galván-Magaña, F., Ochoa-Díaz, R., Hernández-Aguilar, S. B., & Koch, P. L. (2012). Carbon and nitrogen discrimination factors for elasmobranch soft tissues based on a long-term controlled feeding study. *Environmental Biology of Fishes*, *95*(1), 37–52. https://doi.org/10.1007/s10641-011-9919-7

Kim, S. L., Eberle, J. J., Bell, D. M., Fox, D. A., & Padilla, A. (2014). Evidence from shark teeth for a brackish Arctic Ocean in the Eocene greenhouse. *Geology*, *42*(8), 695–698. https://doi.org/10.1130/G35675.1

Kim, S. L., Zeichner, S. S., Colman, A. S., Scher, H. D., Kriwet, J., Mörs, T., & Huber, M. (2020). Probing the Ecology and Climate of the Eocene Southern Ocean With Sand Tiger Sharks Striatolamia macrota. *Paleoceanography and Paleoclimatology*, *35*(12), 1–21. https://doi.org/10.1029/2020PA003997

Kim, S. L., Yeakel, J. D., Balk, M. A., Eberle, J. J., Zeichner, S., Fieman, D., & Kriwet, J. (2022). Decoding the dynamics of dental distributions: insights from shark demography and dispersal. *Proceedings of the Royal Society B: Biological Sciences*, *289*(1977). https://doi.org/10.1098/rspb.2022.0808

Kim, S. T., Coplen, T. B., & Horita, J. (2015). Normalization of stable isotope data for carbonate minerals: Implementation of IUPAC guidelines. *Geochimica et Cosmochimica Acta*, *158*, 276–289. https://doi.org/10.1016/j.gca.2015.02.011

Kneebone, J., Chisholm, J., & Skomal, G. B. (2012). Seasonal residency, habitat use, and site fidelity of juvenile sand tiger sharks Carcharias taurus in a Massachusetts estuary. *Marine Ecology Progress Series*, *471*, 165–181. https://doi.org/10.3354/meps09989

Kneebone, J., Chisholm, J., & Skomal, G. (2014). Movement patterns of juvenile sand tigers (Carcharias taurus) along the east coast of the USA. *Marine Biology*, *161*(5), 1149–1163. https://doi.org/10.1007/s00227-014-2407-9

Kocsis, L., Vennemann, T. W., & Fontignie, D. (2007). Migration of sharks into freshwater systems during the Miocene and implications for Alpine paleoelevation. *Geology*,

35(5), 451–454. https://doi.org/10.1130/G23404A.1

Kohn, M. J., & Cerling, T. E. (2003). Stable Isotope Compositions of Biological Apatite. *Reviews in Mineralogy and Geochemistry*, *48*(1), 455–488. Retrieved from https://doi.org/10.2138/rmg.2002.48.12

Kolodny, Y., Luz, B., & Navon, O. (1983). Oxygen isotope variations in phosphate of biogenic apatites, I. Fish bone apatite-rechecking the rules of the game. *Earth and Planetary Science Letters*, *64*(3), 398–404. https://doi.org/10.1016/0012-821X(83)90100-0

Kriwet, J. (2005). Additions to the Eocene selachian fauna of Antarctica with comments on Antarctic selachian diversity. *Journal of Vertebrate Paleontology*, *25*(1), 1–7. https://doi.org/10.1671/0272-4634(2005)025[0001:ATTESF]2.0.CO;2

Kriwet, J., Engelbrecht, A., Mörs, T., Reguero, M., & Pfaff, C. (2016). Ultimate Eocene (Priabonian) chondrichthyans (Holocephali, Elasmobranchii) of Antarctica. *Journal of Vertebrate Paleontology*, *36*(4). https://doi.org/10.1080/02724634.2016.1160911

Krug, A. Z., Jablonski, D., Roy, K., & Beu, A. G. (2010). Differential extinction and the contrasting structure of polar marine faunas. *PLoS ONE*, *5*(12), e15362. https://doi.org/10.1371/journal.pone.0015362

Ladant, J. B., Donnadieu, Y., Bopp, L., Lear, C. H., & Wilson, P. A. (2018). Meridional Contrasts in Productivity Changes Driven by the Opening of Drake Passage. *Paleoceanography and Paleoclimatology*, *33*(3), 302–317. https://doi.org/10.1002/2017PA003211

Lagabrielle, Y., Goddéris, Y., Donnadieu, Y., Malavieille, J., & Suarez, M. (2009). The tectonic history of Drake Passage and its possible impacts on global climate. *Earth and Planetary Science Letters*, *279*(3–4), 197–211. https://doi.org/10.1016/j.epsl.2008.12.037

Langton, S. J., Rabideaux, N. M., Borrelli, C., & Katz, M. E. (2016). Southeastern Atlantic deep-water evolution during the late-middle Eocene to earliest Oligocene (Ocean Drilling Program Site 1263 and Deep Sea Drilling Project Site 366). *Geosphere*, *12*(3), 1032–1047. https://doi.org/10.1130/GES01268.1

Larocca Conte, G., Aleksinski, A., Liao, A., et al. (2024). Data from: Eocene shark teeth from peninsular Antarctica: Windows to habitat use and paleoceanography [Dataset]. https://doi.org/https://doi.org/10.5061/dryad.qz612jmq2

Larocca Conte, G., Lopes, L. E., Mine, A. H., Trayler, R. B., & Kim, S. L. (2024). SPORA, a new silver phosphate precipitation protocol for oxygen isotope analysis of small, organic-rich bioapatite samples. *Chemical Geology*, *651*, 122000. https://doi.org/10.1016/J.CHEMGEO.2024.122000

Latimer, J. C., & Filippelli, G. M. (2002). Eocene to Miocene terrigenous inputs and export production: geochemical evidence from ODP Leg 177, Site 1090. *Palaeogeography, Palaeoclimatology, Palaeoecology*, *182*(3–4), 151–164. https://doi.org/10.1016/S0031-

0182(01)00493-X

Lawver, L. A., & Gahagan, L. M. (2003). Evolution of Cenozoic seaways in the circum-Antarctic region. *Palaeogeography, Palaeoclimatology, Palaeoecology*, *198*(1–2), 11–37. https://doi.org/10.1016/S0031-0182(03)00392-4

Lécuyer, C., Amiot, R., Touzeau, A., & Trotter, J. (2013). Calibration of the phosphate δ18O thermometer with carbonate-water oxygen isotope fractionation equations. *Chemical Geology*, *347*, 217–226.

LeGrande, A. N., & Schmidt, G. A. (2006). Global gridded data set of the oxygen isotopic composition in seawater. *Geophysical Research Letters*, *33*(12), 12604. https://doi.org/10.1029/2006GL026011

Long, D. J. (1992a). Paleoecology of Eocene Antarctic sharks. *The Antarctic Paleoenvironmen: A Perspective on Global Change. Antarctic Research Series*, *56*(January 1992), 131–139. https://doi.org/10.1029/ar056p0131

Long, D. J. (1992b). Sharks from the La Meseta Formation (Eocene), Seymour Island, Antarctic Peninsula. *Journal of Vertebrate Paleontology*, *12*(1), 11–32. https://doi.org/10.1080/02724634.1992.10011428

Longinelli, A., & Nuti, S. (1973a). Oxygen isotope measurements of phosphate from fish teeth and bones. *Earth and Planetary Science Letters*, *20*, 337–340. https://doi.org/10.1016/0012-821X(73)90007-1

Longinelli, A., & Nuti, S. (1973b). Revised phosphate-water isotopic temperature scale. *Earth and Planetary Science Letters*, *19*(3), 373–376. https://doi.org/10.1016/0012-821X(73)90088-5

Lubitz, N., Daly, R., Smoothey, A. F., Vianello, P., Roberts, M. J., Schoeman, D. S., et al. (2024). Climate change-driven cooling can kill marine megafauna at their distributional limits. *Nature Climate Change*, *14*(5), 526–535. https://doi.org/10.1038/s41558-024-01966-8

Marenssi, S. A., Santillana, S. N., & Rinaldi, C. A. (1998). Stratigraphy of the La Meseta Formation (Eocene), Marambio (Seymour) Island, Antarctica. *Asociación Paleontológica Argentina Publicación Especial*, *5*(1), 137–146. Retrieved from https://www.peapaleontologica.org.ar/index.php/peapa/article/view/185

Marenssi, S. A., Net, L. I., & Santillana, S. N. (2002). Provenance, environmental and paleogeographic controls on sandstone composition in an incised-valley system: The Eocene La Meseta Formation, Seymour Island, Antarctica. *Sedimentary Geology*, *150*(3–4), 301–321. https://doi.org/10.1016/S0037-0738(01)00201-9

Marramá, G., Engelbrecht, A., Mörs, T., Reguero, M. A., & Kriwet, J. (2018). The southernmost occurrence of Brachycarcharias (Lamniformes, Odontaspididae) from the Eocene of Antarctica provides new information about the paleobiogeography and paleobiology of Paleogene sand tiger sharks. *Rivista Italiana Di Paleontologia e Stratigrafia*, *124*(2), 283–297.

McArthur, J. M., Howarth, R. J., & Bailey, T. R. (2001). Strontium isotope stratigraphy: LOWESS version 3: Best fit to the marine Sr-isotope curve for 0-509 Ma and accompanying look-up table for deriving numerical age. *Journal of Geology*, *109*(2), 155–170. https://doi.org/10.1086/319243

Met Office. (2015). Cartopy: a cartographic python library with a Matplotlib interface. Exeter, Devon. Retrieved from https://scitools.org.uk/cartopy

Meyers, E. K. M., Tuya, F., Barker, J., Jiménez Alvarado, D., Castro-Hernández, J. J., Haroun, R., & Rödder, D. (2017). Population structure, distribution and habitat use of the Critically Endangered Angelshark, Squatina squatina, in the Canary Islands. *Aquatic Conservation: Marine and Freshwater Ecosystems*, *27*(6), 1133–1144. https://doi.org/10.1002/aqc.2769

Millar, C. I. (1993). Impact of the eocene on the evolution of Pinus L. *Annals of the Missouri Botanical Garden 80:471-498*. Retrieved from https://www.fs.usda.gov/research/treesearch/24277

Montes, M., Nozal, F., Santillana, S., Marenssi, S., & Olivero, E. (2013). Mapa Geológico de Isla Marambio (Seymour), Antártida, escala 1:20,000. *Serie Cartográfica*.

Mörs, T., Reguero, M., & Vasilyan, D. (2020). First fossil frog from Antarctica: implications for Eocene high latitude climate conditions and Gondwanan cosmopolitanism of Australobatrachia. *Scientific Reports*, *10*(1), 1–11. https://doi.org/10.1038/s41598-020-61973-5

Nong, G. T., Najjar, R. G., Seidov, D., & Peterson, W. H. (2000). Simulation of ocean temperature change due to the opening of Drake Passage. *Geophysical Research Letters*, *27*(17), 2689–2692. https://doi.org/10.1029/1999GL011072

Nosal, A. P., Caillat, A., Kisfaludy, E. K., Royer, M. A., & Wegner, N. C. (2014). Aggregation behavior and seasonal philopatry in male and female leopard sharks Triakis semifasciata along the open coast of southern California, USA. *Marine Ecology Progress Series*, *499*, 157–175. https://doi.org/10.3354/meps10632

Otero, R. A., & Soto-Acuña, S. (2015a). New chondrichthyans from Bartonian-Priabonian levels of Río de Las Minas and Sierra Dorotea , Magallanes Basin , Chilean Patagonia, *42*(2), 268–283. https://doi.org/10.5027/andgeoV42n2-a06

Otero, R. A., & Soto-Acuña, S. (2015b). Nuevos condrictios de niveles Bartoniano-priabonianos de Río de Las Minas y Sierra Dorotea, Cuenca de Magallanes, Patagonia Chilena. *Andean Geology*, *42*(2), 268–283. https://doi.org/10.5027/andgeoV42n2-a06

Otero, R. A., Torres, T., Le Roux, J. P., Herve, F., Fanning, C. M., Yury-Yanez, R. E., & Rubilar-Rogers, D. (2012). A Late Eocene age proposal for the Loreto Formation (Brunswick Peninsula, southernmost Chile), based on fossil cartilaginous fishes, paleobotany and radiometric evidence. *Andean Geology*, *39*(1), 180–200. https://doi.org/10.5027/andgeov39n1-a09

Otero, R. A., Oyarzún, J. L., Soto-Acuña, S., Yury-Yáñez, R. E., Gutierrez, N. M., Le Roux,

J. P., et al. (2013). Neoselachians and Chimaeriformes (Chondrichthyes) from the latest Cretaceous-Paleogene of Sierra Baguales, southernmost Chile. chronostratigraphic, paleobiogeographic and paleoenvironmental implications. *Journal of South American Earth Sciences*, *48*, 13–30. https://doi.org/10.1016/j.jsames.2013.07.013

Parmley, D., Cicimurri, D. J., & Campbell, B. (2003). Late Eocene Sharks of the Hardie Mine Local Fauna of Wilkinson County, Georgia. *Georgia Journal of Science*, *61*(3), 153–179. https://doi.org/10.1016/j.jaci.2012.05.050

Pearson, P. N., Foster, G. L., & Wade, B. S. (2009). Atmospheric carbon dioxide through the Eocene-Oligocene climate transition. *Nature*, *461*(7267), 1110–1113. https://doi.org/10.1038/nature08447

Porębski, S. J. (2000). Shelf-valley compound fill produced by fault subsidence and eustatic sea-level changes, Eocene La Meseta Formation, Seymour Island, Antarctica. *Geology*, *28*(2), 147–150. https://doi.org/10.1130/0091-7613(2000)28<147:SCFPBF>2.0.CO;2

Pucéat, E., Joachimski, M. M., Bouilloux, A., Monna, F., Bonin, A., Motreuil, S., et al. (2010). Revised phosphate-water fractionation equation reassessing paleotemperatures derived from biogenic apatite. *Earth and Planetary Science Letters*, *298*(1–2), 135–142. https://doi.org/10.1016/j.epsl.2010.07.034

R Development Core Team. (2024). A language and environment for statistical computing. R Foundation for Statistical Computing, Vienna, Austria. Vienna, Austria.

Raoult, V., Peddemors, V., Rowling, K., & Williamson, J. E. (2020). Spatiotemporal distributions of two sympatric sawsharks (Pristiophorus cirratus and P. nudipinnis) in south-eastern Australian waters. *Marine and Freshwater Research*, *71*(10), 1342–1354. https://doi.org/10.1071/MF19277

Sadler, P. M. (1988). Paleogene units on Seymour Island , northern Antarctic Peninsula.

Sauermilch, I., Whittaker, J. M., Klocker, A., Munday, D. R., Hochmuth, K., Bijl, P. K., & LaCasce, J. H. (2021). Gateway-driven weakening of ocean gyres leads to Southern Ocean cooling. *Nature Communications 2021 12:1*, *12*(1), 1–8. https://doi.org/10.1038/s41467-021-26658-1

Scher, H. D., & Martin, E. E. (2004). Circulation in the Southern Ocean during the Paleogene inferred from neodymium isotopes. *Earth and Planetary Science Letters*, *228*(3–4), 391–405. https://doi.org/10.1016/j.epsl.2004.10.016

Scher, H. D., & Martin, E. E. (2006). Timing and climatic consequences of the opening of drake passage. *Science*, *312*(5772), 428–430. https://doi.org/10.1126/science.1120044

Scher, H. D., Bohaty, S. M., Zachos, J. C., & Delaney, M. L. (2011). Two-stepping into the icehouse: East Antarctic weathering during progressive ice-sheet expansion at the Eocene-Oligocene transition. *Geology*, *39*(4), 383–386. https://doi.org/10.1130/G31726.1

Scher, H. D., Bohaty, S. M., Smith, B. W., & Munn, G. H. (2014). Isotopic interrogation of a

suspected late Eocene glaciation. *Paleoceanography*, *29*(6), 628–644. https://doi.org/10.1002/2014PA002648

Schlaff, A. M., Heupel, M. R., & Simpfendorfer, C. A. (2014, July 24). Influence of environmental factors on shark and ray movement, behaviour and habitat use: a review. *Reviews in Fish Biology and Fisheries*. Springer. https://doi.org/10.1007/s11160-014-9364-8

Shemesh, A., Kolodny, Y., & Luz, B. (1983). Oxygen isotope variations in phosphate of biogenic apatites, II. Phosphorite rocks. *Earth and Planetary Science Letters*, *64*(3), 405–416. https://doi.org/10.1016/0012-821X(83)90101-2

Sijp, W. P., & England, M. H. (2004). Effect of the drake passage throughflow on global climate. *Journal of Physical Oceanography*, *34*(5), 1254–1266. https://doi.org/10.1175/1520-0485(2004)034<1254:EOTDPT>2.0.CO;2

Stickley, C. E., Brinkhuis, H., Schellenberg, S. A., Sluijs, A., Röhl, U., Fuller, M., et al. (2004). Timing and nature of the deepening of the Tasmanian Gateway. *Paleoceanography*, *19*(4), 1–18. https://doi.org/10.1029/2004PA001022

Sulikowski, J. A., Galuardi, B., Bubley, W., Furey, N. B., Driggers, W. B., Ingram, G. W., & Tsang, P. C. W. (2010). Use of satellite tags to reveal the movements of spiny dogfish Squalus acanthias in the western North Atlantic Ocean. *Marine Ecology Progress Series*, *418*, 249–254. https://doi.org/10.3354/meps08821

Trayler, R. B., Landa, P. V., & Kim, S. L. (2023). Evaluating the efficacy of collagen isolation using stable isotope analysis and infrared spectroscopy. *Journal of Archaeological Science*, *151*, 105727. https://doi.org/10.1016/j.jas.2023.105727

Vennemann, T. W., Hegner, E., Cliff, G., & Benz, G. W. (2001). Isotopic composition of recent shark teeth as a proxy for environmental conditions. *Geochimica et Cosmochimica Acta*, *65*(10), 1583–1599. https://doi.org/10.1016/S0016-7037(00)00629-3

Vennemann, T. W., Fricke, H. C., O'Neil, J. R., & Colman, A. (2002). Oxygen isotope analysis of phosphates : A comparison of techniques for for analysis of Ag3PO4. *Chemical Geology*, *185*(October), 321–336. https://doi.org/10.1016/S0009-2541(01)00413-2

Vilmar, M., & Di Santo, V. (2022, March 8). Swimming performance of sharks and rays under climate change. *Reviews in Fish Biology and Fisheries*. Springer. https://doi.org/10.1007/s11160-022-09706-x

Watanabe, Y. Y., Payne, N. L., Semmens, J. M., Fox, A., & Huveneers, C. (2019). Swimming strategies and energetics of endothermic white sharks during foraging. *Journal of Experimental Biology*, *222*(4). https://doi.org/10.1242/jeb.185603

Weigmann, S. (2016). Annotated checklist of the living sharks, batoids and chimaeras (Chondrichthyes) of the world, with a focus on biogeographical diversity. *Journal of Fish Biology*, *88*(3), 837–1037. https://doi.org/10.1111/jfb.12874

Welton, B. J., & Zinsmeister, W. J. (1980). Eocene neoselachians from the La Meseta Formation, Seymour Island, Antarctic Peninsula. *Contributions in Science (Los Angeles)*, *330*(324), 1–10.

Zachos, J. C., Quinn, T. M., & Salamy, K. A. (1996). High-resolution deap-sea foraminiferal stable isotope records of the Eocene-Oligocene transition. *Paleoceanography*, *11*(3), 251–266.

Zachos, J. C., Pagani, H., Sloan, L., Thomas, E., & Billups, K. (2001). Trends, rhythms, and aberrations in global climate 65 Ma to present. *Science*, *292*(5517), 686–693. https://doi.org/10.1126/science.1059412

Zachos, J. C., Dickens, G. R., & Zeebe, R. E. (2008). An early Cenozoic perspective on greenhouse warming and carbon-cycle dynamics. *Nature*, *451*(7176), 279–283. https://doi.org/10.1038/nature06588

Zacke, A., Voigt, S., Joachimski, M. M., Gale, A. S., Ward, D. J., & Tütken, T. (2009). Surface-water freshening and high-latitude river discharge in the Eocene North Sea. *Journal of the Geological Society*, *166*(5), 969–980. https://doi.org/10.1144/0016-76492008-068

Zazzo, A., Lécuyer, C., & Mariotti, A. (2004). Experimentally-controlled carbon and oxygen isotope exchange between bioapatites and water under inorganic and microbially-mediated conditions. *Geochimica et Cosmochimica Acta*, *68*(1), 1–12. https://doi.org/10.1016/S0016-7037(03)00278-3

Zeichner, S. S., Kim, S. L., & Colman, A. S. (2015). Eocene high-latitude temperature gradients over time and space based on on δ18O values of fossil shark teeth. In *AGU Fall Meeting Abstracts* (Vol. 2015, pp. PP53C-2378).

Zhang, Z.-S., Yan, Q., & Wang, H.-J. (2010). Has the Drake Passage Played an Essential Role in the Cenozoic Cooling? *Atmospheric and Oceanic Science Letters*, *3*(5), 288–292. https://doi.org/10.1080/16742834.2010.11446884

Zhu, J., Poulsen, C. J., & Tierney, J. E. (2019). Simulation of Eocene extreme warmth and high climate sensitivity through cloud feedbacks. *Science Advances*, *5*(9), 1–10. https://doi.org/10.1126/sciadv.aax1874

Zhu, J., Poulsen, C. J., Otto-Bliesner, B. L., Liu, Z., Brady, E. C., & Noone, D. C. (2020). Simulation of early Eocene water isotopes using an Earth system model and its implication for past climate reconstruction. *Earth and Planetary Science Letters*, *537*, 116164. https://doi.org/10.1016/j.epsl.2020.116164

Žigaite, Ž., & Whitehouse, M. (2014). Stable oxygen isotopes of dental biomineral: Differentiation at the intra- and inter-tissue level of modern shark teeth. *GFF*, *136*(1), 337–340. https://doi.org/10.1080/11035897.2013.878747

3.11 Tables

Table 3.1. List of elasmobranch taxa and number of tooth specimens per TELM. Fossil shark taxa collected from the Eocene deposits of Seymour Island are expected to live in similar habitats, temperature, and depth ranges of their modern analogs.

Taxon	**n specimens per TELM**						**Modern analog**	**Habitat***	**T (°C)***	**Depth (m b.s.l.)***
	2	3	4	5	6	7				
Abdounia mesetae	-	-	1	-	-	-	*Triaenodon obesus*[l]	benthic	21.1 - 30.0[a]	0 - 330[b]
Brachycarcharias lerichei	5	-	11	9	-	-	*Carcharias taurus*[m]	pelagic	9.0 - 26.9[c]	0 - 100[c]
Carcharias sp. cf. *C. hopei*	11	15	21	13	9	-	*Carcharias taurus*[n]	pelagic	9.0 - 26.9[c]	0 - 100[c]
Carcharocles sokolovi	-	-	-	-	-	1	*Carcharodon carcharias*[g]	pelagic	5.0 - 25.0[d]	0 - 1200[e]
Dalatiidae indet.	-	-	-	2	-	-	*Dalatias lichia*[i]	benthic	2.5 - 14.3[d]	37 - 1794[e]
Eodalatias austrinalis	-	-	-	2	-	-	*Dalatias lichia*[i]	benthic	2.5 - 14.3[d]	37 - 1794[e]
Kallodentis rhytistemma	-	-	-	6	-	-	*Triakis semifasciata*[j]	benthic	12.8 - 24.0[d]	0 - 156[e]
Otodus auricolatus	-	-	7	-	-	-	*Carcharodon carcharias*[n]	pelagic	5.0 - 25.0[d]	0 - 1200[e]
Palaeohypotodus sp cf. *P.rutoti*	-	-	-	-	-	1	*Odontaspis ferox*[g]	pelagic	12.2 - 23.9[d]	10 - 1015[e]
Pristiophorus laevis	-	-	6	16	4	2	*Pristiophorus cirratus*[h]	benthic	14.0 - 17.7[d]	40 - 630[e]
Raja amphitrita	-	-	-	14	1	-	*Bathyraja griseocauda*[p]	benthic	2.7 - 7.7[d]	30 - 1010[e]
Squalus sp	-	-	-	-	1	1	*Squalus acanthias*[g,i]	benthic	4.2 - 18.7[d,f]	0 - 1978[e,f]
Squalus weltoni	-	-	-	11	2	-	*Squalus acanthias*[g,i]	benthic	4.2 - 18.7[d,f]	0 - 1978[e,f]
Squalus woodburnei	-	-	-	7	2	-	*Squalus acanthias*[g,i]	benthic	4.2 - 18.7[d,f]	0 - 1978[e,f]
Squatina sp.	-	-	-	11	4	1	*Squatina squatina*[g,i]	benthic	7.7 - 19.4[d]	2 - 150[e]

Taxon	n specimens per TELM						Modern analog	Habitat*	T (°C)*	Depth (m b.s.l.)*
	2	3	4	5	6	7				
Striatolamia sp cf. *S.macrota*	-	-	-	-	-	4	*Carcharias taurus*[g,k]	pelagic	9.0 - 26.9[c]	0 - 100[c]
Total n specimens	28	22	61	99	23	10				

Note. Headers followed by asterisk (*) indicate habitat, temperature, and depth ranges of modern analogs. [a]Kaschner et al., 2015, [b]Compagno 1984, [c]Kneebone et al., 2016, [d]Froese & Pauly, 2024, [e]Weigmann, 2016, [f]Sulikowsky et al., 2010, [g] Kriwet et al., 2016, [h]Engelbrecht et al., 2016a, [i]Engelbrecht et al., 2017a, [j]Engelbrecht et al., 2017b, [k]Cunningham, 2000, [l]Parmley et al., 2003, [m]Marramà et al., 2018, [n]Kriwet, 2005, [o]Long, 1992b, [p]Engelbrecht et al., 2019.

Table 3.2. Summary statistics of elasmobranchs' $\delta^{18}O_p$ values across TELMs. The table shows the lithostratigraphic unit (TELM), the number of specimens per TELM (n), and $\delta^{18}O_p$ mean, standard deviation (1σ), and range values in V-SMOW scale.

TELM	**n**	**$\delta^{18}O_p$ (V-SMOW)**		
		mean ± 1σ	**median**	**range**
7	10	21.4 ± 1.8	21.9	17.5 - 23.6
6	23	22.5 ± 0.6	22.6	20.6 - 23.4
5	99	21.9 ± 1.2	22.0	16.7 - 24.0
4	61	22.0 ± 1.4	22.4	16.9 - 24.0
3	22	22.4 ± 1.0	22.7	20.6 - 23.8
2	28	22.0 ± 1.5	22.2	16.6 - 23.7

Table 3.3. Pairwise comparison of elasmobranchs' $\delta^{18}O_p$ values between TELM units performed via post-hoc Dunn test. Values in the tables are *p* values performed by the test. Values with asterisk (*) indicate statistically significant difference between groups ($p < 0.05$).

TELM	**2**	**3**	**4**	**5**	**6**
3	0.1525	-	-	-	-
4	0.4291	0.1560	-	-	-
5	0.1786	0.0189	0.0720	-	-
6	0.0877	0.3826	0.0820	0.0062*	-
7	0.1716	0.0463	0.1265	0.3232	0.0269

Table 3.4. Summary statistics and Kruskal-Wallis test of pelagic and benthic elasmobranch' $\delta^{18}O_p$ values from TELM 4 to 7. The table shows the lithostratigraphic unit (TELM), the number of specimens per TELM (n), and $\delta^{18}O_p$ mean, median, and range values. Note that tooth specimens analyzed in TELM 2 and 3 include pelagic individuals only, whose statistics are summarized in Table 2. The test indicates no statistical differences between groups with each TELM.

TELM	**Habitat**	**n**	**$\delta^{18}O_p$ (‰; V-SMOW)**			**Kruskal-Wallis test, pelagic vs benthic elasmobranchs**	
			mean ± 1σ	**median**	**range**	**H value**	***p***
7	pelagic	6	22.1 ± 1.4	22.5	19.7 - 23.6	2.25	0.13
	benthic	4	20.4 ± 2.1	21.2	17.5 - 21.9		
6	pelagic	9	22.2 ± 0.9	22.4	20.6 - 23.4	1.03	0.31
	benthic	14	22.6 ± 0.3	22.6	22.0 - 23.3		
5	pelagic	30	21.6 ± 1.6	22.0	16.7 - 24.0	0.51	0.48
	benthic	69	22.0 ± 0.9	22.1	18.5 - 24.0		
4	pelagic	54	21.9 ± 1.4	22.4	16.9 - 23.9	3.45	0.06
	benthic	7	22.9 ± 1.2	23.2	20.7 - 24.0		

3.12 Figures

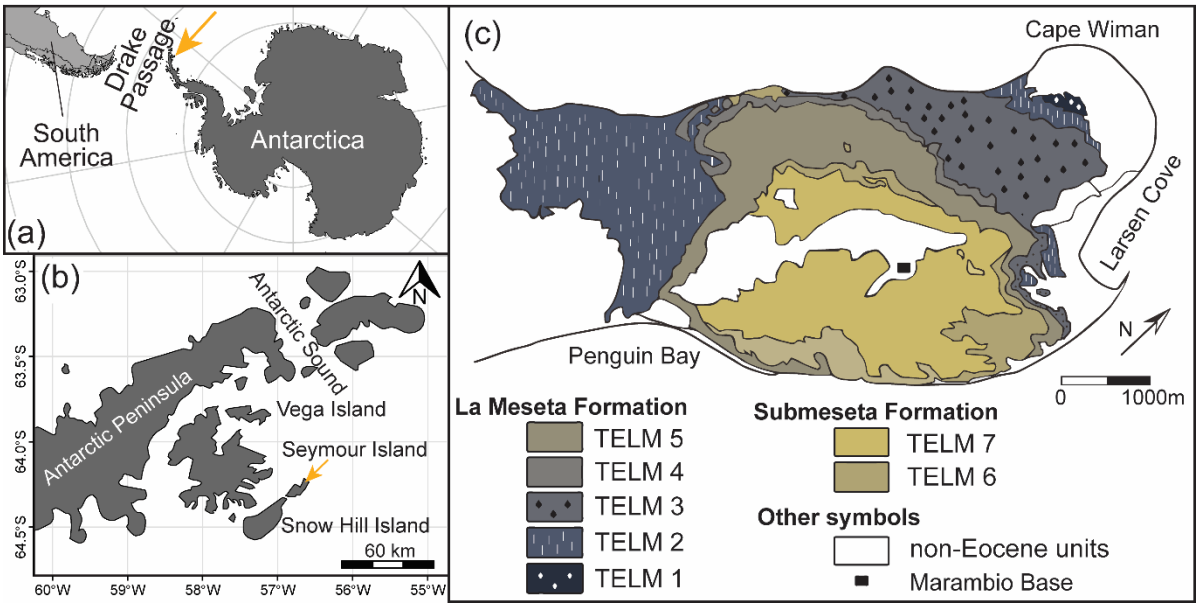

Figure 3.1. (a) Location of Seymour Island (yellow arrow) in relation to the Drake Passage, South America, and (b) other islands around the Antarctic Peninsula. (c) Geographic distribution of TELMs on Seymour Island.

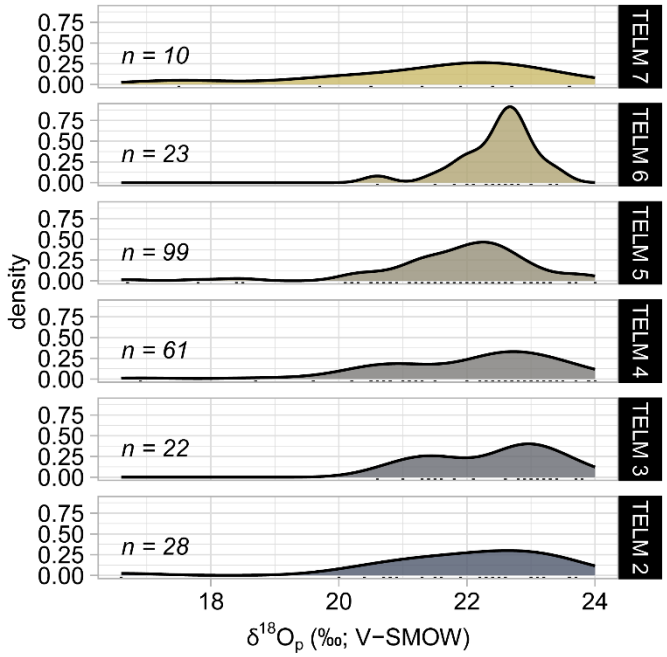

Figure 3.2. Elasmobranchs' $\delta^{18}O_p$ values suggest environmental stasis across TELMs. The figure shows the density distribution of $\delta^{18}O_p$ values measured from elasmobranch tooth specimens collected from LMF (TELM 2 to 5) and SMF (TELM 6 and 7). Colors indicate sharks' and rays' $\delta^{18}O_p$ distributions in different TELMs.

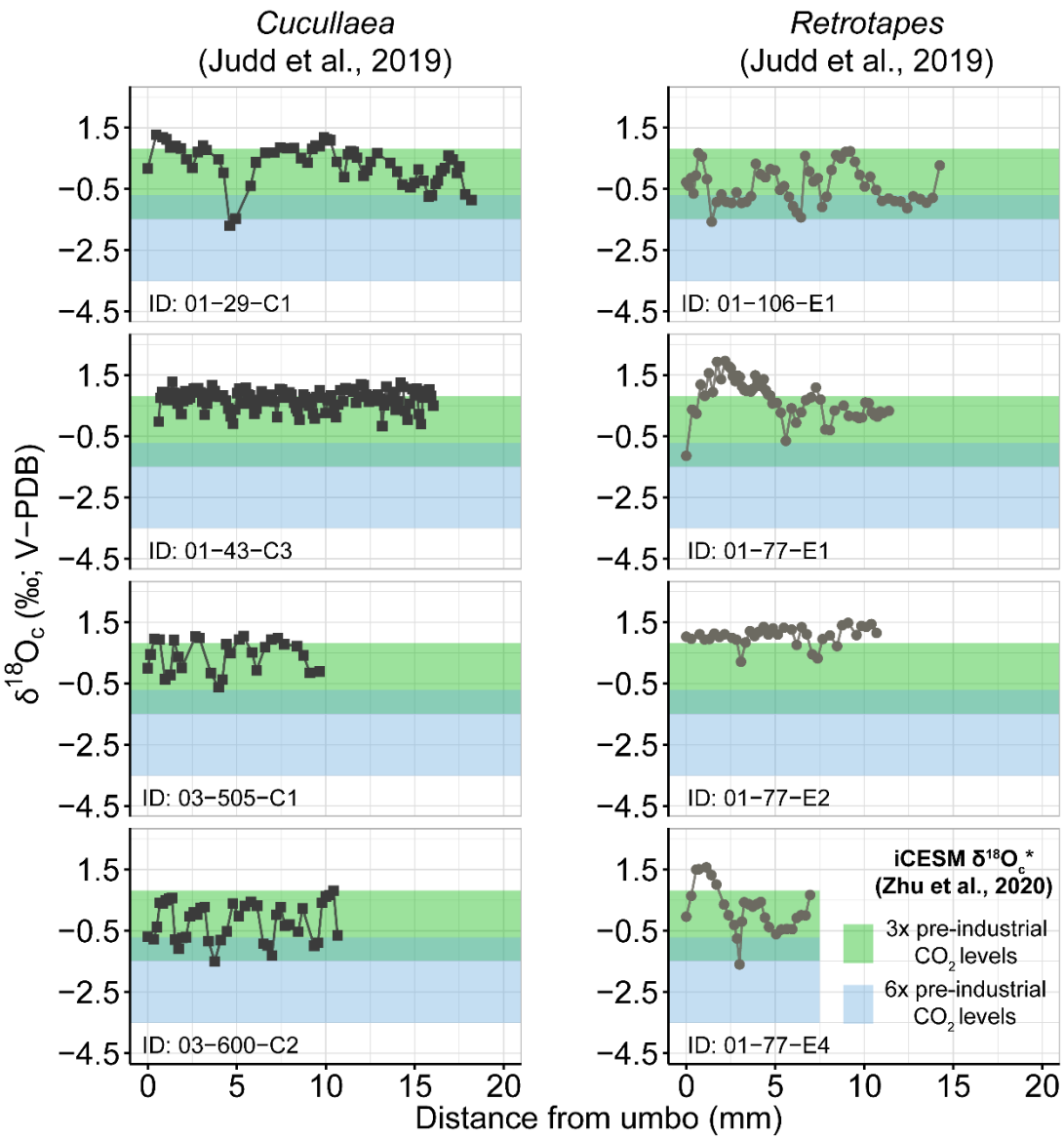

Figure 3.3. $\delta^{18}O_c$ values from individual serial sampled bivalve specimens (Judd et al., 2019) compared to iCESM simulated values for Seymour Island integrated from surface to 25 m (Zhu et al., 2020). The 3× pre-industrial CO_2 case predicts seasonal environmental variation for Seymour Island in excellent agreement with empirical. The plot shows $\delta^{18}O_c$ values of *Cucullaea* (left panel, black squares) and *Retrotapes* (right panel, grey circles) individuals measured along the shell, from the umbo to the outer edge of specimens. The range of simulated monthly averaged $\delta^{18}O_c^*$ values are shown with the green and light blue boxes for the 3× and 6× CO_2 cases, respectively.

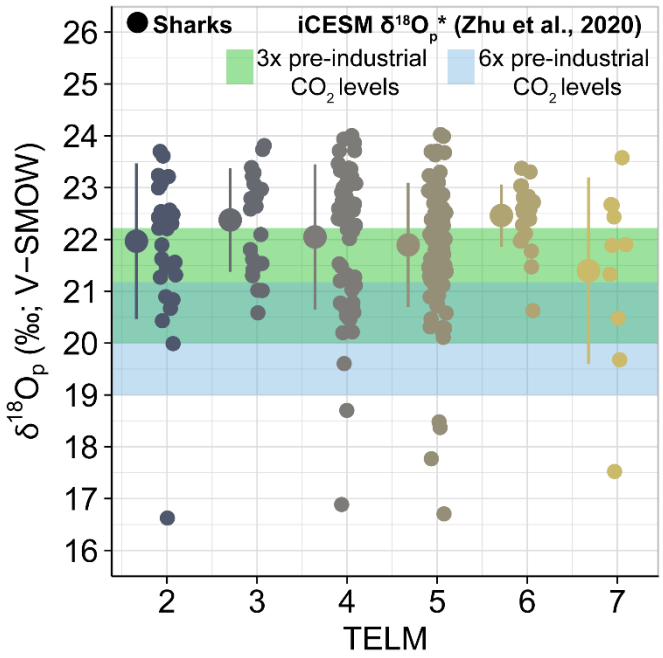

Figure 3.4. Bulk elasmobranch bioapatite $\delta^{18}O_p$ values exhibit a large variation across TELMs, which spans predicted Eocene seasonal values for Seymour Island. Colors for sharks $\delta^{18}O_p$ values vary by TELMs with larger circles and bars indicating mean ± 1σ per TELM (points have been horizontally jittered slightly for visual clarity). The green and blue shaded rectangles indicate the seasonal range of $\delta^{18}O_p^*$ values for the 3× and 6× pre-industrial CO_2 levels predicted by the iCESM simulation integrated from surface to 25 m (Zhu et al., 2020).

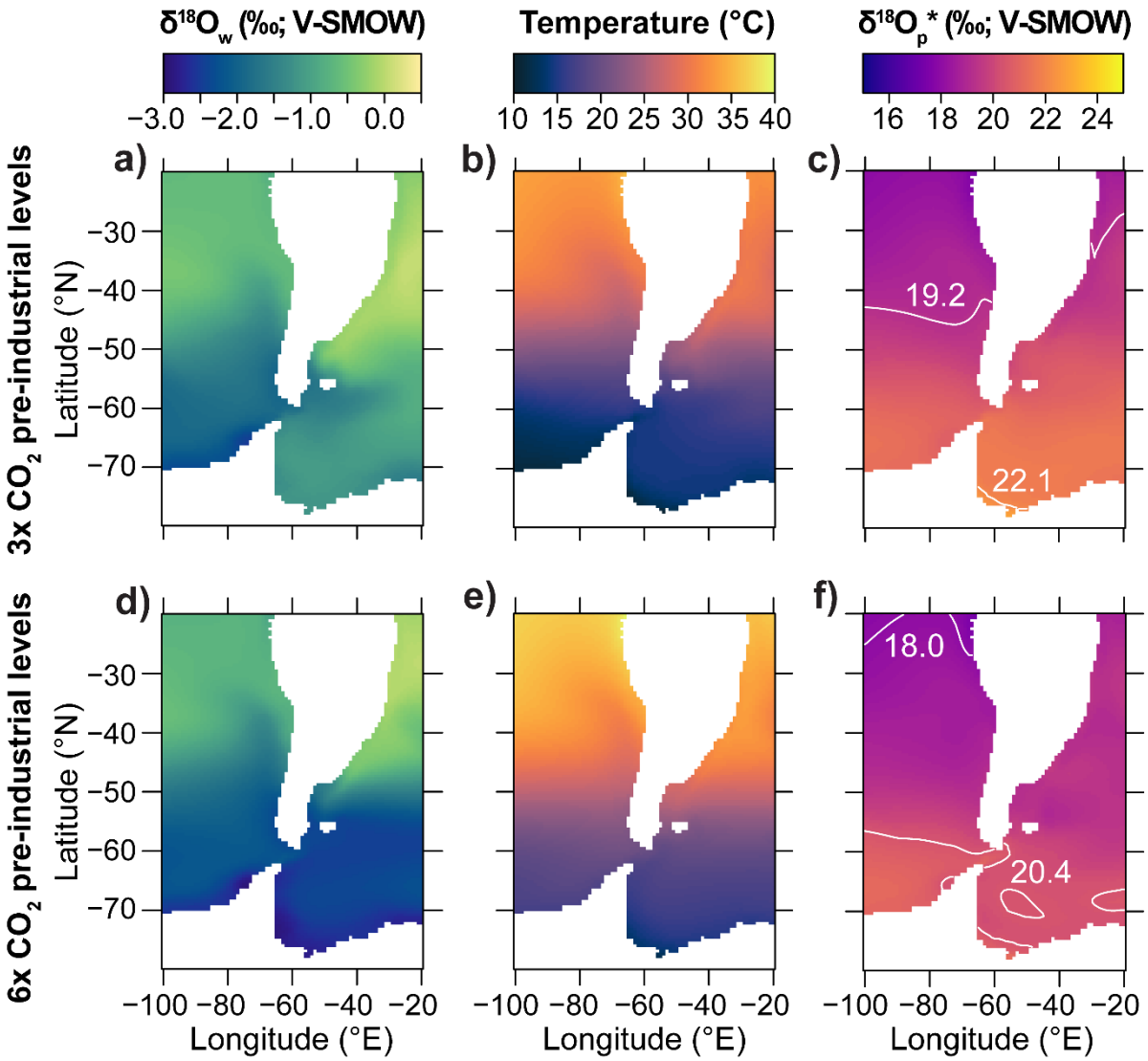

Figure 3.5. Early Eocene simulations from Zhu et al. (2020) model sea surface temperature (b&e) and $\delta^{18}O_w$ values (a&c) across a spatial distribution within 25 m b.s.l. Arrays of these environmental conditions under 3× (first row) and 6× (second row) pre-industrial CO_2 levels were used to predict $\delta^{18}O_p^*$ values (c&f) using equation (2) (Lécuyer et al., 2013) to compare to empirical values from shark enameloid. The simulated $\delta^{18}O_p^*$ values for both simulations report the mean ± 2σ isoscape values in white to define the spatial variation captured by simulations.

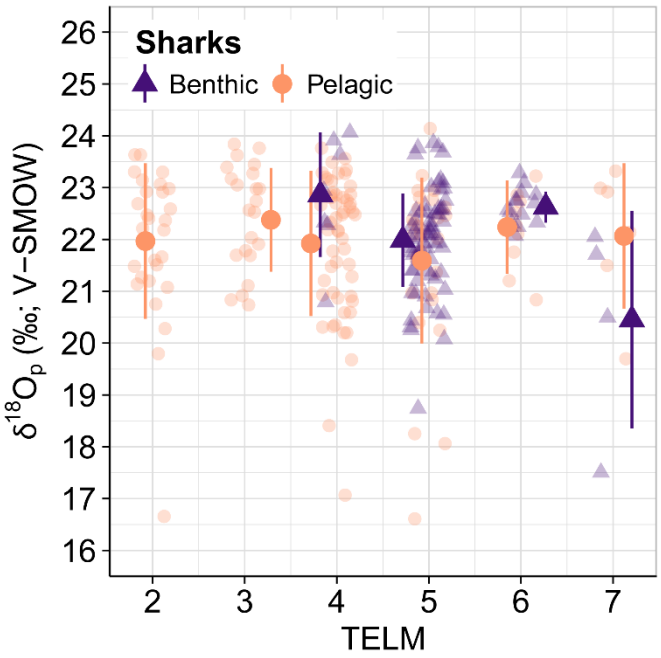

Figure 3.6. Pelagic (orange circles) and benthic (violet diamonds) elasmobranchs from LMF and SMF have similar $\delta^{18}O_p$ values that suggest they lived in very similar environments across TELMs. Shaded points are individual observations, while solid points and bars are mean ± 1σ values of groups across TELMs (points have been horizontally jittered slightly for visual clarity).

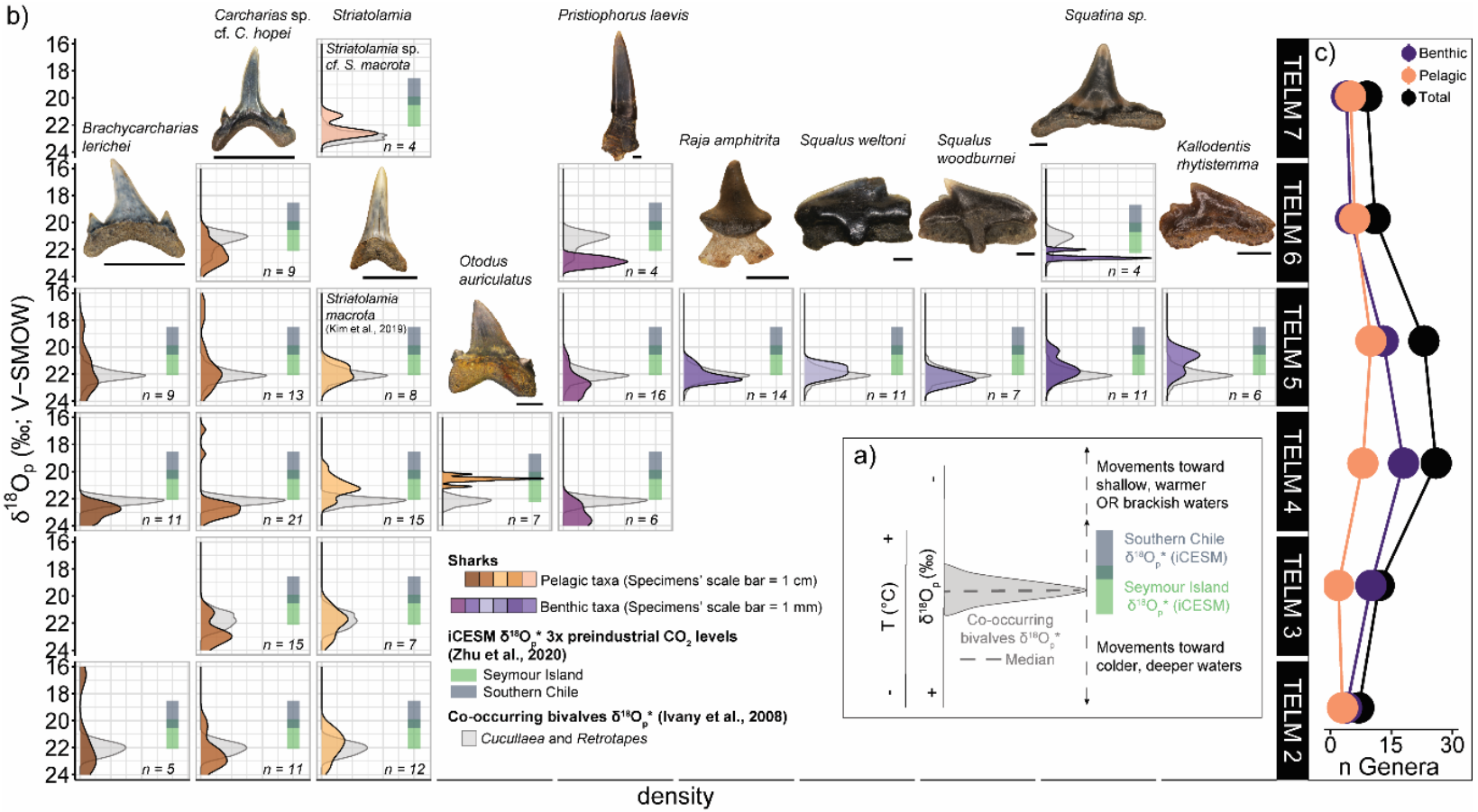
b)
Carcharias sp. cf. C. hopei
Striatolamia
Pristiophorus laevis
Squatina sp.
Brachycarcharias lerichei
Striatolamia sp. cf. S. macrota
Raja amphitrita
Squalus weltoni
Squalus woodburnei
Kallodentis rhytistemma
Otodus auriculatus
Striatolamia macrota (Kim et al., 2019)
TELM 7
TELM 6
TELM 5
TELM 4
TELM 3
TELM 2
δ18Op (‰; V–SMOW)
density
Sharks
Pelagic taxa (Specimens' scale bar = 1 cm)
Benthic taxa (Specimens' scale bar = 1 mm)
iCESM δ18Op* 3x preindustrial CO2 levels (Zhu et al., 2020)
Seymour Island
Southern Chile
Co-occurring bivalves δ18Op* (Ivany et al., 2008)
Cucullaea and Retrotapes
a)
T (°C)
δ18Op (‰)
Co-occurring bivalves δ18Op*
Median
Movements toward shallow, warmer OR brackish waters
Southern Chile δ18Op* (iCESM)
Seymour Island δ18Op* (iCESM)
Movements toward colder, deeper waters
c)
Benthic
Pelagic
Total
0
15
30
n Genera

Figure 3.7. Deciphering the habitat use of elasmobranchs offers context to understand the rise and fall in diversity across TELMs. (a) A schematic representation of the framework adopted to investigate sharks' habitat use. Co-occurring bivalves' $\delta^{18}O_p^*$ distribution is in grey, with the dashed line representing the median. Model seasonal $\delta^{18}O_p^*$ values for southern Chile and Seymour Island are represented as dark grey and green boxes, respectively. Dashed arrows indicate shifts toward lower (i.e., warmer, shallow waters or brackish environments) or higher $\delta^{18}O_p$ values (i.e., colder, deeper waters) than predicted $\delta^{18}O_p^*$. (b) Comparison between $\delta^{18}O_p$ values of pelagic and benthic taxa with transposed values from co-occurring bivalves and $\delta^{18}O_p^*$ values based on iCESM simulations reveals potential habitat use of different species. The density distribution of shark taxa (columns) across different TELM units (rows). The figure features representative tooth specimens of taxa used for stable isotope analysis. All specimens are depicted in labial view, except for the *S. macrota* specimen, which is shown in lingual view. The scale bar represents 1 cm for pelagic taxa and 1 mm for benthic species. c) Number of chondrichthyan genera (i.e., sharks, rays, and chimeras) trends across TELM units. The list of taxa was compiled from the literature (Engelbrecht et al., 2016a, 2016b, 2017a, 2017b, 2019; Kriwet, 2005; Kriwet et al., 2016; Long, 1992b; Marramá et al., 2018). Colors indicate trends for the total number of chondrichthyan genera (black), benthic (purple), or pelagic taxa (orange) per TELM unit.

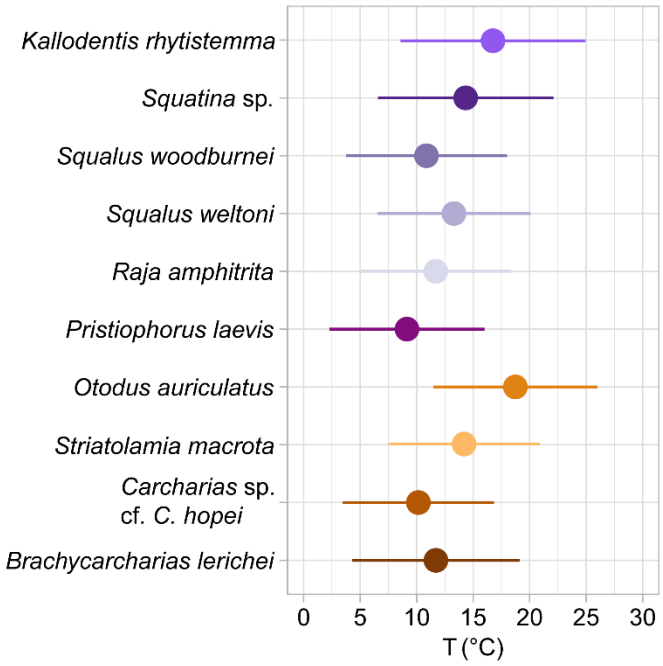

Figure 3.8. Temperature estimates from $\delta^{18}O_p$ measurements of pelagic (brown-yellow color palette) and benthic taxa (purple-gray color palette) using the Bayesian framework explained in Appendix 3.13.2. Dots indicate mean temperature values, while bars are 95% confidence intervals. The simulation uses prior model seawater temperature and $\delta^{18}O_w$ with a range of -0.43 – 35.58°C and -2.85 – 0.00‰, respectively (Appendix 3.13.3).

3.13 Appendix

3.13.1 Sampling and Strategies for Silver Phosphate (Ag_3PO_4) Precipitation Procedures

We adopted two different strategies to precipitate silver phosphate from tooth apatite for oxygen stable isotope measurements based on the specimen size. Large shark tooth specimens (i.e., crown height > 2 cm) were drilled with a Dremel equipped with a 300 μm diamond-coated bit along the tooth crown surface to obtain a fine powder of enameloid. A total of 136 tooth specimens were sampled by drilling, which includes all pelagic taxa in our dataset and 22 rostral tooth specimens of the benthic saw shark *Pristiophorus laevis* (Data Set S1). Given the high crystallinity and low amount of collagen content in tooth enameloid (i.e., <5 %wt.) (Enax et al., 2012; Raquel Zapanta LeGeros, 1981; Lübke et al., 2015; Miake et al., 1991; Vennemann et al., 2001), phosphate from powdered fossil enameloid does not require pretreatments or resin purification steps to remove organics (Grimes & Pellegrini, 2013; Mine et al., 2017; Wiedemann-Bidlack et al., 2008).

Tooth specimens from benthic taxa were typically too small to warrant drilling as a viable sampling strategy. We crushed with an agate mortar and pestle 65 tooth specimens assigned to benthic taxa obtaining a mixture of enameloid and dentin per tooth specimen (Data Set S1). Like bones, dentin a has a porous structure and higher collagen (>20 %wt.) and structural carbonate (~6 %wt.) contents than enameloid (Enax et al., 2012; Raquel Zapanta LeGeros, 1981; Lübke et al., 2015). High collagen contents or inclusions of secondary organics or carbonates (e.g., calcite) within dentin pores during the fossilization processes could alter *in vivo* oxygen isotopic signals (Enax et al., 2012; Koch et al., 1997; Larocca Conte et al., 2024; Lécuyer, 2004; Lee-Thorp, 2002; Raquel Zapanta LeGeros, 1981; Pederzani et al., 2020; Trueman et al., 2008). To prevent potential isotopic effects from secondary carbonates, crushed teeth were soaked for 24h in 300 μL 1M acetic acid buffered with a calcium acetate solution (Koch et al., 1997). The pretreatment dissolves potential secondary carbonates occluding dentin pore spaces while preserving the chemical, structural, and isotopic integrity of the tooth mineral component. We avoided pretreatments to remove collagen and other organics (e.g., sodium hydroxide) because these procedures can be sources of isotopic bias (Grimes & Pellegrini, 2013; Larocca Conte et al., 2024; Pederzani et al., 2020). Instead, recent methods resulted in pristine phosphate using an anion exchange purification step within the silver phosphate precipitation procedure to prevent the isotopic effect of organics (Larocca Conte et al., 2024, Pederzani et al., 2020; section 3.2.3).

3.13.1.1 Rapid University of Chicago Dilute Silver Phosphate Precipitation Protocol (Rapid UC)

Phosphate from powdered enameloid was extracted and precipitated via Rapid University of Chicago Dilute protocol (Rapid UC) (Mine et al., 2017). Approximately 1.0-1.5 mg of powdered enameloid from shark tooth specimens were dissolved in 50 μL 2 M HNO_3 for ~17 hours in a 2 mL microcentrifuge tube. Then, 30 μL 2.9 M HF and 50 μL 2.0 M NaOH were added to precipitate calcium fluoride. The phosphate-rich supernatant was transferred to a microcentrifuge tube and Ag_3PO_4 precipitation was initiated with 180 μL

1.09 M NH_4OH and 0.37 M $AgNO_3$ (i.e., silver ammine solution) at circumneutral pH. Crystals were rinsed five times with deionized water and dried overnight.

3.13.1.2 Silver Phosphate Oxygen Resin Analysis (SPORA) Silver Phosphate Precipitation Protocol

Phosphate from carbonate-pretreated, crushed samples were precipitated using the Silver Phosphate Oxygen Resin Analysis silver phosphate precipitation protocol (SPORA) (Larocca Conte et al., 2024). The crushed specimens were weighed to ~1.5 mg and dissolved in a 300 µL 2 M HF solution for 24 h in a 2 mL microcentrifuge tube. The supernatant was transferred into the filter unit of a Millipore Sigma centrifugal device along with ~0.4 mL of Bio-Rad AG 1-X8 anion exchange resin in hydroxide form. The resin isolates and adsorbs phosphate from the organic compounds present in the supernatant. Following, the supernatant was centrifuged and the filter unit loaded with phosphate-bound resin was transferred into a clean collector tube. The resin was rinsed seven times with a 200 µL 0.44 M $NaNO_3$ to elute phosphate into an organic-free solution. The final supernatant was transferred into a 2 mL microcentrifuge tube for the Ag_3PO_4 precipitation step. Precipitation of crystals occurred at circumneutral pH by adding a 180 µL 0.22 M $AgNO_3$ and 1.09 M NH_4OH silver ammine solution. Silver phosphate crystals were rinsed five times and dried overnight.

3.13.2 Fourier Transform Infrared Spectroscopy (FTIR) Data

We analyzed infrared features in a subset of tooth specimens to assess the degree of diagenetic alteration in elasmobranch teeth collected from La Meseta and Submeseta formations. Although these deposits show minimal diagenetic alteration following the burial (Marenssi et al., 2002), porous mediums like dentin could be sensitive to *post-mortem* alteration driven by pore water or microbial activity. While enameloid is the preferred substrate compared to dentin apatite, for $\delta^{18}O$ analysis, enameloid is not exempt from alteration when exposed to high acidic conditions (Grunenwald et al., 2014a; Lee-Thorp, 2002; Shemesh, 1990; Trueman et al., 2008; Zazzo et al., 2004). A potential source of contaminations in LMF and SMF deposits is secondary carbonate inclusions of chemical composition similar to the cement found within sandstones and cracks in mollusk specimens (Douglas et al., 2014; Ivany et al., 2008; Marenssi et al., 2002). In addition to carbonate, exposure to acidic waters, like, for example, those percolating from the overlaying soils (Souza et al., 2014) could lead to rearrangement of the phosphate bonds in its mineral fraction, including dissolution and subsequent recrystallization. Both secondary carbonate inclusions and phosphate alteration can impact the phosphate isotope composition of apatite materials.

We performed qualitative and quantitative analysis on several untreated, crushed samples (i.e., enameloid and dentin mixture; n = 4) and compared them with enameloid and dentin infrared spectra of larger tooth specimens (n = 10). Dentin samples from large teeth were drilled from the crown and, when preserved, from the root portion of tooth specimens. Due to the presence of several outliers in our $\delta^{18}O_p$ dataset, we analyzed the infrared spectra of two of these specimens exhibiting such observations (NRM-PZ P19679 and NRM-PZ P19676). Additionally, we used naturally occurring calcite (IAEA-603, International Atomic Energy Agency), Carrara marble (IAEA-CO-1, International Atomic Energy Agency), phosphate rock (NIST SRM 120c, National Institute of Standards and Technology), and synthetic hydroxyapatite (Sigma Aldrich, CAS 12167-74-7) as reference inorganic materials to compare infrared features with those of shark tooth specimens. We compared phosphate, carbonate, and amide I peak, with the latter being a proxy for nitrogen-based compounds like collagen (Amir et al., 2004; Dorozhkin, 1997; Enax et al., 2012, 2014; Grimes & Pellegrini, 2013; Grunenwald et al., 2014b; Lebon et al., 2016; Lécuyer et al., 2010; Racquel Z. LeGeros et al., 1978; Raquel Zapanta LeGeros, 1981; Leventouri, 2006; Lopes et al., 2018; Ren et al., 2014; Roche et al., 2010; Al Sekhaneh et al., 2021; Trayler et al., 2023). Infrared absorbance peaks of inorganic and organic groups are summarized in Table A3.1.

The degree of phosphate peaks' sharpness coupled to infrared features of carbonate bands are powerful tools to assess the quality of the apatite mineral lattice. We calculated the crystallinity index (CI) to evaluate phosphate peaks' sharpness as follows:

$$CI = \frac{\upsilon_4 PO_{4\ 565 cm^{-1}} + \upsilon_4 PO_{4\ 603 cm^{-1}}}{\upsilon_4 PO_{4\ 587 cm^{-1}}}$$

Where $\nu_4PO_{4\ 565\ cm\text{-}1}$ and $\nu_4PO_{4\ 603 cm\text{-}1}$ are the phosphate bending infrared modes and $\nu_4PO_{4\ 587\ cm\text{-}1}$ is the valley between the two bands at ~587 cm^{-1} (Pucéat et al., 2004; Shemesh, 1990;

Trueman et al., 2008). Carbonate content in the apatite mineral lattice is evaluated with the ν_3CO_3/ν_3PO_4 ratio ($r_{c/p}$) calculated as follows:

$$r_{c/p} = \frac{\text{area } (\upsilon_3 CO_3)}{\text{area}(\upsilon_1\upsilon_3 PO_4)}$$

Where area (ν_3CO_3) is the area included within the Type-A and Type-B carbonate bands at 1456 and 1545 cm^{-1} and area ($\nu_1\nu_3PO_4$) is the area under curve of phosphate stretching bands at 1025 cm^{-1}; Table A3.1) (Grunenwald et al., 2014a, 2014b). Pristine apatite materials have CI values <3.8, with enamel and enameloid materials showing values closer to this threshold than dentin or bones due to the lower amount of collagen and structural carbonate in the mineral lattice (i.e., sharper, and well-separated phosphate peaks). Structural carbonate content (i.e., carbonate included in apatite minerals during tooth formation) ranges from 1 to 4%wt. in enamel and enameloid of modern animals in contrast with the 4.5-7 %wt. in dentin or bone apatite of the same (Aoba et al., 1991; Enax et al., 2012; Grunenwald et al., 2014a, 2014b; Raquel Zapanta LeGeros, 1981; Lübke et al., 2015; Moreno & Aoba, 1991). Carbonate content is proportional to ν_3CO_3/ν_3PO_4 ratio and is quantified following the linear equation provided in Grunenwald et al., 2014b ($R^2 = 0.985$):

$$CO_3 \text{ wt\%.} = 28.62 * (r_{c/p}) + 0.0843$$

Table A3.1. Infrared absorbance peaks of functional groups for apatite inorganic and organic components and other materials (i.e., diagenetic carbonates).

Wavenumber (cm^{-1})	**Functional group**	**Apatite components or other material**
565	ν_4PO_4 - P-O-P bending	Apatite phosphate
603	ν_4PO_4 - P-O-P bending	Apatite phosphate
632	OH - OH-P libration	Apatite hydroxyl
668	OH - OH-P libration	Adsorbed water (diagenesis)
712	ν_4CO_3 - C-O scissoring	Diagenetic CO_3
870	ν_2CO_3 - C-O bending	Type-A, Type-B, or diagenetic CO_3
960	ν_1PO_4 - P-O-P stretch	Apatite phosphate
1025	ν_3PO_4 - P-O-P stretch	Apatite phosphate
1410	ν_3CO_3 - C-O bending	Type-B or diagenetic CO_3
1456	ν_3CO_3 - C-O bending	Type-B or diagenetic CO_3
1545	ν_3CO_3 - C-O stretching	Type-A
1620	Water – H-O-H vibration	Adsorbed water (diagenesis)
1636	Amide I + water C=O stretching	Collagen

Unaltered biogenic materials have variably collagen and carbonate content, with the latter negatively correlated with the crystallinity index. Among biogenic apatite materials, tooth enamel or enameloid shows the highest CI values and lowest organic and structural carbonate content (Enax et al., 2012; Grunenwald et al., 2014a, 2014b; Raquel Zapanta LeGeros, 1981; Shemesh, 1990). If shark teeth from LMF and SMF show minimal diagenetic alteration features, we expect 1) low to no collagen content in enameloid and low to high collagen content in dentin and crushed samples (i.e., intensity occurrence of Amide I infrared peak), 2) CI index negatively correlates to $r_{c/p}$, with enameloid materials showing higher crystallinity values and lower $r_{c/p}$ values than dentin or crushed materials, 3) carbonate content in all materials is within the expected ranges, and 4) no correlation between $\delta^{18}O_p$ and FTIR metrics.

Infrared spectra of selected tooth specimens display the expected absorbance peaks for apatite specimens (Figure A3.1a). Specimens show the typical phosphate infrared features, with sharper and well-separated bands ν_4PO_4 bands in enameloid materials. Amide I peaks are usually below the detection limit, but they could be substantially present in samples with dentin fractions (e.g., P19639 and P15940, Figure A3.1a). No samples display ν_4CO_3 or pronounced ν_2CO_3 peaks typical of calcite materials, indicating no inclusion of diagenetic carbonate in the mineral lattice (Figure A3.1a). Structural carbonate features are present in all analyzed samples except for the dentin in P15940 specimen. This specimen is unique in exhibiting variably alteration features in enameloid and dentin (Figure A3.1a-c). The dentin displays severe alteration features, with broad and low phosphate peaks when present, absence of amide I and structural carbonate, and infrared features at 712 and 1620 cm^{-1} that indicate water adsorption (Figure A3.1a; Table A3.1). Water infrared bands occur when teeth are exposed to acidic fluids that dissolve the mineral apatite lattice. This mechanism results in the removal of hydroxyl and fluorine ions followed by water adsorption (Dorozhkin, 1997; Racquel Z. LeGeros et al., 1978). The enameloid collected from the labial side of P15940 also displays similar infrared features due to water adsorption, but it preserves both phosphate and structural carbonate Type-B bands (i.e., carbonate that substitutes phosphate in the mineral lattice as teeth form; Figure A3.1a-b, Table A3.1; Enax et al., 2012, Ren et al., 2014). Diagenetic alteration, likely from apatite dissolution, is evident on the specimen. Both enameloid and dentine exhibit weathering features such as cracks on both labial and lingual views and poorly-preserved enemeloid in the lingual view only (Figure A3.1a-b). No dissolution-like alteration features are shown in other analyzed specimens (Figure A3.1d-i). In summary, the infrared features of specimens examined suggest differing degrees of exposure to diagenetic changes. However, the crystallographic sites containing carbonate and phosphate are largely intact, except for the dentin portion and part of the enameloid in one single specimen. We remark that such substrates from P15940 were not sampled for $\delta^{18}O_p$ analysis, as we drilled the enameloid preserved in its labial view.

Crystallinity and carbonate content proxies obtained from infrared spectra exhibit the expected patterns for minimal diagenetic alteration (Figure A3.2). Tooth enameloid materials consistently exhibit the highest CI and lowest $r_{c/p}$ ratio values ranging from 3.6 to 4.2 and 0.026 to 0.070, respectively (Figure A3.2a). Conversely, dentin materials from the same specimens, or enameloid-dentin mixtures, have lower CI and higher $r_{c/p}$ values (Figure

A3.2a). The CI index negatively correlates with $r_{c/p}$ ratio values (R^2= 0.71) and the majority of samples clustered below the threshold value for pristine apatite materials reported in Shemesh (1990; CI < 3.8) (Figure A3.2a). While some enameloid samples cluster above the suggested bottom limit, we consider these samples as pristine enameloid materials for several reasons. First, Shemesh (1990) does not include any apatite material with CI values between 3.8 and 4.5. Second, different taxa yield apatite materials of varying CI values that could be higher than 3.8 (Pucéat et al., 2004). Third, if alteration occurred, samples including dentin powder should display similar CI and carbonate content values, which is not the case here (Figure A3.2b). The equation extracted from Grunenwald et al.'s (2014b) dataset estimates carbonate content (CO_3 wt%) for different biogenic apatite materials that lie between the expected carbonate content range for modern enamel, enameloid, dentin, and bone materials (Figure A3.2b). All enameloid samples have carbonate content within 1 to 3 %wt., while dentin materials have higher carbonate content up to ~7%wt (Figure A3.2b). The carbonate content of enemaloid-dentin mixtures lies anywhere between the enameloid and dentin-bone endmembers (Figure A3.2b). Again, carbonate content estimates from apatite materials in shark tooth specimens show the expected patterns. Finally, when comparing $\delta^{18}O_p$ with CI and $r_{c/p}$, no significant correlation emerges between these FTIR metrics and isotopic composition of the specimens. This lack of correlation remains consistent regardless of the apatite type (i.e., enameloid and its mixture with dentin; Figure A3.3).

In conclusion, apatite materials sampled for $\delta^{18}O_p$ analysis underwent minimal diagenetic alteration, as evidenced by specimens predominantly featuring moderate to negligible organic content, intact phosphate bands, and anticipated carbonate levels. Therefore, all $\delta^{18}O_p$ values reported in this study reflect signals mediated by biological-environmental processes instead of diagenetic alteration.

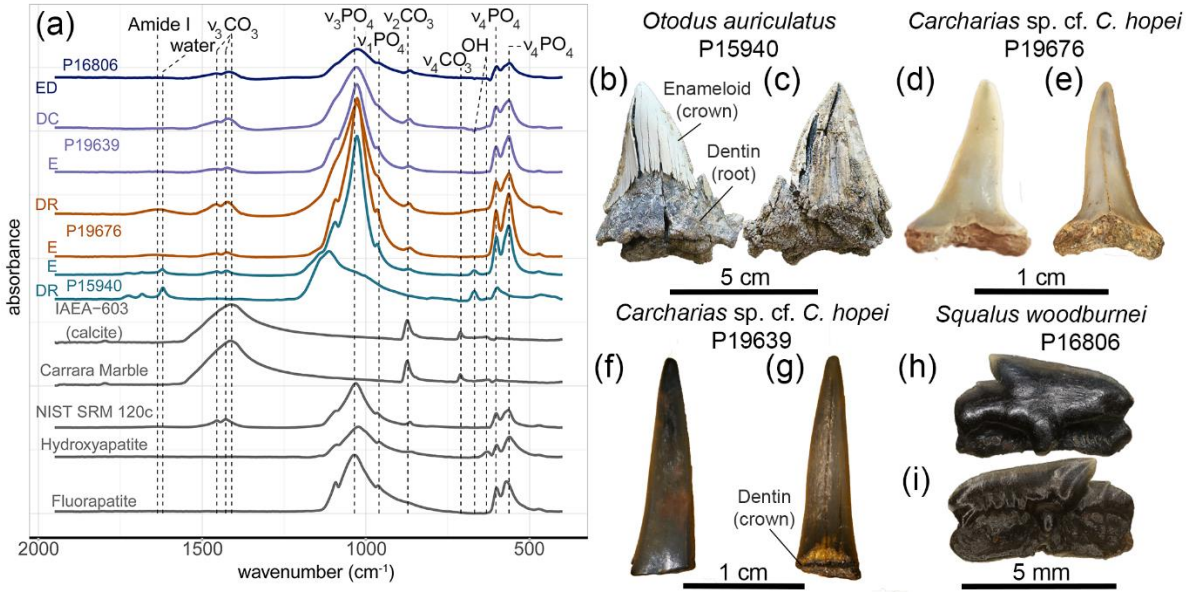

Figure A3.1. Examples of FTIR spectra collected from the NRM-PZ specimens P15940 (*Otodus auriculatus*), P19676 (*Carcharias* sp. cf. *C. hopei*), P19639 (*Carcharias* sp.), and P16806 (*Squalus woodburnei*). (a) FTIR spectra of selected representative teeth and reference materials. Enameloid, dentine, and mixed materials from shark tooth specimens display phosphate, structural carbonate, and varying amide I peaks indicating minimal alteration. The dentin portion of P15940 is uniquely characterized by severe diagenetic alteration, resulting in water adsorption and broad or missing phosphate bands. None of the samples contain inclusions of diagenetic calcite in their mineral structure, as confirmed by comparing spectra between calcite and apatite materials. Reference materials' infrared spectra are shown in grey. (b-i) Representative tooth specimens used as an example for FTIR spectra in labial (b, d, f, h) and lingual (c, e, g, i) views. Specimens P15940 and P19639 are used as examples to define enameloid and dentin areas of crown and root portions of teeth (b, g). The specimen P15940 exhibits cracks on both sides and poorly-preserved enameloid in lingual view only in contrast to other specimens. *Abbreviations*: DC, dentin sampled from the crown; DR, dentin sampled from the root; E, enameloid; ED, enameloid-dentin mixture.

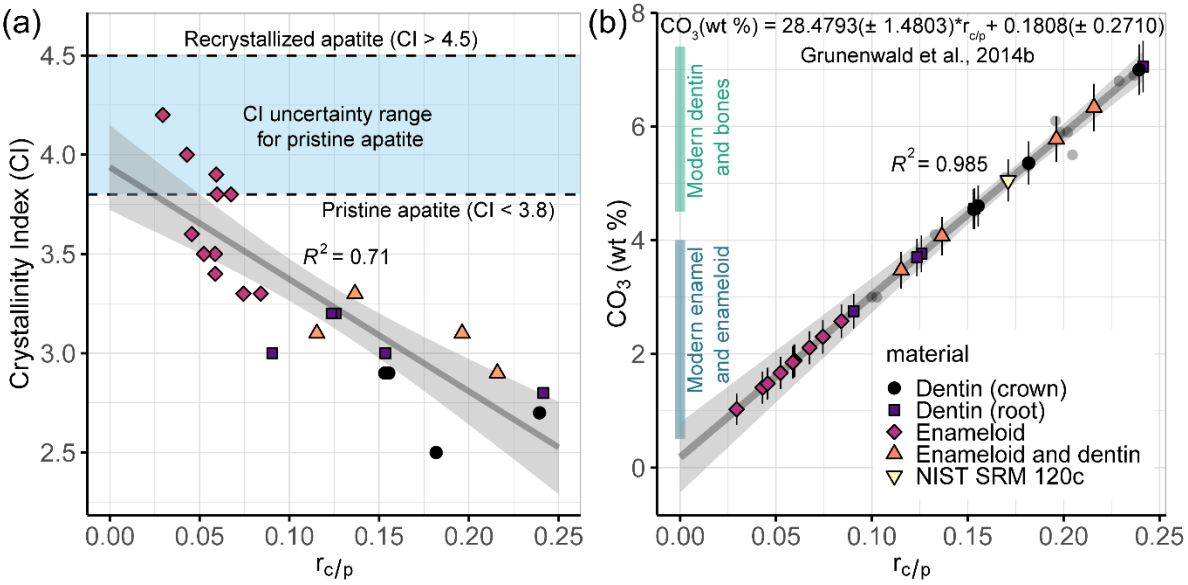

Figure A3.2. Crystallinity and carbonate content proxies calculated from infrared spectra of shark tooth samples indicate that their apatite materials are pristine. (a) Crystallinity index (CI) plotted against carbonate to phosphate ratio ($r_{c/p}$). Enameloid materials have higher CI and lower $r_{c/p}$ values than dentin apatite. The sky-blue area indicates the uncertainty range of CI values for pristine apatite materials after Shemesh (1990). (b) Carbonate content (CO_3 (wt%)) estimated from $r_{c/p}$ values following Grunenwald et al., 2014b. Enameloid and dentin materials have carbonate content within the expected ranges indicated by the blue and green lines (0.5 – 4.0 wt% and 4.5 – 7.4%, respectively). Vertical bars indicate the error of estimates within 1σ. We also estimated carbonate content for the NIST SRM 120c reference material for cross-validating the accuracy of estimates. The equation estimates a carbonate content of 5.05 ± 0.37 wt% (mean ± 1σ), which overlaps with the accepted value reported by

the National Institute of Standards and Technology (1988; mean CO_3 (wt%) ± 1σ = 4.46 ± 0.16 wt%).

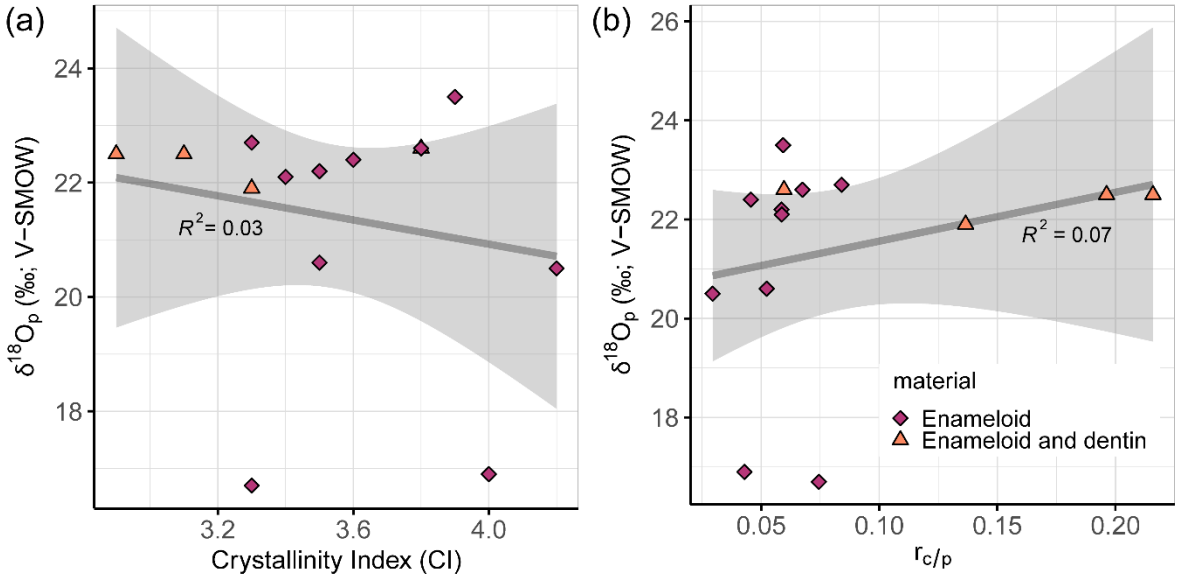

Figure A3.3. The lack of correlation between $\delta^{18}O_p$ and FTIR metrics suggests that phosphate oxygen isotope composition in shark tooth apatite is mediated by biological-environmental processes instead of being a result of diagenetic alteration. (a) $\delta^{18}O_p$ values plotted against Crystallinity index (CI; R^2 = 0.03). (b) $\delta^{18}O_p$ values plotted against $r_{c/p}$ values (R^2 = 0.07).

3.13.3 Bayesian Framework for Temperature Estimates From Sharks' $\delta^{18}O_p$ Measurements

We adopted and modified the Bayesian framework found in Griffith et al. (2023) to estimate environmental conditions from sharks with elasmobranchs' $\delta^{18}O_p$ values. Along with elasmobranchs' $\delta^{18}O_p$ data, we used model temperature and $\delta^{18}O_w$ data as prior information. The conditional probabilities of environmental variables given sharks' $\delta^{18}O_p$ are as follows:

$$P\left(T, \delta^{18}O_w \middle| \delta^{18}O_p\right) = \frac{P\left(\delta^{18}O_p \mid T, \delta^{18}O_w\right)}{P\left(\delta^{18}O_p\right)} * P\left(T, \delta^{18}O_w\right) \quad [5]$$

where $P(T, \delta^{18}O_w \mid \delta^{18}O_p)$ is the conditional probability of posterior temperature and $\delta^{18}O_w$ estimates given $\delta^{18}O_p$ data, $P(\delta^{18}O_p \mid T, \delta^{18}O_w)/P(\delta^{18}O_p)$ is the likelihood of measured $\delta^{18}O_p$ values (i.e., posterior $\delta^{18}O_p$ values) given the prior model temperature and $\delta^{18}O_w$ assumptions (Figure A3.4), which are expressed as $P(T, \delta^{18}O_w)$. Prior probabilities for seawater oxygen isotope composition of temperature use density distributions extracted from the 3× pre-industrial CO_2 model simulation within -85 - -20 °N and -105 - -15 °E grid (Figure A3.4) and are indicated as:

$$P(T) = F(T) \quad [6]$$

$$P(\delta^{18}O_w) = F(\delta^{18}O_w) \quad [7]$$

The likelihood of measured $\delta^{18}O_p$ values can be expressed as a normal distribution per given data point:

$$\delta^{18}O_p \sim N(\mu, \sigma) \quad [8]$$

where μ is the mean and σ the estimated dispersion. Finally, the joint combination of equations [5] to [8] provides the following conditional probability:

$$P\left(T, \delta^{18}O_w \middle| \delta^{18}O_p\right) = N(\mu, \sigma) * F(T) * F(\delta^{18}O_w) \quad [9]$$

Because diagenetic alteration or drastic salinity shifts (e.g., marine to brackish environments) result in lower $\delta^{18}O_p$ values and erroneous, high temperature estimates, we checked for outliers in our dataset and excluded them, if any, before executing the Bayesian framework explained above. This check ensured to capture probable temperature and $\delta^{18}O_w$ estimates in a marine environment only (see Results and Discussion sections in the main text).

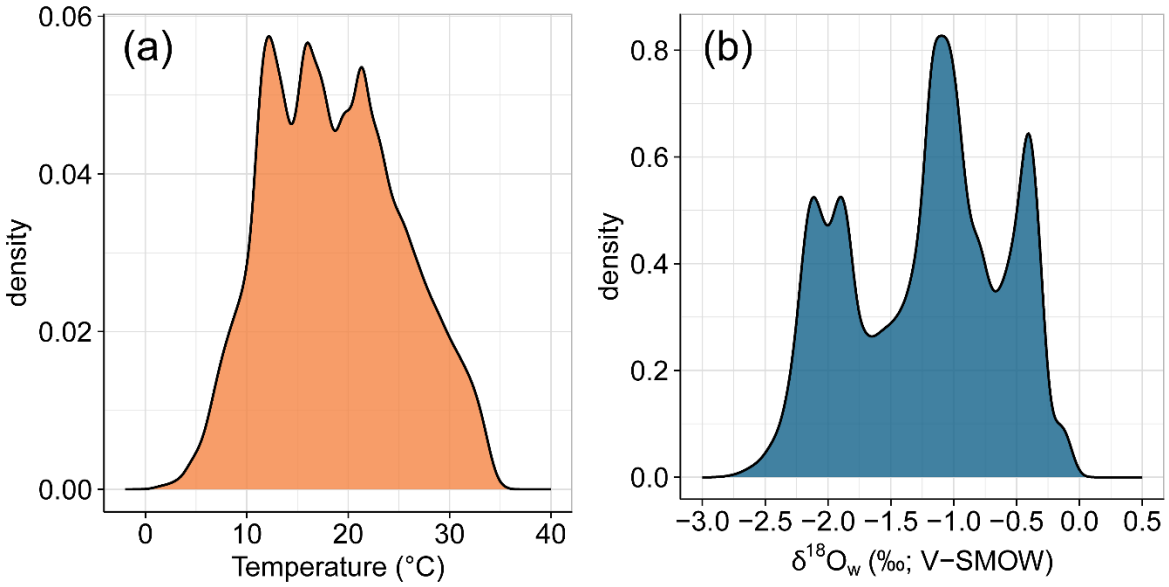

Figure A3.4. Density distributions of iCESM seawater temperature (a) and $\delta^{18}O_w$ (b) values from the 3× pre-industrial CO_2 model simulation (Zhu et al., 2020). Values were extracted from the grid spanning latitudes -85 - -20 °N and longitudes to -105 - -15 °E, covering an area that includes South America and parts of Antarctica's continent. Temperatures and $\delta^{18}O_w$ range values are -0.43 – 35.58 °C and -2.85 – 0.00 ‰, respectively.

3.13.4 iCESM Seasonal Values for Seymour Island During the Eocene

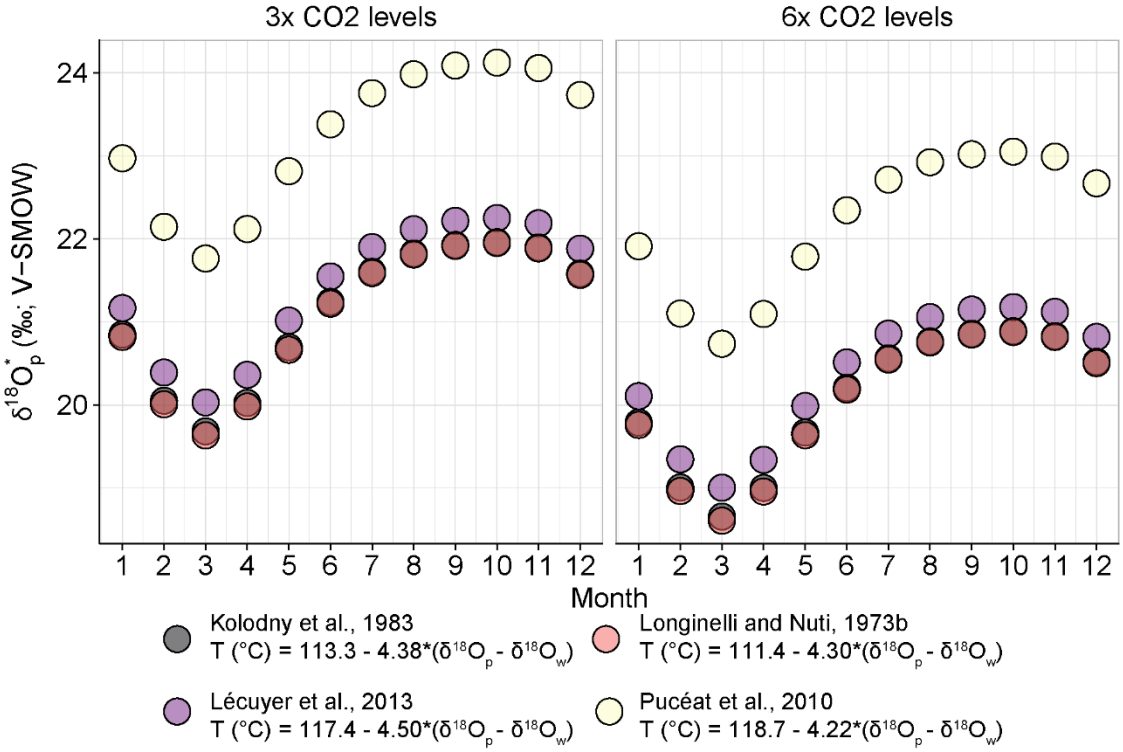

Figure A3.5. Simulated $\delta^{18}O_p$* values could vary significantly depending on the paleothermometer equation used. The plot shows monthly averaged $\delta^{18}O_p$* values for Seymour Island, extracted from the 3× (left panel) and 6× CO_2 pre-industrial level (right panel) iCESM simulations within water column of 25 m b.s.l (Zhu et al., 2020). Simulated $\delta^{18}O_p$* were estimated using model temperature and $\delta^{18}O_w$ values for Seymour Island listed in Table SI4.1 for each simulation. Note that there are small differences in $\delta^{18}O_p$* estimates when using the paleothermometers after Lécuyer et al., (2013; recalibrated from Kolodny et al., (1983); purple circles), Kolodny et al., (1983; grey circles), and Longinelli & Nuti (1973b; orange circles). Estimates can vary up to few per mill when using the equation after Pucéat et al., (2010; yellow circles). These differences likely stem from experimental errors because the Pucéat et al. equation was derived from controlled experiments on fish in aquaria, where the isotopic composition of the water tank was not consistently maintained. Such uncontrolled factor likely leads to significant noise in the determination of the oxygen-isotope fractionation equation (Lécuyer et al., 2013; Pucéat et al., 2010).

Table A3.2. Simulated monthly averaged temperature (T(°C)), $\delta^{18}O_w$, $\delta^{18}O_p$ ($\delta^{18}O_p$*), and $\delta^{18}O_c$ ($\delta^{18}O_c$*) values for the iCESM model simulation for 3× and 6× CO_2 pre-industrial levels within water column of 25 m b.s.l (Zhu et al., 2020). Simulated $\delta^{18}O_p$* values are estimated using the paleothermometer equation after Kolodny et al. (1983) recalibrated by Lécuyer et al. (2013). Simulated $\delta^{18}O_c$* values are performed using the equation after Grossman & Ku (1986) for aragonite bivalve shells.

Month	Seymour Island seasonal trends from iCESM model (25 m b.s.l.)							
	3× pre-industrial CO_2 levels				6× pre-industrial CO_2 levels			
	$\delta^{18}O_w$ (‰; V-SMOW)	T (°C)	$\delta^{18}O_p$*(‰; V-SMOW)	$\delta^{18}O_c$*(‰ ; V-PDB)	$\delta^{18}O_w$ (‰; V-SMOW)	T (°C)	$\delta^{18}O_p$*(‰ ; V-SMOW)	$\delta^{18}O_c$*(‰ ; V-PDB)
1	-1.37	15.97	21.2	-0.3	-2.43	19.14	20.1	-2.1
2	-1.40	19.32	20.4	-1.1	-2.45	23.18	19.3	-3.0
3	-1.43	20.82	20.0	-1.5	-2.46	25.14	19.0	-3.5
4	-1.44	19.27	20.4	-1.1	-2.47	23.68	19.3	-3.2
5	-1.43	16.39	21.0	-0.5	-2.46	20.47	20.0	-2.4
6	-1.41	14.10	21.5	0.1	-2.44	17.73	20.5	-1.8
7	-1.38	12.63	21.9	0.5	-2.42	15.79	20.9	-1.3
8	-1.34	11.83	22.1	0.7	-2.40	14.54	21.1	-1.0
9	-1.31	11.52	22.2	0.8	-2.38	13.75	21.1	-0.8
10	-1.30	11.43	22.3	0.8	-2.37	13.41	21.2	-0.7
11	-1.31	11.65	22.2	0.7	-2.38	13.71	21.1	-0.8
12	-1.34	12.89	21.9	0.4	-2.41	15.48	20.8	-1.2

3.13.5 Bulk Bivalve $\delta^{18}O$ Values

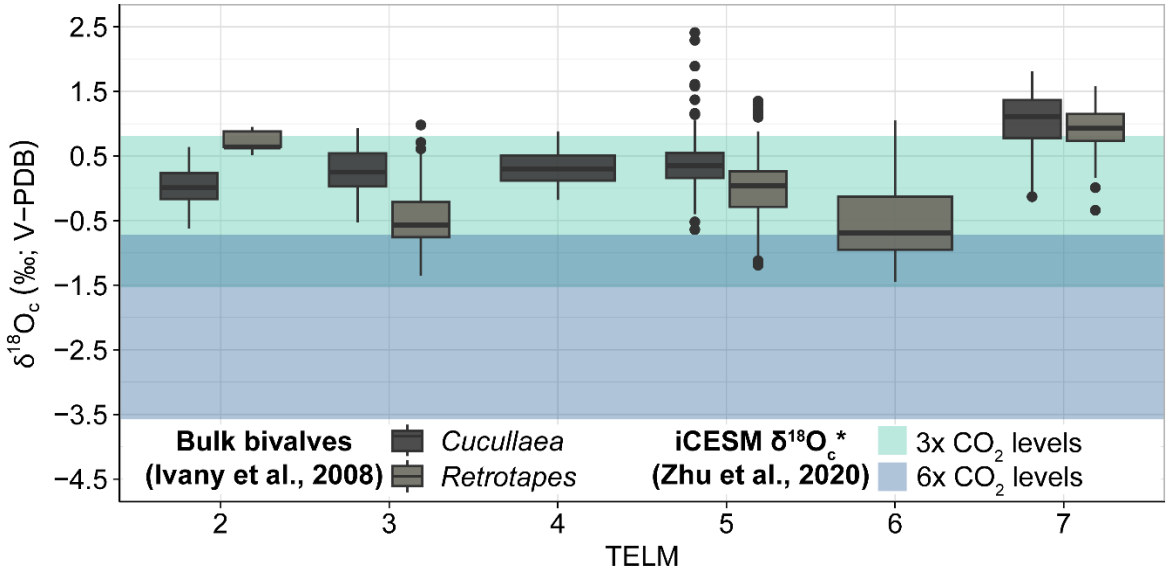

Figure A3.6. Bulk $\delta^{18}O_c$ values of co-occurring *Cucullaea* and *Retrotapes* exhibit a cooling trend towards TELM 7 (Ivany et al., 2008). These bivalves grow in alternating seasons and reflect environmental conditions consistent with seasonal $\delta^{18}O_c$* values estimated using the forward iCESM simulation for 3× CO_2 pre-industrial levels within the water column at 25 m b.s.l (Zhu et al., 2020), calculated using the equation after Grossman & Ku (1986). A discrepancy between model and empirical data arises in TELM 7, where median and 75th percentile values exceed the simulated range. This suggests that local temperatures dropped towards the late Eocene, a change not predicted fully by the simulation scaled with such CO_2 boundary conditions. The green and light blue shaded areas are simulated $\delta^{18}O_c$* values for 3× and 6× CO_2 pre-industrial levels, respectively (Table A3.3).

Table A3.3. Summary statistics of bulk $\delta^{18}O_c$ values of co-occurring *Cucullaea* and *Retrotapes* per TELM unit (Zhu et al., 2020).

Telm	**Bulk bivalves $\delta^{18}O_c$ values (‰; V-PDB)**			
	Cucullaea		***Retrotapes***	
	mean ± 1σ	**median**	**mean ± 1σ**	**median**
2	0.02 ± 0.34	0.01	0.72 ± 0.18	0.64
3	0.27 ± 0.34	0.25	-0.47 ± 0.49	-0.57
4	0.32 ± 0.26	0.30	-	-
5	0.39 ± 0.40	0.35	-0.00 ± 0.48	0.04
6	-	-	-0.49 ± 0.64	-0.69
7	1.04 ± 0.43	1.11	0.90 ± 0.32	0.93

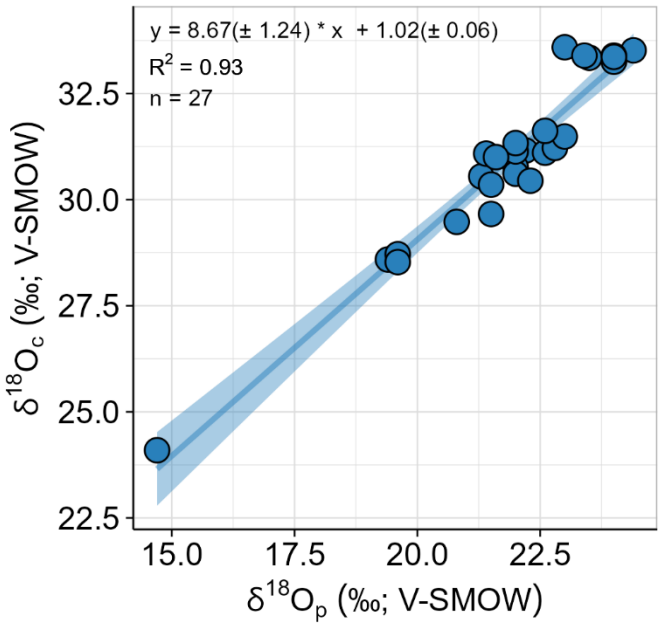

Figure A3.7. Correlation between oxygen isotope values of phosphate (x-axis) and carbonate (y-axis) from marine invertebrates (n = 27) after Longinelli & Nuti (1973b). The isotopic composition of both phosphate and carbonate is in the V-SMOW scale. Data plotted here are raw measurements from marine invertebrates. The linear fit has a slope close to one ($R^2 = 0.93$).

Table A3.4. Summary statistics of bulk $\delta^{18}O_p$* values of co-occurring bivalves per TELM. Estimates were performed by converting $\delta^{18}O_c$ (V-PDB) to $\delta^{18}O_c$ (V-SMOW) and to $\delta^{18}O_p$* (V-SMOW) using transfer functions after Kim et al. (2015) and Longinelli & Nuti (1973).

Telm	**Bulk bivalves $\delta^{18}O_p$* values (‰; V-SMOW)**	
	mean ± 2σ	**median**
2	22.1 ± 0.9	22.1
3	21.7 ± 1.1	21.8
4	22.2 ± 0.5	22.2
5	22.1 ± 1.0	22.1
6	21.4 ± 1.3	21.2
7	22.8 ± 0.7	22.8

3.13.6 iCESM Seasonal Values for Southern Chile During the Eocene

Table A3.5. Simulated monthly averaged temperature (T(°C)), $\delta^{18}O_w$, and $\delta^{18}O_p$ ($\delta^{18}O_p$*), values for the iCESM model simulation for 3× CO_2 pre-industrial levels within water column of 25 m b.s.l (Zhu et al., 2020).

Month	**Southern Chile seasonal trends from 3× pre-industrial CO_2 iCESM model (25 m b.s.l.)**		
	$\delta^{18}O_w$ (‰; V-SMOW)	**T (°C)**	**$\delta^{18}O_p$*(‰; V-SMOW)**
1	-1.59	21.68	19.7
2	-1.59	24.41	19.1
3	-1.59	26.14	18.7
4	-1.59	25.90	18.7
5	-1.59	24.00	19.2
6	-1.58	21.65	19.7
7	-1.58	19.68	20.1
8	-1.58	18.34	20.4
9	-1.57	17.50	20.6
10	-1.58	17.20	20.7
11	-1.58	17.64	20.6
12	-1.59	19.17	20.2

3.13.7 $\delta^{18}O_p$ Values of Elasmobranch Taxa per TELM Units

Table A3.6: Tooth specimens with outlier $\delta^{18}O_p$ values in TELMs have *z*-scores lower than -2.

Sample ID	Taxon	TELM	$\delta^{18}O_p$ (‰; V-SMOW)	Environment	*z* score
P15838	*Brachycarcharias lerichei*	2	16.6	pelagic	-3.64
P19661	*Carcharias* sp. cf. C. *hopei*	4	18.7	pelagic	-2.44
P19676	*Carcharias* sp. cf. C. *hopei*	4	16.9	pelagic	-3.76
P15778	*Brachycarcharias lerichei*	5	18.4	pelagic	-2.91
P15821	Dalatiidae indet.	5	18.5	benthic	-2.83
P19687	*Carcharias* sp. cf. C. *hopei*	5	17.8	pelagic	-3.41
P19679	*Carcharias* sp. cf. C. *hopei*	5	16.7	pelagic	-4.34
P19696	*Carcharias* sp. cf. C. *hopei*	6	20.6	pelagic	-3.07
P16005	*Squatina* sp.	7	17.5	benthic	-2.20

Table A3.7. Summary statistics of $\delta^{18}O_p$ values of pelagic and benthic elasmobranch taxa per TELM unit. The table reports values for taxa with n specimens ≥ 4 across TELMs.

Taxon	TELM 2			TELM 3			TELM 4			TELM 5			TELM 6			TELM 7		
	n	$\delta^{18}O_p$ (‰; V-SMOW)		n	$\delta^{18}O_p$ (‰; V-SMOW)		n	$\delta^{18}O_p$ (‰; V-SMOW)		n	$\delta^{18}O_p$ (‰; V-SMOW)		n	$\delta^{18}O_p$ (‰; V-SMOW)		n	$\delta^{18}O_p$ (‰; V-SMOW)	
		mean ± 1σ	median		mean ± 1σ	median		mean ± 1σ	median		mean ± 1σ	median		mean ± 1σ	median		mean ± 1σ	median
Brachycarcharias lerichei	5	21.4 ± 2.8	22.6	-	-	-	11	22.9 ± 0.5	22.9	9	21.8 ± 1.7	22.5	-	-	-	-	-	-
Carcharias sp. cf. *C. hopei*	11	22.4 ± 1.1	22.5	15	22.6 ± 0.9	22.8	21	22.4 ± 1.6	22.7	13	21.3 ± 2.0	22.0	9	22.2 ± 0.9	22.4	-	-	-
Kallodentis rhytistemma	-	-	-	-	-	-	-	-	-	6	21.0 ± 0.7	20.8	-	-	-	-	-	-
Otodus auriculatus	-	-	-	-	-	-	7	20.6 ± 0.3	20.5	-	-	-	-	-	-	-	-	-
Pristiophorus laevis	-	-	-	-	-	-	6	23.2 ± 0.7	23.4	16	22.7 ± 0.9	22.8	4	22.9 ± 0.3	22.9	-	-	-
Raja amphitrita	-	-	-	-	-	-	-	-	-	14	22.1 ± 0.5	22.4	-	-	-	-	-	-
Squalus weltoni	-	-	-	-	-	-	-	-	-	11	21.8 ± 0.4	21.7	-	-	-	-	-	-
Squalus woodburnei	-	-	-	-	-	-	-	-	-	7	22.4 ± 0.4	22.4	-	-	-	-	-	-
Squatina sp.	-	-	-	-	-	-	-	-	-	11	21.6 ± 0.8	21.6	4	22.5 ± 0.3	22.6	-	-	-
Striatolamia macrota	12	21.8 ± 1.0	21.6	7	21.9 ± 0.9	21.8	15	21.2 ± 0.8	21.3	8	21.9 ± 0.6	22.0	-	-	-	-	-	-
Striatolamia sp. cf. *S. macrota*	-	-	-	-	-	-	-	-	-	-	-	-	-	-	-	4	22.3 ± 0.7	22.5

3.13.8 Temperature Estimates From $\delta^{18}O_p$ Values of Elasmobranchs

Table A3.8. Temperature (T (°C)) estimates from $\delta^{18}O_p$ values of pelagic and benthic elasmobranch taxa. These estimates were performed using the Bayesian framework described in SM3. The model was fed by grouping $\delta^{18}O_p$ values by taxa measured across all TELM units, providing mean and confidence interval at 95% (CI) values that reflect general temperature preferences of species.

Taxon	**T (°C) - mean**	**T (°C) - CI**
Brachycarcharias lerichei	11.7	7.4
Carcharias sp. cf. *C. hopei*	10.2	6.7
Striatolamia macrota	14.2	6.7
Otodus auriculatus	18.7	7.3
Pristiophorus laevis	9.1	6.9
Raja amphitrita	11.7	6.6
Squalus weltoni	13.3	6.8
Squalus woodburnei	10.9	7.1
Squatina sp.	14.3	7.8
Kallodentis rhytistemma	16.8	8.2

3.13.9 References From the Appendix

Amir, S., Hafidi, M., Merlina, G., Hamdi, H., & Revel, J.-C. (2004). Elemental analysis, FTIR and 13C-NMR of humic acids from sewage sludge composting. Agronomie, 24, 13–18. https://doi.org/10.1051/agro

Aoba, T., Miake, Y., Shimoda, S., Prostak, K., Moreno, E. C., & Suga, S. (1991). Dental Apatites in in Vertebrate Species: Morphology and Chemical Properties BT - Mechanisms and Phylogeny of Mineralization in Biological Systems. In S. Suga & H. Nakahara (Eds.) (pp. 459–463). Tokyo: Springer Japan.

Dorozhkin, S. V. (1997). Surface reactions of apatite dissolution. Journal of Colloid and Interface Science, 191(2), 489–497. https://doi.org/10.1006/jcis.1997.4942

Douglas, P. M. J., Affek, H. P., Ivany, L. C., Houben, A. J. P., Sijp, W. P., Sluijs, A., et al. (2014). Pronounced zonal heterogeneity in Eocene southern high-latitude sea surface temperatures. Proceedings of the National Academy of Sciences of the United States of America, 111(18), 6582–6587. https://doi.org/10.1073/pnas.1321441111

Enax, J., Prymak, O., Raabe, D., & Epple, M. (2012). Structure, composition, and mechanical properties of shark teeth. Journal of Structural Biology, 178(3), 290–299. https://doi.org/10.1016/j.jsb.2012.03.012

Enax, J., Janus, A. M., Raabe, D., Epple, M., & Fabritius, H. O. (2014). Ultrastructural organization and micromechanical properties of shark tooth enameloid. In Acta Biomaterialia (Vol. 10, pp. 3959–3968). Elsevier Ltd. https://doi.org/10.1016/j.actbio.2014.04.028

Griffiths, M. L., Eagle, R. A., Kim, S. L., Flores, R. J., Becker, M. A., IV, H. M. M., et al. (2023). Endothermic physiology of extinct megatooth sharks. Proceedings of the National Academy of Sciences, 120(27), e2218153120. https://doi.org/10.1073/PNAS.2218153120

Grimes, V., & Pellegrini, M. (2013). A comparison of pretreatment methods for the analysis of phosphate oxygen isotope ratios in bioapatite. Rapid Communications in Mass Spectrometry, 27(3), 375–390. https://doi.org/10.1002/rcm.6463

Grossman, E. L., & Ku, T. L. (1986). Oxygen and carbon isotope fractionation in biogenic aragonite: Temperature effects. Chemical Geology: Isotope Geoscience Section, 59(C), 59–74. https://doi.org/10.1016/0168-9622(86)90057-6

Grunenwald, A., Keyser, C., Sautereau, A. M., Crubézy, E., Ludes, B., & Drouet, C. (2014a). Novel contribution on the diagenetic physicochemical features of bone and teeth minerals, as substrates for ancient DNA typing. Analytical and Bioanalytical Chemistry, 406(19), 4691–4704. https://doi.org/10.1007/s00216-014-7863-z

Grunenwald, A., Keyser, C., Sautereau, A. M., Crubézy, E., Ludes, B., & Drouet, C. (2014b). Revisiting carbonate quantification in apatite (bio)minerals: A validated FTIR methodology. Journal of Archaeological Science, 49(1), 134–141. https://doi.org/10.1016/j.jas.2014.05.004

Ivany, L. C., Lohmann, K. C., Hasiuk, F., Blake, D. B., Glass, A., Aronson, R. B., & Moody, R. M. (2008). Eocene climate record of a high southern latitude continental shelf: Seymour Island, Antarctica. Bulletin of the Geological Society of America, 120(5–6), 659–678. https://doi.org/10.1130/B26269.1

Kim, S. T., Coplen, T. B., & Horita, J. (2015). Normalization of stable isotope data for carbonate minerals: Implementation of IUPAC guidelines. Geochimica et Cosmochimica Acta, 158, 276–289. https://doi.org/10.1016/j.gca.2015.02.011

Koch, P. L., Tuross, N., & Fogel, M. L. (1997). The effects of sample treatment and diagenesis on the isotopic integrity of carbonate in biogenic hydroxylapatite. Journal of Archaeological Science, 24(5), 417–429. https://doi.org/10.1006/jasc.1996.0126

Kolodny, Y., Luz, B., & Navon, O. (1983). Oxygen isotope variations in phosphate of biogenic apatites, I. Fish bone apatite-rechecking the rules of the game. Earth and Planetary Science Letters, 64(3), 398–404. https://doi.org/10.1016/0012-821X(83)90100-0

Larocca Conte, G., Lopes, L. E., Mine, A. H., Trayler, R. B., & Kim, S. L. (2024). SPORA, a new silver phosphate precipitation protocol for oxygen isotope analysis of small, organic-rich bioapatite samples. Chemical Geology, 651, 122000. https://doi.org/10.1016/J.CHEMGEO.2024.122000

Lebon, M., Reiche, I., Gallet, X., Bellot-Gurlet, L., & Zazzo, A. (2016). Rapid quantification of bone collagen content by ATR-FTIR spectroscopy. Radiocarbon, 58(1), 131–145. https://doi.org/10.1017/RDC.2015.11

Lécuyer, C. (2004). Oxygen Isotope Analysis of Phosphate. Handbook of Stable Isotope Analytical Techniques, (September 2004), 482–496. https://doi.org/10.1016/B978-044451114-0/50024-7

Lécuyer, C., Balter, V., Martineau, F., Fourel, F., Bernard, A., Amiot, R., et al. (2010). Oxygen isotope fractionation between apatite-bound carbonate and water determined from controlled experiments with synthetic apatites precipitated at 10-37 °C. Geochimica et Cosmochimica Acta, 74(7), 2072–2081. https://doi.org/10.1016/j.gca.2009.12.024

Lécuyer, C., Amiot, R., Touzeau, A., & Trotter, J. (2013). Calibration of the phosphate δ18O thermometer with carbonate-water oxygen isotope fractionation equations. Chemical Geology, 347, 217–226.

Lee-Thorp, J. (2002). Two decades of progress towards understanding fossilization processes and isotopic signals in calcified tissue minerals. Archaeometry, 44(3), 435–446. https://doi.org/10.1111/1475-4754.t01-1-00076

LeGeros, Racquel Z., Bonel, G., & Legros, R. (1978). Types of "H2O" in human enamel and in precipitated apatites. Calcified Tissue Research, 26(1), 111–118. https://doi.org/10.1007/BF02013245/METRICS

LeGeros, Raquel Zapanta. (1981). Apatites in biological systems. Progress In Crystal Growth And Characterization, 4(1–2), 1–45. https://doi.org/10.1016/0146-3535(81)90046-0

Leventouri, T. (2006). Synthetic and biological hydroxyapatites: Crystal structure questions. Biomaterials, 27(18), 3339–3342. https://doi.org/10.1016/j.biomaterials.2006.02.021

Longinelli, A., & Nuti, S. (1973). Revised phosphate-water isotopic temperature scale. Earth and Planetary Science Letters, 19(3), 373–376. https://doi.org/10.1016/0012-821X(73)90088-5

Lopes, C. de C. A., Limirio, P. H. J. O., Novais, V. R., & Dechichi, P. (2018, October 21). Fourier transform infrared spectroscopy (FTIR) application chemical characterization of enamel, dentin and bone. Applied Spectroscopy Reviews. Taylor & Francis. https://doi.org/10.1080/05704928.2018.1431923

Lübke, A., Enax, J., Loza, K., Prymak, O., Gaengler, P., Fabritius, H. O., et al. (2015). Dental lessons from past to present: Ultrastructure and composition of teeth from plesiosaurs, dinosaurs, extinct and recent sharks. RSC Advances, 5(76), 61612–61622. https://doi.org/10.1039/c5ra11560d

Marenssi, S. A., Net, L. I., & Santillana, S. N. (2002). Provenance, environmental and paleogeographic controls on sandstone composition in an incised-valley system: The Eocene La Meseta Formation, Seymour Island, Antarctica. Sedimentary Geology, 150(3–4), 301–321. https://doi.org/10.1016/S0037-0738(01)00201-9

Miake, Y., Aoba, T., Moreno, E. C., Shimoda, S., Prostak, K., & Suga, S. (1991). Ultrastructural studies on crystal growth of enameloid minerals in elasmobranch and teleost fish. Calcified Tissue International, 48(3), 204–217. https://doi.org/10.1007/BF02570556

Mine, A. H., Waldeck, A., Olack, G., Hoerner, M. E., Alex, S., & Colman, A. S. (2017). Microprecipitation and δ18O analysis of phosphate for paleoclimate and biogeochemistry research. Chemical Geology, 460(March), 1–14. https://doi.org/10.1016/j.chemgeo.2017.03.032

Moreno, E. C., & Aoba, T. (1991). Formation and Solubility of Carbonated Tooth Minerals BT - Mechanisms and Phylogeny of Mineralization in Biological Systems. In S. Suga & H. Nakahara (Eds.) (pp. 179–186). Tokyo: Springer Japan.

National Institute of Standards and Technology. (1988). Standard Reference Material 120c Florida Phosphate Rock. Gaithersburg.

Pederzani, S., Snoeck, C., Wacker, U., & Britton, K. (2020). Anion exchange resin and slow precipitation preclude the need for pretreatments in silver phosphate preparation for oxygen isotope analysis of bioapatites. Chemical Geology, 534, 119455. https://doi.org/10.1016/j.chemgeo.2019.119455

Pucéat, E., Reynard, B., & Lécuyer, C. (2004). Can crystallinity be used to determine the degree of chemical alteration of biogenic apatites? Chemical Geology, 205(1–2), 83–97. https://doi.org/10.1016/j.chemgeo.2003.12.014

Pucéat, E., Joachimski, M. M., Bouilloux, A., Monna, F., Bonin, A., Motreuil, S., et al. (2010). Revised phosphate-water fractionation equation reassessing paleotemperatures derived from biogenic apatite. Earth and Planetary Science Letters, 298(1–2), 135–142. https://doi.org/10.1016/j.epsl.2010.07.034

Ren, F., Ding, Y., & Leng, Y. (2014). Infrared spectroscopic characterization of carbonated apatite: A combined experimental and computational study. Journal of Biomedical Materials Research - Part A, 102(2), 496–505. https://doi.org/10.1002/jbm.a.34720

Roche, D., Ségalen, L., Balan, E., & Delattre, S. (2010). Preservation assessment of Miocene-Pliocene tooth enamel from Tugen Hills (Kenyan Rift Valley) through FTIR, chemical and stable-isotope analyses. Journal of Archaeological Science, 37(7), 1690–1699. https://doi.org/10.1016/j.jas.2010.01.029

Al Sekhaneh, W., Akkam, Y. H., Kamel, G., Drabee, A., & Popp, J. (2021). Investigation of ancient teeth using Raman spectroscopy and synchrotron radiation Fourier-transform infrared (SR-μFTIR): mapping and novel method of dating. Digest Journal of Nanomaterials and Biostructures, 16(2), 713–724.

Shemesh, A. (1990). Crystallinity and diagenesis of sedimentary apatites. Geochimica et Cosmochimica Acta, 54(9), 2433–2438. https://doi.org/10.1016/0016-7037(90)90230-I

Souza, K. K. D., Schaefer, C. E. G. R., Simas, F. N. B., Spinola, D. N., & de Paula, M. D. (2014). Soil formation in Seymour Island, Weddell Sea, Antarctica. Geomorphology, 225(C), 87–99. https://doi.org/10.1016/j.geomorph.2014.03.047

Trayler, R. B., Landa, P. V., & Kim, S. L. (2023). Evaluating the efficacy of collagen isolation using stable isotope analysis and infrared spectroscopy. Journal of Archaeological Science, 151, 105727. https://doi.org/10.1016/j.jas.2023.105727

Trueman, C. N., Privat, K., & Field, J. (2008). Why do crystallinity values fail to predict the extent of diagenetic alteration of bone mineral? Palaeogeography, Palaeoclimatology, Palaeoecology, 266(3–4), 160–167. https://doi.org/10.1016/j.palaeo.2008.03.038

Vennemann, T. W., Hegner, E., Cliff, G., & Benz, G. W. (2001). Isotopic composition of recent shark teeth as a proxy for environmental conditions. Geochimica et Cosmochimica Acta, 65(10), 1583–1599. https://doi.org/https://doi.org/10.1016/S0016-7037(00)00629-3

Wiedemann-Bidlack, F. B., Colman, A. S., & Fogel, M. L. (2008). Phosphate oxygen isotope analysis on microsamples of bioapatite: removal of organic contamination and minimization of sample size. Rapid Communications in Mass Spectrometry, 22, 1457–1466. https://doi.org/10.1002/rcm.3553

Zazzo, A., Lécuyer, C., & Mariotti, A. (2004). Experimentally-controlled carbon and oxygen isotope exchange between bioapatites and water under inorganic and microbially-

mediated conditions. Geochimica et Cosmochimica Acta, 68(1), 1–12. https://doi.org/10.1016/S0016-7037(03)00278-3

Zhu, J., Poulsen, C. J., Otto-Bliesner, B. L., Liu, Z., Brady, E. C., & Noone, D. C. (2020). Simulation of early Eocene water isotopes using an Earth system model and its implication for past climate reconstruction. Earth and Planetary Science Letters, 537, 116164. https://doi.org/10.1016/j.epsl.2020.116164

4. Chapter 3: Bridging Past and Future Ecology of Sand Tiger Sharks Through the Lens of Isotope Geochemistry and Tooth Morphometry

4.1 Abstract

Understanding habitat use and diet is crucial for assessing ecological redundancy among sympatric sharks, especially given their significant decline in recent decades and the potential impact of their removal on ecosystems. However, studying the ecology of predators with complex life history details like sharks poses challenges. Throughout geological time, sharks have undergone multiple evolutionary diversifications, and their fossil record can provide valuable insights for modern conservation efforts, offering a window into how ancient species responded to similar climatic pressures and environmental changes. Here, we document the ecological redundancy of the fossil sand tiger sharks *Carcharias* sp. cf. *C. hopei* and *Striatolamia macrota*, both closely related to the critically endangered extant *Carcharias taurus*, from the Middle and Middle-Late Eocene deposits of Seymour Island (Antarctica). We analyzed multiple metrics from isolated fossil teeth, including crown morphology, $\delta^{18}O_p$, $\delta^{66}Zn$, and crown height to quantify general trophic ecology and habitat preference between fossil taxa and changes through time and ontogeny. We compared geochemical proxies and size metrics with those of *C. taurus* to identify which fossil sand tiger sharks serve as the closest ecological analog. Comparison in tooth morphology between fossil sand tiger sharks could suggest similarities in resource use between fossil sharks, which was further highlighted by integrating geochemical and morphometric proxies. Tooth $\delta^{18}O_p$ and $\delta^{66}Zn$ values in fossil sand tigers are similar, but lower than those of the extant *C. taurus*, indicating preferences for higher temperatures, lower salinity, and potentially higher trophic levels. Among sand tigers, *S. macrota* is often larger than *Carcharias* individuals. While $\delta^{66}Zn$ values and body size values are invariant, $\delta^{18}O_p$ values in *Carcharias* sp. and *S. macrota* suggest habitat use shift through time, likely adjusting their habitat preferences during the cooling that occurred during the Late Eocene. When considering ontogeny, we found some variations in habitat use and foraging strategies within and between fossil sand tiger sharks of varying sizes. Notably, juvenile *Carcharias* sp. could be more opportunistic, likely utilizing estuarine habitats, whereas adult individuals exploit deeper and shallower marine environments. In contrast, *S. macrota* shows a tendency to occupy pelagic zones, potentially feeding at lower trophic levels until reaching larger sizes or most of its diet consists of prey from offshore areas. This multiproxy approach underscores the high ecological redundancy among Eocene sand tiger sharks, suggesting that the ecological roles of *Carcharias* sp. can serve as valuable analogs for understanding the habitat preferences and resource use of modern *C. taurus*. Our study provides critical insights into the evolutionary ecology of sand tiger sharks, enhancing conservation strategies for extant species in the context of ongoing climatic changes.

4.2 Introduction

Sharks (Elasmobranchii) are a diverse group of marine predators that occupy trophic positions along a continuum from meso- to apex predators, depending on the structure of the marine ecosystems (Compagno, 2002; Heithaus et al., 2008; Latour & Gartland, 2020; Roff et al., 2016). As predators, they play critical roles in regulating prey populations and behaviors, contributing to ecosystem stability through both top-down and bottom-up effects (Ferretti et al., 2010; Roff et al., 2016). Shark populations have dramatically declined over recent decades due to fishing pressure and climate change, with potentially detrimental consequences for the ecosystems they inhabit (Baum et al., 2003; Birkmanis et al., 2020; Ferretti et al., 2010; Pantoja-Echevarría et al., 2022; Reid et al., 2011; Roff et al., 2016). The impact of these declines remains uncertain, as it depends on species diversity and the extent of ecological redundancy, both of which affect interactions and stability within ecosystems (Rosenfeld, 2002). Many sharks are sympatric, often occurring in the same habitats and exploiting similar resources depending on their ontogeny, seasonality, and prey availability (Ferretti et al., 2010; Heithaus et al., 2007; Heupel et al., 2019; Hussey et al., 2011; Pantoja-Echevarría et al., 2022; Roff et al., 2016). However, the degree of habitat and resource overlap among extant shark species in space and time is largely unexplored. Conservation efforts could benefit from understanding habitat use and trophic positions in coexisting shark species to assess the impact of their removal, but could also be informed by how ancient species have adapted under similar climatic pressure in ancient settings.

Elasmobranchs originated during the Ordovician, around 400 million years ago (Cappetta, 2012), and survived mass extinction and climate change events. In addition, past periods of climate change, such as the Late Cretaceous, the Eocene, and the Miocene spurred diversification (Condamine et al., 2019; Cooper & Pimiento, 2024). Among these geological times, the Eocene Epoch (56 – 33.9 Ma) offers valuable parallels to today's climate crisis (Burke et al., 2018) and preserves the highest diversity of shark genera in the Cenozoic (Cappetta, 2012; Condamine et al., 2019; Cooper & Pimiento, 2024). Therefore, the Eocene is a likely Epoch to document the ecological redundancy between elasmobranch predators in terms of habitat use and trophic ecology, potentially providing essential context for assessing the ecological roles of extant sharks.

Although most Eocene sharks are preserved as isolated teeth (Cappetta, 2012), their geochemistry, size, and shape serve as crucial archives of habitat use and feeding ecology. Stable oxygen isotopes from phosphate in tooth enameloid bioapatite ($^{18}O/^{16}O$; $\delta^{18}O_p$) preserve environmental signals, such as temperature and salinity, that individuals experience during tooth mineralization as they grow and migrate (Kim et al., 2020; Picard et al., 1998; Vennemann et al., 2001; Zacke et al., 2009). In addition to oxygen, zinc is incorporated into tooth enameloid as a trace element, and its stable isotope composition ($^{66}Zn/^{64}Zn$; $\delta^{66}Zn$) reflects trophic position, as demonstrated in both marine (Jaouen, Szpak, et al., 2016; McCormack et al., 2022, 2023) and terrestrial (Bourgon et al., 2020) ecosystems. Along with trophic level from $\delta^{66}Zn$ values, body size is another valuable trait in understanding feeding ecology, trophic position, and population structure (Keppeler et al., 2020; Kim et al., 2022). Many sharks are gape-limited and tooth crown size corresponds to body length and age for sharks. Therefore, tooth size and shape further complement geochemical values to infer feeding preferences (Bazzi et al., 2021; Cooper & Pimiento, 2024). Although geochemical

proxies reconstruct shark habitat use (Kim et al., 2020; Kocsis et al., 2009, 2014; Zacke et al., 2009) and morphological metrics link evolutionary and ecological processes (Bazzi et al., 2018, 2021; Condamine et al., 2019; Cooper et al., 2023; McCormack et al., 2022, 2023), few studies integrate geochemical and morphological datasets into an integrative framework. The combination of $\delta^{18}O_p$, $\delta^{66}Zn$, and tooth morphometrics can enhance our understanding of the ecological roles of fossil shark apex predators and offer valuable analogs for predicting the responses of modern species to climate change.

4.2.1 Sand Tiger Sharks

We delve into the paleoecology of two extinct Eocene sand tiger sharks *Striatolamia macrota* and *Carcharias* sp. cf. *C. hopei (Lamniformes, Odontaspididae; Figure 4.1a)*. Their fossil records primarily consist of isolated teeth and reveal that these species frequently coexisted in Eocene depositional environments, often dominating shark assemblages. Their wide distribution highlights their ecological plasticity, spanning waters from the Arctic (Kim et al., 2014, 2022; Padilla et al., 2014) to the Antarctic (Kim et al., 2020; Kriwet et al., 2016; Long, 1992b; Zeichner et al., 2015), including low-latitude waters (Beard & Dawson, 2009; Westgate, 2001).

The closest living analog to these fossil taxa is the modern sand tiger shark, *Carcharias taurus*, which is a critically endangered apex predator (Rigby et al., 2021) and the sole surviving member of its lineage (Cappetta, 2012; Cunningham, 2000; Kriwet et al., 2016; Long, 1992a, 1992b). Taxonomic and ecological similarities are typically suggested by their tooth morphologies, as all three taxa possess tearing-type teeth (i.e., blade-like shapes) with slender secondary cusplets on each margin (Cappetta, 2012; Cunningham, 2000). However, visual differences in tooth size between species (Figure 1a) suggest potential ecological differences, though the extent of their ecological redundancy remains largely unexplored. Modern *C. taurus* grows up to ~300 cm, feeds primarily on small teleosts and elasmobranchs (Gelsleichter et al., 1999; Smale, 2005), and is known for its high site fidelity, limited temperature range (17–24 °C), and seasonal, shallow-water migrations (Kneebone et al., 2012, 2014; Otway & Ellis, 2011; Teter et al., 2015). Juvenile and subadult individuals also frequent brackish environments (Kneebone et al., 2012). Given the close taxonomic relationship with modern *C. taurus*, it is often inferred that the Eocene taxa, *S. macrota,* and *Carcharias* sp., shared similar ecological preferences, but studies that quantify the degree of resource use among fossil sand tiger sharks are limited (e.g., Larocca Conte, Aleksinski, et al., 2024).

In this study, we present preliminary $\delta^{18}O_p$, $\delta^{66}Zn$, and tooth morphometric results to compare the habitat, feeding ecology, and population structure of *S. macrota* and *Carcharias* sp. cf. *C. hopei* (hereafter = referred to as *Carcharias* sp.) from the coastal sediments of the La Meseta Formation (Seymour Island, Antarctica, James Ross Basin), dating from the Middle (~46 Ma) to the Late Eocene (37 Ma) (Amenábar et al., 2020; Douglas et al., 2014; Ivany et al., 2008). We compare these ecological components to assess the degree of similarity between the species and investigate whether their overlap shifted over time. Additionally, we construct a multidimensional niche space that includes geochemical and morphometric data to account for potential differences in niche occupation. Lastly, we

provide a comparison of total length distributions, $\delta^{18}O_p$, and $\delta^{66}Zn$ values with comparisons between the modern *C. taurus* from Delaware Bay (Karnes et al., 2024; McCormack et al., 2023) and the Eocene sand tiger sharks.

In this study, we present preliminary $\delta^{18}O_p$, $\delta^{66}Zn$, and tooth morphometric results to compare the habitat, feeding ecology, and population structure of *S. macrota* and *Carcharias* sp. cf. *C. hopei* (hereafter = referred to as *Carcharias* sp.) from the coastal sediments of the La Meseta Formation (Seymour Island, Antarctica, James Ross Basin), dating from the Middle (~46 Ma) to the Late Eocene (37 Ma) (Amenábar et al., 2020; Douglas et al., 2014; Ivany et al., 2008). We compare these ecological components to assess the degree of similarity between the species and investigate whether their overlap shifted over time. Additionally, we construct a multidimensional niche space that includes geochemical and morphometric data to account for potential differences in niche occupation. Lastly, we provide a comparison of total length distributions, $\delta^{18}O_p$, and $\delta^{66}Zn$ values with comparisons between the modern *C. taurus* from Delaware Bay (Karnes et al., 2024; McCormack et al., 2023) and the Eocene sand tiger sharks.

4.3 Geological Setting

The La Meseta Formation is exposed on Seymour Island, located east of the Antarctic Peninsula within the James Ross Basin at 64°17′S, 56°45′W (Figure 4.1b) (Dutton et al., 2002; Elliot, 1988). This sedimentary succession is bounded by angular unconformities and is divided into lithofacies units known as Tertiary Eocene La Meseta (TELMs, Figure 4.1c) (Marenssi et al., 1998; Porębski, 2000; Sadler, 1988). The succession is also divided into six allomembers based on both lithology and facies: Valle de Las Focas (TELM 1), Acantilados I (TELM 2), Acantilados II/Campamento (TELM 3), Cucullaea I and II (TELMs 4 and 5). These deposits consist of shell beds, siltstones, and sandstones, indicating deposition in a shallow, marine-dominated environment (Amenábar et al., 2020; Ivany et al., 2008; Montes et al., 2013).

The absolute age of the TELM units remains debated, though robust biostratigraphic analyses suggest deposition occurred between the Middle and Late Eocene (Amenábar et al., 2020; Douglas et al., 2014; see also Kim et al., 2020 for a summarized age model based on these works). The lower TELM 1 unit contains endemic "Transantarctic" dinoflagellate cyst taxa, calibrated to approximately 46 – 45 Ma (Amenábar et al., 2020; Douglas et al., 2014). Additional dinocysts recorded in TELMs 2 and 3, such as *Enneadocysta diktyostila*, *Arachnodinium antarcticum*, and *Hystricosphaerodinium truswelliae*, suggest deposition between ~45 Ma and ~38 Ma (Amenábar et al., 2020; Douglas et al., 2014). The palynological content of TELM 4 differs from TELMs 3 and 5, with the co-occurrence of *Deflandrea granulata* and *Glaphyrocysta semitecta* indicating an age of ~41–39 Ma (Amenábar et al., 2020; Douglas et al., 2014). Finally, the diverse palynological content in TELM 5 indicates deposition between ~41- ~37 Ma for this unit (Amenábar et al., 2020; Douglas et al., 2014). The palynological content in TELM units is coeval with the Eocene deposits from the Río Turbo, Río Baguales, and Loreto formations that outcrop in Chile (Sierra Dorotea, Río Baguales, and Río de Las Minas; Magallanes Basin) (Amenábar et al.,

2020; Estebenet et al., 2017). To summarize, TELM 1 to 4 formed between the Middle Lutetian-Bartonian (~46 – ~41 Ma, Middle Eocene; Figure 4.1c), while TELM 5 deposited during the Bartonian and Priabonian (~41– ~37 Ma, Middle to Late Eocene; Figure 4.1c) (Amenábar et al., 2020; Douglas et al., 2014; Kim et al., 2020).

4.4 Materials and Methods

4.4.1 Materials

We report geochemical and morphometric data from 37 fossil specimens, taxonomically identified as *Striatolamia macrota* and *Carcharias* sp. (Table 4.1). The fossil material analyzed herein comes from TELM 4 (n = 18; Table 4.1) and 5 deposits (n = 19; Table 4.1). Specimens were obtained from the Paleozoological Collections at the Swedish Museum of Natural History (NRM-PZ, Stockholm, Sweden), the California Museum of Paleontology (UCMP, Berkeley, CA, USA), and the Zinsmeister Collection at the Paleontological Research Institute (PRI, Ithaca, NY, USA). The UCMP and PRI specimens include *S. macrota* teeth previously described by Long (1992b) and Welton & Zinsmeister (1980). The NRM-PZ material includes *Carcharias* sp. specimens collected during the 2011–2013 summer campaigns led by the Instituto Antártico Argentino (DNA-IAA) and the Swedish Polar Research Secretariat (SPFS) on Seymour Island. This material is currently under taxonomic revision and is tentatively assigned to *Carcharias* sp. cf. *C. hopei* (Engelbrecht et al., 2016b, 2016a, 2017b, 2017a; Kriwet et al., 2016) and herein will be referred to as *Carcharias* sp. Except for three *S. macrota* specimens (PRI68692 tooth #2, PRI68692 tooth #3, and PRI68694 tooth #2), oxygen isotope values from phosphate of biological apatite were previously analyzed (Kim et al., 2020; Larocca Conte, Aleksinski, et al., 2024; Zeichner et al., 2015).

4.4.2 Phosphate Oxygen Isotope Analysis

The methodology below describes the phosphate oxygen isotope analysis of the new results generated for this study, but previously published results also follow a similar protocol. Approximately ~1mg aliquots of tooth crown enameloid were drilled using a Dremel at low speed equipped with a diamond-coated bit. The enameloid bioapatite powder was treated with the Rapid University of Chicago Dilute (Rapid UC) silver phosphate precipitation protocol following Mine et al. (2017). The enameloid powder was digested in a 2.0M nitric acid solution for ~17h in a 1.5 mL microcentrifuge vial. Following, aliquots of 2.9M hydrofluoric acid (HF) and 2.0M sodium hydroxide (NaOH) solutions were added to precipitate calcium fluoride (CaF_2), which was pelleted via centrifugation. The phosphate-rich supernatant was transferred into a new microcentrifuge tube. The CaF_2 pellets were rinsed once 0.1M with a sodium fluoride (NaF) solution to recover phosphate adsorbed on pellets. Silver phosphate crystals (Ag_3PO_4) were precipitated using a silver ammine solution containing silver nitrate and ammonium hydroxide (final concentration: 0.37M $AgNO_3$ + 1.09M NH_4OH). Crystals were rinsed five times with deionized water and dried overnight at 50°C. Alongside tooth enameloid samples, aliquots of the working reference materials NIST

SRM 120c (n = 1) and naturally occurring fluorapatite (n = 1; Fisher Scientific, CAS: 1306-05- 4) were precipitated following the same procedure to ensure equal treatment.

Specimens were run in triplicate analyses of ~0.2 mg Ag_3PO_4 that were packed into silver capsules. Samples were run in a Thermal Conversion Elemental Analyzer (TC/EA)-ConFlo IV-Delta V Plus continuous flow isotope ratio mass spectrometer system (Thermo Scientific, Bremen, Germany) at the Stable Isotope Ecosystem Laboratory of (SIELO) University of California, Merced (California, USA). The TC/EA reactor was set at 1,450 °C to promote Ag_3PO_4 reduction to CO gas. The USGS 80 and 81 reference materials (USGS; >99 % purity) were used to correct raw measurements for drift and linearity effects. Corrected $\delta^{18}O_p$ measurements were calibrated to the Vienna Standard Mean Ocean Water scale (V-SMOW) applying a 2-point calibration using the same Ag_3PO_4 reference materials (USGS 80 $\delta^{18}O_p$ = 13.1‰, USGS 81 $\delta^{18}O_p$ = 35.4‰). Measurements of the NIST SRM 120c and fluorapatite had $\delta^{18}O_p$ values of 22.1 ± 0.1‰ and 9.2 ± 0.1‰ (mean ± 1σ, n = 3 for each working reference material) respectively. These compare well with the consensus values for NIST SRM 120c (21.7 ± 0.5‰) and fluorapatite (9.0 ± 0.4‰) values reported in the literature (Chenery et al., 2010; Larocca Conte, Lopes, et al., 2024; Pucéat et al., 2010). Analytical precision in the run is 0.2‰ for USGS 80 (n = 15) and 0.1‰ for USGS 81 (n = 15). Sharks $\delta^{18}O_p$ values are reported as mean ± 1σ.

4.4.3 Stable Zinc Isotope Analysis

Fossil tooth specimens were prepared for zinc stable isotope analysis using the same procedure applied to measure $\delta^{66}Zn$ values in *C. taurus* specimens (McCormack et al., 2023). All teeth were sonicated in deionized water for 5 minutes and dried at 50°C. Aliquots of ~7mg enameloid were abraded from the tooth crown surface using a Dremel at low speed equipped with a diamond-coated bit. Samples were dissolved in perfluoroalkoxy (PFA) vials with a 1.0 M hydrochloric acid (HCl) solution on a hotplate at 120°C until the solvent evaporated (~1h). The pellet residues were dissolved in 1.5 M hydrobromic acid (HBr) and sonicated for 30 minutes. Zinc purification was performed using a two-step ion-exchange method (Jaouen, Beasley, et al., 2016; Moynier et al., 2006). Briefly, 1 ml of AG-1×8 resin (100–200 mesh) was loaded into 10 ml hydrophobic interaction columns (Macro-Prep® Methyl HIC) and cleaned twice with a 3% HNO_3 followed by deionized water. The resin was conditioned with a 1.5 M HBr solution. Samples were loaded in the column followed by an addition of HBr to elute the matrix residue. Elution of Zn was achieved by adding HNO_3. After this second column step, the solution was evaporated at 100°C for 13 hours, and the residue was re-dissolved in 3% HNO_3.

Zinc isotope measurements from 25 fossil shark tooth specimens (n run = 2) were performed using a Thermo Fisher Neptune MC-ICP-MS at the Max Planck Institute for Evolutionary Anthropology (Leipzig, Germany). The remaining tooth specimens (n = 13) will be treated and analyzed following the same procedures. Instrumental mass fractionation was corrected via Cu doping (Maréchal et al., 1999; Toutain et al., 2008). Standard bracketing was conducted using the in-house reference material Zn Alfa Aesar solution-MPI. All $\delta^{66}Zn$ values are reported relative to the JMC-Lyon standard material, with a mass-dependent offset of +0.27‰ for $\delta^{66}Zn$, as per Alfa Aesar-MPI. Samples were usually run in duplicates showing an analytical precision (1σ) equal to or less than 0.05‰. Analytical

precision expressed as 2σ of the Zn Alfa Aesar-MPI standard is 0.03‰ (n = 44). The reference material NIST SRM 1400 and a chemistry blank were prepared and analyzed alongside the tooth specimens to monitor contamination and elution during the column chemistry procedure. Zinc contamination was negligible as Zn blanks contributed <0.43% to the samples' Zn signal in both runs. The reference material NIST SRM 1400 showed a value of 0.97% ± 0.07 (mean ± 2σ) considering both runs (n = 4).

4.4.4 Morphometric Techniques: Tooth Measurements and Two-Dimensional Landmark Digitalization

The fossil shark specimens used in this study exhibit varying degrees of taphonomic preservation, ranging from well-preserved teeth to specimens represented by only the main cusp. Since the height of the main cusp generally reflects the overall crown dimension (Cunningham, 2000; Shimada, 2004), we measured this variable to estimate total body length (TL) using the linear allometric equations from Shimada (2004). Because these allometric relationships are specific to tooth position, we first identified the likely position of isolated teeth (i.e., upper vs. lower and symphyseal vs. intermediate vs. anterior vs. lateral) based on the descriptions provided by Cunningham (2000) and Shimada (2004) to properly estimate total body length. Tooth crown height (Figure 1a) for each specimen was measured with calipers to the nearest 0.01 mm.

Fossil tooth specimens were photographed to digitalize dental shapes using two-dimensional landmark-based geometric morphometrics (Bazzi et al., 2018, 2021; Zelditch et al., 2012). The tooth view (labial) and cusp orientation (main cusp pointing distally) were standardized before morphometric digitalization to trace the crown outline of each specimen. Three fixed landmarks were used to define the general triangular shape of the tooth crown, located at the apex and the mesial and distal junctions. Alongside the fixed landmarks, 100 sliding semi-landmarks were applied to track the mesial and distal perimeters. Geometric morphometrics were digitalized using *tipsDig2* v.2.32 (Rohlf, 2017).

4.4.5 Data Analysis

We initially quantify similarities between *S. macrota* and *Carcharias* sp. with geometric morphometric data, which are analyzed following the protocol described in Bazzi et al. (2021). Non-shape dental attributes like size and tooth orientation, are removed using Generalized Procrustes Analysis (GPA), implemented in the *R* package *geomorph* v.4.0.8 (Baken et al., 2021; R Development Core Team, 2024). Procrustes shape coordinates are used to compute morphological disparity between fossil species using Procrustes Variance (PV), defined as the summed squared distances of observations relative to the grand mean, standardized by degrees of freedom. Pairwise differences in PV scores between species are permuted to assess statistical significance. Dental morphologies are additionally grouped and based on their tooth position (i.e., symphyseal, anterior, intermediate, and lateral teeth) to account for the effect of dental heterodonty in our dataset. Lastly, Procrustes shape coordinates are plotted via Principal Component Analysis (PCA) to generate morphospaces that illustrate shape attributes driving variance among groups. All visualizations of

ecological variables are produced using the *R* package *ggplot2* v.3.5.1 (R Development Core Team, 2024; Wickham, 2016).

Following, we assess ecological similarities between *S. macrota*, *Carcharias* sp., and the modern *Carcharias taurus* individuals from Delaware Bay (Florida, USA). Stable zinc and oxygen isotope values and total body length measurements of *C. taurus* individuals (n = 31) were found in the literature (Karnes et al., 2024; McCormack et al., 2023), yet no morphometric digitalization of tooth shapes is available from these studies of extant *C. taurus*. Total body length estimates (and actual measurements from *C. taurus* individuals), $\delta^{18}O_p$, and $\delta^{66}Zn$ values are compared to evaluate functional redundancies between modern and fossil sand tiger sharks. Data of fossil specimens are then grouped by taxa and TELM units to document potential habitat and/or dietary shifts across the time of deposition units, as well as species-specific differences. To assess general and pairwise statistical similarities between fossil and modern species, we use Kruskal-Wallis and post-hoc Dunn tests to test statistical significance between groups.

We further explore size-related habitat use and trophic ecology of sand tiger sharks through binary plots and two-dimensional niche size analyses, using the same variables across geochemical proxies and total body size. Niche spaces of extant and fossil sand tiger sharks were analyzed and compared with the *nicheRover* package for *R* (R Development Core Team, 2024; Swanson et al., 2015). This package employs a Bayesian framework to estimate the most probable 95% confidence standard ellipses for species groups by calculating the joint probability density of the selected variables. Additionally, the package generates hypervolumes by integrating all variables to assess the degree of niche overlap between species using 1000 Monte Carlo draws. This approach allowed us to quantify ecological similarities between sand tiger shark populations and evaluate how these species partition their habitats and resources. Niche hypervolume overlap is reported as mean overlap among draws along with the 95% credible interval (95% CI).

4.5 Results

4.5.1 Dental Morphospaces and Disparity of Eocene Sand Tiger Sharks

Procrustes shape coordinates highlight similar dental morphospaces for the fossil sand tiger sharks *Striatolamia macrota* and *Carcharias* sp. (Figure 4.2). The first two principal components (PC1 and PC2) capture the majority of variance in the Procrustes coordinates. PC1 explains 71.19% of the total variance, representing a gradient from wider to narrower cusps, indicated by negative and positive eigenvalues, respectively (Figure 4.2). PC2 accounts for 11.50% of the variance, reflecting variation in crown roundness and asymmetry between dental morphologies. Positive PC2 eigenvalues correspond to sharper, distally recurved teeth with medially bent mesial edges and straight distal margins, while negative values represent upright, symmetric cusps with rounded apexes (Figure 4.2). Neither principal component shows a significant linear correlation with crown height (PC1 ~ crown height $R^2 = 0.01$, $p = 0.54$; PC2 ~ crown height $R^2 = 0.04$, $p = 0.46$), indicating that the size effect is effectively removed by the GPA analysis.

Although *S. macrota* exhibits a broader morphospace along both principal components ($PV_{Carcharias\ \text{sp. cf. } C.\ hopei} = 0.010$, $PV_{Striatolamia\ macrota} = 0.015$), there is no statistically significant disparity between the two species ($p = 0.481$). Additionally, dental morphotypes grouped by jaw position—symphyseal, anterior, intermediate, and lateral—are scattered without forming distinct clusters (Figure 4.2). Pairwise comparisons between these groups also show no statistically significant differences ($p > 0.05$; Table 4.2).

4.5.2 Isotope Geochemistry and Total Body Length Values of Fossil and Modern Sand Tiger Sharks

Geochemical proxies from tooth enameloid and total body length distributions of sand tiger sharks provide insights into the environmental and dietary preferences as well as population structure in ancient marine ecosystems (Figure 4.3). There is substantial overlap between species with similar mean and median values: *Carcharias* sp. mean $\delta^{18}O_p = 21.6 \pm 2‰$ and median $\delta^{18}O_p = 22.2‰$; *S. macrota* mean $\delta^{18}O_p = 21.6 \pm 0.8‰$, median $\delta^{18}O_p = 22.2‰$; Table 3). Pairwise comparison shows no significant differences between the two fossil groups ($Z = 1.14$; $p = 0.13$; Dunn test). The $\delta^{18}O_p$ density distributions for all species are skewed, resulting in statistically significant differences between groups ($H = 45.99$; $df = 2$, $p = 1 * 10^{-3}$; Kruskal-Wallis test). Variability in $\delta^{18}O_p$ values for *S. macrota* and *Carcharias* sp. is greater than for *C. taurus* (Figure 4.3a; Table 4.3).

Similarly, $\delta^{66}Zn$ values significantly vary between fossil and modern sand tiger shark taxa (Figure 4.3b). All distributions are multimodal (Figure 4.3b) and statistically differ from each other ($H = 9.32$, $df = 2$, $p = 9.47 * 10^{-3}$; Kruskal-Wallis test). The $\delta^{66}Zn$ values for *S. macrota* exhibit greater variation, overlapping with values of both modern and fossil *Carcharias* taxa (Figure 4.3b). The $\delta^{66}Zn$ of *S. macrota* (mean $\delta^{66}Zn = -0.2 \pm 0.3‰$, median $\delta^{66}Zn = -0.2‰$; Table 4.3) and *Carcharias* sp. (mean $\delta^{66}Zn = -0.2 \pm 0.2‰$, median $\delta^{66}Zn = -0.2‰$; Table 4.3) are statistically invariant when performing pairwise comparisons ($Z = 0.24$, $p = 0.39$; Dunn test). In contrast, $\delta^{66}Zn$ values of *C. taurus* (mean $\delta^{66}Zn = 0.0 \pm 0.2‰$, median $\delta^{66}Zn = 0.0‰$; Table 4.3) differ significantly from the fossil sand tiger sharks (*C. taurus* - *Carcharias* sp. comparison gives $Z = -2.24$ and $p = 0.01$, while *C. taurus*-*S. macrota* comparison yields $Z = 2.63$ and $p = 4.20 * 10^{-3}$; Dunn test).

Finally, total body length distributions significantly differ between sand tiger sharks (Figure 4.3c; $H = 11.68$, $df = 2$, $p = 2.90 * 10^{-3}$; Kruskal-Wallis test). Among the three species, *S. macrota* exhibits significant statistical differences when compared to the *Carcharias* taxa (*S. macrota* - *Carcharias* sp. comparison yields $Z = -3.18$ and $p = 7.00 * 10^{-4}$, while *S. macrota* - *C. taurus* comparison yields $Z = -2.89$ and $p = 1.90 * 10^{-3}$; Dunn test), exhibiting the largest range with higher mean (280.5 ± 106.6 cm) and median values (253.1 cm) (Figure 4.3c, Table 4.3). Although *Carcharias* sp. has higher variability than the modern *C. taurus*, their distributions are statistically invariant ($Z = -0.61$, $p = 0.27$; Dunn test), and both show similar central tendency values (Figure 4.3c, Table 4.3).

4.5.3 Isotope Geochemical and Total Body Length Values of Eocene Sand Tiger Sharks Across TELMs

The Eocene sand tiger sharks *Striatolamia macrota* and *Carcharias* sp. exhibit varying degrees of overlap in their $\delta^{18}O_p$ distributions when comparing different TELMs (Figure 4.4a). Although intra-specific differences over time are statistically invariant (*Carcharias* sp. between TELM 4 and 5 yields H = 2.29, df= 1, p = 0.13; *S. macrota* between TELM 4 and 5 yields H = 1.89, df= 1, p = 0.17; Kruskal-Wallis test), $\delta^{18}O_p$ distributions between species within TELM units can be distinct (Figure 4.4a). For example, in TELM 4, *Carcharias* sp. significantly differs from *S. macrota*, with higher mean and median values (Table 4.3; H = 4.18, df= 1, p = 0.04, Kruskal-Wallis test). In TELM 5, *S. macrota* exhibits a narrower variation in $\delta^{18}O_p$ values, and its distribution overlaps substantially with that of *Carcharias* sp. (H = 0.03, df = 1, p = 0.87; Kruskal-Wallis test). The $\delta^{18}O_p$ values of Eocene taxa are statistically distinct from those of the modern *C. taurus* within both TELMs (*C.taurus* - *Carcharias* sp.$_{\text{TELM 4}}$, H = 16.52, df = 1, $p = 4.73\ .05 * 10^{-3}$; *C.taurus* - *Carcharias* sp.$_{\text{TELM 5}}$, H = 19.92, df = 1, $p = 8.08 * 10^{-6}$; *C.taurus* - *S. macrota*$_{\text{TELM 4}}$, H = 19.84, df = 1, $p = 8.44 * 10^{-6}$; *C.taurus* - *S. macrota*$_{\text{TELM 5}}$, H = 19.26, df = 1, $p = 1.14 * 10^{-3}$; Kruskal-Wallis test).

The zinc isotope values are statistically invariant between fossil species within TELM units and among species across different TELM units (Figure 4.4b and Table 4.3) (*Carcharias* sp. - *S. macrota* TELM 4, H = 1.66, df = 1, p = 0.20; *Carcharias* sp. - *S. macrota* TELM 5, H = 0.64, df = 1, p = 0.42; *Carcharias* sp.$_{\text{TELM 4}}$ - *Carcharias* sp.$_{\text{TELM 5}}$, H = 0.41, df = 1, p = 0.52; *S. macrota*$_{\text{TELM 4}}$ - *S. macrota*$_{\text{TELM 5}}$, H = 1.31, df = 1, p = 0.25; Kruskal-Wallis test). The $\delta^{66}Zn$ values of Eocene sand tiger sharks are generally unimodal and overlap significantly (Figure 4.4b). In TELM 5, the variability of $\delta^{66}Zn$ values in *S. macrota* (-0.2 ± 0.3‰;) is slightly greater than that of *Carcharias* sp. (-0.2 ± 0.2‰) (Figure 4.4b and Table 4.3). Both Eocene sand tiger sharks show statistically similar $\delta^{66}Zn$ distributions compared to the modern *Carcharias taurus* within TELM 5 only (*C. taurus* - *Carcharias* sp.$_{\text{TELM 4}}$, H = 1.15, df = 1, p = 0.28; *C. taurus* - *Carcharias* sp.$_{\text{TELM 5}}$, H = 6.11, df = 1, p = 0.01; *C. taurus* – *S. macrota*$_{\text{TELM 4}}$, H = 7.05, df = 1, $p = 7.93 * 10^{-3}$; *C. taurus* – *S. macrota*$_{\text{TELM 4}}$, H = 1.33, df = 1, p = 0.25; Kruskal-Wallis test).

Estimated total body length distributions differ significantly between the fossil species within TELM units (TELM 4, H = 5.34, df = 1, p = 0.02; TELM 5, H = 1.71, df = 1, p = 0.19; Kruskal-Wallis test), but no significant intra-species differences are observed across time (*Carcharias* sp.$_{\text{TELM 4}}$ - *Carcharias* sp.$_{\text{TELM 5}}$, H = 0.28, df = 1, p = 0.60; *S. macrota*$_{\text{TELM 4}}$ - *S. macrota*$_{\text{TELM 5}}$, H = 1.56, df = 1, p = 0.21; Kruskal-Wallis test) (Figure 4.4c and Table 4.3). *Striatolamia macrota* shows the largest range and higher mean and median values in both TELMs compared to *Carcharias* sp., suggesting that *S. macrota* individuals were generally larger than those of *Carcharias* sp. (Figure 4.4c and Table 4.3). Total body length estimates of *S. macrota* are statistically invariant in both TELMs relative to the modern *C. taurus* (*C. taurus* – *S. macrota*$_{\text{TELM 4}}$, H = 8.95, df = 1, $p = 2.78 * 10^{-3}$; *C. taurus* – *S. macrota*$_{\text{TELM 5}}$, H = 4.23, df = 1, p = 0.04; Kruskal-Wallis test), while those of *Carcharias* sp. significantly differ from those of the modern sand tiger shark (*C. taurus* - *Carcharias* sp.$_{\text{TELM 4}}$, H = 0.94, df = 1, p = 0.33; *C. taurus* - *Carcharias* sp.$_{\text{TELM 5}}$, H = 0.21, df = 1, p = 0.65; Kruskal-Wallis test).

4.5.4 Bivariate Scatterplots Plots and Niche Spaces of Isotope Geochemistry and Total Body Length Values of Fossil and Modern Sand Tiger Sharks

Bivariate scatterplots and two-dimensional Bayesian standard ellipses based on $\delta^{18}O_p$, $\delta^{66}Zn$, and total body size values highlight the ecological roles of fossil and extant sand tiger sharks (Figure 4.5a-c). There is no linear correlation between $\delta^{18}O_p$ and total body length, or between $\delta^{18}O_p$ and $\delta^{66}Zn$ (Figure 4.5a-c and Table 4.4). In contrast, $\delta^{66}Zn$ moderately correlates with body total length for all sand tiger sharks (Figure 4.5a-c and Table 4.4).

Bayesian ellipses differ in size among all sand tiger shark species, with varying degrees of overlap (Figure 4.5d-f). The extant *Carcharias taurus* displays the smallest two-dimensional Bayesian ellipse along both x- and y-axes when considering different pairs of geochemical proxies and body size values (Figure 4.5d-f). The projected niche regions show limited overlap with those of *S. macrota* (Figure 4.5d-f), but they fall within the Bayesian niche regions for *Carcharias* sp. (Figure 4.5d-f). *Carcharias* sp. occupies a broader niche space along the $\delta^{18}O_p$ axis compared to its fossil counterpart, while *S. macrota* exhibits wider niche spaces along the $\delta^{66}Zn$ and total body length dimensions (Figure 4.5d-f).

To further quantify the extent of niche overlap, we calculated niche hypervolumes using $\delta^{18}O_p$, $\delta^{66}Zn$, and total body length as proxies (Figure 4.6). Posterior probabilities indicate affinities between the Eocene sand tiger sharks. Specifically, *Carcharias* sp. shares 56.5% (95% CI = 23.5 - 83.6%) of its niche region with *S. macrota*, while *S. macrota* has a 53.9% (95% CI = 26.4 - 78.6%) probability of occurring within the niche space of *Carcharias* sp. (Figure 6). In contrast, both Eocene sharks show a minimal average overlap with the modern *C. taurus* niche (mean overlap = 12.9, 95% CI = 8.7 – 26.9% for *Carcharias* sp.; mean overlap = 3.0, 95% CI = 0.2 – 9.4% for *S. macrota*). The niche of modern *C. taurus* overlaps with *Carcharias* sp. by 85.33% on average (95% CI = 51.1 – 100%), but there is little probability that its niche space overlaps with that of *S. macrota* (mean overlap = 27.2%, 95% CI = 2.7 - 82.5%; Figure 4.6).

4.6 Discussion

4.6.1 Dental Morphologies Could Support Functional Similarities Among Eocene Sand Tiger Sharks

Tooth morphology has been used as a proxy to address sharks' evolutionary relationships across geologic time (Bazzi et al., 2018; Condamine et al., 2019) and to investigate intraspecific population differences in modern shark species (Berio et al., 2022). While biomechanical tests on shark teeth yield conflicting results regarding the functional signals conveyed by different morphotypes (Bergman et al., 2017; Huber et al., 2009; Whitenack & Motta, 2010), recent morphometric studies support tooth morphology as a reliable indicator of feeding mechanisms and diet in sharks (Bazzi et al., 2021; Cooper et al., 2023; Cooper & Pimiento, 2024). For instance, tooth width serves as a proxy for both diet and feeding strategy, whereas longitudinal tooth outlines tend to reflect feeding mechanisms

only (Cooper et al., 2023). These traits form the primary components of our multivariate analysis of Eocene sand tiger sharks, with tooth width representing the first principal component and tooth shape representing the second, explaining most of the variance in dental morphology (Figure 4.2).

Our results show limited morphological disparity between *Striatolamia macrota* and *Carcharias* sp., suggesting similar tooth structures and, by extension, comparable feeding strategies and dietary preferences (Figure 4.2). Although *S. macrota* exhibits greater variation along both components, its dental morphospace largely overlaps with *Carcharias* sp., indicating similar ecological roles. Both taxa have tearing-type teeth (Cappetta, 2012), with slender cusps and smooth edges optimized for puncturing and swallowing prey whole (Lucifora et al., 2009; Whitenack & Motta, 2010). This morphology is particularly effective for feeding on teleosts and small elasmobranchs—key prey items in modern *Carcharias taurus* populations across various latitudes (Gelsleichter et al., 1999; Lucifora et al., 2009; Smale, 2005).

While our GPA analysis suggests that both taxa likely consumed fish as their primary prey, the principal components may be influenced by morphological variation associated with tooth position along jaws (Figure 4.2). Although our results show no distinct morphological disparity related to tooth position (Figure 4.2 and Table 4.2), differences between wider versus narrower teeth (PC1) and symmetric versus asymmetric teeth (PC2) are closely linked to their positions along jaws. Sand tiger sharks, both extant and fossil, exhibit monognathic dentition (i.e., similar teeth in the upper and lower jaws) but display a high degree of heterodonty (i.e., variation along the jaw), with tooth width and cusp asymmetry progressively increasing from anterior to lateral teeth (Cappetta, 2012; Cunningham, 2000; Lucifora et al., 2001; Shimada, 2004). Given these patterns of dental morphology across both jaws, we cautiously support ecological redundancies between fossil sand tiger sharks based solely on tooth morphology. Expanding the sample size and incorporating outgroup taxa will help determine whether the high overlap in dental shapes among Eocene sand tiger sharks holds.

4.6.2 Enameloid $\delta^{18}O_p$ Values Reveals Varying Habitat Preferences in Sand Tiger Sharks

The $\delta^{18}O_p$ distributions in extant and Eocene sand tiger sharks reflect preferred environmental conditions and movement patterns given their tooth replacement rates (Figures 4.2a and 4.3a). Sharks continuously replace their teeth in a conveyor-belt system, incorporating oxygen isotopes from the surrounding water and in temperature equilibrium during mineralization (Vennemann et al., 2001; Žigaite & Whitehouse, 2014). Once formed, teeth move toward the functional row and are eventually shed (Jambura et al., 2018). Teeth are shed either individually or in groups up to the entire functional file in some squaliform sharks (Reif, 1980; Smith et al., 2016; Strasburg, 1963; Underwood et al., 2016). Since replacement rates are species-specific (e.g., 55 days in *Triakis semifasciata* and 8 days in *Negaprion brevirostris*) (Botella et al., 2009; Bruner, 1998; Kim & Koch, 2012) and teeth are not often formed and shed synchronously (Reif, 1980; Smith et al., 2016; Strasburg, 1963; Underwood et al., 2016), each tooth records an environmental snapshot from its time

of formation. Although replacement and shedding modalities rates for extant sand tigers are unknown, their highly migratory behavior (Kneebone et al., 2014; Teter et al., 2015) likely introduces variability in $\delta^{18}O_p$ values related to environmental water temperature and oxygen isotope composition (Kim et al., 2020; Larocca Conte, Aleksinski, et al., 2024).

Extant and fossil sand tiger sharks inhabit various coastal and embayment habitats, moving across broad temperature and salinity gradients in response to seasonal movements and ontogeny (Kim et al., 2014; Kneebone et al., 2012, 2014; Larocca Conte, Aleksinski, et al., 2024; McCormack et al., 2023). The $\delta^{18}O_p$ values from modern *Carcharias taurus* reflect the environmental conditions experienced during migration (Figures 4.3a and 4.4a). Tagging data from the western North Atlantic population show seasonal movements from the Gulf of Maine to Cape Canaveral, Florida, with individuals spending brief periods in Delaware Bay during summer and fall (less than 150 days) when temperatures range from 18 to 22°C (Haulsee et al., 2018; Kneebone et al., 2014; Teter et al., 2015). The analyzed teeth show a large variation in $\delta^{18}O_p$ values likely reflecting such coastal movements (Figures 4.3a and 4.4a). These specimens were collected during fieldwork in August 2012 (McCormack et al., 2023). At that time, these sharks were likely moving northward from the North Carolina shore during the winter season, experiencing cooler waters (~15°C) than those of Delaware Bay during the same period resulting in higher $\delta^{18}O_p$ values (Haulsee et al., 2018; Kneebone et al., 2014; Teter et al., 2015). Thus, the $\delta^{18}O_p$ values in *C. taurus* likely represent marine signals from both North Carolina and Delaware Bay shore. These migration pathways are commonly followed by male and female sharks of all size classes (Figures 4.3a, 4.3c, and 4.5a), but migration timing may vary due to ontogeny and sex (Kneebone et al., 2012, 2014; McCormack et al., 2023; Teter et al., 2015), contributing to variability in $\delta^{18}O_p$ values.

Despite *C. taurus* $\delta^{18}O_p$ values reflecting primarily marine signals (Figures 4.3a and 4.4a), individuals from the same or different populations from other geographic areas often move to brackish waters. For example, Plymouth Bay Complex in Massachusetts serves as a seasonal nursery area for the young-of-the-year and juvenile sand tiger shark population in the North Atlantic (Kneebone et al., 2012), but juveniles from South Africa and eastern Australia spend a considerable amount of time (4-5 years) in estuarine nurseries (Bansemer & Bennett, 2011; Smale et al., 2012). In fossil settings, nursery areas of ancient sand tiger sharks are often identified in estuarine, brackish settings where small, isolated teeth dominate in fossil assemblages, such as the Eocene deposits of Red Hot Truck Spot (Texas) and Eureka Sounds (Canada) localities (Kim et al., 2022). Brackish waters are ^{18}O-depleted relative to marine environments due to mixing with freshwater inputs, shifting $\delta^{18}O_p$ values in tooth enamel toward the same direction (Kim et al., 2014). Further, female individuals often move to more offshore areas depending on the season and life stage. Young females nearly mature could segregate in such areas during the winter season to avoid mature males and delay pregnancy until they reach optimal sizes (Teter et al., 2015). Gestation and parturition occur in offshore environments; South African and Australian individuals move to high-latitude areas, and colder areas during the winter season, while pregnant females from the North Atlantic move to warmer low latitudes during the summer. This reproductive cycle in sand tiger sharks is often two years long and results in predictable migration movements as suggested by tagging data of female individuals from sand tiger populations in the North Atlantic (Teter et al., 2015), South Africa (Smale et al., 2012), and Australia

(Bansemer & Bennett, 2011). In summary, variability in tooth apatite $\delta^{18}O_p$ values reflects environmental conditions experienced by sand tiger sharks upon movements related to life history traits and ontogeny.

The migratory behavior of sand tigers is likely a conserved evolutionary trait, though fossil taxa preferred different environmental conditions than extant individuals. Eocene sand tigers, *Striatolamia macrota,* and *Carcharias* sp., lived in similar, warmer waters than their modern counterparts despite the high latitude of Seymour Island (Figure 4.3a). Their $\delta^{18}O_p$ distributions could potentially indicate local environmental conditions only. If sand tiger shark teeth have high replacement rates and are shed during a specific season on Seymour Island, they might capture environmental signals over that time frame, reflecting only local conditions. However, their variability is too large to explain exclusively local conditions. First, the variability in $\delta^{18}O_p$ values for fossil sand tiger sharks is comparable to or larger in magnitude than that of the extant *C. taurus* (Figure 4.3a and Table 4.3). Second, comparisons with co-occurring bivalves (Ivany et al., 2008; Judd et al., 2019) and Eocene model simulations (Zhu et al., 2019) suggest their variation exceeds that for local, seasonal conditions in Seymour Island (Larocca Conte, Aleksinski, et al., 2024). Therefore, variability in $\delta^{18}O_p$ values in sand tiger sharks likely reflects environmental signals experienced during their movements to or off Seymour Island (Figures 4.3a and 4.4a).

Both Eocene taxa likely preferred similar waters, yet differences in habitat use are evident (Figure 4.3a), particularly over time (Figure 4.4a). The sand tiger *S. macrota* preferred warmer and shallower waters than *Carcharias* sp. and potentially migrated toward lower latitudes, contributing to the large variability in $\delta^{18}O_p$ (Figures 4.3a, 4.4a and Table 4.3; Larocca Conte, Aleksinski, et al., 2024b). Through time, *S. macrota* narrowed its $\delta^{18}O_p$ range, overlapping more with *Carcharias* sp. (Figure 4.4a), potentially indicating a reduced geographical range as lower latitudes cooled in the late Eocene (Figure 4.4a) (Kim et al., 2020; Larocca Conte, Aleksinski, et al., 2024). In contrast, *Carcharias* sp. favored colder, possibly deeper environments compared to *S. macrota* (Figures 4.3a and 4.4a; Larocca Conte, Aleksinski, et al., 2024b). Several $\delta^{18}O_p$ outliers in *Carcharias* sp. (Figures 4.3a and 4.4a) suggest occasional movements into brackish conditions (Larocca Conte, Aleksinski, et al., 2024). During TELM 5, mean and median $\delta^{18}O_p$ values are lower than those in TELM 4 (Figures 4.3a, 4.4a, and Table 4.3), which could indicate a shift in preference for warmer waters. These shifts may have coincided with the formation of deep, strong water currents around the Antarctic continent as the Drake Passage opened (Amenábar et al., 2020; Cristini et al., 2012; Sauermilch et al., 2021), rendering deeper areas too cold and/or inhospitable for the taxon. These shifts in habitat use by S. *macrota* and *Carcharias* sp. through time likely reflect the taxon's plasticity in coping with climate changes (Kim et al., 2010; Larocca Conte et al., 2024b). However, variability in their $\delta^{18}O_p$ values could also reflect ontogenetic differences in habitat use like those observed for extant individuals (Bansemer & Bennett, 2011; Kneebone et al., 2012, 2014; McCormack et al., 2023; Smale et al., 2012; Teter et al., 2015), although fossil evidence remains limited.

4.6.3 Multi-Proxy Analysis Highlights the Diversity in Habitat Use Between Sand Tiger Sharks

We explore intra-specific habitat uses based on size structure by estimating the total body size from the cusp height of fossil specimens. However, they should not be considered absolute for several reasons. These estimates rely on analogies with modern *C. taurus* (Cunningham, 2000; Shimada, 2004), but complete jaws of Eocene sand tigers are unavailable (Cappetta, 2012), complicating tooth position assignment. Additionally, body size scales allometrically with tooth size, influenced by environmental temperature, as sharks in warmer waters grow faster (Berio et al., 2022; West et al., 2001). Consequently, the scaling relationships between tooth size and body size likely vary among populations of the same species in different locations (Berio et al., 2022). Despite these uncertainties, the estimates enable comparisons of population structures and ecological preferences.

Both fossil and modern sand tiger sharks show similar population structures, with juveniles dominating in occurrence over adults (Figures 4.3c and 4.4c), though *S. macrota* individuals may have larger sizes (Figures 4.3c and 4.4c). Comparisons of $\delta^{18}O_p$–body length reveal differences in environmental preferences between modern and fossil sand tigers (Figures 4.5a and 4.5d). Individuals of *S. macrota* display a larger body size variability and lower $\delta^{18}O_p$ values (Figures 4.5a and 4.5d), indicative of higher temperatures or lower salinity. Geochemical, morphometric, and paleontological evidence supports the idea that this taxon inhabited brackish waters at both low and high latitudes in the Arctic, indicating potential movements toward lower salinity environments (Kim et al., 2014, 2022; Padilla et al., 2014). However, when compared with model simulations for the Eocene, the distribution of $\delta^{18}O_p$ values falls within the range of seasonal environmental conditions between Seymour Island and South America (Larocca Conte, Aleksinski, et al., 2024; Zhu et al., 2020), suggesting a broad marine signal between the two continents rather than migration to estuarine habitats. Furthermore, individuals of *S. macrota* on Seymour Island appear to have preferred similar environmental conditions regardless of ontogenetic stage (Figures 4.5a and 4.5d). If younger sharks had migrated to lower salinity areas, such as estuarine environments, we would expect clearer segregation between smaller and larger individuals, with the latter showing higher $\delta^{18}O_p$ values indicative of marine conditions, which is not the case (Figures 4.5a and 4.5d). In summary, both smaller and larger *S. macrota* individuals from Seymour Island seem to have shared similar marine environmental preferences.

Among sand tigers, *Carcharias* sp. exhibited the broadest range of temperature and salinity preferences, though with a narrower size distribution compared to *S. macrota* (Figures 4.5a and 4.5d). Smaller individuals either had $\delta^{18}O_p$ values comparable to larger specimens or showed a significant shift toward much lower values (Figures 4.5a and 4.5d). This shift may indicate population segregation, with juveniles utilizing both brackish and marine environments, while adults predominantly remained in marine habitats (Figure 4.5a). Bayesian niche spaces suggest, however, that adults (individuals larger than ~200 cm; Figure 4.5d; Branstetter & Musick, 1994; Goldman et al., 2006) could also inhabit these areas. There are two possible explanations for this pattern. First, the estuarine environments within the La Meseta Formation may have functioned as nurseries, where juveniles dispersed to reduce predation risk as they grew or gave birth (Heupel et al., 2007; Kim et al., 2022; Kneebone et al., 2012; Teter et al., 2015). However, only three small individuals in our

dataset indicate movements to brackish individuals (Figures 4.5a and 4.5d). Perhaps environmental and paleoecological reconstructions of TELMs at higher temporal resolutions are necessary. The changing environmental conditions near Antarctica may have significantly influenced the structure of these populations (Kim et al., 2020, 2022; Larocca Conte, Aleksinski, et al., 2024). Analyzing population structure shifts through stratigraphic intervals within TELMs could provide further insights into whether Seymour Island functioned as a nursery area. Until further data is available, we cannot rule out whether Seymor Island served as a nursery area for *Carcharias* sp. Alternatively, these estuarine-coastal areas on Seymour Island (Marenssi et al., 2002; Porębski, 2000) may have been temporary stopovers for both juveniles and adults along migration routes, similar to how Delaware Bay serves the extant *C. taurus* (Haulsee et al., 2018; Kneebone et al., 2014; Teter et al., 2015). In this case, juveniles might have occupied the shallower, brackish portions of the estuary, while adults occasionally moved into the embayment residing in deeper, saltier sections of the embayment (Haulsee et al., 2018). This spatial segregation could also explain the clustering observed between some juveniles and adult individuals (Figures 4.5a and 4.5d). Finally, movements to areas beyond Seymour Island shore, as documented in Eocene sand tiger sharks (Larocca Conte, Aleksinski, et al., 2024), could have influenced their diet through access to different resources (Jaouen, Szpak, et al., 2016; McCormack et al., 2023).

Foraging habits further support movements in predators with complex life-history age and sex classes like sharks (McCormack et al., 2023). Tooth $\delta^{66}Zn$ measurements could provide additional insights into habitat use, potentially differentiating between brackish, coastal, offshore, or deeper environments. Zinc is supplied through diet, and the isotopic fractionation during food digestion is mass- and food-type-dependent. Within organisms, fractionation is tissue-dependent; hard tissues discriminate over the heavier isotopes as they bind to ligands with stronger electronegativity (oxygen>nitrogen>sulfur). As a result, soft tissues in animals are ^{66}Zn-depleted relative to bones, teeth, and average composition of the body, leading to lower $\delta^{66}Zn$ values in predators with increasing trophic levels. On average, enameloid $\delta^{66}Zn$ values decrease by 0.4‰ per trophic level in both terrestrial and marine ecosystems (Bourgon et al., 2020; Jaouen, Beasley, et al., 2016; Jaouen, Szpak, et al., 2016; McCormack et al., 2022, 2023). Similar to the traditional $\delta^{13}C$ and $\delta^{15}N$ dietary proxies, differences in baseline $\delta^{66}Zn$ values among the regions in which highly migratory animals swim provide additional support for habitat use (Jaouen, Beasley, et al., 2016; McCormack et al., 2023). Rivers and oceanic circulation largely control Zn concentrations, which typically range from 0.1 to 10 nmol μg^{-1}, with deeper waters more enriched than shallower ones (Little et al., 2014; Vance et al., 2019; Zhao et al., 2014). The ocean is enriched in $\delta^{66}Zn$ relative to rivers (average $\delta^{66}Zn = 0.33‰$), as dinoflagellates preferentially take up the lighter isotope (Zhao et al., 2014). While $\delta^{66}Zn$ values in the deep ocean are nearly invariant, areas above the oxygen minimum levels between 20 and 50 m b.s.l. are isotopically lower than shallower waters given the primary biomass production at the surface (Little et al., 2014; Zhao et al., 2014). Across a spatial gradient, low-productivity offshore areas have $\delta^{66}Zn$ values around 0.4‰ lower than upwelling and/or highly productive $\delta^{66}Zn$ values (Vance et al., 2019; Zhao et al., 2014). Thus, the migratory animals utilizing different habitats (e.g., *Carcharias* sp. moving in deeper or brackish waters and *S. macrota* moving offshore) may rely on distinct resources as they move across environments. For example, the lowest $\delta^{66}Zn$ values observed in adult female *C. taurus* individuals may indicate movements

to offshore environments close to the edge of the slope compared to younger sharks and adult males, likely to meet physiological demands during gestation (McCormack et al., 2023). Baseline effects are also observed in seasonal migratory mammals (e.g., walrus) from archeological deposits, foraging to areas with isotopically distinct baselines of $\delta^{66}Zn$, $\delta^{13}C$, and $\delta^{15}N$ compared to co-occurring year-round mammals (e.g., polar bear and ringed seal) (Jaouen, Szpak, et al., 2016). Finally, foraging in different areas could be linked to the environmental conditions these taxa encountered, as reflected in the ecological signals recorded in their enameloid $\delta^{18}O_p$ values.

We found no correlation between $\delta^{18}O_p$ and $\delta^{66}Zn$ values (Figures 4.5b and 4.5e). The lack of correlation is also true for the extant *C. taurus* individuals (Figure 4.5b and 4.5e). Several factors could explain the absence of a strong correlation between these metrics. First, while temperature and salinity influence zinc concentrations in the ocean, its isotopic composition remains relatively conservative unless there are significant productivity or source changes (Little et al., 2014; Vance et al., 2019; Zhao et al., 2014). Second, there could be a mismatch between zinc and oxygen incorporation rates in tooth enameloid. When considering other nutrients, such as carbon and nitrogen in tooth dentine, their incorporation can take 32–85 days in species like *Triakis semifasciata* (Kim & Koch, 2012; Zeichner et al., 2017), which is within the time of phosphate integration into enameloid during tooth mineralization (i.e., weeks) (Amini et al., 2020). While the incorporation pathways and timings are still uncertain, zinc could substitute for calcium or occupy vacant sites in biological apatites to bind with phosphate oxygen via surface adsorption following apatite crystallization and post-eruptive phase of teeth (Barrea et al., 2003; Brudevold et al., 1963; Fatima et al., 2016). This temporal offset suggests that dietary signals in $\delta^{66}Zn$ may not align precisely with the environmental signals recorded in $\delta^{18}O_p$ values during tooth mineralization. Future studies characterizing spatial $\delta^{66}Zn$ baselines from Eocene environments could further elucidate the ecological dynamics of fossil migratory animals.

4.6.4 Fossil Sand Tiger Sharks Have Larger Trophic Niches Relative to the Extant Carcharias taurus

Sharks are commonly opportunistic feeders, preying on both herbivores and carnivores, including other sharks. Larger body size increases the range of potential prey, but does not necessarily reflect a preference for larger prey items (Ferreira et al., 2017; Keppeler et al., 2020; Kiszka et al., 2015; Smale, 2005), Additionally, baseline effects in prey introduce further variability as habitat use and foraging strategies vary within species based on sex, ontogeny, and migration timing (Ferreira et al., 2017; Hussey et al., 2011; McCormack et al., 2023). Altogether, these confounding factors result in a moderate correlation between $\delta^{66}Zn$ values and total body mass.

Sympatric taxa like Eocene sand tiger sharks could share similar resources, but intra- and inter-specific differences due to ontogeny can exist. Enameloid zinc isotope values and population size structure offer a flexible, general framework to document foraging habits in *Carcharias* sp. and *S. macrota* (Figures 4.5c and 4.5f). The $\delta^{66}Zn$ values of *Striatolamia macrota* and *Carcharias* sp. are largely invariant across TELMs and exhibit similar overall distributions, but they differ significantly from those of the extant *Carcharias taurus*

(Figures 4.3b and 4.4b). These similarities and differences become more apparent when accounting for population size structure (Figures 4.5c and 4.5f). In general, δ^{66}Zn values decline as body size and trophic position increase, aligning with expectations for a gape-limited marine predator (Figure 4.5c). Notably, the niche regions of fossil and modern sand tiger sharks largely overlap, though *C. taurus* exhibits the narrowest size range along both axes (Figure 4.5f).

The trophic ecology of individuals could differ between taxa upon varying foraging strategies. For example, young individuals of *Carcharias* sp. could feed at higher trophic levels than similarly sized individuals of other species (Figure 4.5c). This could suggest that juvenile *Carcharias* sp. were more opportunistic than both *C. taurus* and *S. macrota*, consuming a broader range of prey from varying habitats and higher trophic levels. Given that *Carcharias* sp. preferred cooler conditions (Figures 4.3a, 4.4a, 4.5a, 4.5b, 4.5d, and 4.5e), their foraging behavior could mirror that of adult male *C. taurus* from Delaware Bay, which exploits deeper waters in marine settings to access larger prey from various habitats and trophic levels (McCormack et al., 2023). Alternatively, δ^{66}Zn values in juvenile *Carcharias* sp. could indicate feeding in embayments or estuarine environments close to the Seymour Island shore (Marenssi et al., 2002; Porębski, 2000). Given their movements to brackish environments (Figures 4.3a, 4.4a, 4.5a-b, and 4.5d-e; see also Section 4.6.3) and the low δ^{66}Zn values of rivers (~0.33‰) (Zhao et al., 2014), the incorporation of this signal through diet could cause the shift in enameloid δ^{66}Zn toward lower values compared to other juveniles of different sand tiger shark taxa (Figures 4.5c and 4.5f). If so, this could result in a resource partitioning strategy to limit competition between species, a mechanism often adopted by sympatric sharks in modern ecosystems (Pantoja-Echevarría et al., 2022; Tamburin et al., 2019; Weideli et al., 2023). Adult *Carcharias* sp. individuals could feed at similar trophic levels to younger individuals, indicating little change in trophic position through ontogeny as also shown by the lower correlation with total body size (Figures 4.5c). The lower correlation between the two metrics could also be explained as a difference in the foraging areas between the juveniles and adults, with the latter feeding in more coastal or offshore environments. Indeed, female *C. taurus* often move offshore (Haulsee et al., 2018; McCormack et al., 2023; Teter et al., 2015), where δ^{66}Zn baseline values vary from estuarine and coastal settings (Zhao et al., 2014), allowing them to access a variety of prey across different trophic positions.

Striatolamia macrota individuals exhibit the largest niche breadth among the studied groups (Figure 4.5f). The wide range of body sizes and δ^{66}Zn values suggest that individuals moved toward higher trophic levels as they grew, though their δ^{66}Zn values remain lower compared to modern and fossil *Carcharias* individuals of similar sizes (Figures 4.4e and 4.4f). We propose that *S. macrota* typically fed at lower trophic levels until reaching larger sizes, with occasional smaller individuals preying at higher levels. One specimen, estimated to be ~200 cm in length, shows a comparably low δ^{66}Zn value to that of the largest individual (~500 cm; Figure 4.5e). However, baseline effects cannot be ruled out entirely. Given that *S. macrota* primarily occupied pelagic and warmer habitats (Figures 4.3a, 4.4a, 4.5a, 4.5b, 4.5d, and 4.5e) (Larocca Conte, Aleksinski, et al., 2024), it is plausible that this species relied primarily on pelagic prey in contrast to predators like *Carcharias* sp. and adult male individuals of *C. taurus* that could occupy more coastal areas with higher δ^{66}Zn baseline values (Little et al., 2014; Zhao et al., 2014).

Overall, fossil sand tiger sharks display broader ecological niches than their modern counterparts, and their larger niche sizes likely reflect both resource availability and habitat use across different environments.

4.6.5 Eocene Sand Tiger Sharks from Seymour Island are Functionally Redundant and Provide Context for the Ecology of the Extant Carcharias taurus

Our multiproxy approach—integrating habitat use, feeding ecology, and population size structure—supports ecological redundancy among Eocene sand tiger sharks (Figures 4.2-4.5). Despite some differences across time (Figure 4.3) and ontogeny (Figure 4.5), both juvenile and adult individuals of *Carcharias* sp. and *S. macrota* often occupied similar environments and exploited similar resources. However, the extant *C. taurus* from Delaware Bay seems to prefer different environmental conditions and resources (Figures 4.3-4.5). Some overlaps exist between the niches of *C. taurus* and its fossil counterparts, particularly *Carcharias* sp. (Figures 4.5 and 4.6).

Given the high degree of resource and ontogenetic overlap among these taxa, our results suggest that the ecological roles of fossil sand tiger sharks align closely. Moreover, the modern *C. taurus* could have analogs in ancient settings like those of the Eocene (Figure 4.6). The narrower niche observed for *C. taurus* likely reflects the temporal and spatial limitations of the isotope proxies, which capture only a snapshot of habitat and resource use for the population (see section 4.6.1; McCormack et al., 2023). This dataset is also skewed toward small individuals (74.91% of specimens) when accounting for length at maturity for male (185-193 cm) and female (218-235 cm) individuals (Lucifora et al., 2002). This bias affects the distribution of the isotopic values for the population, as younger individuals show different migration timing and forage in areas with different baselines (McCormack et al., 2023). Expanding the sampling of isotopic values would provide a more comprehensive view of the environmental preferences and resource use of *C. taurus* across its spatial, temporal, and ontogenetic ranges (e.g., Cape Ann, Massachusetts, to Cape Canaveral, Florida; Kneebone et al., 2014), likely yielding a broader niche space. Until such data is available, we propose that the ancient *Carcharias* sp. from the Eocene deposits of Seymour Island could serve as the most suitable analog for the modern *C. taurus*, given their substantial niche overlap (Figure 6).

4.7 Conclusions

Tooth morphology, morphometry, and geochemistry document the extent of resource sharing among sympatric predators in ancient environments. The tooth morphology of Eocene sand tiger sharks, *Carcharias* sp. and *S. macrota*, suggests a high degree of ecological redundancy between the two species. This initial evaluation is further refined using geochemical proxies and morphometrics to discern patterns of habitat use, diet, and population size structure over time, leveraging the ecology of their closest extant relative, *C. taurus*, to support our interpretations.

Overall, we found that the Eocene fossil taxa exhibit similar $\delta^{18}O_p$ and $\delta^{66}Zn$ values, indicating comparable environmental preferences and trophic ecology. Body size

distributions suggest that both juveniles and adults of these species occupied Eocene environments in Antarctica. Compared to their extant relative, $\delta^{18}O_p$ and $\delta^{66}Zn$ values in fossil sand tiger sharks are lower than those of *C. taurus* individuals from Delaware Bay, suggesting that the fossil sharks inhabited warmer environments and likely occupied higher trophic levels. Additionally, *S. macrota* was, on average, larger than any *Carcharias* individual.

While the population size structure and trophic ecology of fossil sand tiger sharks remain consistent, shifts in habitat use are evident over time. In TELM 4, variability in $\delta^{18}O_p$ values for *Carcharias* sp. suggests movement into colder, potentially deeper waters and brackish environments, while *S. macrota* preferred warmer, shallower habitats, likely spanning a broad latitudinal range. By TELM 5, the two taxa show increasing overlap in environmental preferences, with shifts in $\delta^{18}O_p$ values toward opposite directions and reduced variability, possibly reflecting an adaptive response to global cooling.

Given size-related differences in habitat preferences and trophic ecology in modern *C. taurus*, habitat and resource use in fossil sand tiger sharks are expected to vary throughout their ontogeny. There is no clear evidence of habitat segregation between juveniles and adults in *S. macrota*, as both groups appear to have shared similar marine conditions, indicated by comparable $\delta^{18}O_p$ values. For *Carcharias* sp., smaller individuals likely utilized both brackish and marine environments, while adults likely remained predominantly in marine habitats. Limited evidence suggests that the estuarine areas of Seymour Island may have served as nurseries for *Carcharias* sp., as only a few juveniles show movements to brackish environments. Until further data is available, Seymour Island habitats could have acted as temporary stopovers for juveniles and adults along migration routes for both fossil taxa.

This study is the first to combine $\delta^{18}O_p$ and $\delta^{66}Zn$ values to interpret environmental preferences and foraging ecology, providing a joint understanding of habitat use between species. Interestingly, we found that the two metrics correlate poorly with each other, as salinity and temperature are typically weak predictors of $\delta^{66}Zn$ baseline values, and zinc isotopes may be incorporated into tooth enameloid after mineralization. Despite this weak correlation, the dietary signals reflected in $\delta^{66}Zn$ values could support movements across different areas throughout the ontogeny of fossil sand tiger sharks. As expected, $\delta^{66}Zn$ values generally decline across all taxa, consistent with the behavior of gape-limited marine predators. The low $\delta^{66}Zn$ values in juvenile *Carcharias* sp. suggest either feeding at higher trophic levels compared to similarly sized individuals of other species or foraging in environments with lower $\delta^{66}Zn$ baseline values, such as estuaries. Adult individuals also exhibit lower $\delta^{66}Zn$ values, indicating they may be feeding at similar trophic positions or foraging across a broad latitudinal gradient. In contrast, *Striatolamia macrota* shows the broadest range of $\delta^{66}Zn$ values; however, the generally low values in both juveniles and adults, compared to similar-size classes of *Carcharias* taxa, suggest that they primarily feed at lower trophic levels or in offshore areas with lower $\delta^{66}Zn$ baseline values. *S. macrota* feeds at the highest trophic levels when individuals are very large, yet smaller individuals may feed at a high trophic level as well.

Our multiproxy approach is a powerful tool for assessing how similar species coexisted during periods of climate change, with the potential to identify fossil analogs that can inform conservation practices in modern ecosystems. The integration of habitat use, feeding ecology, and population size structure supports the concept of ecological redundancy among Eocene sand tiger sharks, as observed in tooth morphology. Despite some differences observed across time and ontogeny that influence niche variability, *Carcharias* sp. and *S. macrota* occupied similar environmental and trophic niches, further reinforcing their ecological redundancy. This framework provides a flexible approach to assessing the degree of ecological similarities between fossil and extant relatives. The projected niche space for *C. taurus* indicates a high overlap with that of *Carcharias* sp., suggesting trait conservation across the evolutionary lineage of sand tiger sharks. This assessment can provide valuable context to enhance future conservation practices for endangered species like *C. taurus* in light of the imminent climatic crisis.

4.8 References

Amenábar, C. R., Montes, M., Nozal, F., & Santillana, S. (2020). Dinoflagellate cysts of the la Meseta Formation (middle to late Eocene), Antarctic Peninsula: Implications for biostratigraphy, palaeoceanography and palaeoenvironment. *Geological Magazine*, *157*(3), 351–366. https://doi.org/10.1017/S0016756819000591

Amini, S., Razi, H., Seidel, R., Werner, D., White, W. T., Weaver, J. C., et al. (2020). Shape-preserving erosion controlled by the graded microarchitecture of shark tooth enameloid. *Nature Communications*, *11*(1), 1–11. https://doi.org/10.1038/s41467-020-19739-0

Baken, E. K., Collyer, M. L., Kaliontzopoulou, A., & Adams, D. C. (2021). geomorph v4.0 and gmShiny: enhanced analytics and a new graphical interface for a comprehensive morphometric experience. *Methods in Ecology and Evolution*, (12), 2355–2363.

Bansemer, C. S., & Bennett, M. B. (2011). Sex- and maturity-based differences in movement and migration patterns of grey nurse shark, Carcharias taurus, along the eastern coast of Australia. *Marine and Freshwater Research*, *62*(6), 596–606. https://doi.org/10.1071/MF10152

Barrea, R. A., Pérez, C. A., Ramos, A. Y., Sánchez, H. J., & Grenón, M. (2003). Distribution and incorporation of zinc in biological calcium phosphates. *X-Ray Spectrometry*, *32*(5), 387–395. https://doi.org/10.1002/XRS.657

Baum, J. K., Myers, R. A., Kehler, D. G., Worm, B., Harley, S. J., & Doherty, P. A. (2003). Collapse and conservation of shark populations in the Northwest Atlantic. *Science*, *299*(5605), 389–392. https://doi.org/10.1126/science.1079777

Bazzi, M., Kear, B. P., Blom, H., Ahlberg, P. E., & Campione, N. E. (2018). Static Dental Disparity and Morphological Turnover in Sharks across the End-Cretaceous Mass Extinction. *Current Biology*, *28*(16), 2607-2615.e3. https://doi.org/10.1016/j.cub.2018.05.093

Bazzi, M., Campione, N. E., Kear, B. P., Pimiento, C., & Ahlberg, P. E. (2021). Feeding ecology has shaped the evolution of modern sharks. *Current Biology*, *31*(23), 5138-5148.e4. https://doi.org/10.1016/j.cub.2021.09.028

Beard, K. C., & Dawson, M. R. (2009). Early Wasatchian Mammals of the Red Hot Local Fauna, Uppermost Tuscahoma Formation, Lauderdale County, Mississippi. *Https://Doi.Org/10.2992/007.078.0301*, *78*(3), 193–243. https://doi.org/10.2992/007.078.0301

Bergman, J. N., Lajeunesse, M. J., & Motta, P. J. (2017). Teeth penetration force of the tiger shark Galeocerdo cuvier and sandbar shark Carcharhinus plumbeus. *Journal of Fish Biology*, *91*(2), 460–472. https://doi.org/10.1111/JFB.13351

Berio, F., Bayle, Y., Baum, D., Goudemand, N., & Debiais-Thibaud, M. (2022). Hide and seek shark teeth in Random Forests: machine learning applied to Scyliorhinus canicula populations. *PeerJ*, *10*, e13575. https://doi.org/10.7717/peerj.13575

Birkmanis, C. A., Freer, J. J., Simmons, L. W., Partridge, J. C., & Sequeira, A. M. M. (2020). Future Distribution of Suitable Habitat for Pelagic Sharks in Australia Under Climate Change Models. *Frontiers in Marine Science*, *7*(July), 1–11. https://doi.org/10.3389/fmars.2020.00570

Botella, H., Valenzuela-Ríos, J. I., & Martínez-Perez, C. (2009). Tooth replacement rates in early chondrichthyans: A qualitative approach. *Lethaia*, *42*(3), 365–376. https://doi.org/10.1111/j.1502-3931.2009.00152.x

Bourgon, N., Jaouen, K., Bacon, A. M., Jochum, K. P., Dufour, E., Duringer, P., et al. (2020). Zinc isotopes in Late Pleistocene fossil teeth from a Southeast Asian cave setting preserve paleodietary information. *Proceedings of the National Academy of Sciences of the United States of America*, *117*(9), 4675–4681. https://doi.org/10.1073/PNAS.1911744117/SUPPL_FILE/PNAS.1911744117.SAPP.PDF

Branstetter, S., & Musick, J. A. (1994). Transactions of the American Fisheries Society Age and Growth Estimates for the Sand Tiger in the Northwestern Atlantic Ocean. https://doi.org/10.1577/1548-8659

Brudevold, F., Steadman, L. T., Spinelli, M. A., Amdur, B. H., & Grøn, P. (1963). A study of zinc in human teeth. *Archives of Oral Biology*, *8*(2), 135–144. https://doi.org/10.1016/0003-9969(63)90051-7

Bruner, J. C. (1998). Tooth replacement rate of Carcharodon carcharias (Linnaeus, 1758). In *AES 14th annual meeting, Program and Abstracts* (p. 98).

Burke, K. D., Williams, J. W., Chandler, M. A., Haywood, A. M., Lunt, D. J., & Otto-Bliesner, B. L. (2018). Pliocene and Eocene provide best analogs for near-future climates. *Proceedings of the National Academy of Sciences of the United States of America*, *115*(52), 13288–13293. https://doi.org/10.1073/pnas.1809600115

Cappetta, H. (2012). *Handbook of paleoichthyology volume 3E. Chondrichthyes. Mesozoic*

and Cenozoic elasmobranchii: Teeth. (H.-P. Schultze, Ed.) (Vol. 3E). Munich: Verlag Dr. Friedrich Pfeil.

Chenery, C., Müldner, G., Evans, J., Eckardt, H., & Lewis, M. (2010). Strontium and stable isotope evidence for diet and mobility in Roman Gloucester, UK. *Journal of Archaeological Science*, *37*(1), 150–163. https://doi.org/10.1016/j.jas.2009.09.025

Cicimurri, D. J., Ebersole, J. A., & Martin, G. (2020). Two new species of *Mennerotodus* Zhelezko, 1994 (Chondrichthyes: Lamniformes: Odontaspididae), from the Paleogene of the southeastern United States. *Fossil Record*, *23*(2), 117–140. https://doi.org/10.5194/FR-23-117-2020

Compagno, L. J. (2002). Sharks of the world: An Annotated and illustrated catalogue of shark species known to date. *Food and Agriculture Organization of the United Nations*, *2*(1), 249. Retrieved from http://www.fao.org/3/x9293e/x9293e00.htm

Condamine, F. L., Romieu, J., & Guinot, G. (2019). Climate cooling and clade competition likely drove the decline of lamniform sharks. *Proceedings of the National Academy of Sciences of the United States of America*, *116*(41), 20584–20590. https://doi.org/10.1073/pnas.1902693116

Cooper, J. A., & Pimiento, C. (2024). The rise and fall of shark functional diversity over the last 66 million years, (June), 1–17. https://doi.org/10.1111/geb.13881

Cooper, J. A., Griffin, J. N., Kindlimann, R., & Pimiento, C. (2023). Are shark teeth proxies for functional traits? A framework to infer ecology from the fossil record. *Journal of Fish Biology*, *103*(4), 798–814. https://doi.org/10.1111/jfb.15326

Cristini, L., Grosfeld, K., Butzin, M., & Lohmann, G. (2012). Influence of the opening of the Drake Passage on the Cenozoic Antarctic Ice Sheet: A modeling approach. *Palaeogeography, Palaeoclimatology, Palaeoecology*, *339–341*, 66–73. https://doi.org/10.1016/j.palaeo.2012.04.023

Cunningham, S. B. (2000). A comparison of isolated teeth of early Eocene Striatolamia macrota (Chondrichthyes , Lamniformes), with those of a Recent sand shark , Carcharias taurus. *Tertiary Research*, *20*(1–4), 17–31.

Douglas, P. M. J., Affek, H. P., Ivany, L. C., Houben, A. J. P., Sijp, W. P., Sluijs, A., et al. (2014). Pronounced zonal heterogeneity in Eocene southern high-latitude sea surface temperatures. *Proceedings of the National Academy of Sciences of the United States of America*, *111*(18), 6582–6587. https://doi.org/10.1073/pnas.1321441111

Dutton, A. L., Lohmann, K. C., & Zinsmeister, W. J. (2002). Stable isotope and minor element proxies for Eocene climate of Seymour Island, Antarctica. *Paleoceanography*, *17*(2), 6-1-6–13. https://doi.org/10.1029/2000pa000593

Elliot, D. H. (1988). Tectonic setting and evolution of the James Ross Basin, northern Antarctic Peninsula. *Memoir - Geological Society of America*, *169*(January 1988), 541–555. https://doi.org/10.1130/mem169-p541

Engelbrecht, A., Mörs, T., Reguero, M. A., & Kriwet, J. (2016a). A new sawshark, Pristiophorus laevis, from the Eocene of Antarctica with comments on Pristiophorus lanceolatus. *Historical Biology*, *29*(6), 841–853. https://doi.org/10.1080/08912963.2016.1252761

Engelbrecht, A., Mörs, T., Reguero, M. A., & Kriwet, J. (2016b). Revision of Eocene Antarctic carpet sharks (Elasmobranchii, Orectolobiformes) from Seymour Island, Antarctic Peninsula. *Journal of Systematic Palaeontology*, *15*(12), 969–990. https://doi.org/10.1080/14772019.2016.1266048

Engelbrecht, A., Mörs, T., Reguero, M. A., & Kriwet, J. (2017a). Eocene squalomorph sharks (Chondrichthyes, Elasmobranchii) from Antarctica. *Journal of South American Earth Sciences*, *78*, 175–189. https://doi.org/10.1016/j.jsames.2017.07.006

Engelbrecht, A., Mörs, T., Reguero, M. A., & Kriwet, J. (2017b). New carcharhiniform sharks (Chondrichthyes, Elasmobranchii) from the early to middle Eocene of Seymour Island, Antarctic Peninsula. *Journal of Vertebrate Paleontology*, *37*(6). https://doi.org/10.1080/02724634.2017.1371724

Estebenet, M. S. G., Guerstein, G. R., Rodríguez Raising, M. E., Ponce, J. J., & Alperín, M. I. (2017). Dinoflagellate cyst zonation for the middle to upper Eocene in the Austral Basin, southwestern Atlantic Ocean: Implications for regional and global correlation. *Geological Magazine*, *154*(5), 1022–1036. https://doi.org/10.1017/S0016756816000601

Fatima, T., Rahim, Z. B. H. A., Lin, C. W., & Qamar, Z. (2016). Zinc: A precious trace element for oral health care? *JPMA. The Journal of the Pakistan Medical Association*, *66*(8), 1019–1023. Retrieved from https://pubmed.ncbi.nlm.nih.gov/27524540/

Ferreira, L. C., Thums, M., Heithaus, M. R., Barnett, A., Abrantes, K. G., Holmes, B. J., et al. (2017). The trophic role of a large marine predator, the tiger shark Galeocerdo cuvier. *Scientific Reports*, *7*(1), 1–14. https://doi.org/10.1038/s41598-017-07751-2

Ferretti, F., Worm, B., Britten, G. L., Heithaus, M. R., & Lotze, H. K. (2010, August 1). Patterns and ecosystem consequences of shark declines in the ocean. *Ecology Letters*. John Wiley & Sons, Ltd. https://doi.org/10.1111/j.1461-0248.2010.01489.x

Gelsleichter, J., Musick, J. A., & Nichols, S. (1999). Food habits of the smooth dogfish, Mustelus canis, dusky shark, Carcharhinus obscurus, Atlantic sharpnose shark, Rhizoprionodon terraenovae, and the sand tiger, Carcharias taurus, from the northwest Atlantic Ocean. *Environmental Biology of Fishes*, *54*(2), 205–217. https://doi.org/10.1023/A:1007527111292/METRICS

Goldman, K. J., Branstetter, S., & Musick, J. A. (2006). A re-examination of the age and growth of sand tiger sharks, Carcharias taurus, in the western North Atlantic: the importance of ageing protocols and use of multiple back-calculation techniques, 241–252. https://doi.org/10.1007/978-1-4020-5570-6_4

Haulsee, D. E., Breece, M. W., Brown, L. M., Wetherbee, B. M., Fox, D. A., & Oliver, M.

J. (2018). Spatial ecology of Carcharias taurus in the northwestern Mid-Atlantic coastal ocean. *Marine Ecology Progress Series*, *597*, 191. https://doi.org/10.3354/meps12592

Heithaus, M. R., Burkholder, D., Hueter, R. E., Heithaus, L. I., Pratt, H. L., & Carrier, J. C. (2007). Spatial and temporal variation in shark communities of the lower Florida Keys and evidence for historical population declines. *Canadian Journal of Fisheries and Aquatic Sciences*, *64*(10), 1302–1313. https://doi.org/10.1139/F07-098

Heithaus, M. R., Frid, A., Wirsing, A. J., & Worm, B. (2008). Predicting ecological consequences of marine top predator declines. *Trends in Ecology and Evolution*, *23*(4), 202–210. https://doi.org/10.1016/j.tree.2008.01.003

Heupel, M. R., Carlson, J. K., & Simpfendorfer, C. A. (2007). Shark nursery areas: Concepts, definition, characterization and assumptions. *Marine Ecology Progress Series*, *337*(Nmfs 2006), 287–297. https://doi.org/10.3354/meps337287

Heupel, M. R., Munroe, S. E. M., Lédée, E. J. I., Chin, A., & Simpfendorfer, C. A. (2019). Interspecific interactions, movement patterns and habitat use in a diverse coastal shark assemblage. *Marine Biology*, *166*(6), 1–17. https://doi.org/10.1007/S00227-019-3511-7/TABLES/5

Huber, D. R., Claes, J. M., Mallefet, J., & Herrel, A. (2009). Is extreme bite performance associated with extreme morphologies in sharks? *Physiological and Biochemical Zoology*, *82*(1), 20–28. https://doi.org/10.1086/588177/ASSET/IMAGES/LARGE/FG5.JPEG

Hussey, N. E., Dudley, S. F. J., McCarthy, I. D., Cliff, G., & Fisk, A. T. (2011). Stable isotope profiles of large marine predators: Viable indicators of trophic position, diet, and movement in sharks? *Canadian Journal of Fisheries and Aquatic Sciences*, *68*(12), 2029–2045. https://doi.org/10.1139/F2011-115

Ivany, L. C., Lohmann, K. C., Hasiuk, F., Blake, D. B., Glass, A., Aronson, R. B., & Moody, R. M. (2008). Eocene climate record of a high southern latitude continental shelf: Seymour Island, Antarctica. *Bulletin of the Geological Society of America*, *120*(5–6), 659–678. https://doi.org/10.1130/B26269.1

Jambura, P. L., Pfaff, C., Underwood, C. J., Ward, D. J., & Kriwet, J. (2018). Tooth mineralization and histology patterns in extinct and extant snaggletooth sharks, hemipristis (carcharhiniformes, hemigaleidae)—evolutionary significance or ecological adaptation? *PLoS ONE*, *13*(8), e0200951. https://doi.org/10.1371/journal.pone.0200951

Jaouen, K., Szpak, P., & Richards, M. P. (2016). Zinc isotope ratios as indicators of diet and trophic level in arctic marine mammals. *PLoS ONE*, *11*(3), 13. https://doi.org/10.1371/journal.pone.0152299

Jaouen, K., Beasley, M., Schoeninger, M., Hublin, J. J., & Richards, M. P. (2016). Zinc isotope ratios of bones and teeth as new dietary indicators: results from a modern food

web (Koobi Fora, Kenya). *Scientific Reports 2016 6:1*, *6*(1), 1–8. https://doi.org/10.1038/srep26281

Judd, E. J., Ivany, L. C., DeConto, R. M., Halberstadt, A. R. W., Miklus, N. M., Junium, C. K., & Uveges, B. T. (2019). Seasonally Resolved Proxy Data From the Antarctic Peninsula Support a Heterogeneous Middle Eocene Southern Ocean. *Paleoceanography and Paleoclimatology*, *34*(5), 787–799. https://doi.org/10.1029/2019PA003581

Karnes, M. E., Chan, R. L., Kuntz, J. P., Griffiths, M. L., Shimada, K., Becker, M. A., et al. (2024). Enigmatic carbonate isotope values in shark teeth: Evidence for environmental and dietary controls. *Palaeogeography, Palaeoclimatology, Palaeoecology*, *635*, 111943. https://doi.org/10.1016/j.palaeo.2023.111943

Keppeler, F. W., Montaña, C. G., & Winemiller, K. O. (2020). The relationship between trophic level and body size in fishes depends on functional traits. *Ecological Monographs*, *90*(4), e01415. https://doi.org/10.1002/ecm.1415

Kim, S. L., & Koch, P. L. (2012). Methods to collect, preserve, and prepare elasmobranch tissues for stable isotope analysis. *Environmental Biology of Fishes*, *95*(1), 53–63. https://doi.org/10.1007/s10641-011-9860-9

Kim, S. L., Eberle, J. J., Bell, D. M., Fox, D. A., & Padilla, A. (2014). Evidence from shark teeth for a brackish Arctic Ocean in the Eocene greenhouse. *Geology*, *42*(8), 695–698. https://doi.org/10.1130/G35675.1

Kim, S. L., Zeichner, S. S., Colman, A. S., Scher, H. D., Kriwet, J., Mörs, T., & Huber, M. (2020). Probing the Ecology and Climate of the Eocene Southern Ocean With Sand Tiger Sharks Striatolamia macrota. *Paleoceanography and Paleoclimatology*, *35*(12), 1–21. https://doi.org/10.1029/2020PA003997

Kim, S. L., Yeakel, J. D., Balk, M. A., Eberle, J. J., Zeichner, S., Fieman, D., & Kriwet, J. (2022). Decoding the dynamics of dental distributions: insights from shark demography and dispersal. *Proceedings of the Royal Society B: Biological Sciences*, *289*(1977). https://doi.org/10.1098/rspb.2022.0808

Kiszka, J. J., Aubail, A., Hussey, N. E., Heithaus, M. R., Caurant, F., & Bustamante, P. (2015). Plasticity of trophic interactions among sharks from the oceanic south-western Indian Ocean revealed by stable isotope and mercury analyses. *Deep-Sea Research Part I: Oceanographic Research Papers*. https://doi.org/10.1016/j.dsr.2014.11.006

Kneebone, J., Chisholm, J., & Skomal, G. B. (2012). Seasonal residency, habitat use, and site fidelity of juvenile sand tiger sharks Carcharias taurus in a Massachusetts estuary. *Marine Ecology Progress Series*, *471*, 165–181. https://doi.org/10.3354/meps09989

Kneebone, J., Chisholm, J., & Skomal, G. (2014). Movement patterns of juvenile sand tigers (Carcharias taurus) along the east coast of the USA. *Marine Biology*, *161*(5), 1149–1163. https://doi.org/10.1007/s00227-014-2407-9

Kocsis, L., Vennemann, T. W., Hegner, E., Fontignie, D., & Tütken, T. (2009). Constraints

on Miocene oceanography and climate in the Western and Central Paratethys: O-, Sr-, and Nd-isotope compositions of marine fish and mammal remains. *Palaeogeography, Palaeoclimatology, Palaeoecology*, *271*(1–2), 117–129. https://doi.org/10.1016/j.palaeo.2008.10.003

Kocsis, L., Gheerbrant, E., Mouflih, M., Cappetta, H., Yans, J., & Amaghzaz, M. (2014). Comprehensive stable isotope investigation of marine biogenic apatite from the late Cretaceous-early Eocene phosphate series of Morocco. *Palaeogeography, Palaeoclimatology, Palaeoecology*, *394*, 74–88. https://doi.org/10.1016/j.palaeo.2013.11.002

Kriwet, J., Engelbrecht, A., Mörs, T., Reguero, M., & Pfaff, C. (2016). Ultimate Eocene (Priabonian) chondrichthyans (Holocephali, Elasmobranchii) of Antarctica. *Journal of Vertebrate Paleontology*, *36*(4). https://doi.org/10.1080/02724634.2016.1160911

Larocca Conte, G., Aleksinski, A., Liao, A., Kriwet, J., Mörs, T., Trayler, R. B., et al. (2024). Eocene shark teeth from peninsular Antarctica: Windows to habitat use and paleoceanography. *Paleoceanography and Paleoclimatology*, *39*(11), e2024PA004965. https://doi.org/10.1029/2024PA004965

Larocca Conte, G., Lopes, L. E., Mine, A. H., Trayler, R. B., & Kim, S. L. (2024). SPORA, a new silver phosphate precipitation protocol for oxygen isotope analysis of small, organic-rich bioapatite samples. *Chemical Geology*, *651*, 122000. https://doi.org/10.1016/J.CHEMGEO.2024.122000

Latour, R. J., & Gartland, J. (2020). Dynamics of the shark community in the Mid-Atlantic Bight. *Marine Biology*, *167*(7), 1–14. https://doi.org/10.1007/S00227-020-03720-Y/FIGURES/5

Little, S. H., Vance, D., Walker-Brown, C., & Landing, W. M. (2014). The oceanic mass balance of copper and zinc isotopes, investigated by analysis of their inputs, and outputs to ferromanganese oxide sediments. *Geochimica et Cosmochimica Acta*, *125*, 673–693. https://doi.org/10.1016/J.GCA.2013.07.046

Long, D. J. (1992a). Paleoecology of Eocene Antarctic sharks. *The Antarctic Paleoenvironmen: A Perspective on Global Change. Antarctic Research Series*, *56*(January 1992), 131–139. https://doi.org/10.1029/ar056p0131

Long, D. J. (1992b). Sharks from the La Meseta Formation (Eocene), Seymour Island, Antarctic Peninsula. *Journal of Vertebrate Paleontology*, *12*(1), 11–32. https://doi.org/10.1080/02724634.1992.10011428

Lucifora, L. O., Menni, R. C., & Escalante, A. H. (2001). Analysis of dental insertion angles in the sand tiger shark, Carcharias taurus (Chondrichthyes: Lamniformes). *Cybium*, *25*(1), 23–31.

Lucifora, L. O., Menni, R. C., & Escalante, A. H. (2002). Reproductive ecology and abundance of the sand tiger shark, Carcharias taurus , from the southwestern Atlantic. *ICES Journal of Marine Science*, *59*(3), 553–561.

https://doi.org/10.1006/JMSC.2002.1183

Lucifora, L. O., García, V. B., & Escalante, A. H. (2009). How can the feeding habits of the sand tiger shark influence the success of conservation programs? *Animal Conservation*, *12*(4), 291–301. https://doi.org/10.1111/J.1469-1795.2009.00247.X

Maréchal, C. N., Télouk, P., & Albarède, F. (1999). Precise analysis of copper and zinc isotopic compositions by plasma-source mass spectrometry. *Chemical Geology*, *156*(1–4), 251–273. https://doi.org/10.1016/S0009-2541(98)00191-0

Marenssi, S. A., Santillana, S. N., & Rinaldi, C. A. (1998). Stratigraphy of the La Meseta Formation (Eocene), Marambio (Seymour) Island, Antarctica. *Asociación Paleontológica Argentina Publicación Especial*, *5*(1), 137–146. Retrieved from https://www.peapaleontologica.org.ar/index.php/peapa/article/view/185

Marenssi, S. A., Net, L. I., & Santillana, S. N. (2002). Provenance, environmental and paleogeographic controls on sandstone composition in an incised-valley system: The Eocene La Meseta Formation, Seymour Island, Antarctica. *Sedimentary Geology*, *150*(3–4), 301–321. https://doi.org/10.1016/S0037-0738(01)00201-9

McCormack, J., Griffiths, M. L., Kim, S. L., Shimada, K., Karnes, M., Maisch, H., et al. (2022). Trophic position of Otodus megalodon and great white sharks through time revealed by zinc isotopes. *Nature Communications*, *13*(1), 1–10. https://doi.org/10.1038/s41467-022-30528-9

McCormack, J., Karnes, M., Haulsee, D., Fox, D., & Kim, S. L. (2023). Shark teeth zinc isotope values document intrapopulation foraging differences related to ontogeny and sex. *Communications Biology*, *6*(1), 1–10. https://doi.org/10.1038/s42003-023-05085-6

Montes, M., Nozal, F., Santillana, S., Marenssi, S., & Olivero, E. (2013). Mapa Geológico de Isla Marambio (Seymour), Antártida, escala 1:20,000. *Serie Cartográfica*.

Moynier, F., Albarède, F., & Herzog, G. F. (2006). Isotopic composition of zinc, copper, and iron in lunar samples. *Geochimica et Cosmochimica Acta*, *70*(24), 6103–6117. https://doi.org/10.1016/J.GCA.2006.02.030

Otway, N. M., & Ellis, M. T. (2011). Pop-up archival satellite tagging of Carcharias taurus: movements and depth/temperature-related use of south-eastern Australian waters, 607–620.

Padilla, A., Eberle, J. J., Gottfried, M. D., Sweet, A. R., & Hutchison, J. H. (2014). A sand tiger shark-dominated fauna from the Eocene Arctic greenhouse. *Journal of Vertebrate Paleontology*, *34*(6), 1307–1316. https://doi.org/10.1080/02724634.2014.880446

Pantoja-Echevarría, L. M., Tamburin, E., Elorriaga-Verplancken, F. R., Marmolejo-Rodríguez, A. J., Galván-Magaña, F., Tripp-Valdez, A., et al. (2022). How to stay together? Habitat use by three sympatric sharks in the western coast of Baja California Sur, Mexico. *Environmental Science and Pollution Research*, *29*(41), 61685–61697. https://doi.org/10.1007/S11356-022-19530-2/FIGURES/5

Picard, S., Garcia, J. P., Lécuyer, C., Sheppard, S. M. F., Cappetta, H., & Emig, C. C. (1998). δ 18 O values of coexisting brachiopods and fish: Temperature differences and estimates of paleo-water depths. *Geology*, *26*(11), 975–978. https://doi.org/10.1130/0091-7613(1998)026<0975:OVOCBA>2.3.CO;2

Porębski, S. J. (2000). Shelf-valley compound fill produced by fault subsidence and eustatic sea-level changes, Eocene La Meseta Formation, Seymour Island, Antarctica. *Geology*, *28*(2), 147–150. https://doi.org/10.1130/0091-7613(2000)28<147:SCFPBF>2.0.CO;2

Pucéat, E., Joachimski, M. M., Bouilloux, A., Monna, F., Bonin, A., Motreuil, S., et al. (2010). Revised phosphate-water fractionation equation reassessing paleotemperatures derived from biogenic apatite. *Earth and Planetary Science Letters*, *298*(1–2), 135–142. https://doi.org/10.1016/j.epsl.2010.07.034

R Development Core Team. (2024). A language and environment for statistical computing. R Foundation for Statistical Computing, Vienna, Austria. Vienna, Austria.

Reid, D. D., Robbins, W. D., & Peddemors, V. M. (2011). Decadal trends in shark catches and effort from the New South Wales, Australia, Shark Meshing Program 1950–2010. *Marine and Freshwater Research*, *62*(6), 676–693. https://doi.org/10.1071/MF10162

Reif, W. E. (1980). Pattern regulation in shark dentitions. In G. M. Malacinsk (Ed.), *Pattern formation: a primer in developmental biology* (pp. 603–621). New York: Macmillan.

Rigby, C. L., Carlson, J., Derrick, D., Dicken, M., & Pacoureau, N. Simpfendorfer, C. (2021). Carcharias taurus. *The IUCN Red List of Threatened Species 2021: E.T3854A2876505*. https://doi.org/https://dx.doi.org/10.2305/IUCN.UK.2021-2.RLTS.T3854A2876505.en

Roff, G., Doropoulos, C., Rogers, A., Bozec, Y. M., Krueck, N. C., Aurellado, E., et al. (2016, May 1). The Ecological Role of Sharks on Coral Reefs. *Trends in Ecology and Evolution*. Elsevier Current Trends. https://doi.org/10.1016/j.tree.2016.02.014

Rohlf, F. J. (2017). *TpsDig2, Version 2.3*. Stony Brook: Published by the Author.

Rosenfeld, J. S. (2002). Functional redundancy in ecology and conservation. *Oikos*, *98*(1), 156–162. https://doi.org/10.1034/j.1600-0706.2002.980116.x

Sadler, P. M. (1988). Paleogene units on Seymour Island , northern Antarctic Peninsula.

Sauermilch, I., Whittaker, J. M., Klocker, A., Munday, D. R., Hochmuth, K., Bijl, P. K., & LaCasce, J. H. (2021). Gateway-driven weakening of ocean gyres leads to Southern Ocean cooling. *Nature Communications*, *12*(1), 1–8. https://doi.org/10.1038/s41467-021-26658-1

Shimada, K. (2004). The relationship between the tooth size and total body length in the sandtiger shark, Carcharias taurus (Lamniformes : Odontaspididae). *Journal of Fossil Research*, *37*(2), 76–81. https://doi.org/10.2305/IUCN.UK.2009-2.RLTS.T3854A10132481.en

Smale, M. J. (2005). The diet of the ragged-tooth shark Carcharias taurus Rafinesque 1810

in the Eastern Cape, South Africa. *African Journal of Marine Science*, *27*(1), 331–335. https://doi.org/10.2989/18142320509504091

Smale, M. J., Booth, A. J., Farquhar, M. R., Meÿer, M. R., & Rochat, L. (2012). Migration and habitat use of formerly captive and wild raggedtooth sharks (Carcharias taurus) on the southeast coast of South Africa. *Marine Biology Research*. https://doi.org/10.1080/17451000.2011.617756

Smith, F. A., Payne, J. L., Heim, N. A., Balk, M. A., Finnegan, S., Kowalewski, M., et al. (2016). Body Size Evolution Across the Geozoic. *Annual Review of Earth and Planetary Sciences*, *44*(Volume 44, 2016), 523–553. https://doi.org/10.1146/ANNUREV-EARTH-060115-012147/CITE/REFWORKS

Strasburg, D. W. (1963). The Diet and Dentition of Isistius brasiliensis, with Remarks on Tooth Replacement in Other Sharks. *Copeia*, *1963*(1), 33. https://doi.org/10.2307/1441272

Swanson, H. K., Lysy, M., POwer, M., Stasko, A. D., Johnson, J. D., & Reist, J. D. (2015). A new probabilistic method for quantifying n-dimensional ecological niches and niche overlap. *Ecology*, *96*(2), 318–324. https://doi.org/10.1890/14-0235.1

Tamburin, E., Kim, S. L., Elorriaga-Verplancken, F. R., Madigan, D. J., Hoyos-Padilla, M., Sánchez-González, A., et al. (2019). Isotopic niche and resource sharing among young sharks (carcharodon carcharias and isurus oxyrinchus) in baja California, Mexico. *Marine Ecology Progress Series*, *613*, 107–124. https://doi.org/10.3354/meps12884

Teter, S. M., Wetherbee, B. M., Fox, D. A., Lam, C. H., Kiefer, D. A., & Shivji, M. (2015). Migratory patterns and habitat use of the sand tiger shark (Carcharias taurus) in the western North Atlantic. *Marine and Freshwater Research*, *66*(2), 158–169. https://doi.org/10.1071/MF14129

Toutain, J. P., Sonke, J., Munoz, M., Nonell, A., Polvé, M., Viers, J., et al. (2008). Evidence for Zn isotopic fractionation at Merapi volcano. *Chemical Geology*, *253*(1–2), 74–82. https://doi.org/10.1016/J.CHEMGEO.2008.04.007

Underwood, C., Johanson, Z., & Smith, M. M. (2016). Cutting blade dentitions in squaliform sharks form by modification of inherited alternate tooth ordering patterns. *Royal Society Open Science*, *3*(11). https://doi.org/10.1098/RSOS.160385

Vance, D., de Souza, G. F., Zhao, Y., Cullen, J. T., & Lohan, M. C. (2019). The relationship between zinc, its isotopes, and the major nutrients in the North-East Pacific. *Earth and Planetary Science Letters*, *525*, 115748. https://doi.org/10.1016/j.epsl.2019.115748

Vennemann, T. W., Hegner, E., Cliff, G., & Benz, G. W. (2001). Isotopic composition of recent shark teeth as a proxy for environmental conditions. *Geochimica et Cosmochimica Acta*, *65*(10), 1583–1599. https://doi.org/https://doi.org/10.1016/S0016-7037(00)00629-3

Weideli, O. C., Daly, R., Peel, L. R., Heithaus, M. R., Shivji, M. S., Planes, S., & Papastamatiou, Y. P. (2023). Elucidating the role of competition in driving spatial and

trophic niche patterns in sympatric juvenile sharks. *Oecologia*, *201*(3), 673–688. https://doi.org/10.1007/s00442-023-05355-4

Welton, B. J., & Zinsmeister, W. J. (1980). Eocene neoselachians from the La Meseta Formation, Seymour Island, Antarctic Peninsula. *Contributions in Science (Los Angeles)*, *330*(324), 1–10.

West, G. B., Brown, J. H., & Enquist, B. J. (2001). A general model for ontogenetic growth. *Nature 2001 413:6856*, *413*(6856), 628–631. https://doi.org/10.1038/35098076

Westgate, J. W. (2001). Paleoecology and Biostratigraphy of Marginal Marine Gulf Coast Eocene Vertebrate Localities, (1996), 263–297. https://doi.org/10.1007/978-1-4615-1271-4_11

Whitenack, L. B., & Motta, P. J. (2010). Performance of shark teeth during puncture and draw: implications for the mechanics of cutting. *Biological Journal of the Linnean Society*, *100*(2), 271–286. https://doi.org/10.1111/J.1095-8312.2010.01421.X

Wickham, H. (2016). *ggplot2: Elegant Graphics for Data Analysis*. Springer-Verlag New York. Retrieved from https://ggplot2.tidyverse.org

Zacke, A., Voigt, S., Joachimski, M. M., Gale, A. S., Ward, D. J., & Tütken, T. (2009). Surface-water freshening and high-latitude river discharge in the Eocene North Sea. *Journal of the Geological Society*, *166*(5), 969–980. https://doi.org/10.1144/0016-76492008-068

Zeichner, S. S., Kim, S. L., & Colman, A. S. (2015). Eocene high-latitude temperature gradients over time and space based on on δ18O values of fossil shark teeth. In *AGU Fall Meeting Abstracts* (Vol. 2015, pp. PP53C-2378).

Zeichner, S. S., Colman, A. S., Koch, P. L., Polo-Silva, C., Galván-Magaña, F., & Kim, S. L. (2017). Discrimination factors and incorporation rates for organic matrix in shark teeth based on a captive feeding study. *Physiological and Biochemical Zoology*, *90*(2), 257–272. https://doi.org/10.1086/689192

Zelditch, M., Swiderski, D., & Sheets, H. D. (2012). *Geometric morphometrics for biologists: a primer*. academic press.

Zhao, Y., Vance, D., Abouchami, W., & de Baar, H. J. W. (2014). Biogeochemical cycling of zinc and its isotopes in the Southern Ocean. *Geochimica et Cosmochimica Acta*, *125*, 653–672. https://doi.org/10.1016/j.gca.2013.07.045

Zhu, J., Poulsen, C. J., & Tierney, J. E. (2019). Simulation of Eocene extreme warmth and high climate sensitivity through cloud feedbacks. *Science Advances*, *5*(9), 1–10. https://doi.org/10.1126/sciadv.aax1874

Zhu, J., Poulsen, C. J., Otto-Bliesner, B. L., Liu, Z., Brady, E. C., & Noone, D. C. (2020). Simulation of early Eocene water isotopes using an Earth system model and its implication for past climate reconstruction. *Earth and Planetary Science Letters*, *537*, 116164. https://doi.org/10.1016/j.epsl.2020.116164

Žigaite, Ž., & Whitehouse, M. (2014). Stable oxygen isotopes of dental biomineral: Differentiation at the intra- and inter-tissue level of modern shark teeth. *GFF*, *136*(1), 337–340. https://doi.org/10.1080/11035897.2013.878747

4.9 Tables

Table 4.1. Number (n) of *Striatolamia macrota* and *Carcharias sp.* cf. *C. hopei* specimens analyzed for geochemical and morphometric measurements. The specimens were collected from the Eocene TELM 4 and 5 units on Seymour Island, Antarctica.

Taxon	**TELM 4 (n specimens)**	**TELM 5 (n specimens)**	**Total (by taxon)**
Striatolamia macrota	9	9	18
Carcharias sp. cf. *C. hopei*	10	10	20
Total (by TELM):	18	19	38

Table 4.2. Dental morphological disparity of Eocene sand tiger sharks, grouped by tooth position. Pairwise comparisons between groups are presented as Procrustes Variance (PV) and *p* values.

Morphological Disparity by Tooth Position								
	Anterior		**Intermediate**		**Lateral**		**Symphyseal**	
	PV	***p***	**PV**	***p***	**PV**	***p***	**PV**	***p***
Anterior			0.001208	0.902	0.008946	0.394	0.013321	0.18
Intermediate	0.001208	0.902			0.010154	0.353	0.014529	0.199
Lateral	0.008946	0.394	0.010154	0.353			0.004375	0.685
Symphyseal	0.013321	0.18	0.014529	0.199	0.004375	0.685		

Table 4.3. Summary statistics of $\delta^{18}O_p$, $\delta^{66}Zn$, and total body length for *Carcharias* sp. cf. *C. hopei*, *Carcharias taurus*, and *Striatolamia macrota*. Summary statistics for *Carcharias* sp. and *S. macrota* are also provided for TELM 4 and 5 units. Each variable includes the number of specimens (n), mean ± 1σ, and median values.

ALL SPECIMENS									
Taxon	**$\delta^{18}O_p$ (‰; V-SMOW)**			**$\delta^{66}Zn$ (‰; JMC Lion)**			**Total body length (cm)**		
	n	**mean ± 1σ**	**median**	**n**	**mean ± 1σ**	**median**	**n**	**mean ± 1σ**	**median**
Carcharias sp. cf. *C. hopei*	20	21.6 ± 2.0	22.2	12	-0.2 ± 0.2	-0.2	20	193.4 ± 53.6	173.9
Carcharias taurus	31	23.8 ± 0.6	23.9	31	-0.0 ± 0.2	0.0	31	193.8 ± 31.4	187.0
Striatolamia macrota	18	21.8 ± 0.6	21.6	13	-0.2 ± 0.3	-0.2	18	280.5 ± 106.6	253.1
TELM 5									
Taxon	**$\delta^{18}O_p$ (‰; V-SMOW)**			**$\delta^{66}Zn$ (‰; JMC Lion)**			**Total body length (cm)**		
	n	**mean ± 1σ**	**median**	**n**	**mean ± 1σ**	**median**	**n**	**mean ± 1σ**	**median**
Carcharias sp. cf. *C. hopei*	10	21.4 ± 1.9	22.0	6	-0.2 ± 0.2	-0.2	10	199.2 ± 58.0	173.9
Striatolamia macrota	9	21.9 ± 0.6	21.8	6	-0.2 ± 0.3	-0.1	9	250.2 ± 87.9	240.8
TELM 4									
Carcharias sp. cf. *C. hopei*	10	21.8 ± 2.2	22.6	6	-0.3 ± 0.2	-0.2	10	187.5 ± 51.6	174.7
Striatolamia macrota	9	21.3 ± 0.9	21.3	7	-0.3 ± 0.2	-0.3	9	314.5 ± 121.1	307.7

Table 4.4. Linear model statistics for $\delta^{18}O_p$, $\delta^{66}Zn$, and total body size values of fossil and extant sand tiger sharks. Each model reports the respective group's correlation coefficient (R^2) and *p*-value.

Linear model (y~x)	***Carcharias* sp. cf. *C. hopei***		***Carcharias taurus***		***Striatolamia macrota***	
	R^2	***p***	**R^2**	***p***	**R^2**	***p***
Total body length (cm) ~ $\delta^{18}O_p$ (‰; V-SMOW)	0.06	0.29	$2*10^{-3}$	0.82	0.01	0.68
$\delta^{18}O_p$ (‰; V-SMOW) ~ $\delta^{66}Zn$ (‰; JMC Lyon)	$2.34*10^{-3}$	0.96	0.02	0.48	0.07	0.38
Total body length (cm) ~ $\delta^{66}Zn$ (‰; JMC Lyon)	0.06	0.29	0.6	$3.05*10^{-7}$	0.57	$4*10^{-3}$

4.10 Figures

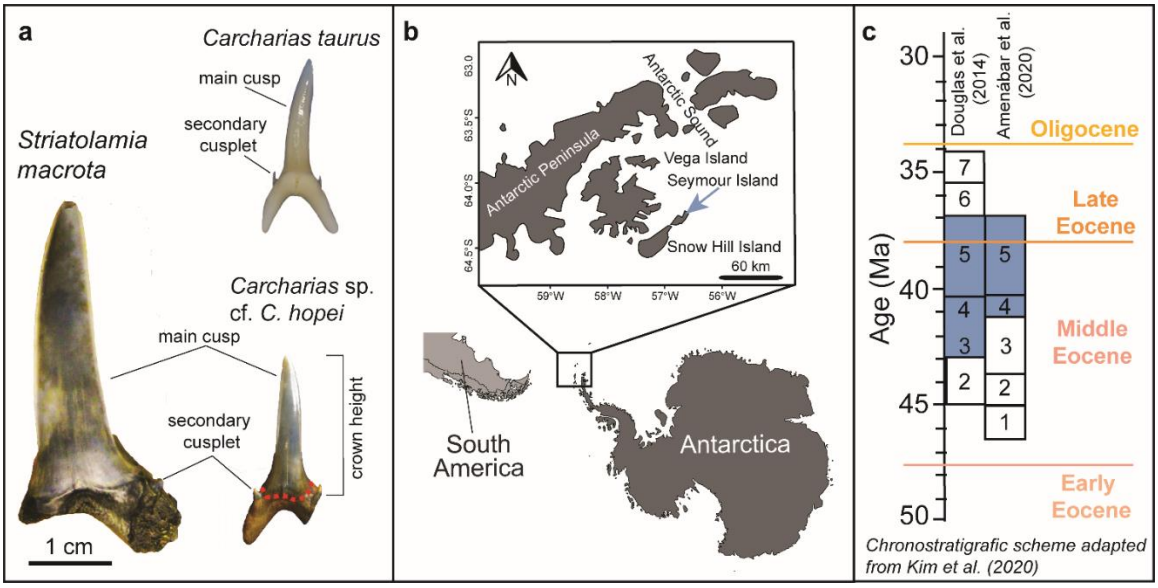

Figure 4.1. The sand tiger sharks *Striatolamia macrota* and *Carcharias* sp. cf. *C. hopei* from the Eocene deposits of the La Meseta Formation (Seymour Island, Antarctica). (a) Tooth specimens of *S. macrota*, *Carcharias* sp., and *Carcharias taurus*. The fossil teeth are shown in labial view, while the *C. taurus* tooth is in lingual view. All teeth feature upright main cusps and secondary cusplets. The dashed red line on the *Carcharias* sp. tooth highlights the junction between the root and main cusp, the lower edge from where the crown height of fossil tooth specimens is measured. The *C. taurus* tooth image is from Cicimurri et al. (2020). (b) Geographic location of Seymour Island, highlighted by the blue arrow in the insert. (c) Proposed chronologies of TELM units (numbered boxes), adapted from the summarized TELM chronostratigraphy by Kim et al. (2020), based on reconstructions by Amenábar et al. (2020) and Douglas et al. (2014). Blue boxes indicate the TELM units where the tooth specimens analyzed in this study were collected. Note that the Douglas et al. (2014) age model has uncertainties in separating TELM 3 from TELM 4, but this distinction is resolved in the biostratigraphy-based model of Amenábar et al. (2020). Colored bars mark the boundaries between the Early, Middle, and Late Eocene, as well as the Oligocene.

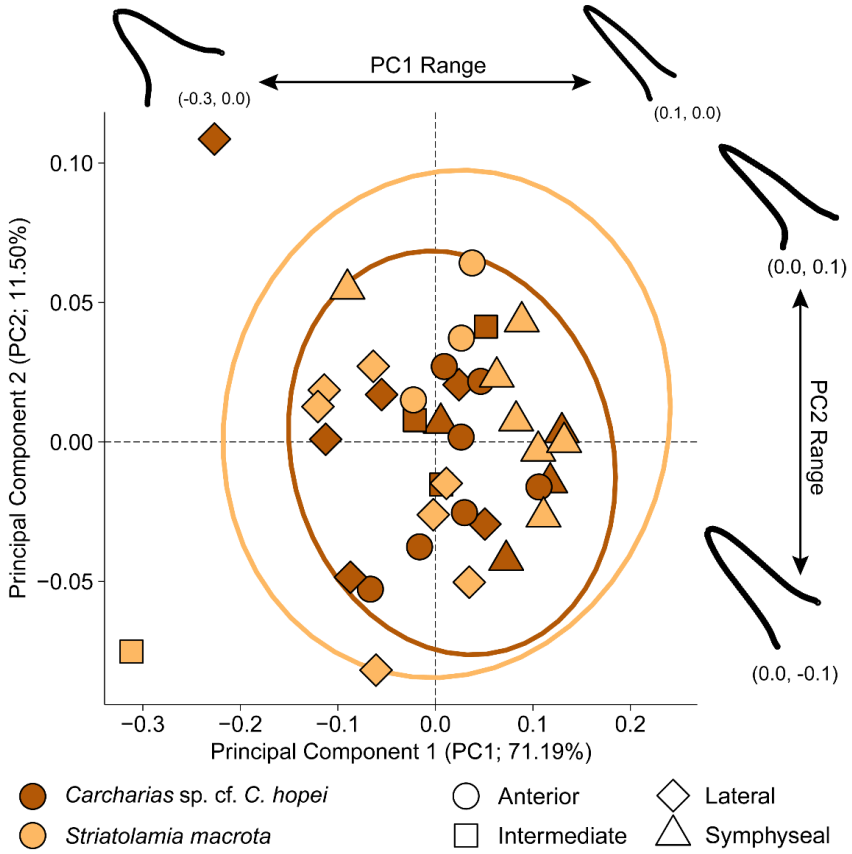

Figure 4.2. Dental morphospaces of *Carcharias* sp. and *Striatolamia macrota* from the Eocene show considerable overlap. The multivariate plot illustrates the dental morphospaces of the Eocene sand tiger taxa along the main principal components PC1 (x-axis) and PC2 (y-axis). Each point represents a specific tooth morphology, with *Carcharias* sp. (orange) and *S. macrota* (yellow) further grouped by artificial jaw positions, denoted by different point shapes. Colored ellipses represent the 95% confidence intervals of each species' morphospace. Dashed horizontal and vertical lines divide the plot into quadrants to assist visual interpretation. Dental silhouettes depict hypothetical maximum and minimum morphological extremes distributed evenly along each axis, as indicated in parentheses.

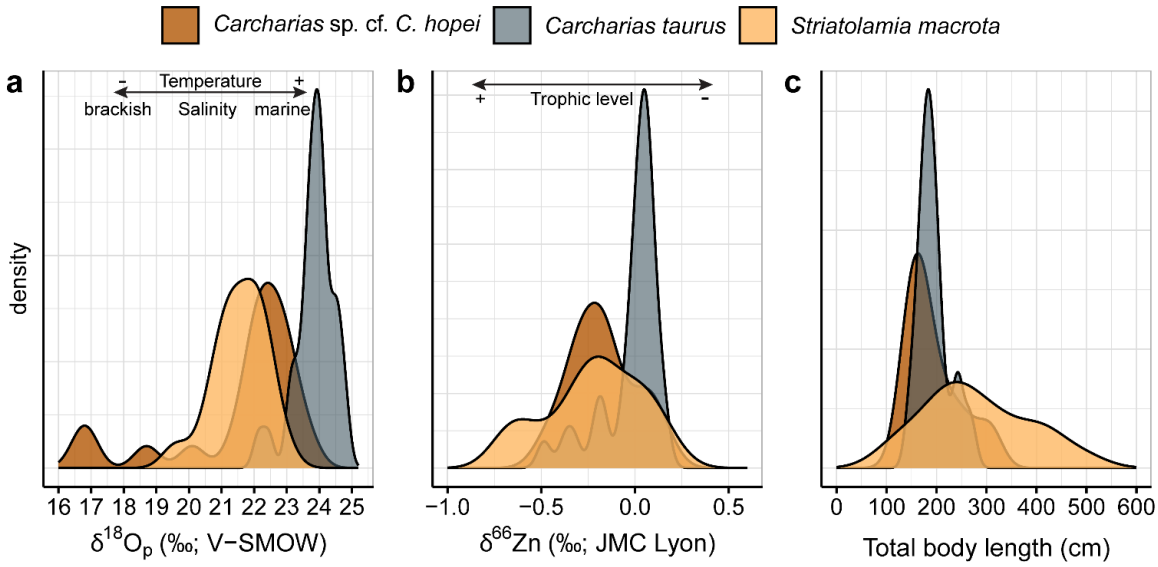

Figure 4.3. Geochemical and total body length values highlight ecological affinities and differences between Eocene and modern sand tiger sharks. Panels (a), (b), and (c) show density distributions of $\delta^{18}O_p$, $\delta^{66}Zn$, and total body length, respectively, for *Carcharias* sp. cf. *C. hopei* (orange), *Carcharias taurus* (grey), and *Striatolamia macrota* (yellow). The direction of $\delta^{18}O_p$ (a) and $\delta^{66}Zn$ (b) values indicate warmer or colder temperatures (or brackish vs marine environments) and higher or lower trophic levels, respectively. Total body length values for fossil sand tiger sharks were estimated using the crown height allometric relationships found in Shimada (2004).

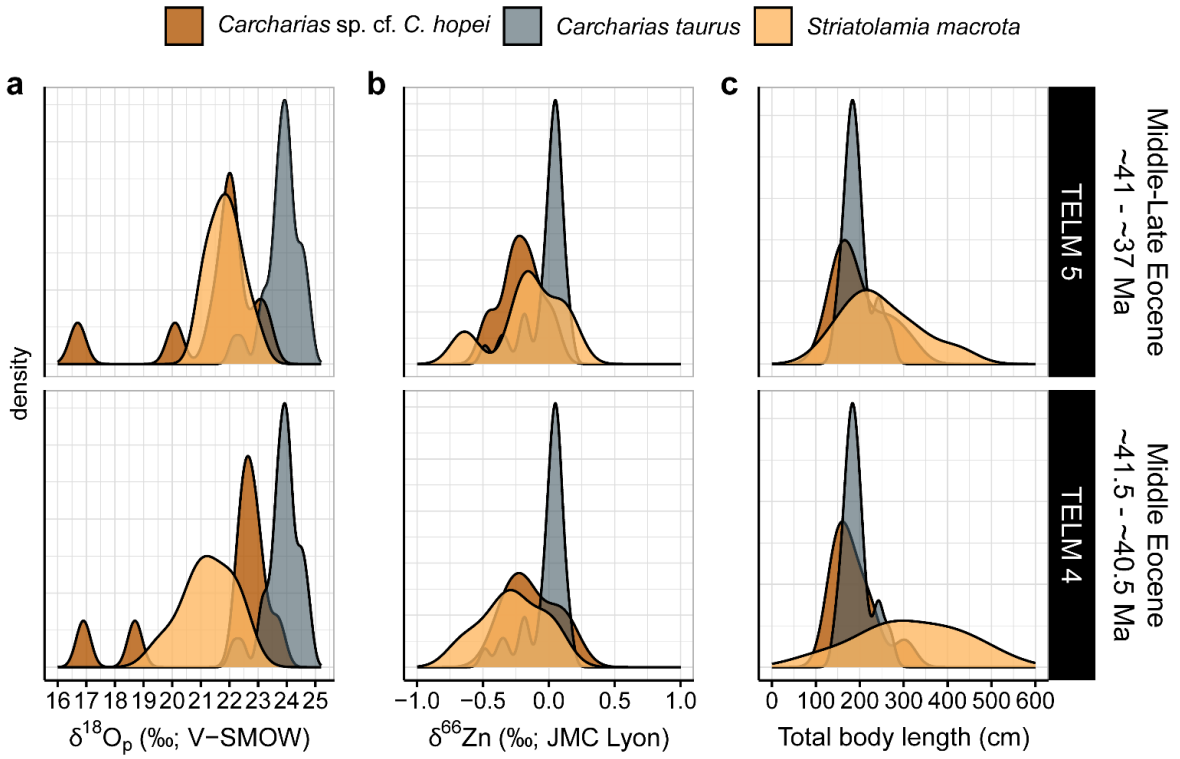

Figure 4.4. Geochemical and estimated total body length values of Eocene sand tiger sharks highlight generally consistent ecological traits over time. Panels (a), (b), and (c) display the density distributions of $\delta^{18}O_p$, $\delta^{66}Zn$, and total body length, respectively, for *Carcharias* sp. cf. *C. hopei* (orange), and *Striatolamia macrota* (yellow) in TELM 4 (lower row) and TELM 5 (upper row). The grey density distributions in all panels are the geochemical and total body length values of the modern *Carcharias taurus* (Karnes et al., 2024; McCormack et al., 2023). Total body length values for fossil sand tiger sharks were estimated using crown height allometric relationships from Shimada (2004). Relative ages for TELM units are based on biostratigraphic models from Amenábar et al. (2020) and Douglas et al. (2014), as summarized by Kim et al. (2020).

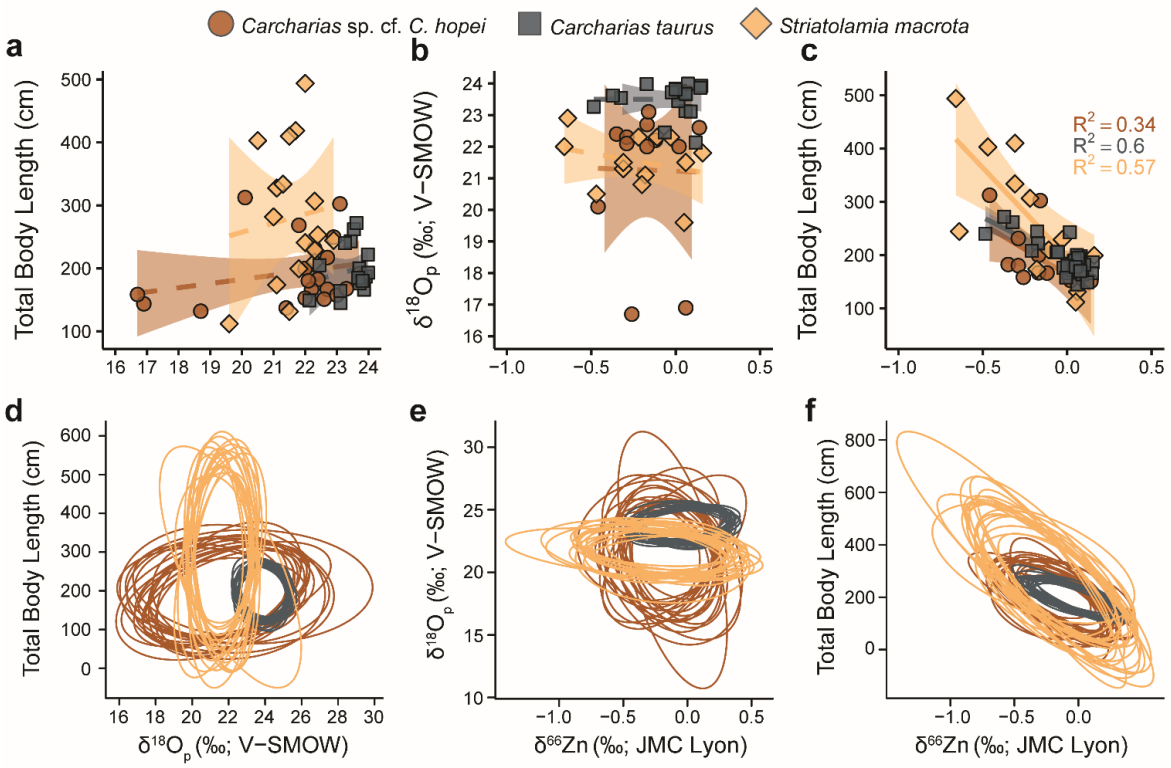

Figure 4.5. The ecological roles of fossil and extant sand tiger sharks are visualized through bivariate scatterplots and Bayesian standard ellipses based on geochemical proxies and total body size. Panels (a), (b), and (c) present the scatterplots, while panels (d), (e), and (f) depict isotopic niche plots. In scatterplots, individual specimens are represented by points with species distinguished by color and shape: *Carcharias* sp. (brown circles), *Carcharias taurus* (gray squares), and *Striatolamia macrota* (yellow diamonds). Linear model fits and their standard error shading are shown in panels (a-c), following the same color scheme. Dashed lines indicate non-significant correlations, while solid lines denote statistically significant correlations. Isotopic niches (panels d-f) are illustrated by twenty randomly generated Bayesian 95% ellipses for each taxon and variable pair. Bayesian ellipses are color-coded by species, following the same scheme.

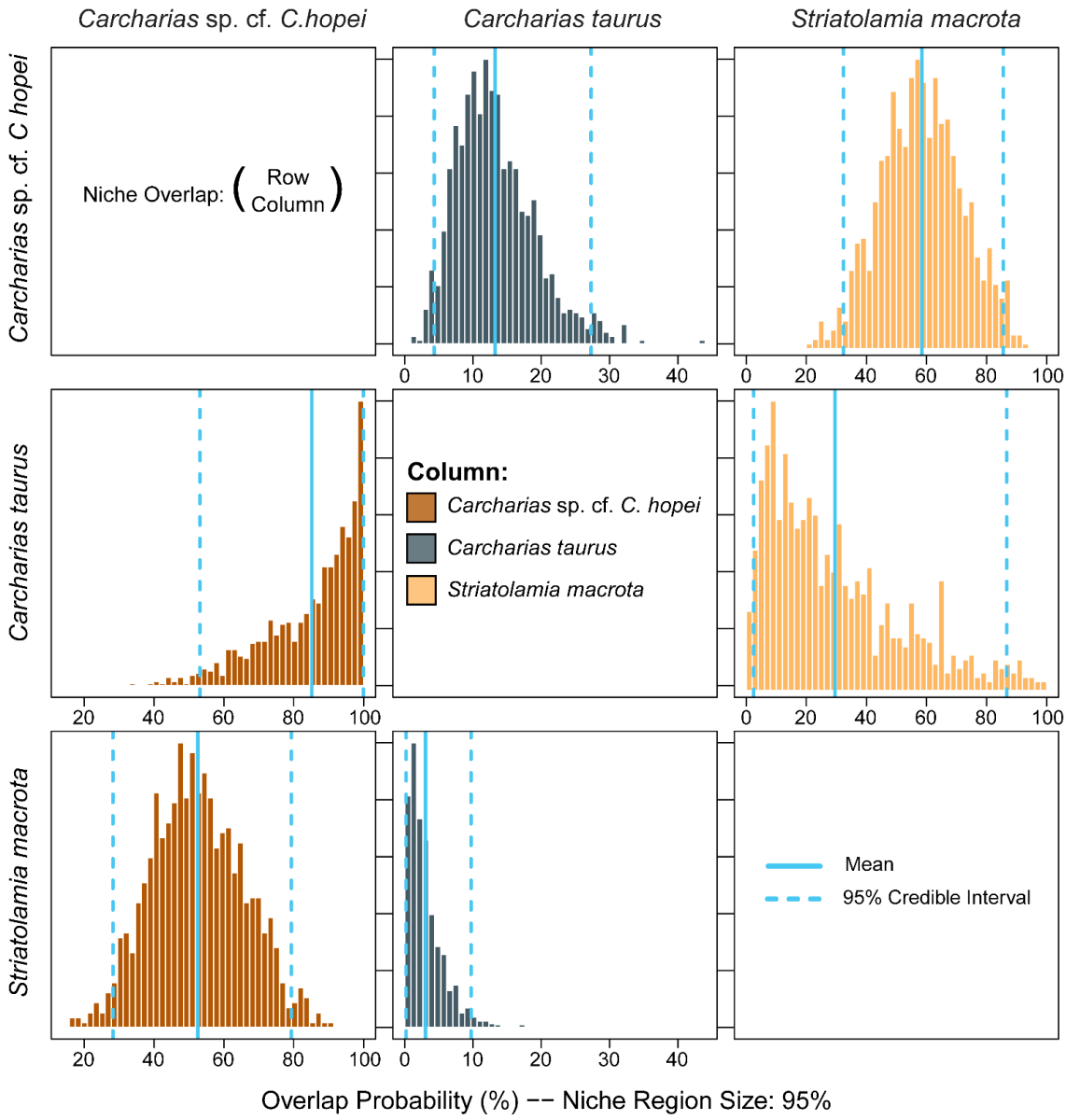

Figure 4.6. Ecological niches of the Eocene sand tiger sharks closely align, with *Caracharias* sp. cf. *C. hopei* serving as a stronger analog for the extant *C. taurus*. Probability distributions are color-covered by taxa. Overlap probability (%) is given as the probability that individuals from taxa in the rows fall within the niche region of species listed in the columns. Solid and dashed turquoise lines indicate mean and 95% credible intervals, respectively.

5. Summary and Conclusions

Understanding the ecology of elasmobranchs in modern settings poses logistical challenges due to their wide geographical distribution, varying with seasons, ontogeny, and prey availability. Moreover, the absence of an extended temporal baseline complicates efforts to assess the impacts of global warming on sharks and rays. To address these challenges, this dissertation examines the habitat and dietary shifts of elasmobranchs across the Eocene Epoch, a period that serves as a valuable analog for the anticipated climatic crisis. Using a multidisciplinary approach, this dissertation reconstructs past environments, investigates environmental preferences, and analyzes the diet of ancient elasmobranchs from isolated tooth remains, with a focus on stable isotope applications. The findings provide critical insights into elasmobranch plasticity and environmental reconstructions during periods of climate change, while also advancing the use of $\delta^{18}O_p$ analysis for small, organic-rich specimens in paleontological, paleoenvironmental, and archaeological research.

Prior to my work, methods for extracting and precipitating biogenic phosphate as silver phosphate salt for $\delta^{18}O_p$ analysis relied on inefficient pretreatments to remove organics like collagen. Existing protocols that incorporate ion exchange resin steps to purify phosphate from contaminants, while effective, typically demand substantial amounts of apatite material (>5 mg). Such sample size is often unavailable when dealing with small specimens like the small shark teeth from the NRM-PZ collection analyzed in this dissertation. The SPORA protocol I developed combines these advantages by utilizing anion exchange resin steps to purify phosphate with a significantly smaller amount of parental, heterogeneous bioapatite material (~1.5 mg), such as small teeth and bones—a threshold previously considered unattainable.

This dissertation resolves a longstanding issue of analytical variability in $\delta^{18}O_p$ measurements caused by organic contamination by identifying, for the first time, the isotopic implications of silver carbonate inclusions, rather than those of nitrogen-based co-precipitation, as a source of variability. The SPORA protocol effectively isolates phosphate from collagen contamination, preventing fractionated-carbonate inclusions of atmospheric CO_2 into silver phosphate crystals. Such isotopic effects are promoted by dissolved collagen during silver phosphate precipitation, adsorbing atmospheric ^{18}O-depleted CO_2 from the vial headspace. Meanwhile, the ^{18}O-enriched CO_2 co-precipitates as silver carbonate (Ag_2CO_3) if a high silver excess is present in the solution, causing isotopic shifts.

To assess its limitations, I tested the SPORA protocol on samples presenting other exogenous compounds included during fossilization, like those having diagenetic carbonate inclusions or those soaked in other organic compounds like tar. Results indicated isotopic shifts exceeding ~0.3‰ relative to pretreated samples. Future studies are needed to evaluate isotopic fractionation in silver phosphate crystals induced by exogenous and endogenous carbonate sources, including the structural carbonate in biogenic apatite, and their effects on phosphate oxygen stable isotopes during the chemical treatments across different protocols.

Elasmobranch fossils are often used to infer global environmental changes, yet their complex ecology can lead to oversimplifications. Shark and rays $\delta^{18}O_p$ measurements from the Eocene deposits of La Meseta and Submeseta formations demonstrate that

elasmobranchs are not passive environmental tracers; their isotopic values provide more insight into their ecology than global environmental changes. This dissertation integrates empirical isotopic data from co-occurring bivalves and offline-simulated oxygen isotope values to reconstruct the habitat use of sharks in relation to oceanographic and environmental changes around the Antarctic Peninsula and the Drake Passage. This framework revealed distinct lifestyles among elasmobranch taxa. For example, *Striatolamia macrota* exhibited extensive latitudinal migrations, while other taxa like *Pristiophorus* preferred colder, potentially deeper waters. Less vagile taxa, such as *Raja* and *Squalus*, reflected seasonal conditions on Seymour Island rather than broader regional signals. Shifts in habitat use over time were evident within taxa. For instance, *Striatolamia macrota* showed broader $\delta^{18}O_p$ variation in TELM 2 and 4 compared to co-occurring bivalves and simulated seasonal values for Seymour Island. In TELM 3 and 5, however, its $\delta^{18}O_p$ values aligned more closely with local conditions, suggesting the taxon adjusted its geographic range as global cooling progressed. By TELM 6, environmental deterioration led to the decline of taxa unable to tolerate colder conditions, while others, like *Carcharias* and *Pristiophorus*, persisted. These results are consistent with the global decline in elasmobranch taxonomic richness during times leading to glaciation throughout the Eocene.

This framework demonstrates how elasmobranch isotopic values can be used to assess their sensitivity to relative depth gradients, as well as local and regional environmental conditions. It also highlights the potential of shark and ray $\delta^{18}O_p$ values to calibrate climate models, improving predictions of local and regional environments, especially for deeper depths that are often underrepresented in simulations. This approach can be extended to other geological settings to advance our understanding of elasmobranch ecology and environmental dynamics.

Elasmobranchs often exhibit a high degree of ecological redundancy in modern ecosystems, but such inferences are more challenging to identify in the fossil record. Comparative analyses of Eocene taxa, such as *S. macrota* and *Carcharias* sp., demonstrate significant ecological redundancy based on tooth morphology. This preliminary finding is further supported by integrating $\delta^{18}O_p$ and $\delta^{66}Zn$ tracers, indicative of comparable environmental preferences and trophic ecology, though differences emerge across time or ontogeny. While trophic position and size structure remained relatively consistent, results suggest shifts in habitat use across time. During TELM 4, $\delta^{18}O_p$ values indicate that *Carcharias* sp. inhabited colder, deeper, or brackish environments, whereas *S. macrota* preferred warmer, shallower marine habitats. By TELM 5, the species exhibited greater overlap in habitat preferences, likely as an adaptive response to global cooling.

Considering size classes could reveal intra- and inter-specific differences in resource use. For instance, higher $\delta^{66}Zn$ values in juvenile *Carcharias* individuals compared to similar age classes of *S. macrota* could suggest that the latter generally fed at lower trophic levels until reaching larger body sizes. Alternatively, lower $\delta^{66}Zn$ values in *S. macrota* could reflect foraging in offshore areas with low baseline $\delta^{66}Zn$ values, consistent with $\delta^{18}O_p$ variability suggesting potential movements across a broad latitudinal gradient. Conversely, juvenile *Carcharias* sp. may have utilized brackish environments, as indicated by their low $\delta^{18}O_p$ and $\delta^{66}Zn$ values, reflecting possible movements and foraging in such habitats. Adult

Carcharias sp. individuals may have preferred marine habitats as suggested by higher $\delta^{18}O_p$ values and lower $\delta^{66}Zn$ values relative to younger ones, respectively. Lower $\delta^{66}Zn$ values in *Carcharias* sp., though, could also indicate that individuals often fed at a higher trophic level than those observed in their fossil and extant relatives. These insights extend to modern analogs, where comparisons with *Carcharias taurus* indicate conserved environmental and dietary strategies across evolutionary timescales, positioning *Carcharias* sp. as a potential analog for extant populations. By linking past and present, this dissertation highlights the conservation potential for endangered species like *Carcharias taurus* and provides a framework for using fossil data to better predict and mitigate the impacts of future climate change on marine ecosystems.

Overall, this dissertation highlights the profound influence of climate on elasmobranch ecology and demonstrates how the fossil record can shed light on the ecological dynamics of modern shark populations. It also informs environmental conditions in their preferred habitats, which are essential for calibrating model simulations to understand patterns and processes in past settings.